UNIVERSIDADE DE LISBOA
FACULDADE DE CIÊNCIAS
DEPARTAMENTO DE QUÍMICA E BIOQUÍMICA

Metal-Organic Frameworks Films for Electrocatalysis

Duarte Nuno Caçador Borralho

Mestrado em Química
Especialização em Química

Dissertação orientada por:
Sara Marlene Quintela Realista
Maria da Estrela Borges de Melo Jorge

2023

Acknowledgements

First off, I'd like to acknowledge my supervisor Dr. Sara Realista for all the guidance, support and patience during this past year, which without them none of this work would have been possible. I'd like to thank as well for all the additional opportunities and experiences offered that challenged me to develop both as a person and as a researcher.

The second acknowledgment goes to my co-supervisor, Prof. Dr. Maria E. Melo Jorge for always finding time to clarify any doubts and giving me additional feedback and ideas that helped me further develop my work, as well as all the numerous samples characterised using PXRD.

I'd like to thank Dr. Paulo Nuno Martinho and all my lab colleagues for getting me accustomed to working in the lab environment, as well as always being available to help with any additional questions, problems and uncertainties that emerged frequently.

I'd like to acknowledge, as well, Dr. Telmo Nunes for all the samples characterised using SEM and Dr. José Augusto for helping with the setup used in the CPE experiments.

Finally, I'd like to thank my friends for always being available to hear me complain in the most stressful moments and offering even more feedback.

Abstract

The need for alternative fuels has been increasing since the latest decades due to climate change. Climate change is caused by the release of greenhouse gases, mainly CO_2 and CH_4, which has increased dramatically with the industrialisation of developing countries. Species like NH_3 can be used as a carrier to produce via its electrocatalytic conversion, H_2 as an alternative carbon-free fuel, offering several advantages when compared with the water splitting process. Advantages such as, a 95% lower standard redox *E* and a 50% higher hydrogen quantity per molecule. Metal-organic frameworks structures that have high crystallinity and permanent porosity constituted by an inorganic centre and organic ligand. These structures show promising results as catalysts due to their properties and the presence of active sites. The use of these structures as electrocatalysts require their immobilisation on a conductive surface, as they are obtained in powder form using the most common method – solvothermal synthesis. There are two different electrochemical methods for the formation of metal-organic framework films, a direct method, consisting of the formation of the metal-organic framework directly on the surface of the conductive substrate and an indirect method, which focuses on immobilising these materials in a powder form post-synthesis. This work focuses on the synthesis, immobilisation, and electrochemical studies of some of these materials as well as their application for the electroconversion of ammonia. The films were formed using the cathodic deposition as the direct method and the electrophoretic deposition as the indirect method. The obtained metal-organic framework powders and films were characterised using X-rays diffraction, Fourier Transform infrared spectroscopy and scanning-electron microscopy. The electrochemical studies were made using cyclic voltammetry and the conversion of NH_3 was investigated using controlled potential electrolysis experiments and its products were quantified using gas chromatography with a thermal conductivity detector.

Keywords: Metal-organic frameworks, electrochemical deposition, films, ammonia conversion, hydrogen.

Resumo

A necessidade de novos combustíveis, especialmente combustíveis verdes, tem vindo a aumentar devido à grande escala da industrialização de países em desenvolvimento nestas últimas décadas, que tem levado ao aumento das alterações climáticas, agravado pela alta emissão de gases com efeito de estufa (do inglês GHGs) na combustão dos combustíveis fósseis, como o dióxido de carbono e metano. Estas mudanças estão a levar a crises climáticas à escala mundial como o aumento dos níveis dos oceanos devido ao aumento da temperatura global, que de acordo com o *Intergovernmental Panel of Climate Change* (IPCC) aumentou cerca de 1.1 ℃ na última década. Os GHGs emitidos em excesso são acumulados na atmosfera, impedindo a reflexão de parte da radiação infravermelha emitida pelo Sol para fora da atmosfera, sendo esta parte absorvida por os gases mencionados. Um possível combustível livre de carbono é o hidrogénio, este que como combustível apresenta diversas propriedades que o tornam promissor, propriedades tais como a sua grande abundância, o facto de ser o elemento mais leve, ser não-tóxico, acessível e oferece uma maior densidade gravimétrica de energia. No entanto apresenta também diversos desafios que impedem a sua implementação em grande escala, sendo esses a sua alta inflamabilidade, volatilidade e a sua baixa densidade volumétrica de energia para além do risco de fragilização dos materiais metálicos onde é armazenado, levando estes riscos a problemas relacionados com o seu armazenamento e transporte. Apesar do hidrogénio ser principalmente produzido a partir dos combustíveis fosseis utilizado processos como o *reforming* do metano e a gasificação do carvão, pode ser também produzido de forma verde usando espécies que contém hidrogénio, tal como a água. A água pode ser convertida de forma verde utilizando energia proveniente de radiação solar (fotocatálise), energia elétrica (eletrocatálise) e energia térmica (termólise), todas estas com o seu processo sofisticado. Focando na eletrocatálise, o grande desafio utilizando este método é a energia necessária para realizar a sua conversão pois a água tem um *E* de redox padrão de cerca de 1,23 V *vs.* SHE, sendo que se procura catalisadores acessíveis e abundantes que consigam reduzir esse valor e ao mesmo tempo aumentar a sua potência. No entanto, existe outra espécie que também consegue ser convertida em hidrogénio que apresenta por si diversas vantagens em relação à água – o amoníaco. O amoníaco, teoricamente, consegue ser convertida com simplesmente uma fração da energia necessária para água, devido ao seu *E* de redox padrão de cerca de 0,06 V *vs.* SHE, o que significa que com a mesma energia é possível produzir cerca de 95% mais hidrogénio utilizando amoníaco ao invés da água, para além de cada molécula de amoníaco conter cerca de 50% mais hidrogénio que a molécula de água. O amoníaco apresenta também diversas vantagens como um transportador de hidrogénio, em relação a outros transportadores de hidrogénio, sendo essas a sua elevada densidade de hidrogénio (17,8 wt%), ser não-inflamável, estável e a sua tecnologia de transporte que é extremamente conhecida (devido a um dos processos industriais mais globalmente utilizado para a produção de amoníaco, o processo Haber-Bosch, sendo o amoníaco utilizada principalmente para fins agrícolas). O amoníaco é, no entanto, um químico tóxico, mas que consegue ser facilmente detetado no caso de fugas devido ao seu cheiro intenso. As estruturas metalo-orgânicas (do inglês MOFs) são materiais recentes (últimas décadas) que mostram grande potencial em várias aplicações, tais como no armazenamento de gases, catalisadores, separação química, como sensores, entre outros. São materiais constituídos por ligandos orgânicos coordenados a um centro metálico e apresentam elevada cristalinidade, elevada porosidade permanente e múltiplos centros ativos. Devido às inúmeras possibilidades de combinações utilizando diferentes centros metálicos e ligandos orgânicos, estes materiais apresentam uma versatilidade extremamente elevada. Estas propriedades são extremamente importantes para potenciais catalisadores. Estes materiais são produzidos mais habitualmente utilizando métodos solvotérmicos (reações em condições de elevada pressão e temperaturas utilizando solventes) dando origem a um pó microporoso. No entanto, para a sua utilização em aplicações de eletrocatálise é necessário a sua imobilização numa superfície condutora e para este fim existem diversos métodos eletroquímicos, ambos diretos e indiretos. Nos métodos diretos,

os precursores iniciais utilizados nas sínteses solvotérmicas são utilizados e a estrutura é formada diretamente na superfície do elétrodo com a aplicação de um determinado *E*. A deposição catódica é um dos métodos diretos que utiliza para além dos precursores, uma probase, que a um determinado potencial irá transformar-se numa base, desprotonando o ligando orgânico dando origem à reação dos precursores na superfície do elétrodo. Nos métodos indiretos a MOF é previamente sintetizada em forma de pó e posteriormente depositada na superfície do elétrodo. A deposição eletroforética é um dos métodos indiretos, onde o pó inicial é utilizado na formação de uma suspensão onde dois elétrodos são imersos em paralelo com áreas e distância fixas e de seguida a MOF em pó é imobilizada a através de um campo elétrico que é originado a partir da aplicação de um potencial. Várias otimizações podem ser realizadas na síntese das MOFs afetando a sua deposição pelo meio indireto. Na forma de pó, a utilização de um modulador ou a modificação pós-sintética permite o controlo de diversas propriedades, tais como o crescimento da sua estrutura cristalina e a incorporação de espécies alternativas ou defeitos na estrutura aumentando a carga das partículas do pó.

Este trabalho consiste na síntese, imobilização e estudos eletroquímicos de alguns de filmes destes materiais na presença de amoníaco aquosa, para estudar o seu comportamento eletroquímico na presença do amoníaco e a sua estabilidade em meio básico e por fim, também a sua aplicação na conversão de amoníaco utilizando a técnica de eletrólise a potencial controlado (do inglês CPE). As sínteses de nove MOFs diferentes foram tentadas, sendo que só seis destas foram bem-sucedidas – ZIF-8, Mg-MOF-74, Ni-MOF-74, HKUST-1, UiO-66 e UiO-66-NH_2. Destas seis, todas à exceção da HKUST-1 apresentaram elevada estabilidade na presença de água. Procedeu-se posteriormente a tentativas de imobilização de algumas destas nove MOFs, utilizando os métodos diretos e indiretos mencionados – a deposição catódica e a deposição eletroforética respetivamente. Pelo método de deposição catódica tentou-se formar filmes utilizando as MOFs que não foram bem-sucedidas na sua síntese e umas que apresentaram alta estabilidade em água – MOF-5, IRMOF-3, Mg-MOF-74, Ni-MOF-74 e UiO-66. Infelizmente, não foi possível obter filmes cristalinos de nenhuma destas MOFs utilizando o método direto. Pelo método de deposição eletroforética, tentou-se depositar as seis MOFs que foram bem-sucedidas na sua síntese - ZIF-8, Mg-MOF-74, Ni-MOF-74, HKUST-1, UiO-66 e UiO-66-NH_2. Destas seis, foi possível imobilizar três MOFs: Ni-MOF-74, UiO-66 e UiO-66-NH_2. Todos os pós sintetizados e todos os filmes promissores foram caracterizados utilizando difração de raios-x de pós (do inglês PXRD), espetroscopia de infravermelho com transformada de Fourier (do inglês FTIR) e microscopia eletrónica de varrimento (do inglês SEM). Os filmes das três MOFs foram posteriormente estudados electroquimicamente utilizando a técnica de voltametria cíclica (do inglês CV) e após os estudos de conversão o hidrogénio produzido foi quantificado utilizando cromatografia gasosa com um detetor de condutividade térmica (do inglês GC-TCD). O filme da Ni-MOF-74 depositado num elétrodo de óxido de estanho dopado com flúor (do inglês FTO) mostrou alta produção de hidrogénio (17,09-28,11 µmol) mas ao mesmo tempo baixa estabilidade, pois o filme degradou-se durante o processo onde se verificou uma completa degradação apenas ao fim de 45 min. O filme de UiO-66 também depositado em FTO produziu resultados promissores (4,21-9,27 µmol) e mostrou, ao contrário do filme de Ni-MOF-74, alta estabilidade mantendo a sua estrutura cristalina após o processo.

Palavras-chave: Estruturas metalo-orgânicas, deposição eletroquímica, filmes, conversão de amoníaco, hidrogénio.

Contents

Figures

Tables

Equations

Schemes

Symbols and Abbreviations

ATR – Attenuated Total Reflectance

BDC – Benzene-1,4-dicarboxylic

BTC – Benzene-1,3,5-tricarboxylic

CE – Counter Electrode

CPE – Controlled Potential Electrolysis

CV – Cyclic Voltammetry

DEF – Diethylformamide

DHTA - 2,5-dihydroxybenzene-1,4-dicarboxylic

DMF – Dimethylformamide

DRIFT – Diffuse Reflectance Infrared Fourier Transform

E – Potential

EDS – Energy Dispersive Spectroscopy

EtOH – Ethanol

FTIR – Fourier Transform Infrared

FTO – Fluorine-doped Tin Oxide

GC– Gas Chromatography

GC-TCD – Gas Chromatography - Thermal Conductivity Detector

GHG – Greenhouse Gas

h – Hour

HKUST-1 – Hong Kong University of Science and Technology-1

Hmim – 2-methylimidazole

I – Current

IPCC – Intergovernmental Panel on Climate Change

IRMOF-3 – Isoreticular Metal-Organic Framework-3

ITO – Indium-doped Tin Oxide

MeOH – Methanol

Mg-MOF-74 – Magnesium Metal-Organic Framework-74

min – Minute

MOF – Metal-Organic Framework

MOF-5 – Metal-Organic Framework-5

NHE – Normal Hydrogen Electrode

Ni-MOF-74 – Nickel Metal-Organic Framework-74

OCP – Open Circuit Potential

PBS – Phosphate-Buffered Saline

PCP – Porous Coordination Polymers

PXRD – Powder X-Ray Diffraction or Powder X-Ray Diffractogram

RE – Reference Electrode

RPM – Rotations Per Minute

SBU – Secondary Building Unit

SEM – Scanning Electron Microscopy

SHE – Standard Hydrogen Electrode

$TBAPF_6$ - Tetrabutylammonium hexafluorophosphate

TCD – Thermal Conductivity Detector

UiO-66 - Universitetet i Oslo-66

UiO-66-NH_2 - Universitetet i Oslo-66-NH_2

WE – Working Electrode

ZIF-8 – Zeolitic Imidazolate Framework-8

ZnMn-ZIF-8 – Zinc/Manganese Zeolitic Imidazolate Framework-8

δ – Bending Vibration

θ – Bragg Angles

ν – Stretching Vibration

η - Overpotential

1 Introduction

1.1 The Importance of Clean Energy

In recent years, climate change has given great cause for concern mainly caused by the increasing use of fossil fuels and their derivatives in the last decades. This increase is associated with the industrialisation of developing countries and the improvement of the quality of life leads to an increase in the world population.[1] Climate change is defined as an unnatural change in the average temperature levels and weather behaviour across the globe, which can lead, in extreme cases, to an increase in catastrophic natural disasters, such as the rise of ocean levels.[2] In comparison to the XIX century the global surface temperature has increased by an average of 1.1 °C in the last decade.[3]

The excessive use of fossil fuels is extremely concerning due to the high volume of greenhouse gases (GHGs) emitted as by-products during their combustion to produce usable energy. Some of those gases are carbon dioxide, methane, nitrous oxide, hydrofluorocarbons, among others. The GHGs produced accumulate in the Earth's atmosphere which excessively traps the infrared radiation emitted from the sun leading to an increase in the overall Earth's temperature, as seen in **Figure 1.1**. Another problem caused by the emission and accumulation of GHGs in the atmosphere is the deterioration of the air quality, which according to the World Health Organisation, approximately 99% of the population lives in locations where the air pollution exceeds their guidelines.[4] The scarcity of fossil fuels is another challenge of the current society, as there is no way to renew them in our demanding time scale.

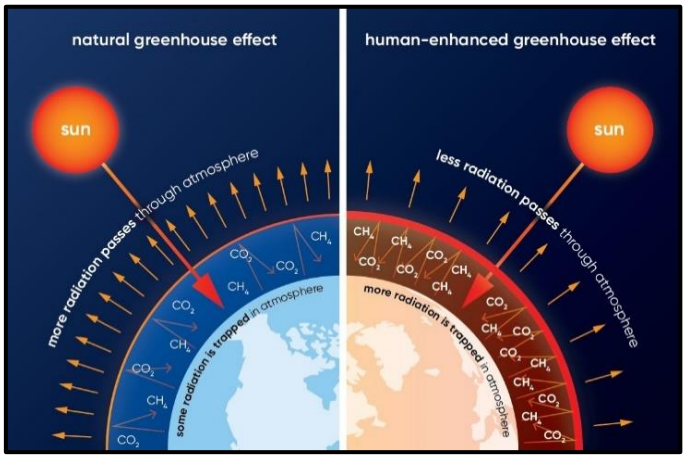

Figure 1.1 – Representation of the natural and human-enhanced greenhouse effect.[5]

For these reasons, it is crucial to start transitioning to clean alternatives to fossil fuels at an accessible rhythm, especially if those are from a renewable and/or readily available abundant sources, such as solar, wind, water, biomass, etc. A clean fuel means that harmful by-products are produced in negligible quantities, non-existent or can be captured to be used in other processes.[6] Another advantage provided by the transition, is lessening the dependency on countries with fossil fuels reserves preventing possible geopolitical crisis. This transition will also lead to an economic growth of the dependent countries in several ways, such as creating more job opportunities in the energy sector and decreasing the need of

fossil fuels. Developing self-sustainability through this increased energy production and reduced fossil fuel usage will eventually eliminate the need for importing fossil fuels.

Currently, the energy transition is being held back because of several problems related to its storage, transport, efficiency, and lack of infrastructure.[7] However, the investment in this area is increasing and consequently the price of clean energy from renewable sources is also becoming more accessible.[8] In parallel with the transition, the development of materials that can capture and convert GHGs is essential especially in cases where its emission are unavoidable, such as in certain industrial processes, agriculture, transportation, and electricity generation.[1,7] Materials such as zeolites, silicas, porous carbons, porous organic polymers, and metal-organic frameworks have been investigated for showing potential in the capture of carbon dioxide followed up by its conversion. Metal-organic frameworks specially get a lot of attention due to their versatility.[9–12]

1.2 Hydrogen as an Alternative Energy Source

Green hydrogen, as a carbon-free fuel, fits the criteria as an alternative energy source to fossil fuels. Hydrogen is the most abundant and lightest element, is non-toxic, extremely accessible and offers higher gravimetric energy density than conventional fuels (**Figure 1.2**). Despite its many advantages, there are limitations related to the hydrogen properties that prevent its widespread implementation. Properties like its flammability and volatility, low volumetric energy density with the risk of causing embrittlement on metal leads to problems related to its storage and transport.[13–17]

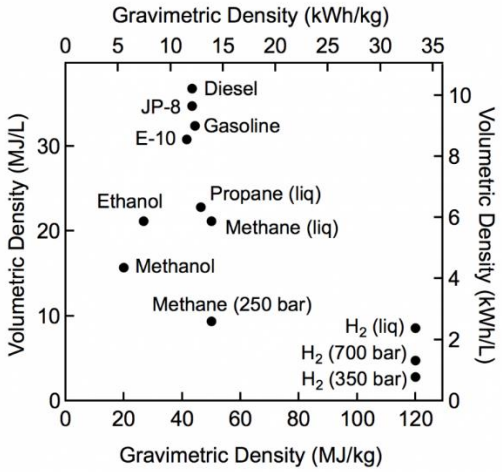

Figure 1.2 – Comparison of the gravimetric and volumetric energy density of hydrogen with other conventional fuels.[18]

Hydrogen can be produced from renewable and non-renewable sources using clean processes and fossil fuels. Depending on the production technology hydrogen can have several names associated to a colour, the more common ones are grey, blue, and green hydrogen. As represented in **Figure 1.3**, grey hydrogen is produced alongside with GHGs from fossil fuels, blue hydrogen is also produced alongside with GHGs but using capture technologies to reduce their release to the atmosphere. Green hydrogen is produced using clean sources such as water where the only by-products are harmless compounds like oxygen.

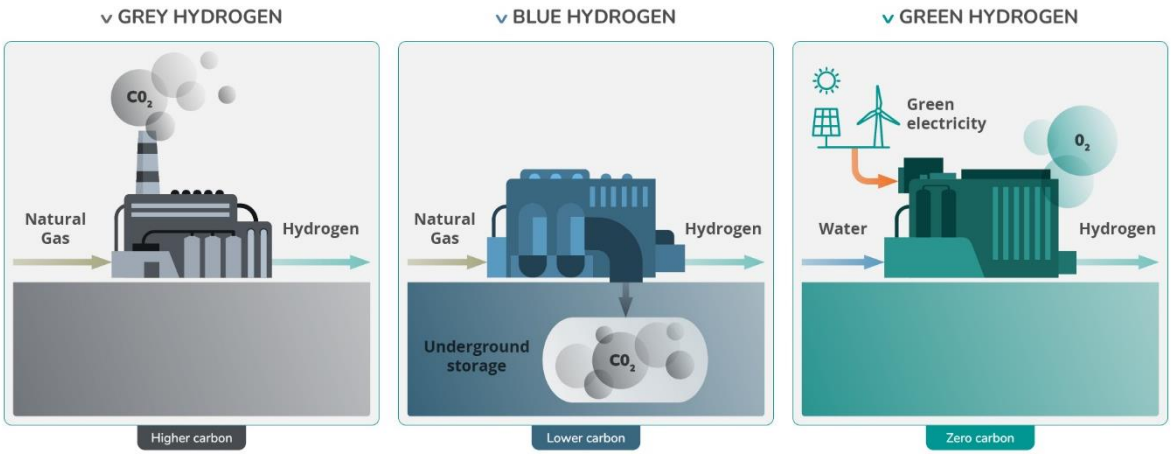

Figure 1.3 – Differences between the productions of grey, blue, and green hydrogen. Adapted from ref.[19]

The hydrogen production sectors need severe improvement. Currently most of the hydrogen is produced from fossil fuels with techniques such as steam methane reforming and coal gasification, while most of green hydrogen is obtained via water splitting. It is essential to increase the production of hydrogen using clean and renewable processes. Apart from its energy applications, hydrogen is also widely used as a crucial component in chemical industries.[20,21] The hydrogen ecosystem is represented in **Figure 1.4**.

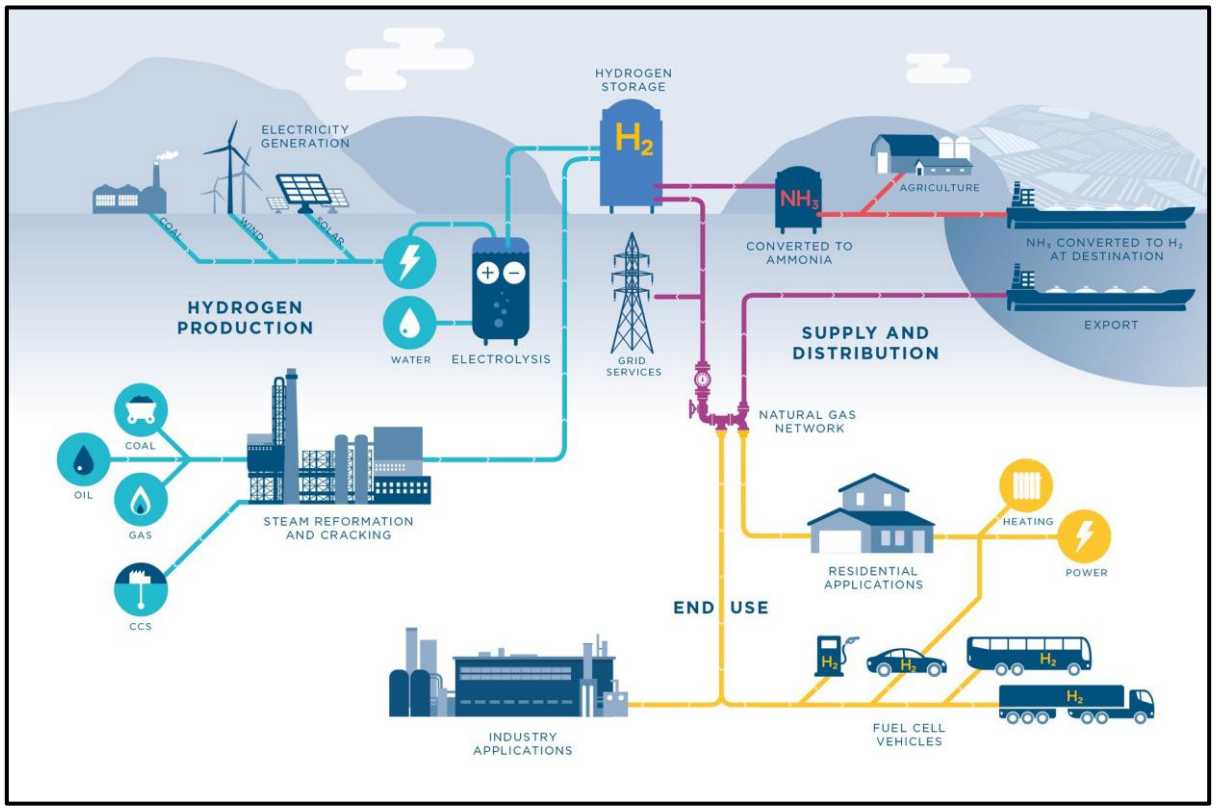

Figure 1.4 - Hydrogen ecosystem: its production, distribution, and applications.[22]

Some of the most predominant technologies for hydrogen production are represented in **Figure 1.5** and will be further discussed below.

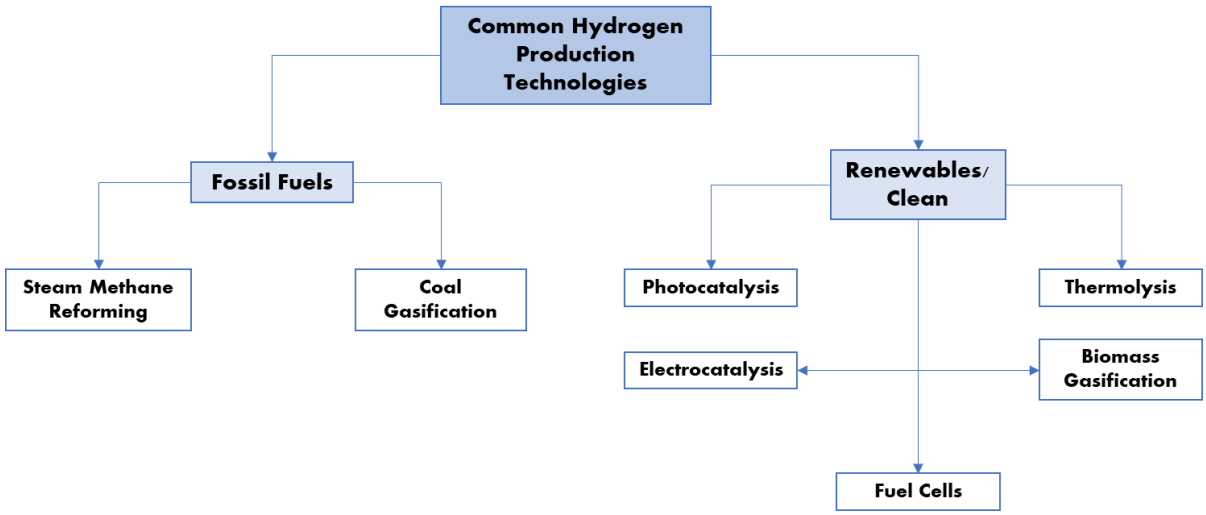

Figure 1.5 - Common hydrogen production technologies using both fossil fuels and renewables/clean sources.

At present, most of the hydrogen production (about 95%) is derived from fossil fuels.[23] The most common method of hydrogen production is steam methane reforming. In this process, methane is mixed with water vapour at high temperatures in a steam reformer, yielding carbon monoxide and hydrogen, a mixture also known as syngas. This reaction is reversible and largely endothermic.[21] Hydrogen can also be produced from coal via its gasification. Coal gasification starts with its pulverisation followed by drying and grinding, After, the introduction of oxygen and water vapour in the flow yields hydrogen and carbon monoxide. In both these processes the carbon monoxide produced may also react with the water vapour forming additional hydrogen and carbon dioxide.[21,24]

Other clean and more sustainable methods may also be used for hydrogen production. Among those, the most used source is the process of water splitting into molecular hydrogen and oxygen, using processes such as electrocatalysis, photocatalysis and thermolysis. The mechanism is the main difference between these processes. In photocatalysis, a catalyst is used to harvest light energy causing its photoexcitation and forming e^-/h^+ pairs which will initiate the reaction. [25–27] In electrocatalysis, an electric current is used instead, through the application of a potential (E).[27,28] In thermolysis, the water splits via its decomposition using high temperatures.[29] However, these processes are not limited to water, other hydrogen containing species, such as ammonia, may also be used.

Green hydrogen can also be produced using biomass in processes such as its gasification. Biomass gasification is a process with relative maturity already used commercially and it uses similar concepts as that of the coal gasification. Oxygen and water vapour are introduced in the flow at high temperatures to producing hydrogen, carbon monoxide, carbon dioxide, nitrogen, and methane.[30] Another valuable alternative are fuel cells, which have been receiving a lot of attention from the research community. Fuel cells rely on a similar operation as batteries, but instead of producing electrical energy using stored energy, they convert chemical energy from the fuel used into electrical energy. The main advantage of these devices is their higher electrochemical conversion efficiency due to its design where the electrodes are separated by the electrolyte. Their compact design makes them ideal for use in mobile applications. [21,31,32]

These are some of the more common hydrogen production technologies, however, several more technologies exist. Technologies such as, steam reforming using other hydrocarbons, water radiolysis, photolysis of biomass, among others.[17,20,21,23,26,30,33,34]

Another matter is the hydrogen storage, where the most common methods are its compression and liquification. Both these methods require the use of extreme conditions such as high pressures (350 to 700 bar) and low temperatures (at 1 atm its boiling point is -252.8 ºC), or a combination of both. These methods allow for a maximum of purity but also present higher risks. As mentioned above, they also suffer from low volumetric energy density, high relative cost, and the need for specialised infrastructure. In a widespread scale and in mobile applications these methods are not viable options.[14,35–37] Alternatives to these storage methods are the adsorption of hydrogen on the surface of solids or absorption within them, using for example microporous materials. The usage of hydrogen containing species, hydrogen carriers, is another alternative, using species like metal hydrides or liquid organic carriers. The use of these methods minimises the risks of using extreme conditions but also have their own challenges. Depending on the compound, challenges like low capacity for hydrogen storage, low reversibility, slow kinetics, the need for efficient catalysts, among others are common.[15,33,35,36]

In conclusion, it is crucial to develop novel and more efficient green hydrogen production methods and storage methods where its combination leads to most of these challenges and risks being reduced or eliminated.

1.3 Ammonia as a Hydrogen Carrier

As a carbon-free hydrogen carrier, ammonia, an alkaline colourless chemical with a strong odour, has a lot of potential as an alternative technology for the storage and transport of hydrogen. It offers valuable advantages such as, high hydrogen density (around 17.8 wt%), a well-known storage technology with long-term stability in its transportation, and it is practically non-flammable. Although it has a relatively high toxicity, due to the strong distinct smell, leakages are easily detected and avoided. Ammonia also has the advantage of requiring less extreme storage conditions (-33 ºC or 10 bar) when compared to the requirements for the compression and liquification of hydrogen.[14,38]

The production of ammonia using the process of Haber-Bosch is one of the most well researched and largest chemical processes used in the industry mainly to produce fertilisers. During this process, nitrogen reacts with hydrogen obtained from methane through a catalysed reaction under high temperatures and pressures (400 to 600 ºC at 200 bar). As a consequence of the well-established process, the infrastructures and technologies required for the storage and transport of ammonia are already developed.[38] However, the ammonia produced using this process is only as clean as the hydrogen used in its synthesis, giving further urgency to develop greener hydrogen production technologies. Aside from the Haber-Bosch process, ammonia may also be produced using methods such as, electrochemical, or thermochemical nitrogen reduction.[14,39,40] The production of ammonia via nitrate reduction in wastewater treatment is also an interesting alternative.[41] Afterwards, to use it as a fuel, ammonia needs to be converted to hydrogen. Hydrogen can be generated from ammonia through its conversion or decomposition using techniques such as electrocatalysis[42], photocatalysis[43] and thermal decomposition[44]. The route taken by the ammonia as a hydrogen carrier in the energy sector is represented in **Figure 1.6**.

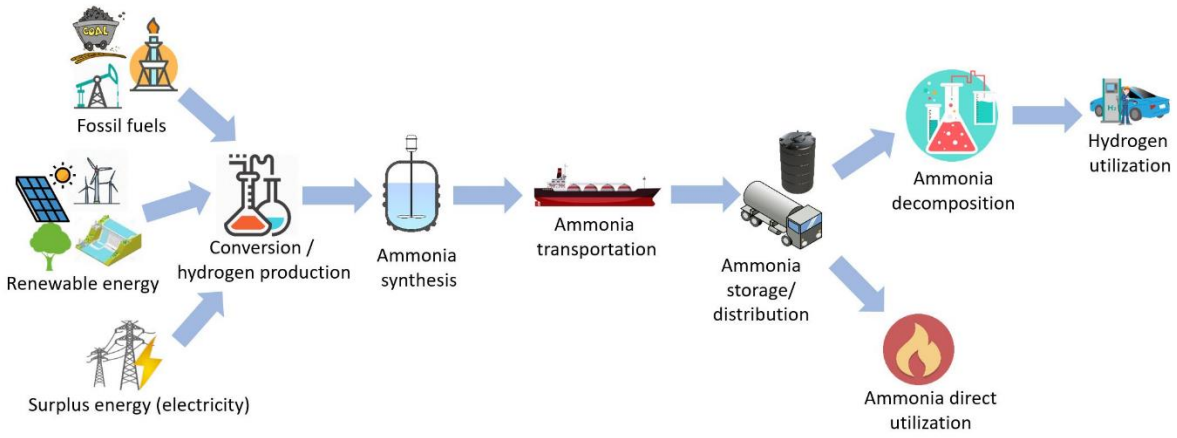

Figure 1.6 - Ammonia production and applications route as a hydrogen carrier in the energy sector.[14]

1.4 Electrocatalytic Ammonia Conversion for Hydrogen Production

Electrocatalysis is a process involving an oxidation and a reduction reaction through the transfer of electrons originated by applying a *E*, where using a catalyst may lead to a reduction in the overpotential (η) of the reactions. The performance of a catalyst will heavily depend on the selectivity and activity of the catalyst towards a specific reaction.[45] An important advantage of electrocatalysis is being able to work under less extreme conditions when compared to other catalytic procedures.

As mentioned in **Chapter 1.3**, when using ammonia as a carbon-free hydrogen carrier, electrocatalysis is a method that allows for its conversion into hydrogen. Both aqueous and liquid ammonia can be converted to hydrogen using electrocatalysis. The reactions for both are represented in **Equations 1.1**, **1.2** and **1.3** for aqueous ammonia and **Equations 1.4**, **1.5** and **1.6** for liquid ammonia.[42,46,47]

Aqueous ammonia:

Anode: $$2NH_{3(aq)} + 6OH^-_{(aq)} \rightarrow N_{2(g)} + 6H_2O_{(l)} + 6e^-$$ **(Equation 1.1)**

Cathode: $$6H_2O_{(l)} + 6e^- \rightarrow 3H_{2(g)} + 6OH^-_{(aq)}$$ **(Equation 1.2)**

Overall: $$2NH_{3(aq)} \rightarrow N_{2(g)} + 3H_{2(g)}$$ E^0 = 0.06 V *vs.* SHE[48,49] **(Equation 1.3)**

Liquid ammonia:

Anode: $$8NH_{3(l)} \rightarrow N_{2(g)} + 6NH^+_{4(l)} + 6e^-$$ **(Equation 1.4)**

Cathode: $$6NH^+_{4(l)} + 6e^- \rightarrow 3H_{2(g)} + 6NH_{3(l)}$$ **(Equation 1.5)**

Overall: $$2NH_{3(l)} \rightarrow N_{2(g)} + 3H_{2(g)}$$ E^0 = 0.08 V *vs.* SHE[50] **(Equation 1.6)**

One advantage of using aqueous ammonia is its ability to work at room temperature and ambient pressure. Under these conditions ammonia is oxidised in the anode while hydrogen is generated in the cathode. Additionally, when ammonia is oxidised several other nitrogen containing products, aside from

molecular nitrogen, may be formed (ex. nitrite and nitrate, as seen in **Figure 1.7**) depending on the ammonia concentration, the solution's pH, and the applied *E* as represented in the Pourbaix diagram in **Figure 1.8**. [42,50]

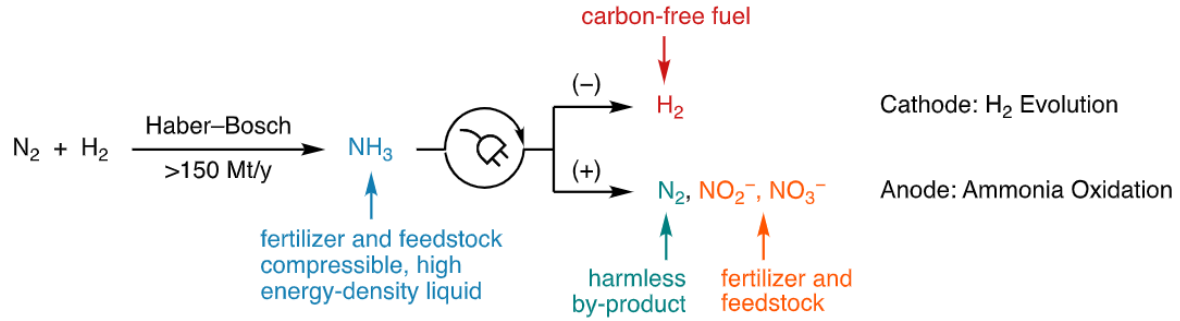

Figure 1.7 - Electrolytic splitting of aqueous ammonia via its oxidation and its possible products.[42]

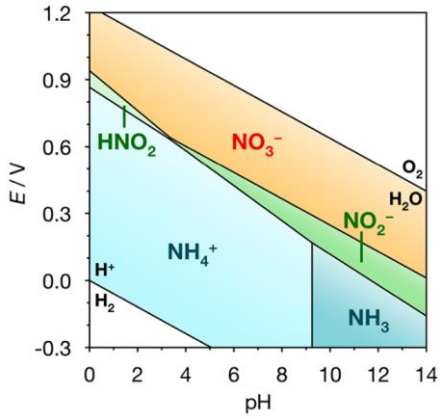

Figure 1.8 - Pourbaix diagram of certain nitrogen species in aqueous conditions.[42,51]

Water is the primary source of green hydrogen, as noted in **Chapter 2**, with electrolysis as the most common process. The water splitting reactions are represented in **Equations 1.7**, **1.8** and **1.9**.

Water:

Anode: $$4OH^-_{(aq)} \rightarrow O_{2(g)} + 2H_2O_{(l)} + 4e^-$$ **(Equation 1.7)**

Cathode: $$2H_2O_{(l)} + 2e^- \rightarrow H_{2(g)} + 2OH^-_{(aq)}$$ **(Equation 1.8)**

Overall: $$2H_2O_{(l)} \rightarrow 2H_{2(g)} + O_{2(g)}$$ E^0 = 1.23 V *vs.* SHE [48,49] **(Equation 1.9)**

Both aqueous ammonia and water have similar reactions, where the only difference is in the oxidation reaction. In aqueous ammonia, ammonia is oxidised alongside the hydroxide ions (**Equation 1.1**) whereas in water its solely the hydroxide ions (**Equation 1.7**). Ammonia has an important advantage in comparison to water, even though production, storage and transport of water is trivially more accessible and poses no risks. The main advantage is the overall standard *E* of aqueous ammonia conversion (0.06

V *vs.* SHE) being lower than water splitting (1.23 V *vs.* SHE). This means that, theoretically, using the same amount of energy it is possible to produce 95% more hydrogen using aqueous ammonia. Additionally, each molecule of ammonia contains 50% more hydrogen than the molecule of water. [48] Since the real conditions of the reaction will differ from ideal conditions, the redox *E* of the reaction will also be different from its standard *E* and to that difference corresponds the overpotential. The main challenge of electrocatalytic ammonia conversion for hydrogen production is finding a suitable catalyst that can minimise the overpotential of the reaction while having high selectivity and activity. Although the overall reaction is thermodynamically favourable, its slow kinetics makes its implementation as a hydrogen carrier unviable.[48] Aside from its slow kinetics, other challenges such as the risk of corrosion and catalyst poisoning caused by the solution pH (approx. 12 at higher concentrations) and unreversible nitrogen adsorption prevents the use of most catalysts. Therefore, it is crucial to find a low-cost catalyst made of Earth-abundant elements that offer high stability in alkaline conditions. Catalysts made of noble metals like platinum, iridium, rhodium, palladium, and ruthenium offer decent performance but suffer drawbacks due to their scarcity and cost.[52]

The mechanism of ammonia oxidation in strong alkaline aqueous solutions using potassium hydroxide as the supporting electrolyte on platinum surfaces were thoroughly studied. According to Oswin, Salomon, and coworkers[53] ammonia is oxidised in steps to M–NH_2, M=NH and M≡N while $N_{2(g)}$ is formed by dimerisation of the $N_{(ads)}$ at the catalysts' surface (**Equations 1.10**, **1.11** and **1.14**, **1.15**). Further studies on fuel cells showed that the adsorption of ammonia on the surface of the electrode takes place prior to its oxidation. An alternative mechanism was proposed where $N_{2(g)}$ is formed via the oxidation of the intermediary N_2H_y species instead of the dimerisation of $N_{(ads)}$ (**Equations 1.10-1.14**).[54]

$$NH_{3(aq/ads)} + OH^-_{(aq)} \rightarrow NH_{2(ads)} + H_2O_{(l)} + e^- \quad \textbf{(Equation 1.10)}$$

$$NH_{2(ads)} + OH^-_{(aq)} \rightarrow NH_{(ads)} + H_2O_{(l)} + e^- \quad \textbf{(Equation 1.11)}$$

$$2NH_{x(ads)} \rightarrow N_2H_{y(ads)} \quad \textbf{(Equation 1.12)}$$

$$N_2H_{y(ads)} + yOH^-_{(aq)} \rightarrow N_{2(g)} + yH_2O_{(l)} + ye^- \quad \textbf{(Equation 1.13)}$$

$$NH_{(ads)} + OH^-_{(aq)} \rightarrow N_{(ads)} + H_2O_{(l)} + e^- \quad \textbf{(Equation 1.14)}$$

$$2N_{(ads)} \rightarrow N_{2(g)} + 2M_{(s)} \quad \textbf{(Equation 1.15)}$$

Considering the catalyst reactivity and selectivity, if the applied *E* is high enough that the oxidation of water simultaneously occurs, competition between the ammonia and water will take place. This will lead to the formation of O_2 and N_2 which may further react to form the cross-combination intermediary NH_2OH. This intermediary will react to produce nitrogen oxyanions NO_2^- and NO_3^- ions or/and nitrogen oxides NO and N_2O.[55]

The ammonia conversion reaction mechanisms are exhaustively studied for specific noble metal platinum surfaces whereas there is a lack of research using non-noble metals as catalysts. However, the studies can be a starting point for further development on different non-noble catalysts.

Finding high-performance alternatives to the noble metal catalysts is essential to the future of these processes and those alternatives lie in the development of new materials composed by accessible and abundant elements. Materials such as metal-organic frameworks offer great potential as catalysts'

materials due to their modular nature that enables the combination of different metal centres and organic ligands.

1.5 Metal-Organic Frameworks as Electrocatalysts

Metal-organic frameworks (MOFs), also known as porous coordination polymers (PCPs) are inorganic-organic hybrid structures. They are composed of an inorganic centre such as metal ions or metal clusters, known as secondary building units (SBUs) and an organic ligand that links these centres, forming an infinite one-, two- or three-dimensional network made of repeating units of these components (**Figure 1.9**).[56–58] The SBUs are the main defining factor of the architecture taken by the structure, owing to its diverse directionality caused by the species involved, the metal oxidation state and its coordination number, and their capacity to have open metal sites.[59–61]

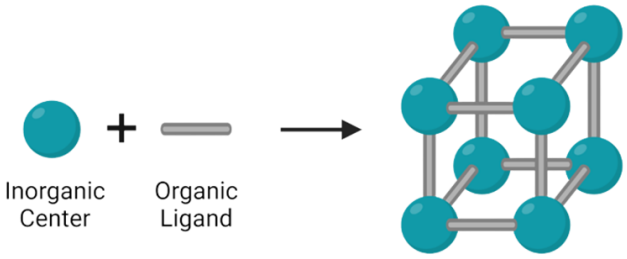

Figure 1.9 – Representation of the formation of MOFs.

The structure is maintained with the use of strong and directional bonds between the rigid molecular building blocks and ligands, to form high crystalline structures with ultrahigh permanent porosity (up to 90% free volume) and surface areas (up to 7000 m^2g^{-1}).[62–64] MOFs also have high versatility due to the abundant quantity of both metal centres and organic ligands, leading to different combinations and topologies.[65,66] Controlling a MOF's chemical composition, functionality, and molecular dimensions systematically to fit the pretended applications without affecting the crystallinity of the structure, is one of the main challenges of these materials' investigation. To accomplish this goal, one effective approach is to employ derivatives of the same organic ligands. It is important that these derivatives maintain the structure's skeleton while varying its functionality and dimensions.[67] Post-synthetic modifications or the incorporation of modulators during the synthesis are alternative approaches of structure modification. For example, the formation of defects on the MOF structure or the incorporation of different functional groups on the organic ligand.[58,68,69]

The chemical and thermal stability of the MOFs are other important properties to consider. MOFs can be tuned to offer thermal stabilities close to zeolites. The thermal stability of the MOFs is mostly related to the cleavage of the metal-ligand bonds, followed by the ligand's decomposition. Regarding the chemical stability, MOFs are more sensible in water than other solvents due to the chemical weak points at the metal-ligand bonds. Hydrolysis of the structure will yield a protonated ligand and a hydroxide-bonded metal centre. Acidic or basic conditions will accelerate the former and latter reactions, respectively. **Figure 1.10** illustrates the different chemical stabilities of several reported MOFs. Some properties that determine these stabilities are the coordination environments, metal compositions and their oxidation state, the nature of the ligand, its flexibility, interpenetration, and dimensionality.[62,64]

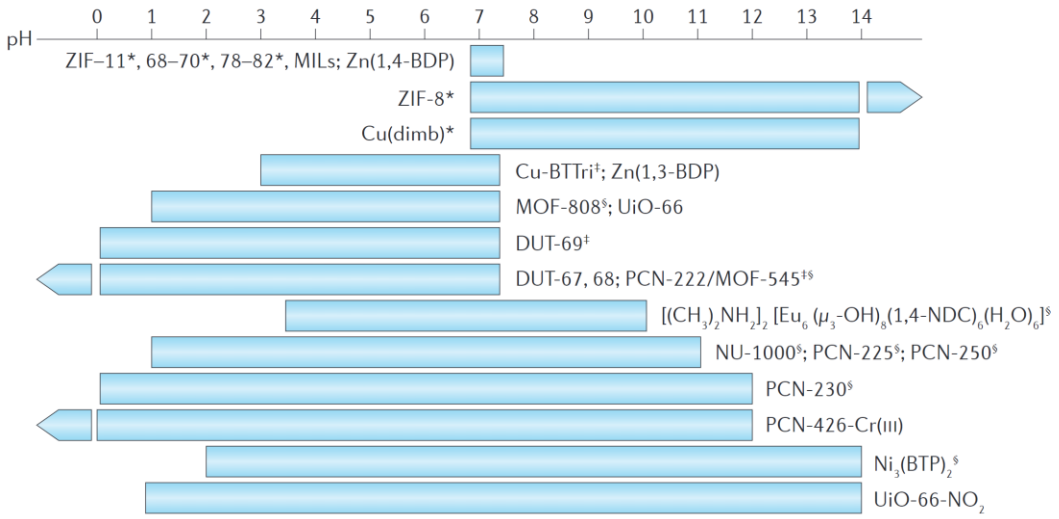

Figure 1.10 – pH range of the chemical stability of several literature-reported MOFs.[64]

Solvothermal and hydrothermal techniques are the main synthesis processes used in the formation of these hybrid materials. In both processes, the MOF precursors are dissolved in a mixture using either organic solvents like DMF or water and are placed under high temperatures and pressures to initiate the reaction.[70] It is important to consider the type and proportion of solvent or solvent mixture used, as well as the presence of any additional species that may act as guests or modulators.[71] The reaction initiates with the self-assembly of the building blocks (inorganic and ligand moieties), which is then followed by their nucleation and crystal growth.[72]

MOFs require access and understanding of their porosity and since these materials are classified as materials with permanent porosity, maintaining their structural integrity with guest sorption and desorption, its study requires measurements of reversible gas sorption isotherms at low pressures and temperatures, such as liquid nitrogen.[58] The use of SBUs instead of single atoms has led to specific topologies determined by the geometry of the SBU (**Figure 1.11**) and being the main reason in the development of permanent porosity.[73]

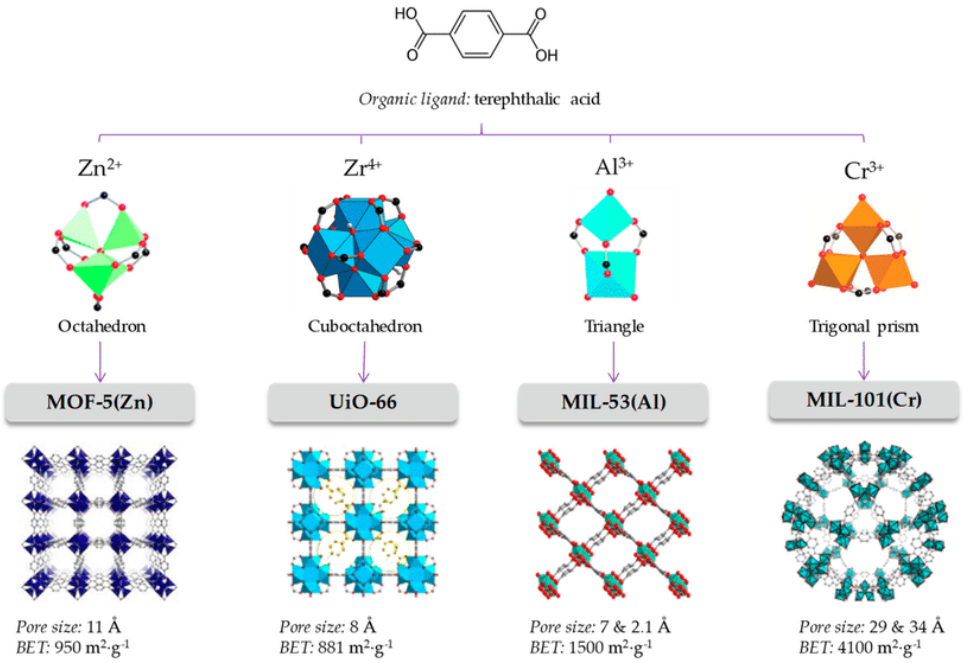

Figure 1.11 – Examples of possible topologies caused by the different geometries of the metal cluster.[74]

These materials can be used in multiple relevant applications such as storage devices[75–80], catalysis[27,81,82] (photocatalysis[83,84] and electrocatalysis[27,85–89]), chemical separation[9,90,91], sensing[92,93], drug delivery[94,95], solar and fuel cells[96–98], among others.[58,85,99–105] Industrial-scale extensive studies have been performed mainly due to MOFs desirable properties offering potential in applications such as in clean energy production or even in the removal of unwanted pollutants.

Focusing on the catalytic potential, MOFs have important properties for these applications, such as high porosity, large internal superficial area and, in some cases, their capacity to form and maintain open metal sites in their structure. Where MOFs fall short are in their thermal and chemical stability which prevents their use in more extreme conditions. There are exceptions where thermal and chemical stability are demonstrated to be high, for example the zirconium family of MOFs: UiO-66 and UiO-67.[106,107] The future of MOFs as catalysts is based on certain envisioned aspects, such as their capacity to use its hybrid architecture as multi-catalyst and their unique metal coordination environment leading to high reactivity.[107] HKUST-1 and MOF-5, for example, were reported used in specific reactions like in Friedel-Crafts alkylation, isomerization, and cyclisation.[107–109]

For electrocatalytic applications, MOFs have several problems related to its poor conductivity and low stability in electrochemical medium. A solution to these problems is their combination with conductive materials such as graphene or carbon nanotubes or even using the MOFs as a sacrificial template to lead the formation of nanostructured materials such as porous carbons or metal oxides.[110] To use MOFs as electrocatalysts, they must be immobilised onto electrodes as they are typically obtained in powder form.[45] As MOFs are insoluble, homogeneous catalysis is not possible. Another option is using an alternative synthesis where the MOF is directly formed or deposited on the surface of the electrode.

1.6 Immobilisation of MOFs in Films for Electrocatalysis

The direct formation of crystalline materials films can be done using techniques such as layer-by-layer, self-assembly and even by mechano- or sonochemical techniques.[111,112] These techniques, however, are limited by their time-consuming and high energy requirements. The use of electrochemical methods enables to overcome these limitations.

The formation of MOFs using electrochemical methods offer several advantages when compared to the traditional methods as the usage of milder conditions and lower formation time. There are several electrochemical techniques such as anodic deposition[113], cathodic deposition[114–116], electrophoretic deposition[117–119], and galvanic displacement.[120–122] Successful MOF depositions using these four methods were reported in the literature. Two of the more common direct methods (anodic and cathodic deposition) and an indirect method (electrophoretic deposition) are represented in **Figure 1.12** and will be further discussed.

The methods represented in **Figure 1.12** can be divided into direct and indirect methods. The anodic and cathodic deposition both fall within the direct method. This method consists in the direct formation of the MOF on the surface of the electrode through its contact with the precursors in an electrolytic solution. In the case of the electrophoretic deposition, it is classified as an indirect method. In this path the MOF is previously synthesised as a powder using traditional methods followed by its immobilisation on the surface of the electrode.

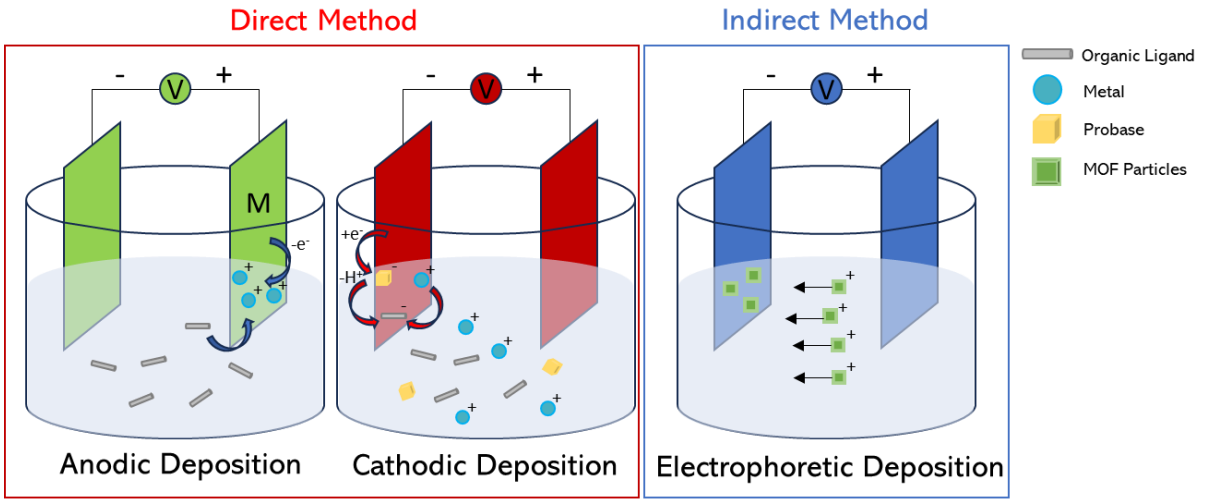

Figure 1.12 - Mechanism of the anodic, cathodic, and electrophoretic deposition techniques applied in MOFs.

Where these two methods differ is in their mechanism, in the case of the anodic deposition, the MOF will be formed on the surface of the anode that is made of the corresponding metal. This plate of metal will be oxidised releasing positively charged metal ions into the electrolytic medium that will react with the ligand to form the MOF on the surface of the electrode.[113] MOFs such as HKUST-1, UiO-66, ZIF-67, among others, were reported formed via this process.[123–131] This method falls short due to its requirement for specific anode materials and corrosion due to the oxidative *E* applied and undesired side reactions.

The cathodic deposition method avoids these limitations by allowing any conductive surface to be used as an electrode (e.g. FTO, ITO and Si).[132] Both the inorganic and organic precursors are dissolved in the electrolytic solution with an additional species that is a probase (e.g. H_2O_2 and Et_3NHCl).[114,133] The

probase is reduced to a base after the application of a reductive *E*, increasing the solution's pH and leading to the deprotonation of the organic ligand and consequent deposition of MOF at the surface of the cathode. By this method MOFs like HKUST-1, MIL-53(Fe) and MOF-5 were successfully deposited as reported in the literature.[114,116,134–136]

The electrophoretic deposition falls in the indirect method category. In the indirect method the MOF is previously synthesised as a powder by solvothermal, or hydrothermal methods. After, a stable suspension must be formed and placed under a strong electric field (30-120 V cm^{-1} are commonly used) and over time the powder is immobilised on the surface of the electrode. Optimisations of the suspension are usually necessary to be able to fabricate a film.[137–139] Post-synthetic modification of MOFs[140], addition of modulators to the previous synthesis[141] or the addition of additional species like acids to control the pH of the suspension[142] are some examples of optimisation reported. Successful depositions of the MOFs NU-1000, MIL-53, HKUST-1, UiO-66, and others were reported.[117–119,140,141,143–145]

1.7 The Objective of the Thesis

The objective of this work is finding MOF-based electrocatalysts to produce hydrogen via the electrocatalytic conversion of ammonia. For this purpose, several attempts to immobilise MOFs using both the direct (cathodic deposition) and the indirect (electrophoretic deposition) routes were performed. Afterwards, electrochemical studies using cyclic voltammetry (CV) were done to determine the performance of the electrocatalysts for the ammonia conversion reaction. The ideal conditions to run the controlled potential electrolysis (CPE) were selected based on the CV studies. After the CPEs, the quantification of the produced hydrogen was done using gas chromatography (GC). The workplan is represented in **Figure 1.13**.

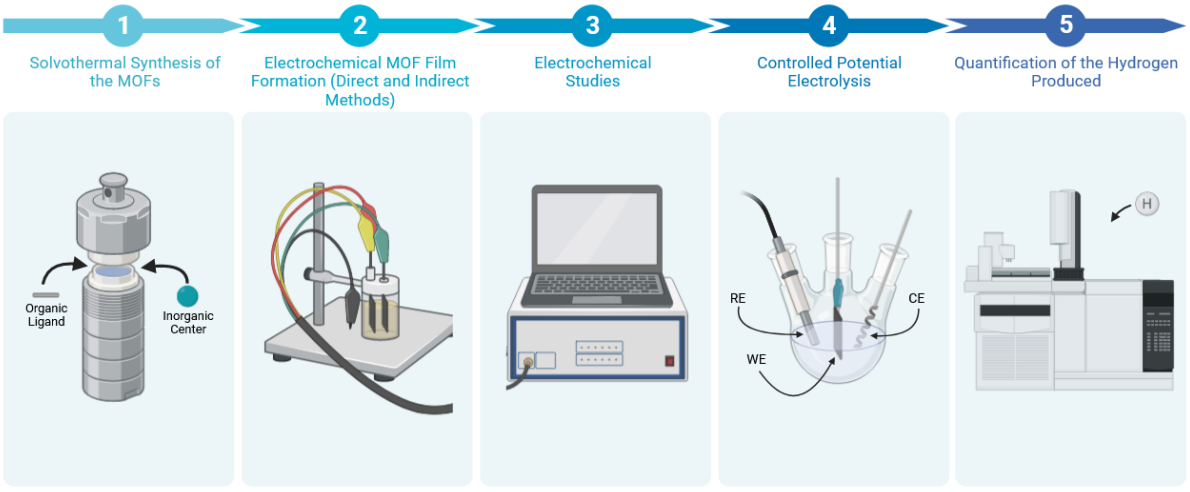

Figure 1.13 - Workplan performed in this thesis.

2 Results and Discussion

2.1 MOFs Solvothermal Synthesis and Powder Characterisation

This chapter will describe the several different synthetic procedures (S) of the following MOFs: MOF-5, IRMOF-3, ZIF-8, ZnMn-ZIF-8, Mg-MOF-74, Ni-MOF-74, HKUST-1, UiO-66 and finally UiO-66-NH_2. The characterisation of the MOFs by powder X-ray diffraction (PXRD), Fourier transform infrared spectroscopy (FTIR) using the techniques diffuse reflectance infrared Fourier transform spectroscopy and attenuated total reflectance (DRIFT/ATR) and scanning-electron microscopy (SEM) is also presented and discussed. PXRD is the most important technique for the characterisation of MOFs due to the high crystallinity expected from their structure, which is determined by the intensity and diffraction patterns observed in the PXRD. All MOFs were characterised by PXRD and FTIR, however only the successful synthesised ones were characterised by SEM. Additionally, the successful prepared MOF powders were tested for their stability in water due to the future application as ammonia electrocatalysts. These were also characterised by PXRD and FTIR.

The yield % was not calculated since we are dealing with porous materials, which led to inconsistencies on the calculations because of the possible adsorbed species on the pores of the structure.

The MOFs activations were all done under the same pressure under vacuum due to equipment limitations, which means that it was not possible to use the specific pressures reported in the literature. After synthesis and activation, all the MOFs were stored in low humidity atmosphere in a desiccator. All MOFs were only characterised, and therefore named, after their activation and unless stated otherwise all respective discussion is after the MOFs activation.

2.1.1 MOF-5 and IRMOF-3

MOF-5 or IRMOF-1 is one of the first MOFs prepared and it was discovered by Li *et al.*[146] in 1999. The synthesis of this MOF occurs through the reaction between the inorganic centre Zn^{2+} and the organic ligands benzene-1,4-dicarboxylic acid (H_2BDC) forming the repeating cluster unit **$Zn_4O(BDC)_3$** (metal:ligand proportion of 4:3). Two different synthetic procedures (S1 and S2) were performed, as seen in **Scheme 2.1**.

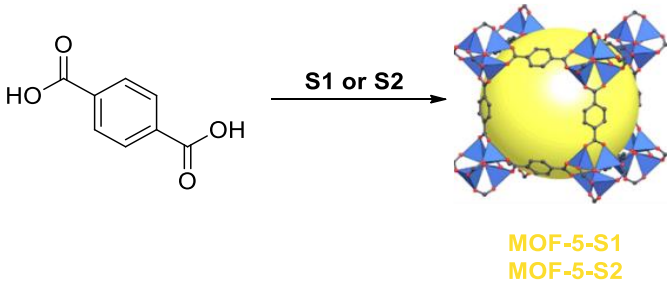

Scheme 2.1 - Synthesis and structure[147] of MOF-5. S1[148]**:** dry DMF, 120 °C, 2 h 30 min. Activation: 90°C, overnight (MOF-5-S1). S2[149]**:** DMF, 25 °C, 2h 30 min. Activation: 120 °C, 6 h (MOF-5-S2).

The two synthesis attempts (**S1** and **S2**) were performed following the reported procedures from Zhao *et al.*[148] and Tranchemontagne *et al.*[149]. The obtained white powders from the two different attempts (**Figure A.1** in the Annexes) were named **MOF-5-S1** and **MOF-5-S2** for the corresponding synthesis.

The PXRD of **MOF-5-S1** obtained by PXRD showed crystallinity but with no corresponding pattern to the expected for MOF-5 reported in the literature (**Figure 2.1**).[146] The two main diffraction patterns of the reported MOF-5 are at the 2θ angles of 6.9º and 9.7º for the planes (200) and (220), respectively. The correspondence of these peaks was not possible since there is no expected species with such peaks, further techniques are necessary for their identification.

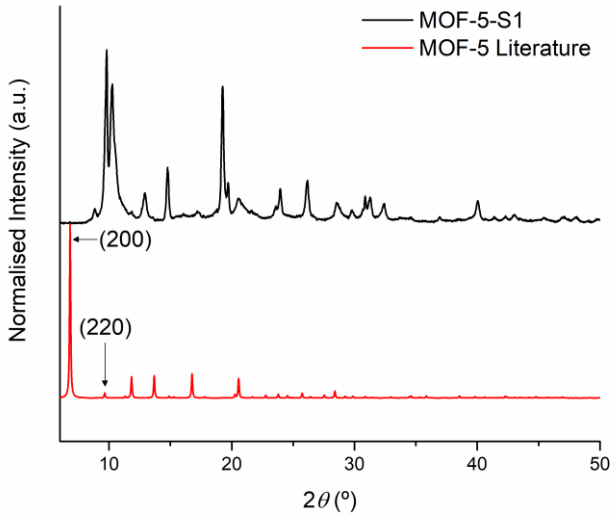

Figure 2.1 - PXRD of **MOF-5-S1** and comparison with MOF-5 diffraction pattern from the literature.[146]

However, although the diffraction pattern was not the expected for **MOF-5-S1**, it was possible to identify via the FTIR spectrum (**Figure 2.2**) the symmetric and asymmetric stretching vibrational modes of the O-C-O bond (1600 and 1389 cm^{-1}) that corresponds to the coordinated and deprotonated ligand. Moreover, the absence of the stretching vibrational mode of the C=O bond from the carboxylic acid function in the 1715-1680 cm^{-1} region confirms deprotonation and suggests coordination to a metal centre. It was not possible to conclude about the presence or absence of the stretching vibrational mode of the O-H bond, as the adsorbed water gives rise to a broad peak in the same region where the peak should appear (3500-3000 cm^{-1}). The spectrum obtained is similar to what would be expected from MOF-5.

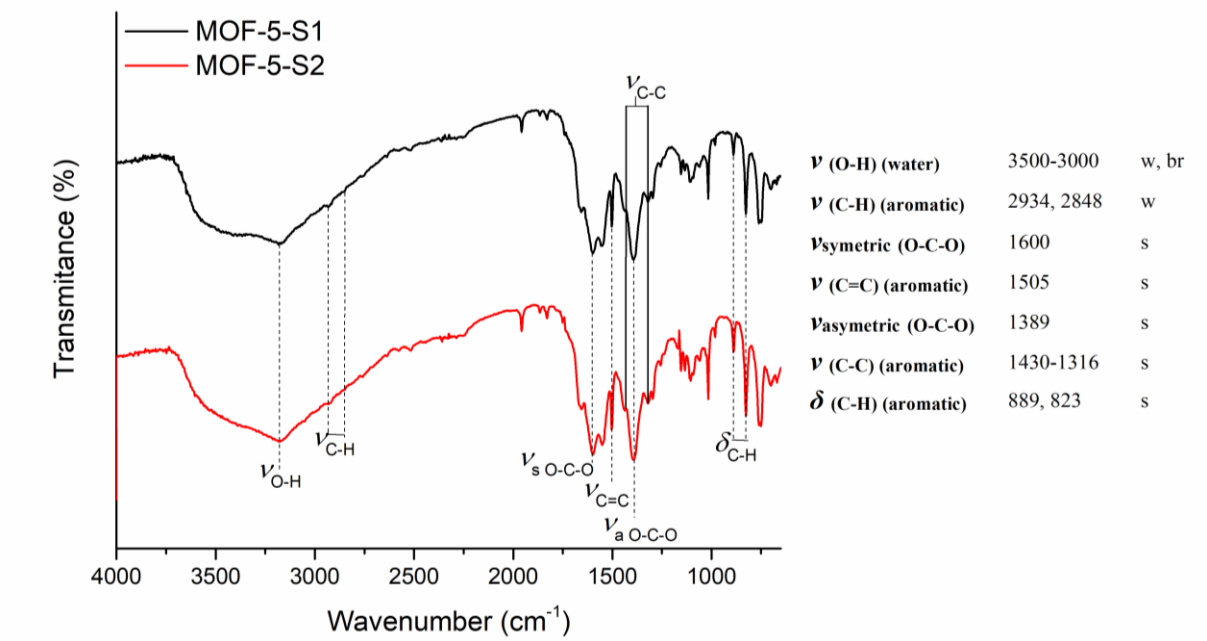

Figure 2.2 - FTIR spectra (DRIFT) of **MOF-5-S1** and **MOF-5-S2** and wavenumber values of the corresponding main vibrational modes.

In the second attempt (**S2**) in comparison with the first (**S1**), the synthesis was performed at ambient temperature and using DMF directly from the commercial flask without further purification. **MOF-5-S2** was also characterised by both PXRD and FTIR. The PXRD obtained also showed crystallinity but with completely different peaks not matching the expected diffraction pattern for MOF-5 (**Figure A.2** in the Annexes). Likewise, obtained infrared spectrum (**Figure 2.2**) was identical to the **MOF-5-S1** spectrum.

In conclusion, we were unable to replicate the syntheses reported. Although FTIR spectra showed typical bands of the vibrational modes of MOF-5, the PXRD does not show the expected diffraction pattern. This can be due to the formation of a different phase or crystalline structures related to the reaction conditions, especially in the initial steps of the self-assembly of the MOF precursors.

Additionally, we also attempted to synthesise IRMOF-3, an amine functionalised version of MOF-5, which was chosen as an alternative for comparison due to its advantage of being more stable and because it also shows a higher capacity for ammonia adsorption.[102] IRMOF-3 was discovered and was first reported and characterised by Eddaoudi *et al.*[150] in 2002. The only difference between MOF-5 and IRMOF-3 is the incorporation of the amine function in the ligand structure yielding the cluster unit (**$Zn_4O(NH_2BDC)_3$**) caused by the reaction of the metal centre Zn^{2+} with the organic ligand 2-aminobenzene-1,4-dicarboxylic acid (NH_2-H_2BDC). Three different synthetic procedures (**S1**, **S2** and **S3**) were performed for IRMOF-3 as seen in **Scheme 2.2**.

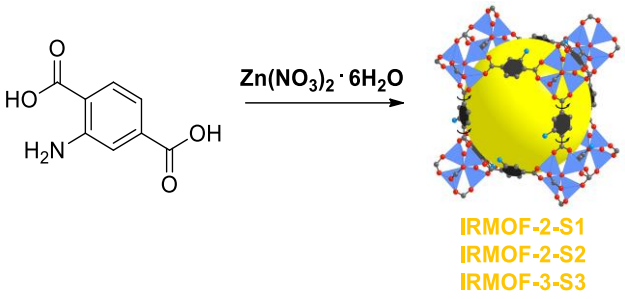

Scheme 2.2 - Synthesis and structure[151] of IRMOF-3. S1[80]: DMF, 90 °C, 4 days. Activation: 120 °C, 3 h (IRMOF-3-S1). S2[152]: DMF, 100 °C, 24 h. Activation: 65 °C, 4 h (IRMOF-3-S2). S3[153]: DMF, 25 °C, 1 h 30 min. Activation: 100 °C, 6 h (IRMOF-3-S3).

The three syntheses attempts (S1, S2 and S3) were performed following the reported procedures from Millward *et al.*[80], Zhang *et al.*[152] and Zhou *et al.*[153]. The pictures of the obtained light-yellow powders from the three different syntheses are in **Figure A.3** in the Annexes and are nicknamed IRMOF-3-S1, IRMOF-3-S2 and IRMOF-3-S3, respectively. A single modification was made for S1, in comparison with the reported procedure, where dimethylformamide (DMF) was used instead of diethylformamide (DEF) due to unavailability of this solvent in the lab.

The obtained PXRD of IRMOF-3-S1 (**Figure 2.3**), although slightly amorphous, contained the expected diffraction patterns for IRMOF-3 from the literature, which are identical to MOF-5 as the topology is not affected by the presence of the amine function in the ligand strucuture.[150]

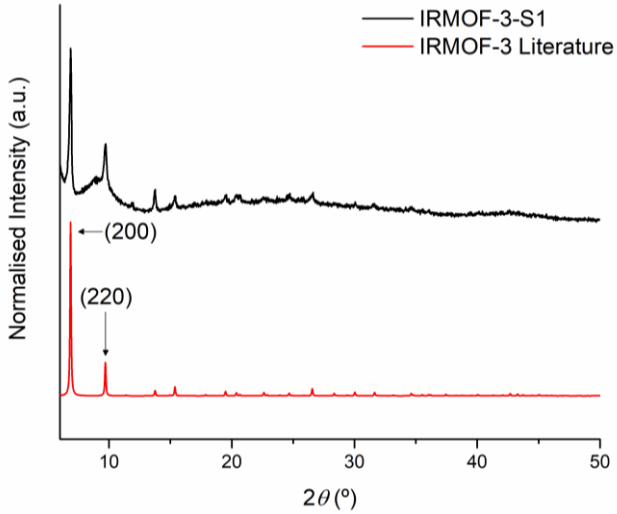

Figure 2.3 - PXRD of IRMOF-3-S1 and comparison with IRMOF-3 diffraction pattern from the literature.[150]

Analysing the obtained FTIR spectrum for IRMOF-3-S1 (**Figure 2.4**) it is possible to observe most of the expected main vibrational modes. Aside from the expected additional stretching vibrational mode of the N-H bond and the C-N bond from the amine function, all vibrational modes are identical to what is expected for MOF-5. The stretching vibration from the N-H bond unfortunately is not visible due to its overlap with the broad band from the stretching vibrational mode from the O-H bond from water. However, the presence of the stretching vibration mode from the C-N bond at 1254 cm^{-1} is detected.

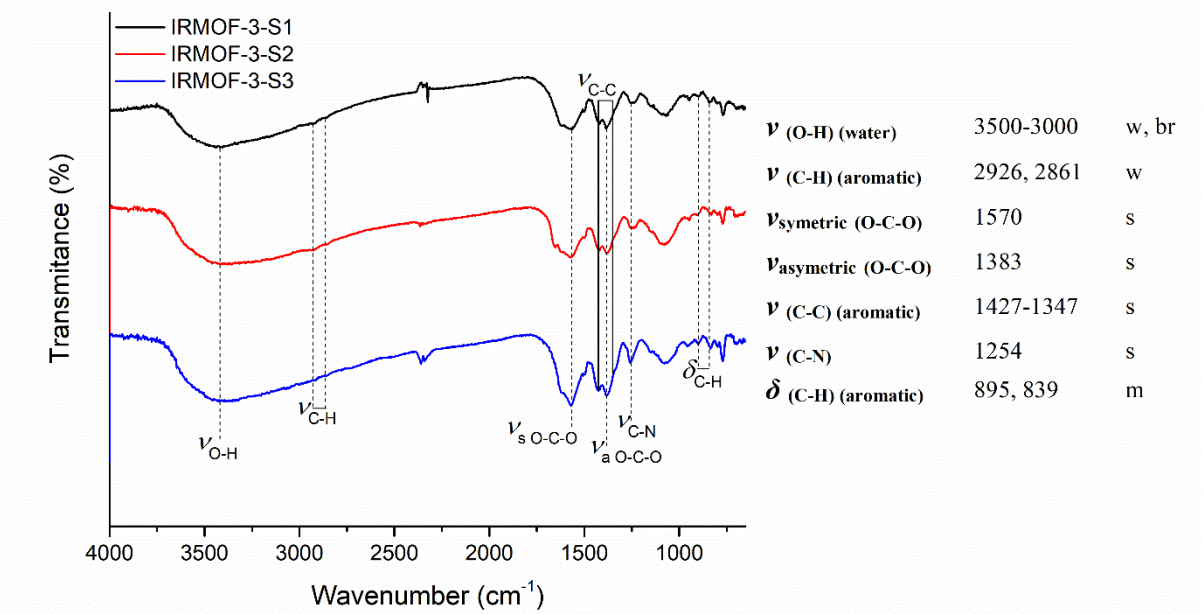

Figure 2.4 – FTIR spectra (DRIFT) of **IRMOF-3-S1**, **IRMOF-3-S2** and **IRMOF-3-S3** and wavenumber values of the corresponding main vibrational modes.

The presence of the amorphous band in the PXRD of **IRMOF-3-S1** led to the use of other two different synthetic (**S2** and **S3**) approaches as mentioned in **Scheme 2.2**. However, the two additional synthetic procedures yielded powders (**IRMOF-3-S2** and **IRMOF-3-S3**) with no crystallinity, indicated by the broad bands in their PXRD (**Figure A.4** in the Annexes). Additionally, in the obtained FTIR spectra (**Figure 2.4**) it is possible to observe mostly identical spectra to **IRMOF-3-S1**. This means that the reaction took place, but amorphous samples were obtained instead.

Since it is not possible to guarantee that the obtained product is IRMOF-3 it will not be used in catalytic assays. No further attempts were performed to optimise the reaction due to time constraints. Likewise with MOF-5, the failure of the obtention of a full crystalline IRMOF-3 structure may be related to the failure to replicate the conditions from the followed procedures, especially during the self-assembly step.

2.1.2 ZIF-8 and ZnMn-ZIF-8

ZIF-8 was first synthesised and characterised by Park *et al.*[154] in 2006 and was chosen due to its easier preparation when compared to other MOFs, as the reaction can occur at ambient temperature and pressure. The synthesis of this MOF occurs through the reaction between the inorganic centre Zn^{2+} and the organic ligand 2-methylimidazole (Hmim) forming the repeating cluster unit **$Zn(Hmim)_2$** (metal:ligand proportion 1:2). Four synthetic procedures (**S1**, **S2**, **S3** and **S4**) were performed, as seen in **Scheme 2.3**.

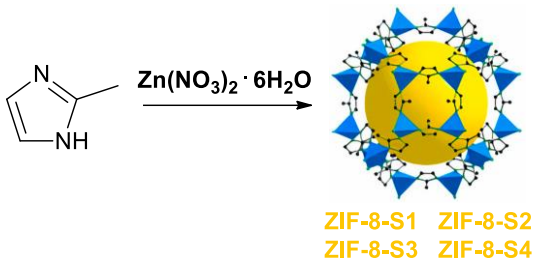

Scheme 2.3 – Synthesis and structure[155] of ZIF-8. S1[156], S2[157]: MeOH, 25 °C, 24 h. Activation: 25 °C, 3 h (ZIF-8-S1-2). S3[88], S4[95]: MeOH, 25 °C, overnight. Activation: 25 °C, 3 h (ZIF-8-S3-4).

The four different syntheses attempts (S1, S2, S3 and S4) were performed following the reported procedures from Cravillon *et al.*[156], Tang *et al.*[157], Wang *et al.*[88], and Pan *et al.*[95]. The obtained white powders from the four different procedures (**Figure A.5** in the Annexes) were named ZIF-8-S1, ZIF-8-S2, ZIF-8-S3 and ZIF-8-S4. Multiple syntheses were performed using different procedures to try and find a synthesis that would lead to a higher amount of solid obtained.

The PXRD obtained for ZIF-8-S1 (**Figure 2.5**) indicated high crystallinity with the same expected diffraction pattern for ZIF-8 from the literature.[154] The main diffraction patterns are at the 2θ angles of 7.3º, 10.4º and 12.7º for the corresponding (110), (200) and (211) planes, respectively.

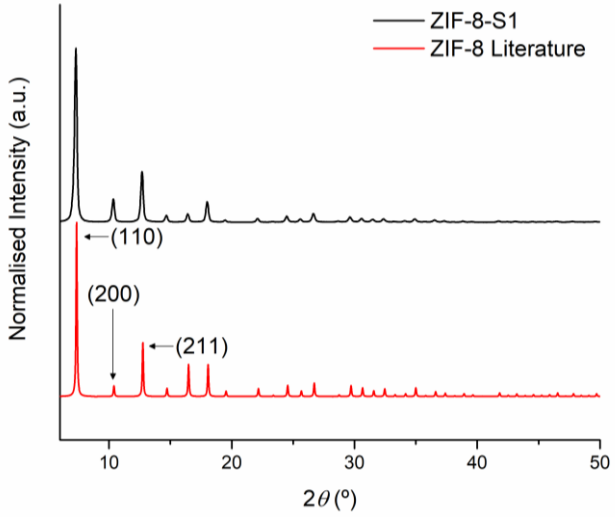

Figure 2.5 - PXRD of ZIF-8-S1 and comparison with the ZIF-8 diffraction pattern from the literature.[154]

By FTIR analysis all the main vibrational modes for ZIF-8-S1 were identified (**Figure 2.6**). However, it was unable to identify the presence or absence of residual Hmim due to the stretching vibrational mode of the N-H bond (3455 cm^{-1}) being overlapped with the adsorbed water vibrational mode in the 3500-3200 cm^{-1} range. The identification of the residual Hmim vibrational mode is important to determine if the powder washing was done correctly. It is possible to conclude we were able to obtain ZIF-8.

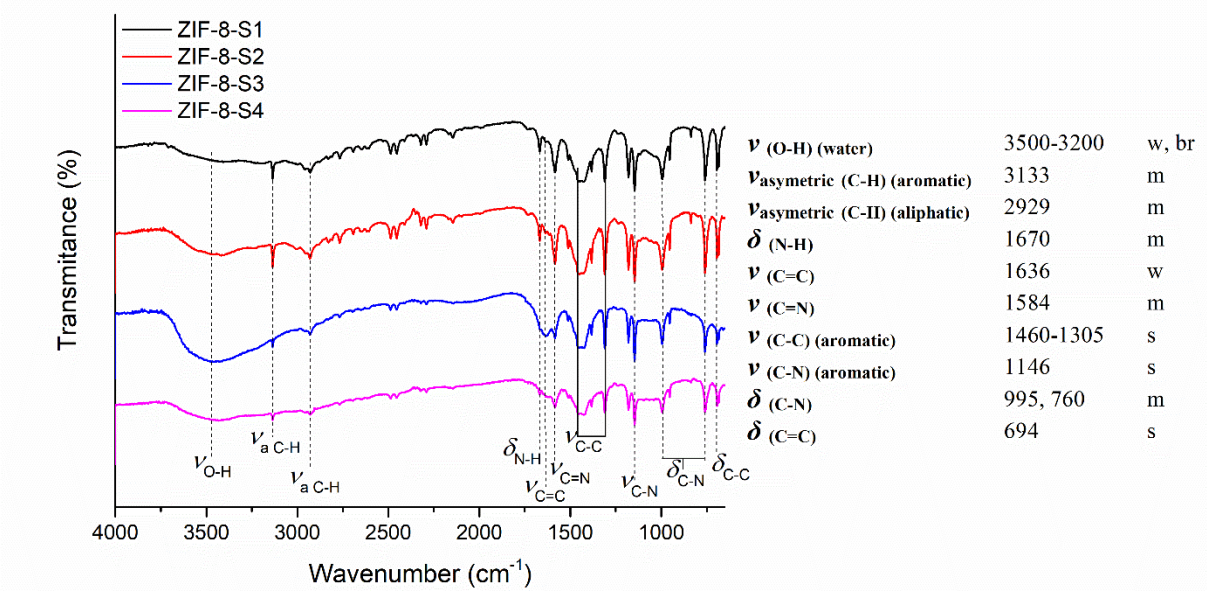

Figure 2.6 – FTIR spectra (DRIFT) of **ZIF-8-S1**, **ZIF-8-S2**, **ZIF-8-S3**, **ZIF-8-S4** and wavenumber values of the corresponding main vibrational modes.

All the remaining powders had similar characterisation, their PXRD are included in **Figure A.6** in the Annexes and FTIR spectra in **Figure 2.6**. Since all the remaining powders were identical, they will not be individually discussed.

The stability in water of **ZIF-8-S1** was also tested after immersing the powder in water for 24 h. The powder was then filtrated and dried in the oven at 70 ℃. Afterwards the powder was characterised by PXRD and FTIR. In comparison with **ZIF-8-S1**, it is possible to conclude the crystallinity was maintained as all the corresponding diffraction peaks were unaltered (**Figure A.7** in the Annexes) as well as the vibrational modes (**Figure A.8** in the Annexes).

Additionally, the powder **ZIF-8-S4** was also characterised via SEM (**Figure 2.7**). By analysing its surface, we were able to determine the size of the aggregates formed, which showed extremely low uniformity varying their size and shape, mostly randomly, from 1 to 100 µm.

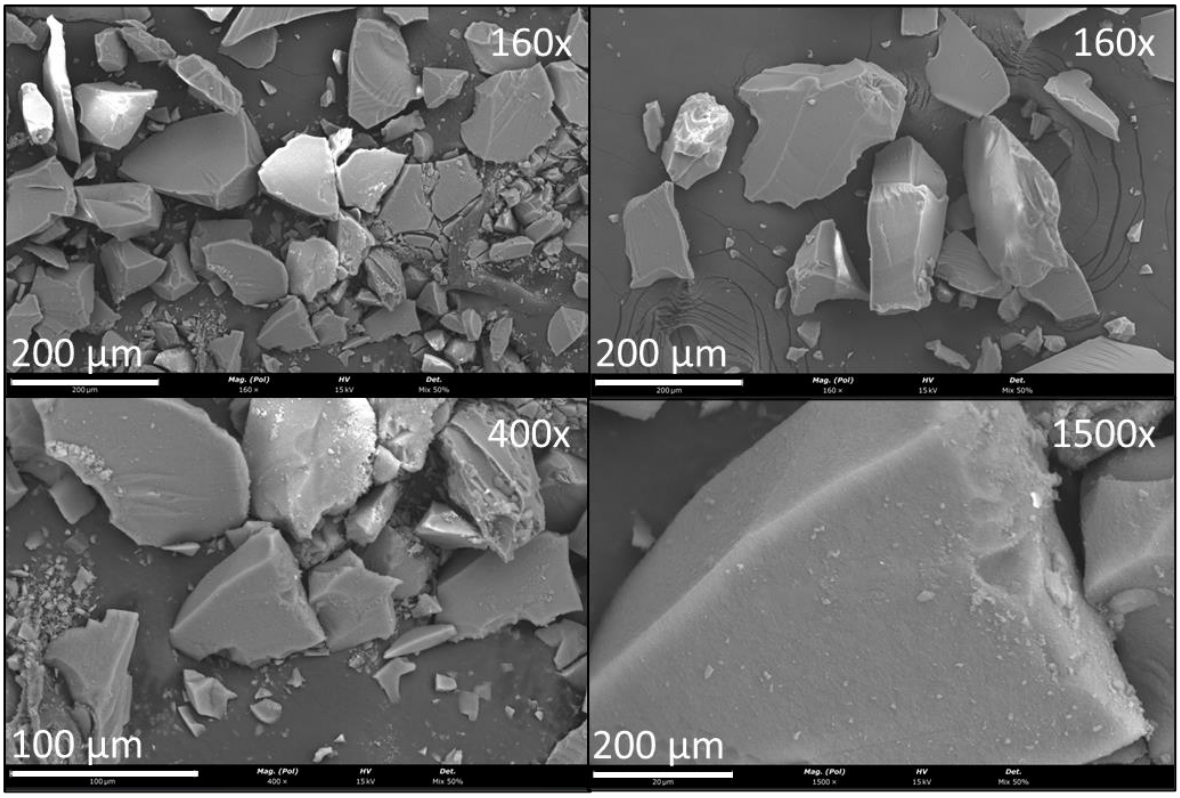

Figure 2.7 - SEM images of ZIF-8-S4. Magnified at 160x, 400x and 1500x.

A metal-exchange of ZIF-8 with Mn^{2+} was also attempted since according to a report in the literature[158] a direct synthesis of a ZIF-8 with Mn^{2+} as the metal node instead of Zn^{2+} is not a possibility because of the thermal decomposition of the manganese salts even though in theory it should be possible since the ZIF-8 structure requires a non-distorted tetrahedral coordination geometry that is offered by Mn^{2+}.[158] The reaction between the alternative inorganic centre Mn^{2+} and the previously synthesised ZIF-8 structure forms the cluster $\mathbf{Zn_{1-x}Mn_x(Hmim)_2}$. Two different synthetic procedures (S1 and S2) were performed as is represented in **Scheme 2.4**.

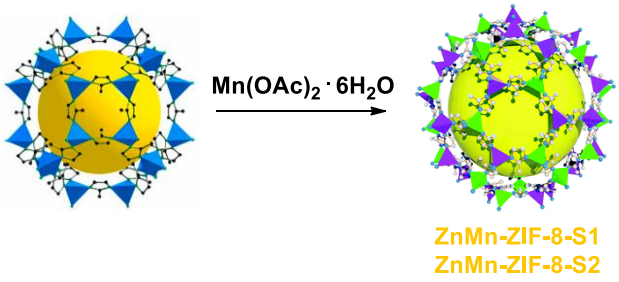

Scheme 2.4 - Synthesis and structure[95] of ZnMn-ZIF-8. S1: MeOH, 25 °C, 1 week (ZnMn-ZIF-8-S1). S2[95]: 60 °C, 48 h. Activation: 25 °C, 6 h (ZnMn-ZIF-8-S2).

Of the two synthesis attempts (S1 and S2) only S2 was performed following the reported procedure from Pan *et al.*[95]. The obtained light pink powders from both attempts (**Figure A.9** in the Annexes) were named ZnMn-ZIF-8-S1 and ZnMn-ZIF-8-S2. To obtain the ZnMn-ZIF-8-S1, we suspended part of the ZIF-8-S1 powder in a methanol solution containing 0.1 M manganese acetate tetrahydrate for 1

week. Afterwards we centrifuged the powder, washed with methanol, and dried it at 70 ℃ in the oven overnight. For **ZnMn-ZIF-8-S2**, the **ZIF-8-S4** powder was used.

For both **ZnMn-ZIF-8-S1** and **ZnMn-ZIF-8-S2** the obtained PXRD (**Figure A.10** and **A.11** in the Annexes) and FTIR spectra (**Figure A.12** and **A.13** in the Annexes) were identical to the obtained for **ZIF-8-S1** and **ZIF-8-S4**, respectively. This was to be expected since theoretically most of the ZIF-8 structure is still intact and there is no change in the structure.

Initially it seemed it was a successful synthesis, however with the techniques used it was not possible to confirm if the metal-exchange took place. Therefore, **ZnMn-ZIF-8-S2** was also characterised by SEM alongside energy dispersive spectroscopy (EDS) (**Figure A.14** in the Annexes) to confirm the presence of manganese in the structure. The morphology of the agglomerates was also identical to that of **ZIF-8-S4**. Finally, by EDS it was possible to observe the elemental constitution of the agglomerates imaged by SEM, and no manganese was detected in the structure of the analysed powder. This suggests that the metal-exchange did not occur. No optimisations were performed to obtain ZnMn-ZIF-8 due to time constraints.

2.1.3 Mg-MOF-74 and Ni-MOF-74

Mg-MOF-74, also known as, CPO-27 was first characterised and published by Dietzel P. *et al.*[159] in 2008. MOF-74 was chosen and synthesised due to its potential in gas absorption applications related to its open metal sites and high-water stability.[160,161] The MOF-74 variation using Mg^{2+} was chosen since it showed a higher uptake of ammonia adsorption both in dry and humid conditions when compared to some of its other metal counterparts. The reaction between the metal centre Mg^{2+} and the organic ligand 2,5-dihidroxybenzene-1,4-dicarboxylic acid (DHTA) forms the repetitive cluster unit **Mg_2(DHTA)** in the metal:ligand proportion of 2:1. Two synthetic procedures (**S1** and **S2**) were performed as seen in **Scheme 2.5**.

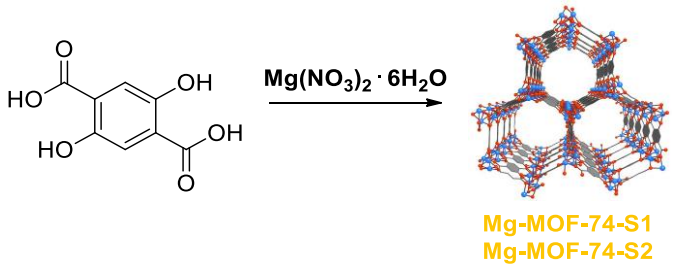

Scheme 2.5 - Synthesis and structure[162] of Mg-MOF-74. **S1**[161]: DMF:H_2O:EtOH (15:1:1), 125 ℃, 24 h. Activation: 200 ℃, 3 h (**Mg-MOF-74-S1**). **S2**[161]: DMF:H_2O:EtOH (15:1:1) 125 ℃, 24 h. Activation: 120 ℃, 6 h (**Mg-MOF-74-S2**).

The two synthesis attempts (**S1** and **S2**) were performed following the same reported procedure from Grant Glover T. *et. al.*[161] The synthesised powders were named **Mg-MOF-74-S1** and **Mg-MOF-74-S2**. One important modification in the procedure was done, the activation temperature of the powder. The reported procedure uses an activation temperature of 250 ℃ but due to limitations of the equipment used, the activation of **Mg-MOF-74-S1** was done at 180-210 ℃. The obtained powders were of a light brown/yellow colour (**Figure A.15** in the Annexes).

The **Mg-MOF-74-S1** PXRD showed high crystallinity containing a diffraction pattern identical to the reported in the literature for Mg-MOF-74 (**Figure 2.8**).[159] The expected main diffraction patterns are in the 2θ angles of 6.8º and 11.8º for the respective (110) and (300) planes.

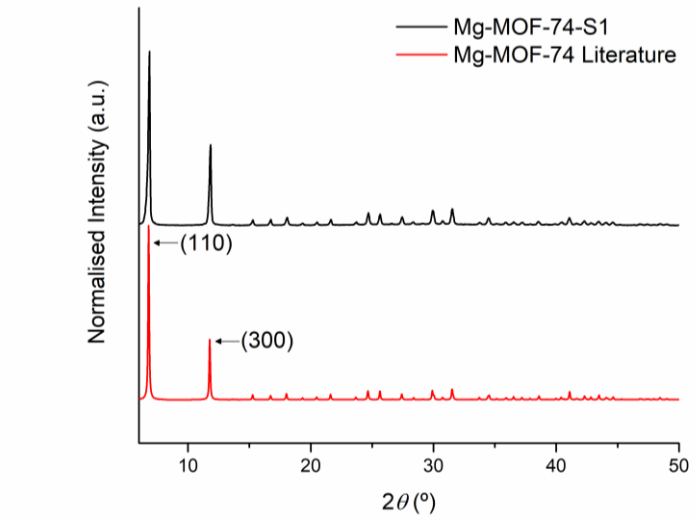

Figure 2.8 – PXRD of **Mg-MOF-74-S1** and comparison with the Mg-MOF-74 diffraction pattern from the literature.[159]

Analysing the obtained FTIR spectrum for **Mg-MOF-74-S1** all the main vibrational modes were also detected (**Figure 2.9**). The presence of the bands at 1581 cm^{-1} and 1420 cm^{-1} indicates the deprotonation and suggests coordination of the carboxylates to the metal. Additionally, it was possible to detect the deprotonation of the hydroxides due to the vibrational mode corresponding to the stretching vibrational mode from the C-O bond from the phenolate at 1208 cm^{-1}.

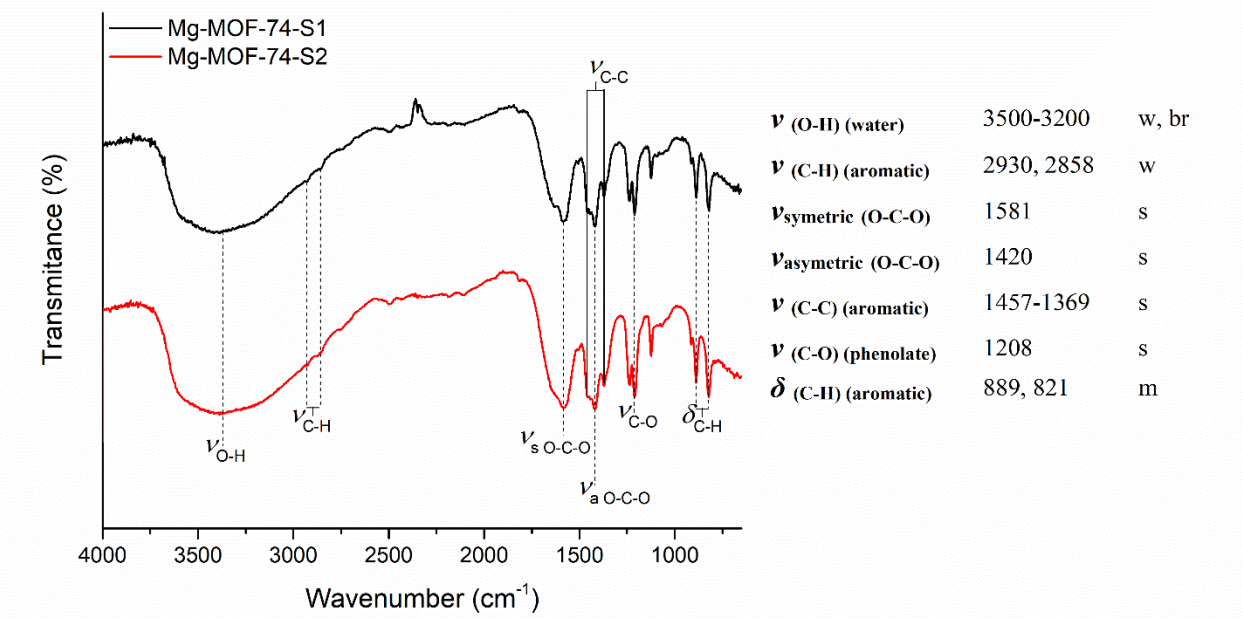

Figure 2.9 – FTIR spectra (DRIFT) of **Mg-MOF-74-S1**, **Mg-MOF-74-S2** and wavenumber values of the corresponding main vibrational modes.

Water stability studies were performed next for **Mg-MOF-74-S1**. After immersion of the powder in water for 24 h the powder was filtrated and dried in an oven at 70 ℃. The powder was characterised by PXRD as well (**Figure A.16** in the Annexes), and an unexpected loss of crystallinity was detected. The intensity of the peaks decreased or completely disappeared, and the formation of a broad peak was observed in the PXRD. The loss of crystallinity was unexpected since in the literature, as mentioned above, there is no noticeable loss of crystallinity in the presence of water. By FTIR analysis, although the spectrum obtained was slightly different all the main vibrational modes were still present (**Figure A.17** in the Annexes). It is presumed these changes were due to the high temperatures of the MOF activation together with the high vacuum pressure used. Unfortunately, it was not possible to confirm this since only **Mg-MOF-74-S1** powder after activation was characterised.

A second synthesis (**Mg-MOF-74-S2**) was performed using the same procedure but this time the activation temperature was reduced to 120 ℃. The obtained PXRD (**Figure A.18** in the Annexes) and FTIR spectrum (**Figure 2.9)** were mostly identical to the literature and to **Mg-MOF-74-S1**. Afterwards, the same water stability test was performed, however the PXRD showed no loss in crystallinity but instead an inversion in the most intense diffraction peaks, which suggests a change in the preferred orientation of the crystals in the structure after the immersion in water (**Figure A.19** in the Annexes). The FTIR spectrum is identical to the one obtained for **Mg-MOF-74-S2** (**Figure A.20** in the Annexes).

Additionally, the surface of the **Mg-MOF-74-S2** powder was also analysed using SEM (**Figure 2.10**). The aggregates formed were mostly uniform with the size varying from 1-10 µm and hexagonal prism as the most noticeable shape, similar to the pore shape of the MOF.[161]

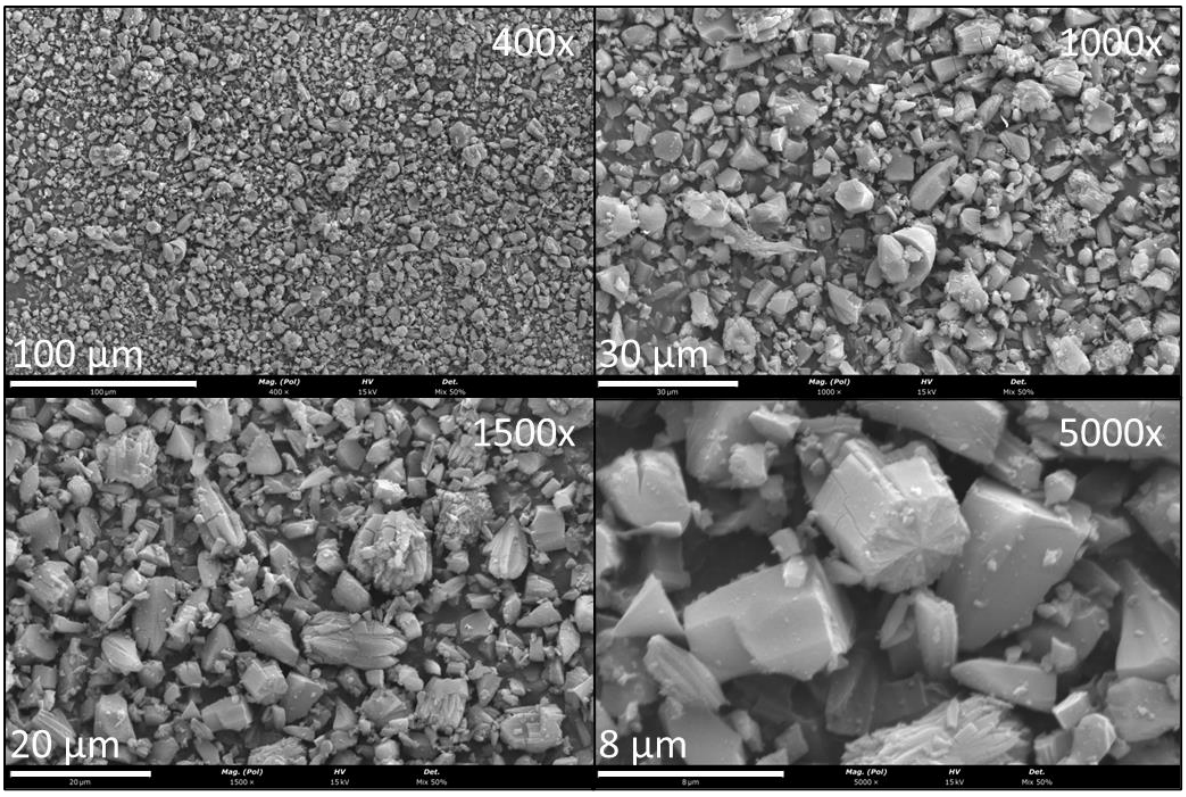

Figure 2.10 - SEM images of **Mg-MOF-74-S2**. Magnified at 400x, 1000x, 1500x and 5000x.

Alternatively, the synthesis of a Ni-MOF-74 was also attempted and was chosen for the same reasons as Mg-MOF-74 but with the advantage that shows a higher stability in the presence of water.[163] The

MOF Ni-MOF-74 or CPO-27-Ni, was characterised and published by the same author in 2006.[164] The synthesis of Ni-MOF-74 occurs through the same reaction as Mg-MOF-74 and the formed cluster is also the same, where the only difference is the metal centre. Two synthetic procedures (S1 and S2) were performed as seen in **Scheme 2.6**.

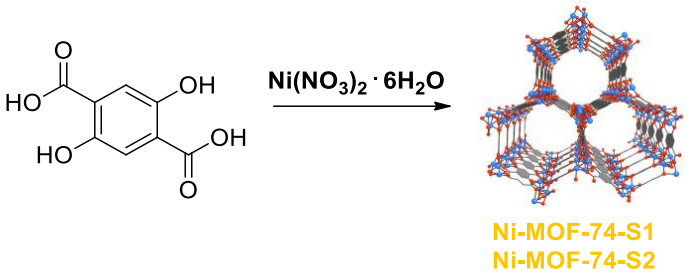

Scheme 2.6 - Synthesis and structure[162] of Ni-MOF-74. S1[161]: DMF:H_2O:EtOH (1:1:1), 100 ℃, 3 days, Activation: 200 ℃, 3 h (Ni-MOF-74-S1). S2[165]: DMF:H_2O:EtOH (15:1:1), 100 ℃, 24 h. Activation: 120 ℃, 6 h (Ni-MOF-74-S2).

The two syntheses attempts (S1 and S2) were performed following the reported procedures from Grant *et al.*[161] and Xie *et al.*[165]. For the first synthesis the activation was performed at 180-210 ℃ for only 3 h instead of 250 ℃ for 5 h for the same reasons as mentioned for Mg-MOF-74-S1. The obtained brown powders Ni-MOF-74-S1 and Ni-MOF-74-S2 can be seen in **Figure A.21** in the Annexes.

Analysing the obtained PXRD of the Ni-MOF-74-S1 (**Figure A.22** in the Annexes) it is possible to observe very low crystallinity and the absence of the main diffraction patterns for Ni-MOF-74.[164] Additionally, the FTIR the spectrum obtained (**Figure 2.11**) it is possible to detect the main vibrational modes (identical to Mg-MOF-74), however less intense and defined.

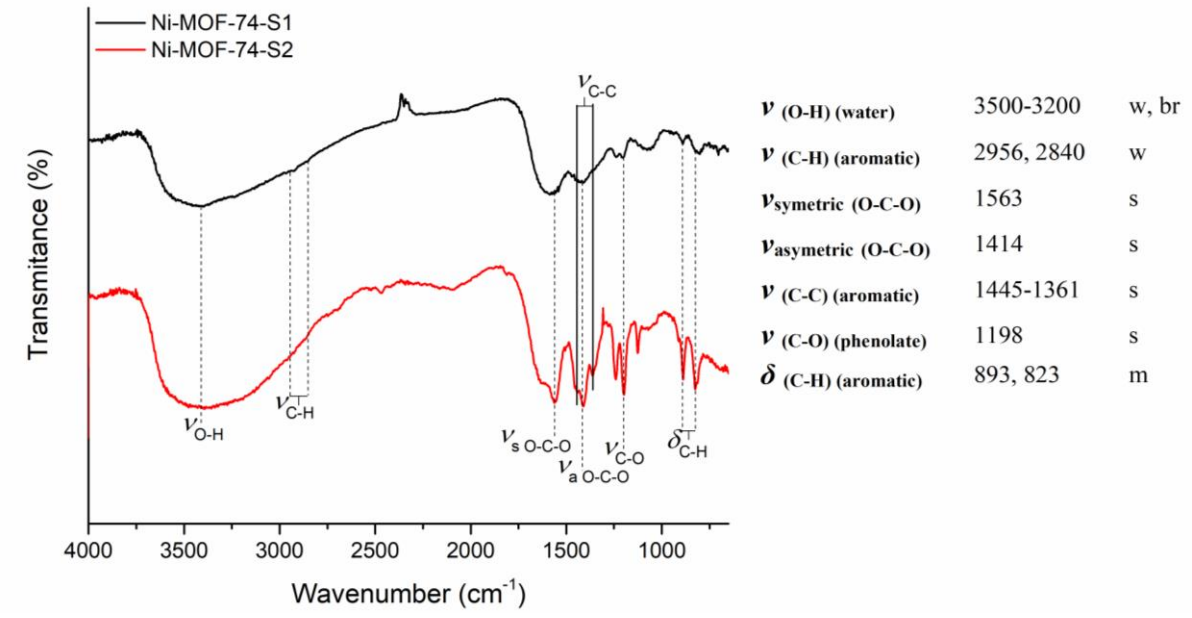

Figure 2.11 – FTIR spectra (DRIFT) of Ni-MOF-74-S1, Ni-MOF-74-S2 and wavenumber values of the corresponding main vibrational modes.

Initially before the activation both the **Ni-MOF-74-S1** and **Mg-MOF-74-S1** powders had a similar light brown/yellow colour. It was possible to visually see the change in colour of the **Ni-MOF-74-S1** powder to a darker brown during its activation. With this in mind and its respective characterisation it is possible to conclude that there was severe degradation of the compound during the activation step due to the combination of high vacuum pressures and high temperatures. Hence, a second synthesis was performed. Aside from the activation, which was done at 120 °C, no significant modifications were made. The PXRD analysis for **Ni-MOF-74-S2** indicates high similarity to the expected diffraction patterns in the literature for Ni-MOF-74, which are identical to the expected for Mg-MOF-74 mentioned above, as can be seen in **Figure 2.12**. The main vibrational modes expected for the Ni-MOF-74 were detected in the FTIR spectrum, with increased definition in comparison with **Ni-MOF-74-S1** (**Figure 2.11**).

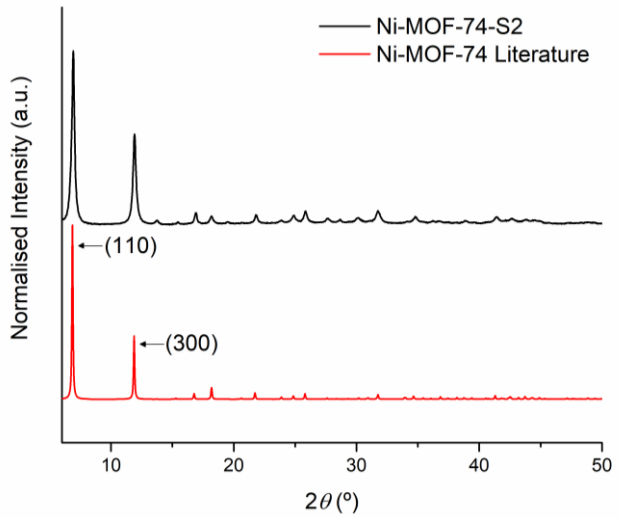

Figure 2.12 - PXRD of **Ni-MOF-74-S2** and comparison with the Ni-MOF-74 diffraction pattern from the literature.[164]

Additionally, the **Ni-MOF-74-S2** powder was also characterised using SEM (**Figure 2.13**). The aggregates formed were mostly uniform with the size varying from 1-10 µm, similar to **Mg-MOF-74-S2** however, slightly more uniform in size and shape.

Part of the **Ni-MOF-74-S2** powder was also used in water stability studies. Both the PXRD and FTIR spectrum can be observed in **Figure A.23** and **Figure A.24** in the Annexes, respectively. Both the crystallinity and its structure suffered no alterations.

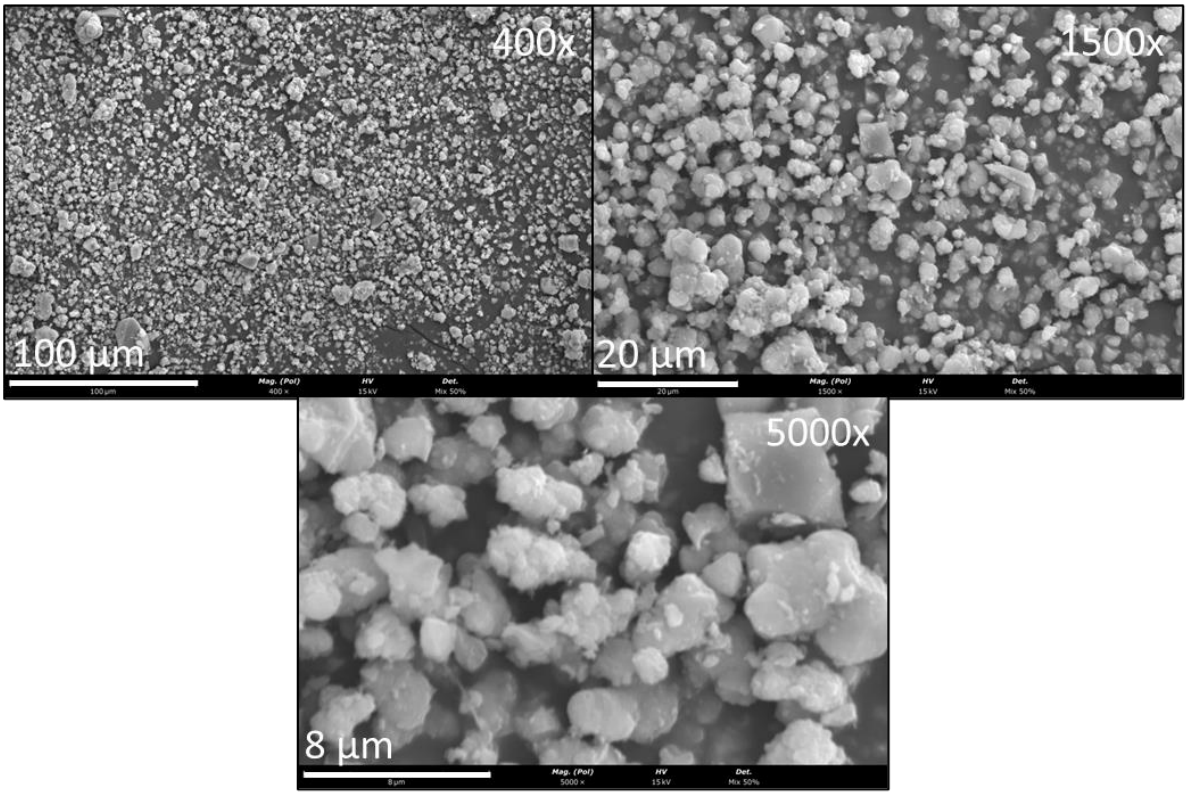

Figure 2.13 – SEM images of Ni-MOF-74-S2. Magnified at 400x, 1500x and 5000x.

Two water resistant high crystalline Mg-MOF-74 and Ni-MOF-74 were able to be synthesised using the reported procedures with only modifications in its activation conditions.

2.1.4 HKUST-1

HKUST-1, also known as MOF-199, was first reported by Chui *et al.*[166] in 1999. Like MOF-74, HKUST-1 is a MOF with open metal sites, enhancing its reactivity. For example, HKUST-1 has been used in gas adsorption due to its high chemical tunability and adsorption capacity.[167] The reaction between the metal centre Cu^{2+} and the organic ligand benzene-1,3,5-tricarboxylic acid (H_3BTC) gives form to the open metal structure using the repetitive cluster unit **$Cu_3(BTC)_2$** in the metal:ligand proportion of 3:2. One synthetic procedure (S1) was performed as represented in **Scheme 2.7.**

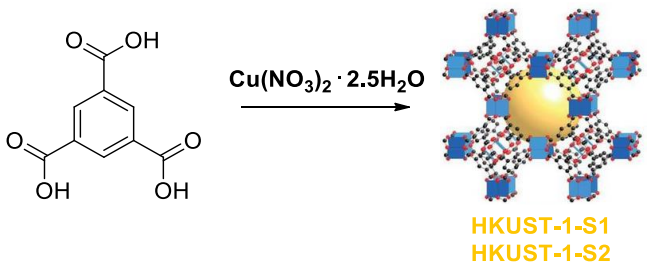

Scheme 2.7 - Synthesis and structure[168] of HKUST-1. S1[77]: H_2O:EtOH:DMF (15:15:1), 80 ºC, 20 h. Activation: 120 ºC, 12 h (HKUST-1-S1-2).

The one synthesis (S1) followed the reported procedure from Peng *et al.*[77]. The powders obtained were named HKUST-1-S1 and HKUST-1-S2. The obtained Persian blue powders can be seen in **Figure A.25** in the Annexes.

By analysing the obtained PXRD for HKUST-1-S1 the expected main diffraction patterns for HKUST-1[166] can be seen at the 6.7º, 9.5º, 11.6º and 13.4º 2θ angles corresponding to the planes (200), (220), (222) and (400), respectively (**Figure 2.14**). However, the intensity of the second most intense diffraction peak corresponding to the plane (220) is slightly lower than the one observed in the literature. This is common for some of the obtained experimental HKUST-1 PXRD, being mostly related to the adsorbed water present in the structure of the MOF, due to its high reactivity and high adsorption capacity.[169,170] When left the powder in contact with air, a rapid change of colour from the Persian blue to light blue is visible (**Figure A.26** in the Annexes). This further confirms the high reactivity with water, hence why it is important to store the powder in an inert atmosphere space.

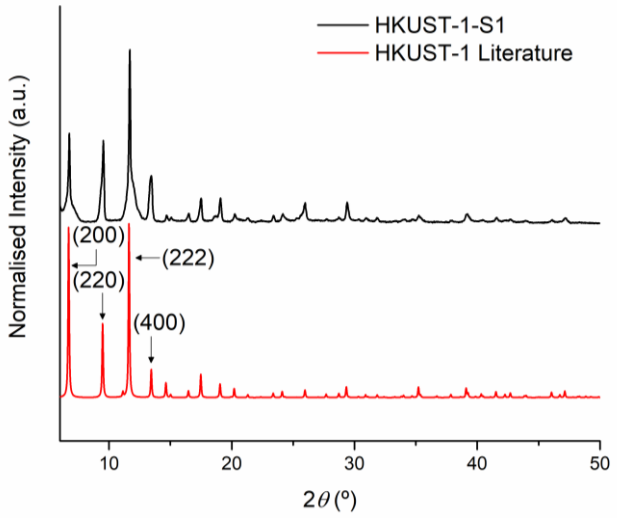

Figure 2.14 – PXRD of HKUST-1-S1 and comparison with the HKUST-1 diffraction pattern from the literature.[166]

The obtained FTIR spectrum for HKUST-1-S1 (**Figure 2.15**) confirms the deprotonation of the ligand and therefore the possibility of its coordination to the metal through the symmetric and asymmetric stretching vibrational mode corresponding to the O-C-O bonds at 1648 cm^{-1}, 1585 cm^{-1}, 1449 cm^{-1} and 1369 cm^{-1}.

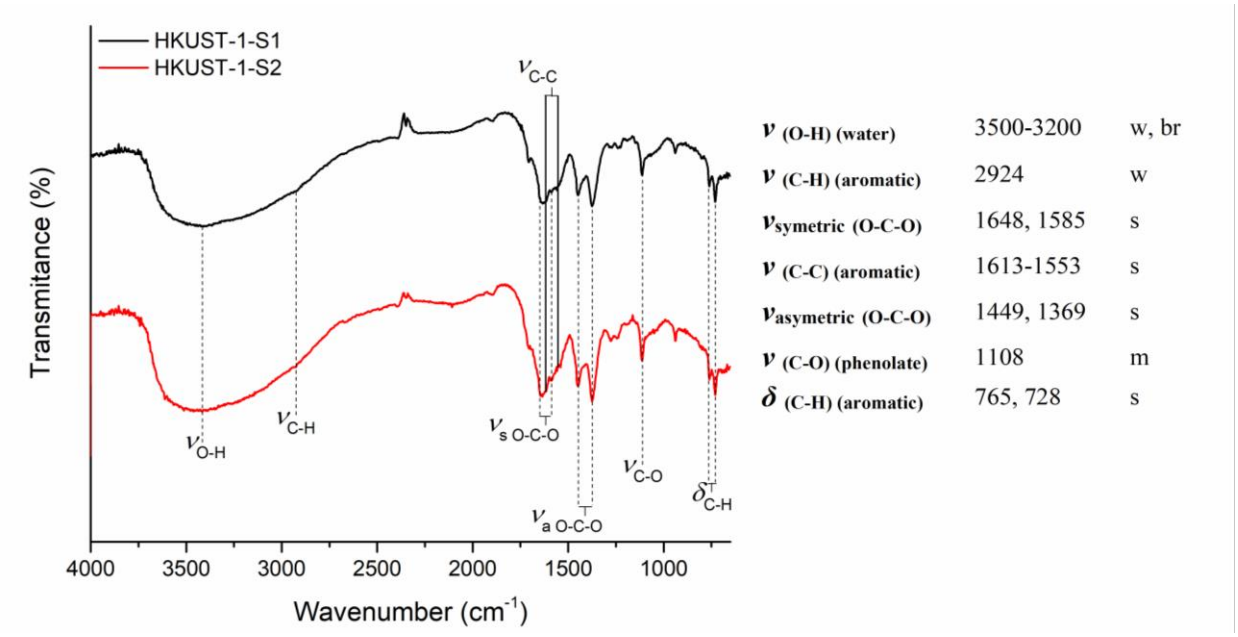

Figure 2.15 – FTIR spectra (DRIFT) of **HKUST-1-S1**, **HKUST-1-S2** and wavenumber values of the corresponding main vibrational modes.

Although the change of colour of the HKUST-1 when exposed to air suggests its decomposition, its stability in water was tested. The **HKUST-1-S1** powder was immersed in water for 24 h to test its stability in aqueous conditions. After its immersion the powder was dried at 70 °C and characterised by PXRD and FTIR, as well. The PXRD and FTIR spectra are present in the **Figure A.27** and **Figure A.28** in the Annexes. As expected by its colour change in the presence of water (**Figure A.26** in the Annexes) and after analysing the PXRD and spectra before and after the immersion in water, it is possible to see a change in the diffraction patterns where new peaks are formed in the 9.2º, 9.9º, 11º and 13.6º 2θ angles and the disappearance of all the main peaks of the HKUST-1 structure.

Additionally, the appearance of new bands in the FTIR spectrum at 1505 cm^{-1} and 1480 cm^{-1}, as well as the increase of the bands near the 1200 cm^{-1} area suggest the formation of new species in the presence of water. The low stability of HKUST-1 in water is to be expected due to the strong reactivity between the open Cu(II) sites and water. This is also reported in the literature.[171]

Aside from the PXRD (**Figure A.29** in the Annexes) and FTIR (**Figure 2.15**) characterisation, which was identical to **HKUST-1-S1**, the second synthesis **HKUST-1-S2** was characterised using SEM (**Figure 2.16**). The morphology of its aggregates is extremely uniform with the shapes of polyhedrons with sizes of 5-10 µm.

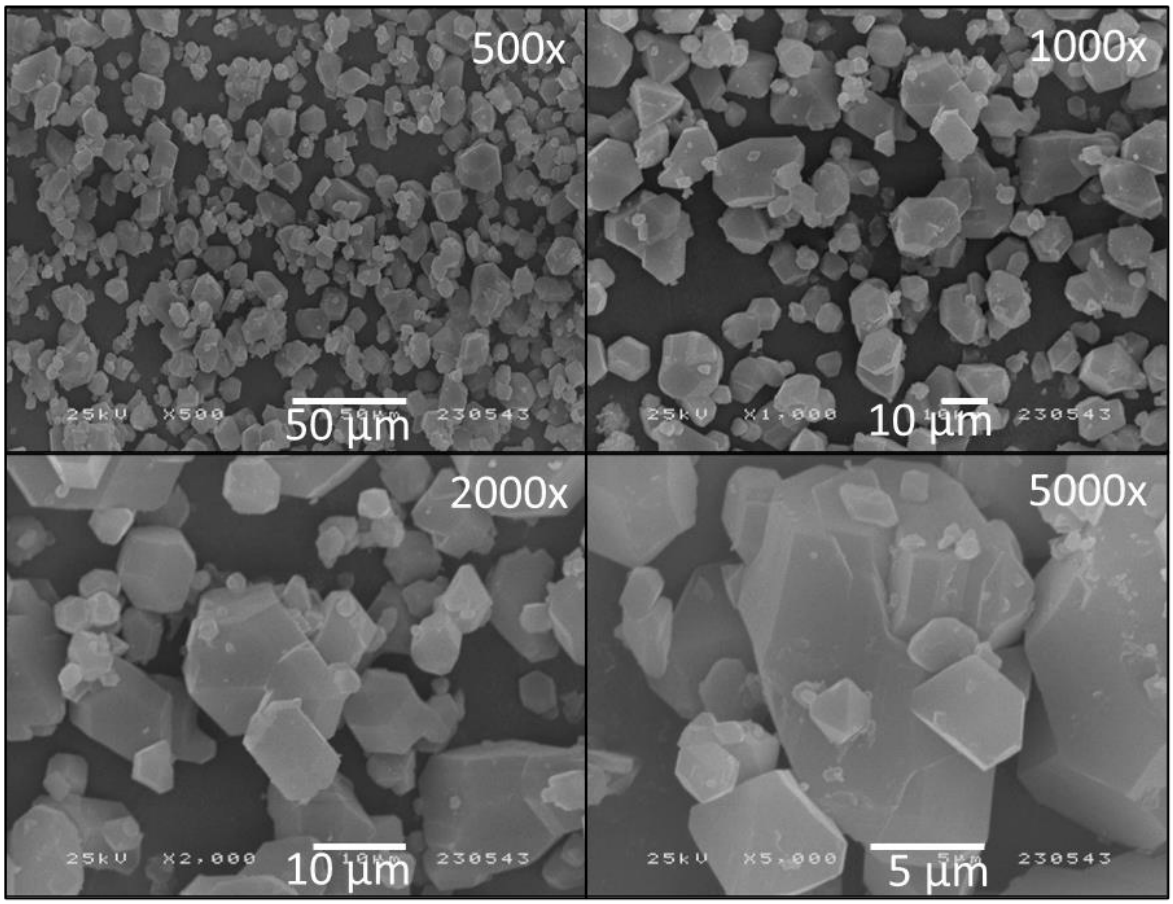

Figure 2.16 – SEM images of HKUST-1-S2. Magnified at 500x, 1000x, 2000x and 5000x.

2.1.5 UiO-66 and UiO-66-NH_2

UiO-66 was first synthesised in 2008 by Cavka *et al.*[172] It is considered to be one of the most stable MOFs, especially in both basic and acid conditions in aqueous environment.[62,173] The reaction between the metal centre Zr^{4+} and the organic ligand benzene-1,4-dicarboxylic acid (H_2BDC) gives form to the repetitive cluster unit **$Zr_6O_4(OH)_4(BDC)_6$** in the metal:ligand proportion 1:1. Two synthetic procedures (S1 and S2) were performed as seen in **Scheme 2.8**.

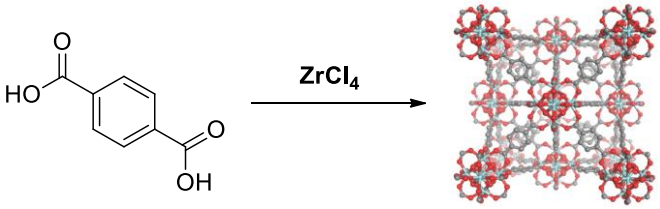

Scheme 2.8 - Synthesis and structure[174] of UiO-66. S1[175]: Dry DMF, 200 °C, 2 days. Activation: 80 °C, 12 h (UiO-66-S1). S2[176]: DMF:HCl (15:1), 80 °C, 24 h. Activation: 100 °C, 6 h (UiO-66-S2).

The two synthesis attempts (S1 and S2) followed the reported procedures from Huang *et. al.*[175] and Katz *et. al.*[176]. The two powders obtained were named UiO-66-S1 and UiO-66-S2 and the obtained light

yellow and white powders can be observed in **Figure A.30** in the Annexes. In the literature the powder is also reported to have the white colour.

The **UiO-66-S1**, by analysing the obtained PXRD (**Figure A.31** in the Annexes), indicated crystallinity and contained the expected diffraction patterns for UiO-66 from the literature[172] at the 2θ angles of 7.4º and 8.5º for the planes (111) and (002), respectively. However, the peaks observed were broader than expected, which indicated lower crystallinity than the desired.

The FTIR spectrum analysis of the **UiO-66-S1** (**Figure 2.17**), it was possible to detect the main vibrational modes. The main vibrational modes are the symmetric (1584 cm^{-1}) and asymetric (1390 cm^{-1}) stretching of the O-C-O bond from the carboxylates which indicate the deprotonated ligand suggesting coordination to the metal centre.

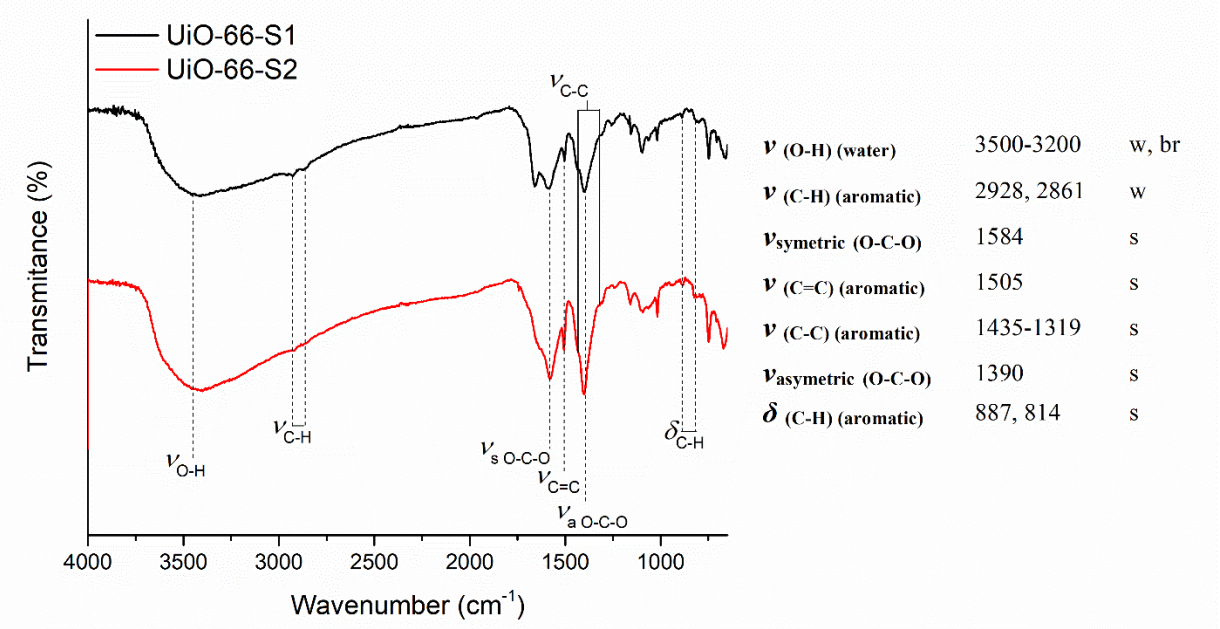

Figure 2.17 – FTIR spectra (DRIFT) of **UiO-66-S1**, **UiO-66-S2** and wavenumber values of the corresponding main vibrational modes.

However, to improve the powder crystallinity another attempt using a different synthetic method was performed. The second attempt, **UiO-66-S2**, was synthesised using hydrochloric acid (HCl) as a modulator. It is discussed in the literature that a modulator helps the zirconium precursor ($ZrCl_4$) to dissolve better in DMF speeding the product formation.[176] The powder FTIR spectrum and PXRD can be seen in **Figure 2.17** and **Figure 2.18**. The FTIR spectrum obtained was practically identical to the first attempt (**UiO-66-S1**), however the PXRD was much closer to the expected and reported in the literature with defined peaks. The obtained powder also has the expected white colour.

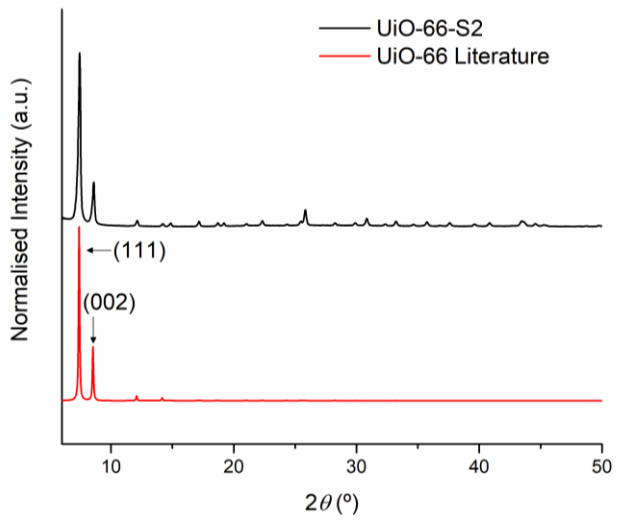

Figure 2.18 – PXRD of UiO-66-S2 and comparison with the UiO-66 diffraction pattern from the literature.[172]

UiO-66-S2 powder was tested for its stability in water like the other MOFs. The obtained PXRD (**Figure A.32** in the Annexes) and FTIR spectrum (**Figure A.33** in the Annexes) showed no changes in the structure and composition when compared with the powder before its immersion. This stability is expected, since in the literature, UiO-66 is stable in aqueous medium.

UiO-66-S2 surface was also characterised using SEM (**Figure 2.19**). The shape observed is extremely uniform, however some areas have agglomeration of smaller particles of the same shape. The size of those smaller particles changes from 0.5-1 µm and the bigger agglomerates have a maximum of 10 µm size.

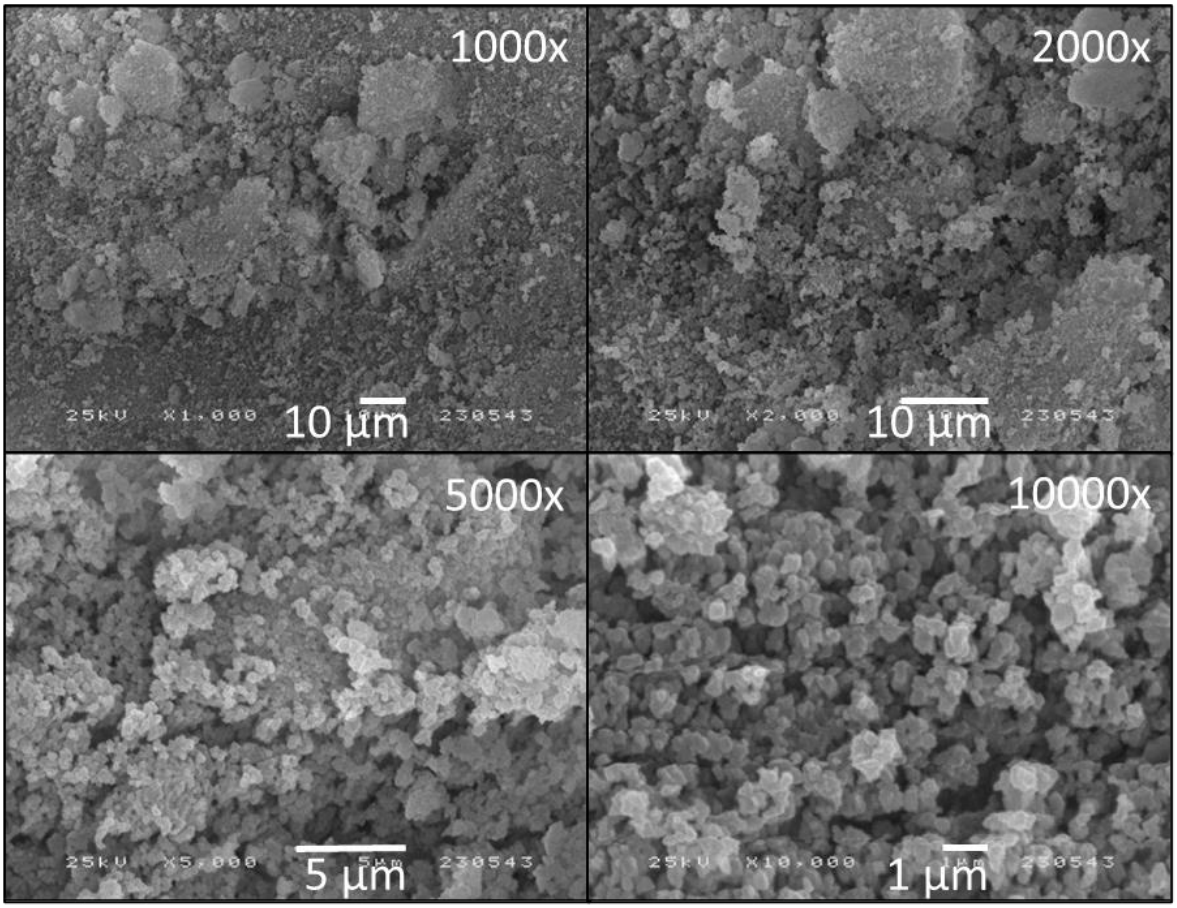

Figure 2.19 – SEM images of UiO-66-S2. Magnified at 1000x, 2000x, 5000x and 10000x.

Additionally, attempts to synthesise an amine functionalised version of UiO-66 was performed. Like IRMOF-3, UiO-66-NH_2 was chosen to study the effect of the amine functional group in the ligand's structure for future application as electrocatalysts. The first functionalised UiO-66-NH_2 was synthesised in 2010 by Gomes Silva *et al.*[173] The only difference between UiO-66 and UiO-66-NH_2 is the incorporation of the amine function in the ligand structure yielding the cluster unit (**$Zr_6O_4(OH)_4(NH_2BDC)_6$**) after the reaction of the metal centre with the organic ligand 2-aminobenzene-1,4-dicarboxylic acid (NH_2-H_2BDC). One synthetic procedure was done as seen in **Scheme 2.9**.

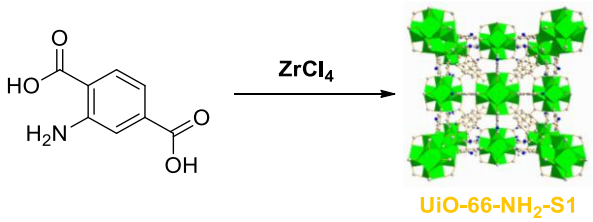

Scheme 2.9 - Synthesis and structure[177] of UiO-66-NH_2. S1[176]: DMF:HCl (15:1), 80 °C, 24 h. Activation: 100 °C, 6 h (UiO-66-NH_2-S1).

The only synthesis attempt (**S1**) was using the same procedure from Katz *et al.*[176] used previously for UiO-66. The light-yellow powder named **UiO-66-NH$_2$-S1** obtained can be seen in **Figure A.34** in the Annexes. Its colour is an indication of the presence of the amine function in the ligand.

As can be seen in the PXRD (**Figure 2.20**), a high crystallinity structure containing the main diffraction patterns expected for UiO-66-NH$_2$ was obtained, as reported in the literature. The main diffraction patterns are the same as the UiO-66 since its functionalisation does not interfere with the final MOF strucutre.

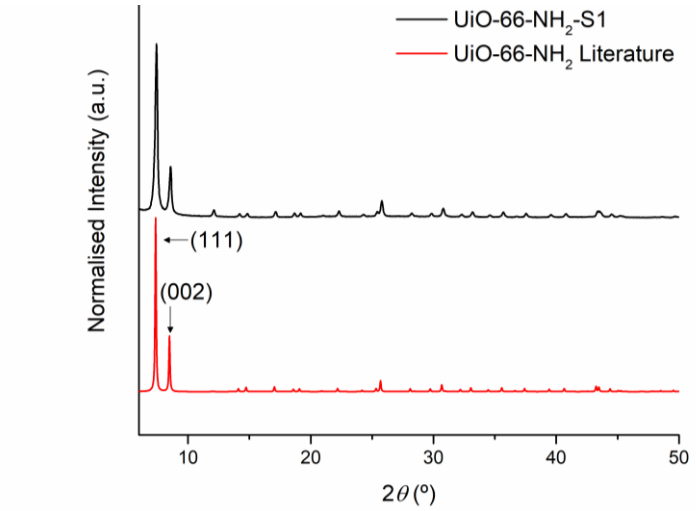

Figure 2.20 - PXRD of **UiO-66-NH$_2$-S1** and comparison with UiO-66-NH$_2$ diffraction patterns from the literature.[178]

Additionally, in the FTIR spectrum of **UiO-66-NH$_2$-S1** (**Figure 2.21**) all the main vibrational modes were observed, which are identical to the UiO-66, with the exception of the additional vibrational modes from the amine group. Similar to ZIF-8 and IRMOF-3, the stretching vibration of the N-H bond from the amine function at approx. 3400 cm^{-1} was not observed. However, the stretching vibration from the C_{aryl}-N_{amine} bond in the 1254 cm^{-1} range was detected confirming the presence of the amine function in the structure.

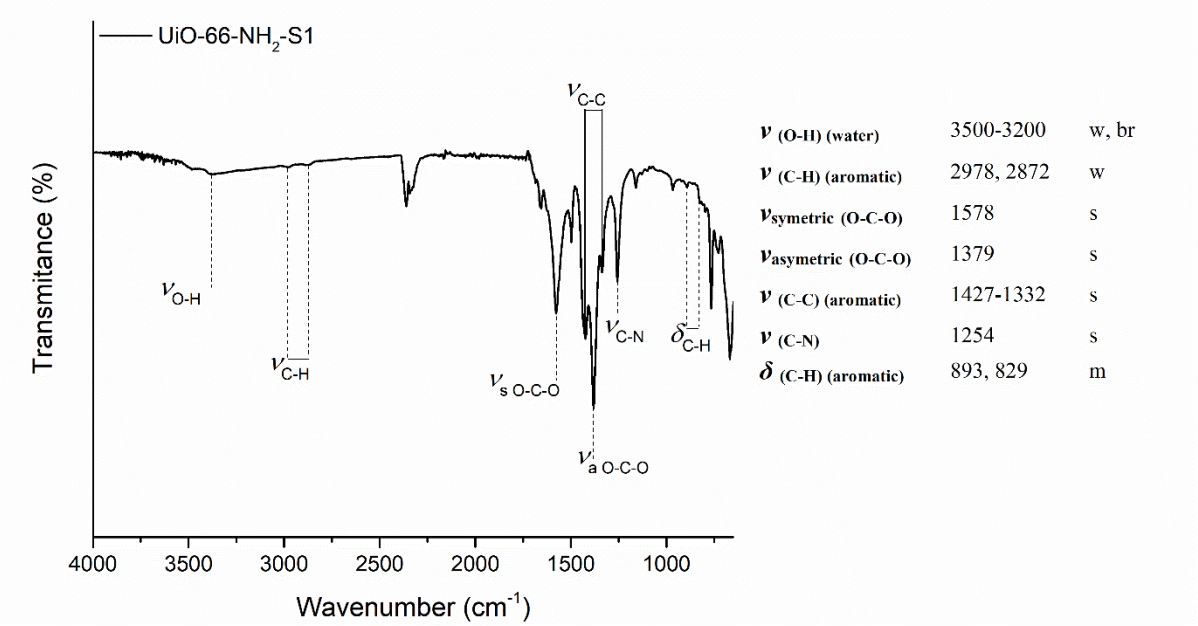

Figure 2.21 – ATR spectrum of **UiO-66-NH2-S1** and wavenumber values of the corresponding main vibrational modes.

Water stability tests were also performed for the **UiO-66-NH2-S1** powder. Identical to UiO-66, there were no major changes in the main vibrational modes and the diffraction patterns, indicated by the FTIR spectra and PXRD in **Figure A.35** and **Figure A.36** in the Annexes. This means the powder is highly stable in water.

Additionally, the surface of the powder **UiO-66-NH2-S1** was also analysed using SEM (**Figure 2.22**). The shape and size (0.5-1 µm) are comparable to the microscope analysis obtained for the **UiO-66-S3** powder, however there is less agglomeration of the particles, yielding a more uniform distribution of the particles.

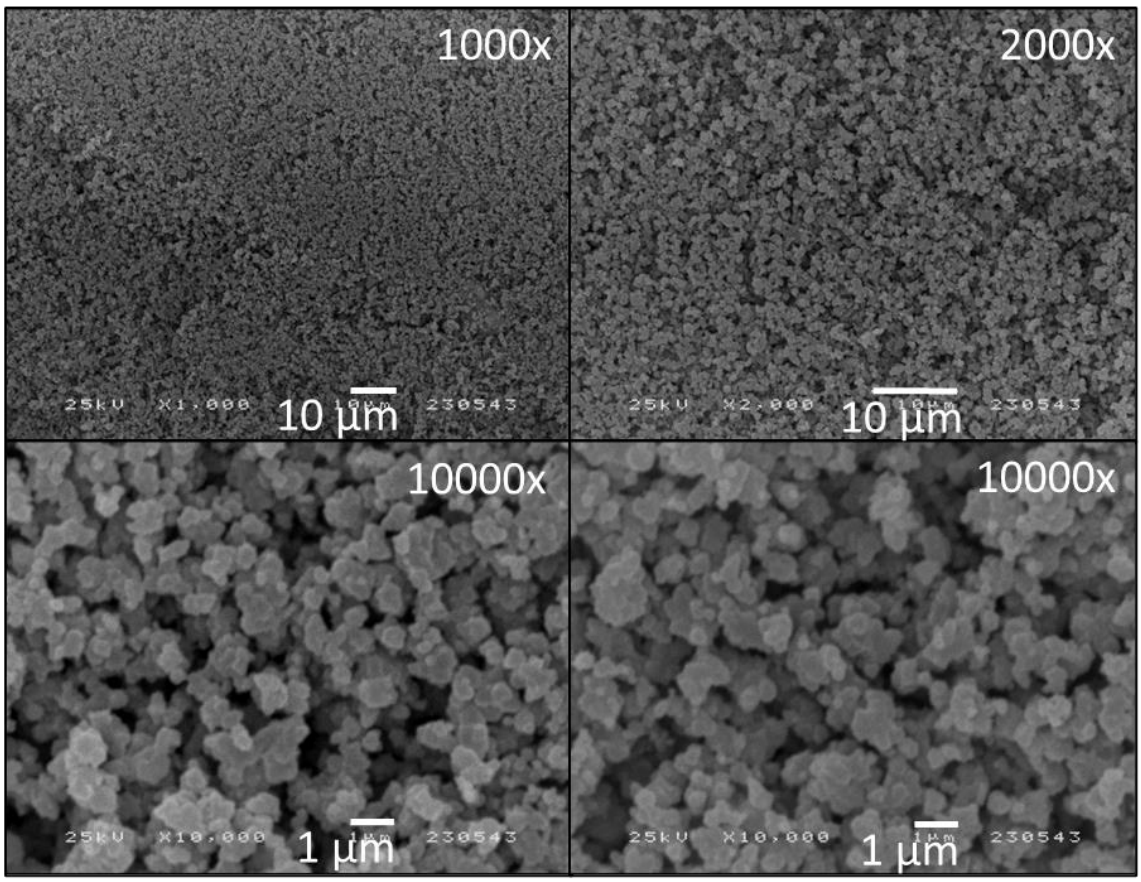

Figure 2.22 – SEM images of UiO-66-NH_2-S1. Magnified at 1000x, 2000x and 10000x.

2.1.6 Conclusions

In conclusion, it was possible to successfully synthesised six out of the nine MOFs proposed for this work with high crystallinity, as can be seen in **Figure 2.23**. Five of those six MOFs indicated high stability in water for at least 24 h.

UiO-66 and UiO-66-NH_2, according to the literature, are the two most stable MOFs, in basic or acidic aqueous media. Mg-MOF-74, Ni-MOF-74 and HKUST-1 seem the most promising to perform tests in adsorption and catalysis due to their high reactivity caused by their open metal sites. In the case of the HKUST-1, however, its application cannot be in aqueous medium due to its high reactivity with water. Finally, ZIF-8 showed the easiest MOF to be synthesised.

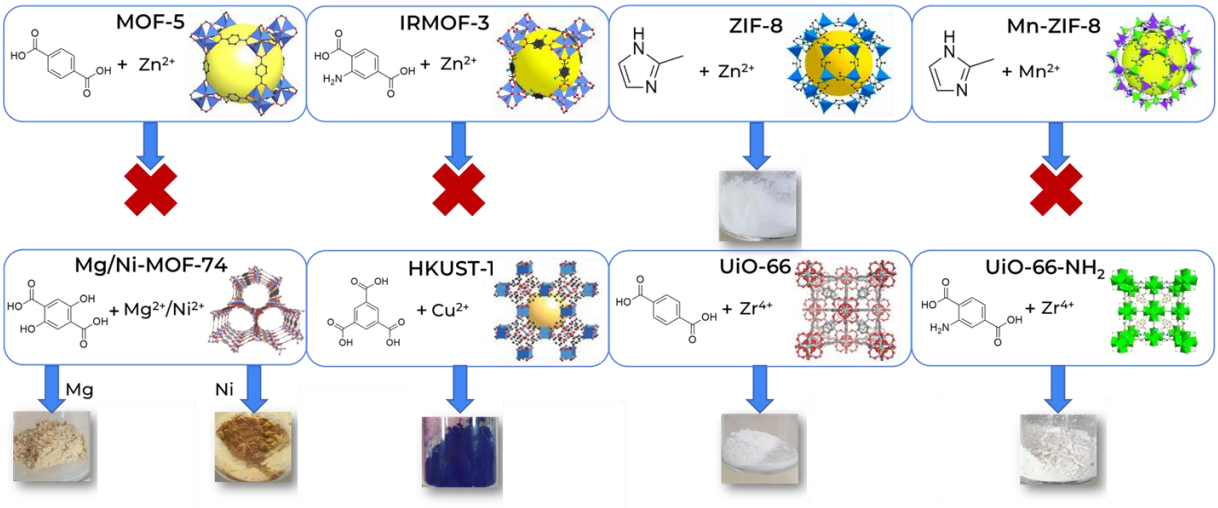

Figure 2.23 – Results of the nine MOFs synthesised using solvothermal procedures.

2.2 Electrochemical Deposition and Films Characterisation

As explained in **Chapter 1.6**, to be able to use MOFs as electrocatalysts we must first immobilise them on a conductive surface. Overall, the electrochemical deposition of MOFs remains unexplored, some specific MOFs like MOF-5 and HKUST-1 have been the most studied.[114,135,141,179]

Two electrochemical depositions techniques will be presented in this chapter, one direct method, the cathodic deposition and one indirect method, the electrophoretic deposition. In the cathodic deposition, it was used the inorganic and organic MOF precursors and attempted to directly form the MOF on the surface of the electrode (FTO). In the electrophoretic deposition, it was used the MOFs previously synthesised via a solvothermal method, and consequently immobilised on the surface of the electrode (FTO).

The MOFs chosen for both methods are included in the nine MOFs that were attempted to synthesise, in **Chapter 2.1** (**Figure 2.23**). The MOFs that were unable to be synthesised via the conventional solvothermal method as well as the ones who showed good stability in water were attempted to be prepared using the direct method – cathodic deposition. The indirect method was used to immobilise all the MOFs that were successfully prepared, focusing on the ones that had a good water stability. The films obtained were characterised by PXRD, FTIR and SEM.

The *E* mentioned in this chapter is always *vs.* Ag/AgCl, 3 M NaCl.

2.2.1 Direct Method – Cathodic Deposition

Cathodic deposition is a versatile method for the formation of compounds on the surface of the electrode using a reductive *E*. The mechanism, already discussed as well in **Chapter 1.6**, is present in **Scheme 2.10**.

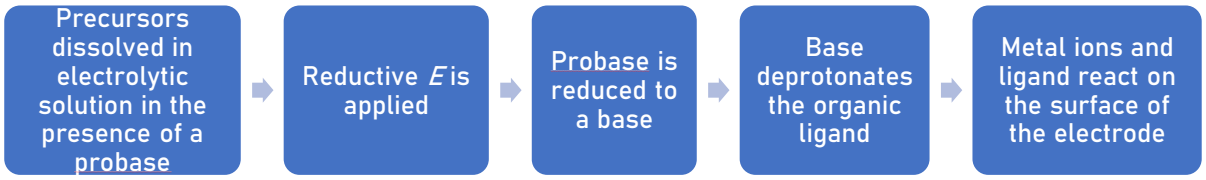

Scheme 2.10 – Cathodic deposition mechanism.

The choice of the probase aside from the MOF precursors is extremely important. All the MOFs deposited using this method were done using DMF as the solvent. The probase chosen must be completely soluble in DMF, in specific concentrations. The probase needs to be reduced at an accessible *E* so as not to affect any of the other MOF precursor species or the electrode.

CVs were also performed before deposition with all the components to assess the contents of the solution (presence of O_2 and impurities which may be visible via the formation of new oxidation and reduction peaks). Some depositions failed and further characterisation was not performed when it was not possible to visually observe a film, the film presented extremely low uniformity, the film fell off the electrode, or its appearance was different than the expected from the MOF.

With this method attempts to directly form films for MOF-5, IRMOF-3, Mg-MOF-74, Ni-MOF-74, and UiO-66 were performed. The deposition of ZIF-8 using this method was not performed as once the precursors are dissolved the MOF immediately starts to be formed at ambient conditions. HKUST-1 was not attempted due to time constraints. Further details on the process and setup used is available in the experimental part (**Chapter 3.4**).

2.2.1.1 MOF-5 and IRMOF-3

Due to the unsuccessful solvothermal synthesis of MOF-5 and the fact that it is one of the most studied MOFs in electrochemical cathodic deposition, MOF-5 was the most focused MOF to attempt and optimise its film formation on the electrode surface.

Considering the time available, extensive tests were performed adapting the conditions for the MOF film formation on some of its literature[114,180] and recent works in the group using a different MOF. The several attempts and respective conditions are represented in **Table A.1** in the Annexes. Modifications were done for both the proportions and concentrations of the precursors ($Zn(NO_3)_2{\cdot}6H_2O$ and H_2BDC) and the probases (Et_3NHCl and H_2O_2) used. The concentrations varied from 10 to 300 mM with proportions using the ligand as the component with the lowest concentration and the metal precursor either in similar or lower concentrations as that of the probase. The *E* applied on the cathode depended on the reduction *E* of the probase. The *E* varied from -1.5 V to -0.5 V. Studies were also performed for the deposition time differing the time from 15 min to 1 h 30 min.

Two of the most promising results (**Table 2.1**) using both probases were chosen to be further analysed, named **MOF-5-C1** (conditions: -1.4 V for 30 min using 10:5:20 mM metal:ligand:probase (M:L:P) proportions using H_2O_2 as the probase) and **MOF-5-C2** (conditions: -1.4 V for 30 min using 100:50:100 mM M:L:P proportions, using Et_3NHCl as the probase). The films can be seen in **Figure A.37** in the Annexes.

Table 2.1 - Conditions and components used in the cathodic deposition of the promising results of MOF-5: **MOF-5-C1** and **MOF-5-C2**.

MOF	Designation	Metal Ion/Cluster	Organic Ligand	Probase	Solvent	Time	E (V)
MOF-5 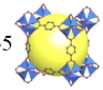	**MOF-5-C1**	10 mM $Zn(NO_3)_2 \cdot 6H_2O$	5 mM H_2BDC	20 mM H_2O_2	10 mL Dry DMF	30 min	-1.4
	MOF-5-C2	100 mM $Zn(NO_3)_2 \cdot 6H_2O$	50 mM H_2BDC	100 mM Et_3NHCl	10 mL DMF		

The PXRD of the **MOF-5-C1** and **MOF-5-C2** films can be seen in **Figure 2.24**.

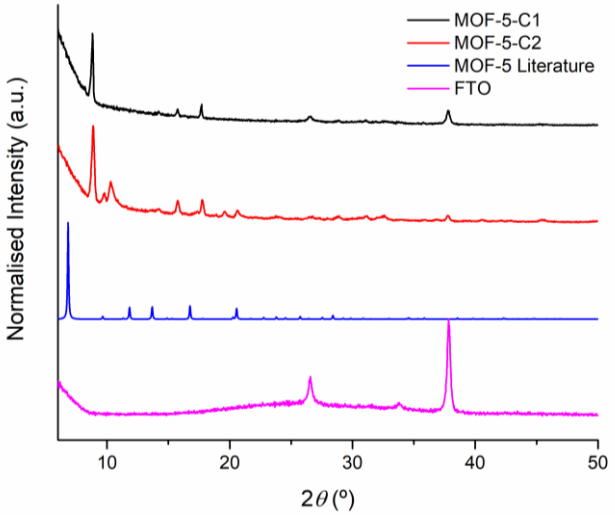

Figure 2.24 – PXRD of **MOF-5-C1**, **MOF-5-C2** and FTO comparison with MOF-5 diffraction pattern from the literature.[146]

By comparison, looking at the FTIR spectra obtained for the **MOF-5-C1** and **MOF-5-C2** films (**Figure 2.25**), one can see similarities between the films and the spectrum obtained for the **MOF-5-S2** powder. This means that most likely completely different crystalline structures are formed that are not MOF-5, similar to what happened when solvothermal synthesis was attempted.

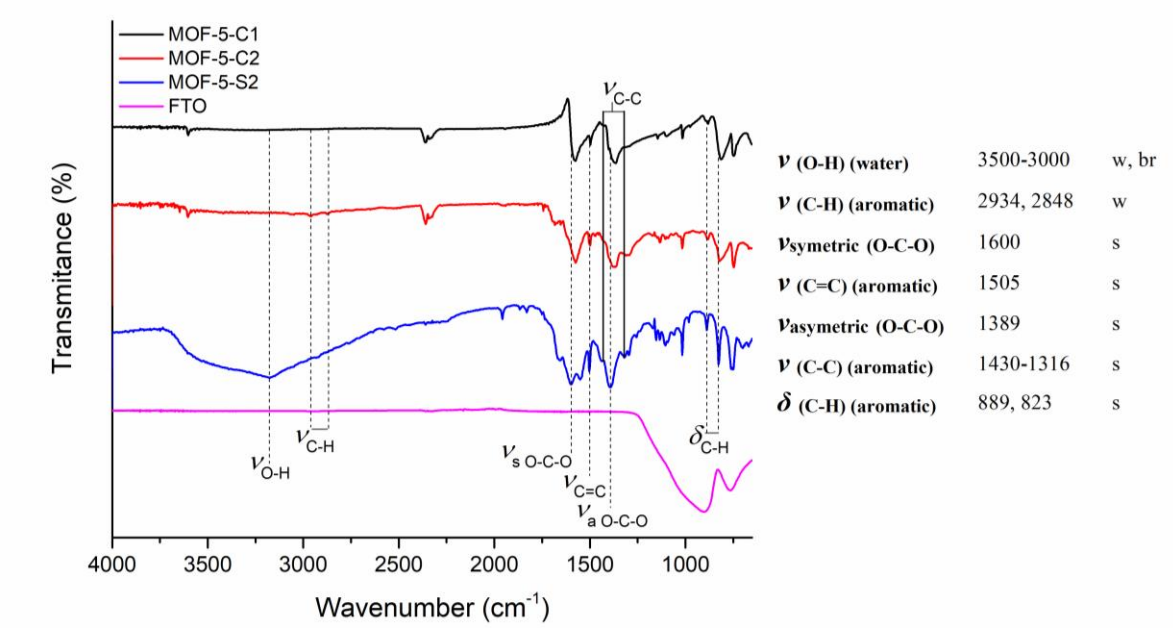

Figure 2.25 – FTIR spectra (DRIFT/ATR) of **MOF-5-C1**, **MOF-5-C2**, **MOF-5-S2**, FTO and wavenumber values of the corresponding main vibrational modes.

Overall, of the several films under different conditions, three results were mostly obtained - a mixture of diffraction patterns not belonging to the crystalline planes of the MOF-5, a high intensity peak belonging to the deposition of either Zn or its oxides or simply a completely amorphous film indicated by no visible diffraction patterns, suggesting unsuccessful formation of MOF-5.

IRMOF-3 film was also tried to be prepared using this method. Only two films were produced, both used the same conditions of **MOF-5-C2** but using the ligand NH_2-H_2BDC instead. However, the films produced were completely amorphous and some kind of reaction was occurring with the ligand under electrochemical conditions as it was possible to see some kind of precipitation during the process (**Figure A.38** in the Annexes).

2.2.1.2 Mg-MOF-74 and Ni-MOF-74

The several attempts to prepare Mg-MOF-74 and Ni-MOF-74 films where several conditions were changed (probase, concentrations, deposition time) are present in **Table A.2** in the Annexes. However, in this section it will be discussed the attempts using the conditions discussed above for MOF 5 (**Ni-MOF-74-C1**, **Chapter 2.2.1.1**) and the previous conditions used in the group when Fe^{2+} is used as the metal ion (**Ni-MOF-74-C2**).[181] The conditions are detailed in **Table 2.2**.

Table 2.2 - Conditions and components used in the cathodic deposition of the promising results of Ni-MOF-74: **Ni-MOF-74-C1** and **Ni-MOF-74-C2**.

MOF	Designation	Metal Ion/Cluster	Organic Ligand	Probase	Solvent	Time	E (V)
Ni-MOF-74 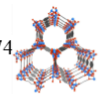	**Ni-MOF-74-C1**	100 mM $Ni(NO_3)_2 \cdot 6H_2O$	50 mM DHTA	100 mM Et_3NHCl	10 mL Dry DMF	30 min	-1.3
	Ni-MOF-74-C2	4 mM $NiCl_2 \cdot 6H_2O$	2 mM DHTA	2 mM Et_3NHCl	10 mL DMF		

The two Mg-MOF-74 films obtained were not further characterised due to their visible low and not uniform deposition (**Figure A.39** in the Annexes). Moreover, the colour is not consistent with the expected for Mg-MOF-74. The two Ni-MOF-74 films reproduced under the same conditions yielded no crystalline MOF-74 films, only amorphous films (**Figure. 2.26**). No relevant vibrational modes corresponding to the MOF were observed via FTIR (**Figure 2.27**).

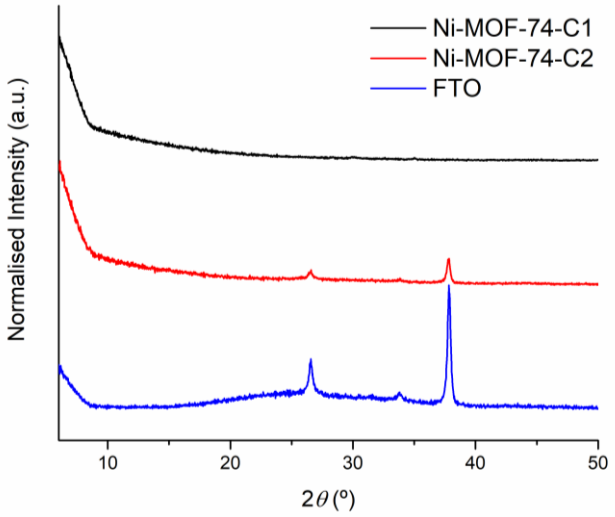

Figure 2.26 – PXRD of **Ni-MOF-74-C1**, **Ni-MOF-74-C2** and FTO.

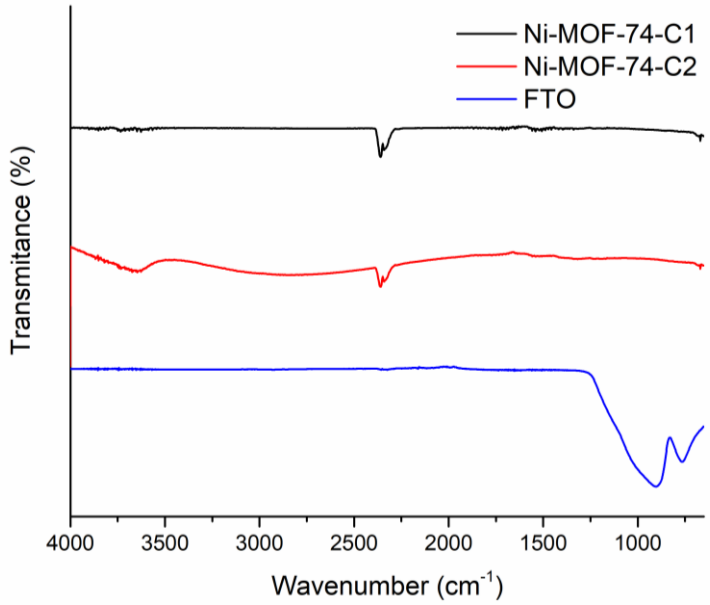

Figure 2.27 – FTIR spectra (DRIFT/ATR) of **Ni-MOF-74-C1**, **Ni-MOF-74-C2** and FTO.

2.2.1.3 UiO-66

Several UiO-66 films were attempted to be deposited following the conditions in **Table A.3** in the Annexes. Those conditions varied from high and low concentrations of the precursors and probase using both probases (4 mM to 200 mM), time (0.5 h to 2 h) and *E* (-1.4 V to -0.5 V).

However, a different problem occurred, that is, the insolubility of the metal precursor ($ZrCl_4$) in DMF. The solvothermal synthesis of UiO-66 uses DMF as the solvent but uses high temperatures and the metal precursor can be dissolved allowing the reaction to take place. Knowing this, previous to its attempt the solution was heated using both high and low concentrations, however, it was only possible to partially dissolve the precursor. Nonetheless the deposition was attempted, although its insolubility would certainly interfere with the process.

All the films attempted to form had little to no deposition and/or uniformity whatsoever.

2.2.2 Indirect Method – Electrophoretic Deposition

Electrophoretic deposition is an electrochemical method that allows the immobilisation of the charged particles of previously synthesised powders on the surface of an electrode with the application of an electric field. The mechanism already discussed as well in **Chapter 1.6**, is present in **Scheme 2.11**.

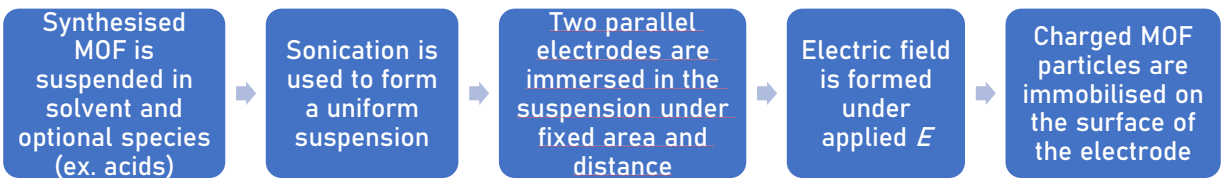

Scheme 2.11 – Electrophoretic deposition mechanism.

Multiple factors need to be taken into consideration when planning on using electrophoretic deposition. A successful immobilisation using electrophoretic deposition requires a stable, uniform suspension with appropriate conductivity. The uniformity of the suspension is highly dependent on the interactions between the solvent, or mixture of solvents, and the powder particles. Other important properties to consider are the particle size, the suspension zeta potential, the suspension pH, the *E* applied, among others. With few exceptions where specific literature was followed, the conditions chosen for the deposition were based on some of the optimal properties found on the review article published by Besra and Liu.[137]

In this chapter it will be discussed the attempts made for the immobilisation of the previously synthesised powders for ZIF-8, Mg-MOF-74, Ni-MOF-74, HKUST-1, UiO-66 and UiO-66-NH_2. With few exceptions, most of the films were characterised by PXRD and FTIR. Only one film, after optimisation, for each successful MOF film was characterised using SEM. Further details are present in the experimental section (**Chapter 3.4**).

The deposition was done mostly in FTO and graphite foil. The reason was to study the comparison between a non-porous (FTO) and a porous (graphite foil) electrode.

2.2.2.1 ZIF-8

Due to the reactivity of the precursors for ZIF-8 at ambient conditions, cathodic deposition is not a viable method for ZIF-8 deposition as a film. Therefore, a procedure was found in the literature where a suspension using the precursors was formed and a *E* was immediately applied generating an electric field.[144,145] In other attempts the ZIF-8 powders were previously synthesised before use. The attempts and respective conditions used are present in **Table A.4** in the Annexes.

Following the procedure from He *et al.*[145], with no modifications, the immobilisation of the MOF using its precursors was attempted, however nothing was deposited on the surface of the electrode.

For the remaining films different electric fields (20 V cm^{-1} and 90 V cm^{-1}), solvents (isopropanol, ethanol (EtOH), and toluene) and deposition times (30 min, 1 h and 2 h 30 min) were experimented with. A suspension was always formed using 10 mg of ZIF-8 powder. Unfortunately, a stable suspension was unable to be formed most of the times since it dissolved in ethanol and isopropanol under sonication while in toluene the powder particles rapidly deposited to the bottom of the beaker.

In **Chapter 2.1.2**, water stability tests were performed and indicated that ZIF-8 did not suffer any major changes in the structure after in contact with water. However, a report from Zhang *et al.*[182] confirms that depending on the contact time and ZIF-8/water ratio, ZIF-8 will decompose overtime into a different soluble species. The study indicates that by filtration after ZIF-8 immersion in water, only the intact particles are recovered while the decomposition stays in the supernatant solution. This explains why the particles recovered in **Chapter 2.1.2** indicated no change in the crystallinity, since only the intact structure was recovered in the filter. It seems to explain, as well, why under sonication ZIF-8 dissolves under 96% ethanol and isopropanol while in toluene does not, since under sonication there is an increase in contact between the solvent and the particles.

2.2.2.2 Mg-MOF-74 and Ni-MOF-74

For the MOF-74 containing Ni^{2+} or Mg^{2+} as metal nodes, multiple depositions were attempted. Different electric fields (30 V cm^{-1}, 60 V cm^{-1} and 90 V cm^{-1}) and solvents (ethanol, toluene, and acetone) were

experimented with using a deposition time of 2 h 30 min or 6 h. The attempts and conditions used are represented in **Table 2.3** for the promising films and **Table A.5** in the Annexes for the remaining.

Table 2.3 - Conditions and components used in the electrophoretic deposition of the promising results of Ni-MOF-74: **Ni-MOF-74-E1-5**.

MOF	Designation	Solvent	Time	Electric Field (V cm^{-1})
Ni-MOF-74 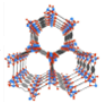	**Ni-MOF-74-E1**	20 mL Toluene	2 h 30 min	60
	Ni-MOF-74-E2			90
	Ni-MOF-74-E3			30
	FTO: **Ni-MOF-74-E4** Graphite foil: **Ni-MOF-74-E5**	20 mL EtOH + Acetic Acid		60

Using toluene, it was possible to form a more stable suspension using Ni-MOF-74 powder particles, however, although not as quickly as in ZIF-8, the powder particles rapidly deposited on the bottom of the beaker. Using the three electric fields conditions (30, 60 and 90 V cm^{-1}) extremely thin films were obtained, named **Ni-MOF-74-E1**, **Ni-MOF-74-E2** and **Ni-MOF-74-E3**, respectively (**Figure A.40** in the Annexes). The diffraction patterns expected for the Ni-MOF-74 were observed in the PXRD of the film (**Figure 2.28**), albeit with extremely low intensity, which is to be expected due to the thickness of the film.

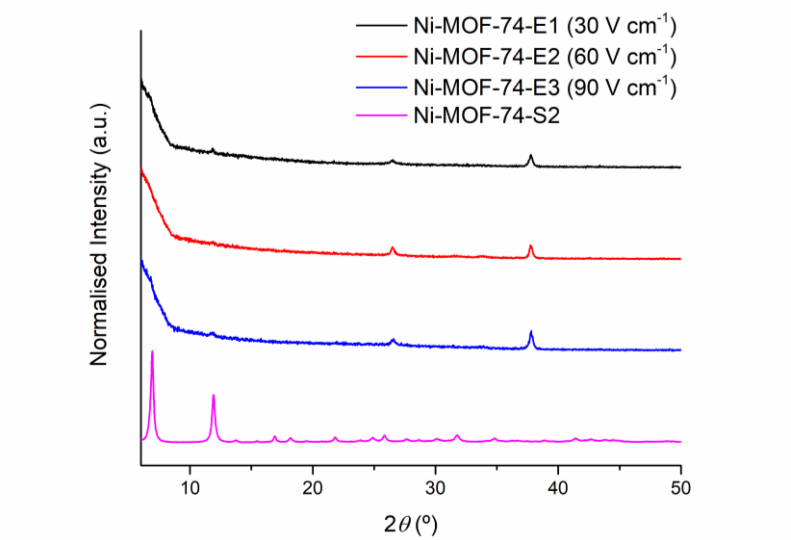

Figure 2.28 – PXRD of **Ni-MOF-74-E1**, **Ni-MOF-74-E2** and **Ni-MOF-74-E3** under different electric field conditions (30, 60 and 90 V cm^{-1}) in toluene, in comparison to the used **Ni-MOF-74-S2** powder.

To further optimise the process, deposition using suspensions in ethanol and acetone were attempted. However, the desired electric field (60 and 90 V cm^{-1}) using these solvents, frequently could not be reached, suggesting the low conductivity of the suspension leading to nothing being deposited. The suspensions in toluene did not have this problem, while in acetone was hardest to reach the electric field desired. A possible explanation for this is due to the fact that ethanol and acetone have low amount of free ions present in the suspension. The electric charges on the oxides in those solvents are insufficient for the electrophoretic deposition.[137]

Moreover, due to the importance of the zeta potential (which is difference between the *E* of the medium and of the stationary layer of fluid attached to the particle) for the stability of the suspension and the effect pH has this parameter, attempts were made to control the pH of the suspension. The pH was chosen according to the literature[137] where a good ratio between the zeta potential and the conductivity in the suspension used was between 2-4 pH. Thus, a weak acid (acetic acid) was used. Due to the insolubility of acetic acid in toluene, the suspensions were formed using ethanol instead. As films were obtained successfully with these modifications, no further attempts to modify the other parameters were performed. A high uniform and crystalline Ni-MOF-74 film using 60 V cm^{-1} for 2 h 30 min and 10 µL of acetic acid in ethanol was obtained where the suspension had pH of 4.4. The film characterisation using PXRD and FTIR is present in **Figure 2.29** and **Figure 2.30**, respectively.

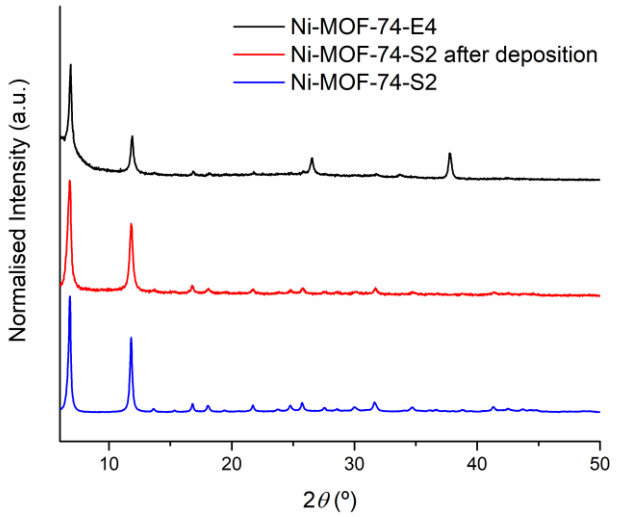

Figure 2.29 – PXRD of **Ni-MOF-74-E4** and used powder **Ni-MOF-74-S2** both before and after deposition.

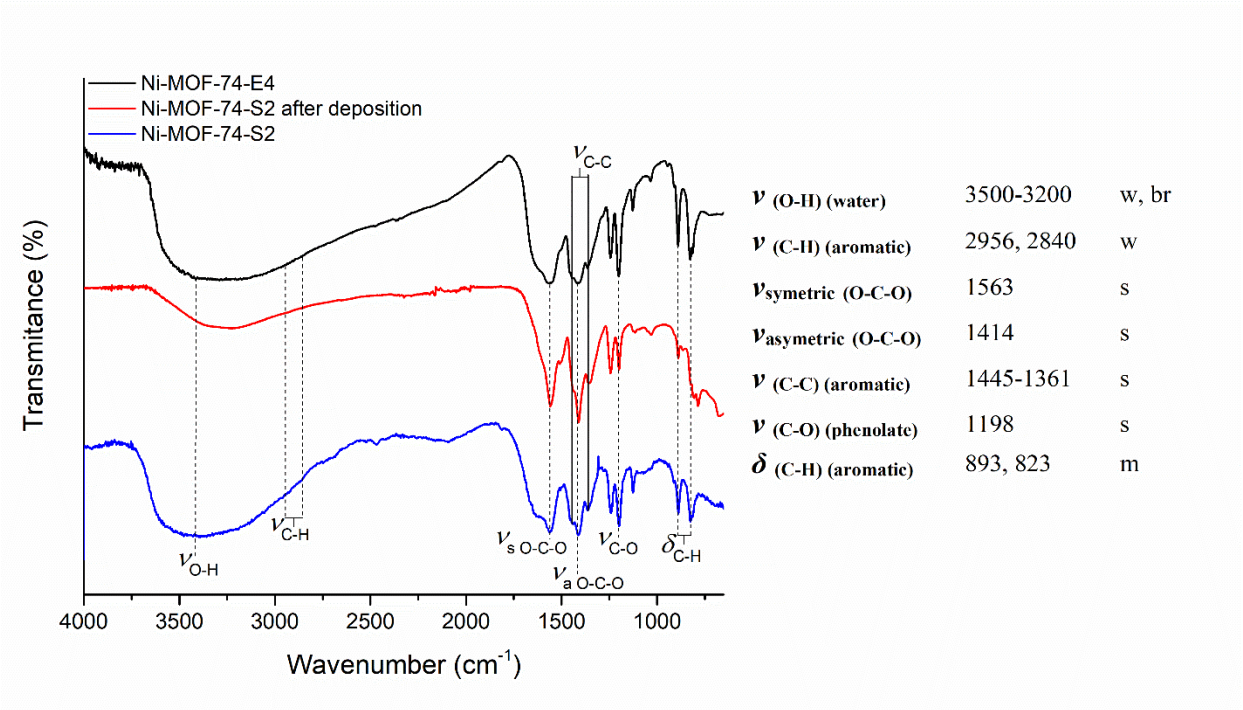

Figure 2.30 – FTIR spectra (DRIFT/ATR) of **Ni-MOF-74-E4** and used powder **Ni-MOF-74-S2** both before and after deposition and wavenumber values of the corresponding main vibrational modes.

Additionally, the **Ni-MOF-74-E4** film was also characterised using SEM (**Figure 2.31**). The obtained surface images are extremely similar to the respective **Ni-MOF-74-S2** powder (**Figure 2.13**). The aggregates have similar size and shape, although slightly more uniform, which confirms the visible homogeneity of the film (**Figure A.41** in the Annexes).

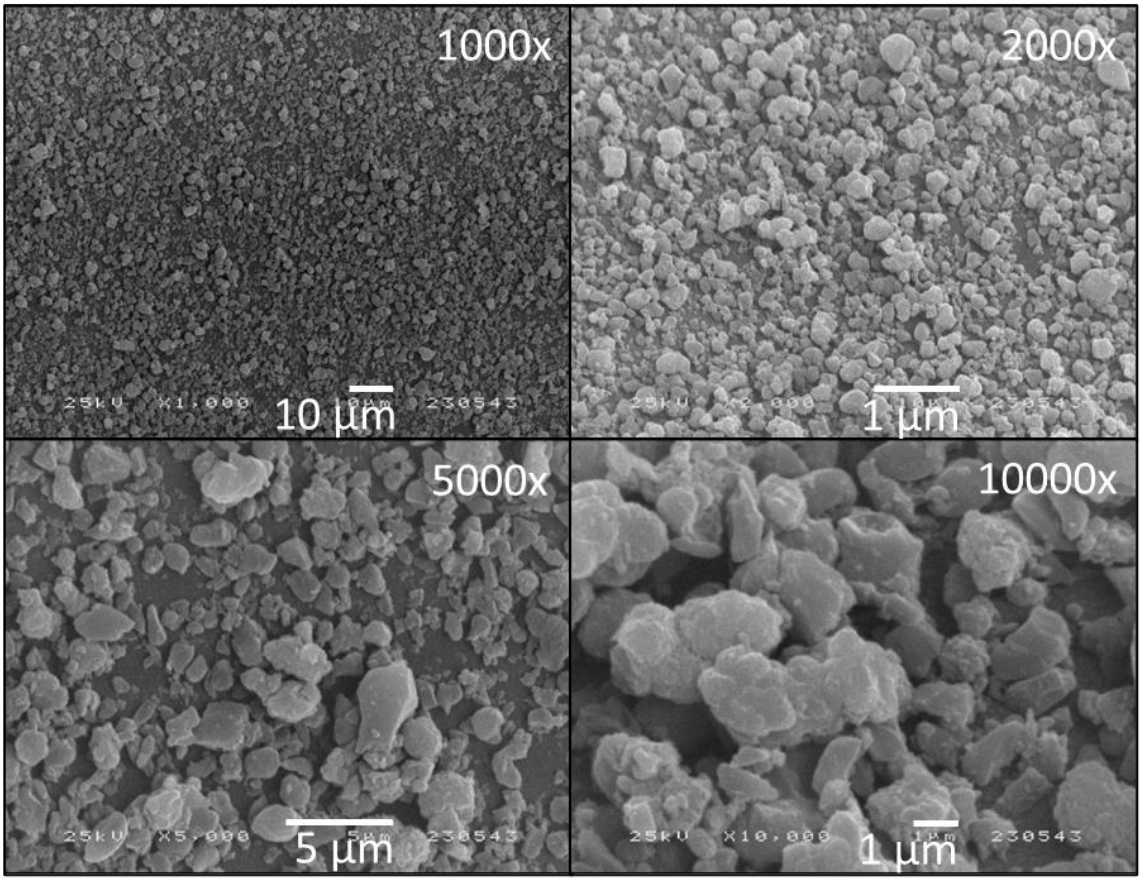

Figure 2.31 – SEM images of **Ni-MOF-74-E4**. Magnified at 1000x, 2000x, 5000x and 10000x.

It was possible to also deposit a Ni-MOF-74 film in graphite foil. The respective characterisation is present in **Figure A.42** and **Figure A.43** in the Annexes. Graphite foil presents an extremely high intensity diffraction peak at the 26.6º 2θ value that overshadows the diffraction patterns of the MOF. Visually it is possible to see the MOF deposited on the graphite foil (**Figure A.44** in the Annexes). Using SEM, the surface of the graphite foil film (**Ni-MOF-74-E5**) was also analysed (**Figure A.45** in the Annexes). In comparison with the **Ni-MOF-74-E4** film (Ni-MOF-74 deposited onto FTO), the **Ni-MOF-74-E5** have a higher aggregation of the particles at the surface of the graphite foil, as well as the fact that the surface is rougher as expected for the graphite foil.

The same conditions were used for the deposition of the Mg-MOF-74. However, the suspension was less stable indicated by a slight change in colour, from a light brown to a greyish brown, as well as the fact that was not possible to change the pH of the suspension using different amounts of acetic acid (10-100 µL). Nonetheless, the deposition was attempted. The desired electric field (60 and 90 V cm^{-1}) could not be reached identical to what was mentioned above. The obtained film named **Mg-MOF-74-E1** is represented in **Figure A.46** in Annexes and was considered a failed attempt due to the unusual film appearance, as well as the slight degradation of the FTO (dark edges around the film) under the extremely high *E* applied. Attempts were also made using just toluene, but nothing was deposited as the powder quickly dropped to the bottom of the beaker.

2.2.2.3 HKUST-1

Attempts were also performed to deposit the HKUST-1 powders using the conditions for the **Ni-MOF-74-E4** both in ethanol with acetic acid and in toluene. As mentioned in **Chapter 2.1**, HKUST-1 decomposes in the presence of water indicated by its rapid change in colour from Persian blue to light blue. This phenomenon occurred in ethanol, and only that light blue species was deposited on the electrode. In toluene nothing was deposited due to the low suspension stability having the powder extremely quickly deposit on the bottom of the beaker.

2.2.2.4 UiO-66 and UiO-66-NH_2

The deposition of UiO-66 and its functionalised version UiO-66-NH_2 was also attempted. Studies using different solvents (toluene and ethanol), electric fields (60 and 90 V cm^{-1}) and deposition times (5 min to 2 h 30 min) were made. The attempts and conditions used are represented in **Table 2.4** for the promising results and **Table A.6** in the Annexes for the remaining attempts.

Table 2.4 - Conditions and components used in the electrophoretic deposition of the promising results of UiO-66: **UiO-66-E1-2**; and UiO-66-NH_2: **UiO-66-NH_2-E1**.

MOF	Designation	Solvent	Time	Electric Field (V cm^{-1})
UiO-66 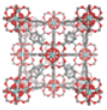	FTO: **UiO-66-E1** Graphite foil: **UiO-66-E2**	20 mL EtOH + 10 µL Acetic Acid	5 min	90
UiO-66-NH_2 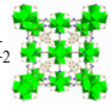	**UiO-66-NH_2-E1**			

It was possible to obtain relatively stable suspensions in toluene and ethanol. However, practically nothing was deposited when using ethanol due to not being able to reach the desired electric field, as mentioned in **Chapter 2.2.2.2**. However, the suspension made in ethanol with the presence of acetic acid (pH = 3.2) yielded films. The films obtained when using a suspension in ethanol and acetic acid had low uniformity. The film grew thicker on the edges of the electrode while thinner in the centre. Additionally, the film fell from the electrode's surface due to its high thickness on the edges and especially when washed with acetone. Unlike Ni-MOF-74, the UiO-66 particles deposit much faster on the electrode. It was possible to form a thick UiO-66 film using only 5 min of deposition time.

The main problem was optimising the process to obtain a more uniform film. Several optimisation attempts were performed varying the electric field and time (increasing one while decreasing the other or vice-versa). The most promising films were obtained by using 90 V cm^{-1} during 5 min (**Figure A.47** in Annexes). The low uniformity led to small differences in subsequent repetitions. The obtained PXRD diffractograms and FTIR spectrum for the film using these conditions (**UiO-66-E1**) is present in **Figure**

2.32 and **Figure 2.33**, respectively. The expected main diffraction patterns and vibrational modes were obtained.

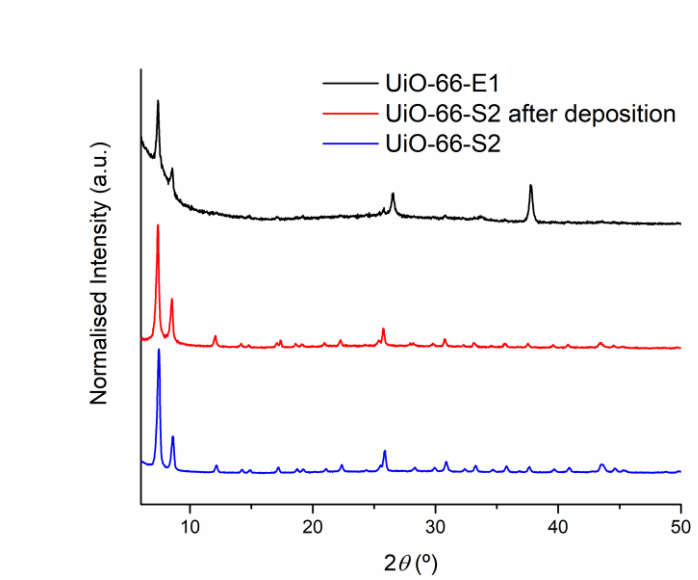

Figure 2.32 - PXRD of **UiO-66-E1** and used powder **UiO-66-S2** both before and after deposition.

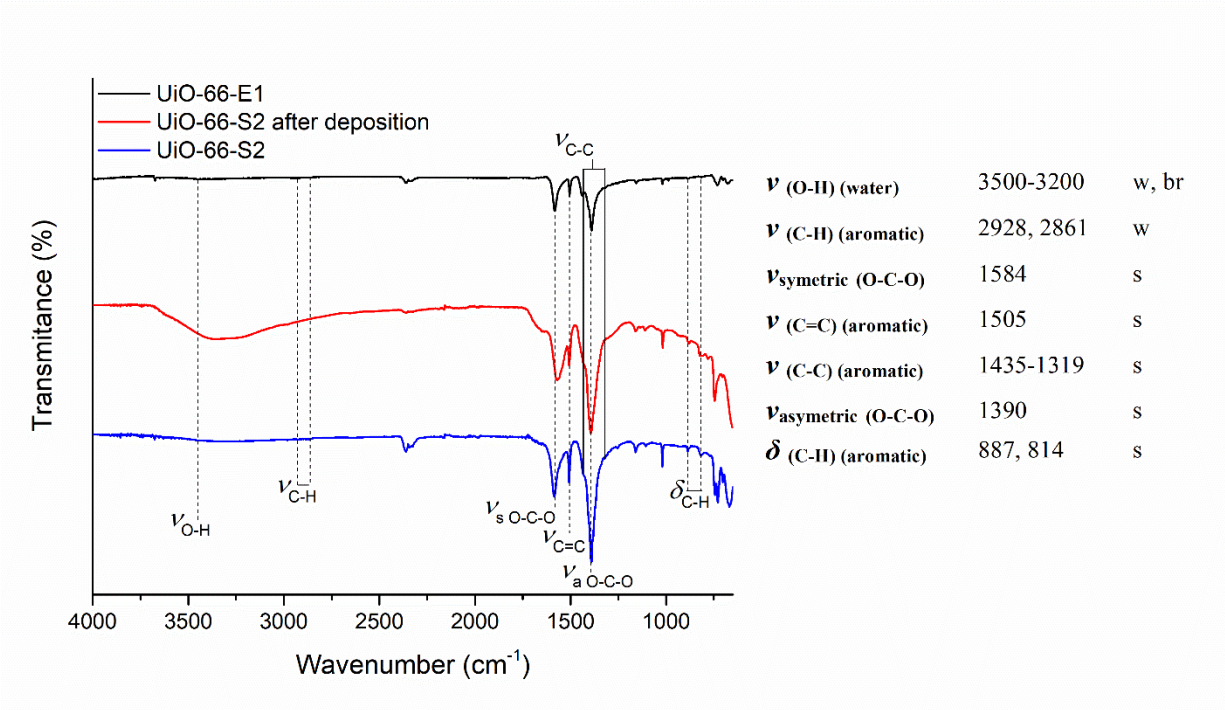

Figure 2.33 - FTIR spectra (ATR) of **UiO-66-E1** and used powder **UiO-66-S2** both before and after deposition and wavenumber values of the corresponding vibrational modes.

The same conditions for the electrophoretic deposition were used for the graphite foil substrate (**Figure A.48** in the Annexes), as well as, to deposit the UiO-66-NH_2 on FTO (**Figure A.49** in the Annexes). The characterisation of UiO-66 film at graphite foil electrode (**UiO-66-E2**) is present in the **Figure A.50**

and **A.51** in the Annexes. The characterisation of the UiO-66-NH_2 film at FTO (**UiO-66-NH_2-E1**) is present in the **Figure A.52** and **A.53** in the Annexes.

Additionally, the three films were characterised using SEM. The surface of the **UiO-66-E1** (**Figure 2.34**) and **UiO-66-E2** (**Figure A.54** in the Annexes) films were similar, with uniform particle size as obtained for the **UiO-66-S2** powder. However due to the low uniformity of the film a few cracks in the surface and some empty zones were observed.

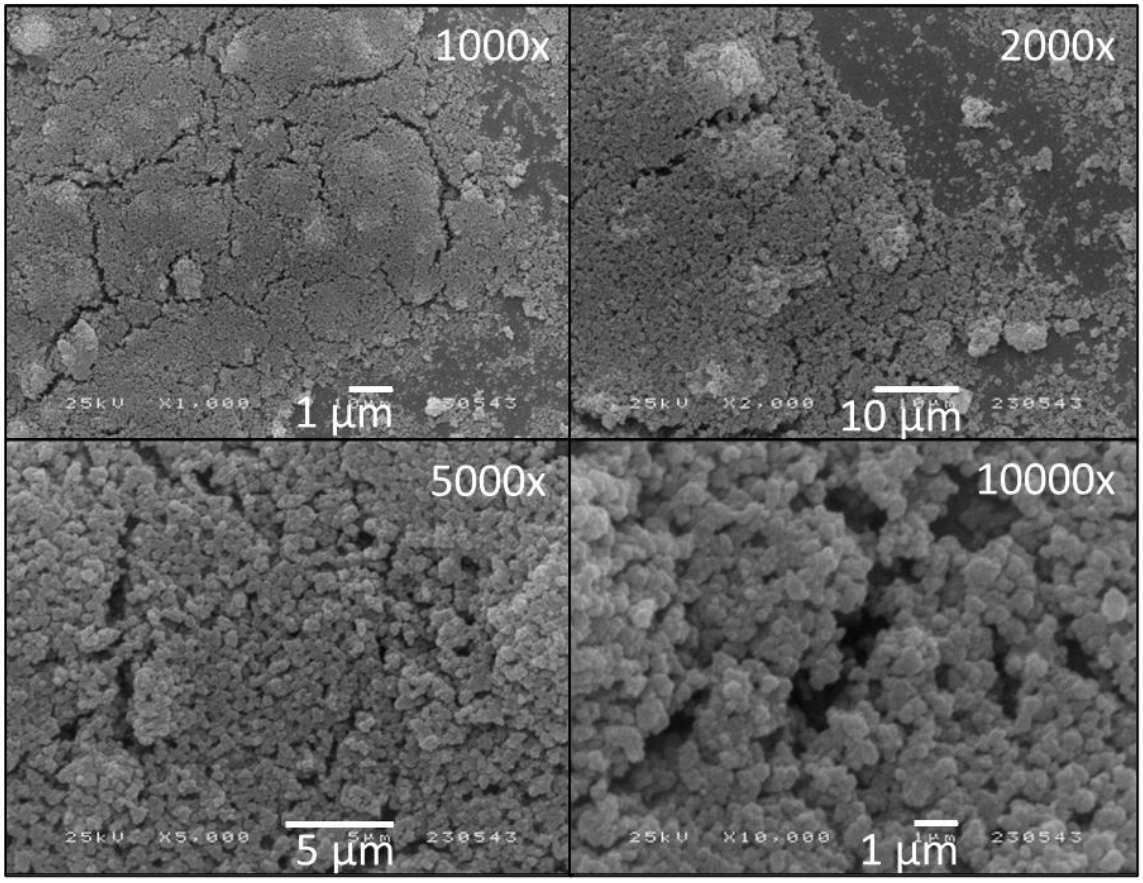

Figure 2.34 – SEM images of **UiO-66-E1**. Magnified at 1000x, 2000x, 5000x and 10000x.

The surface of the **UiO-66-NH_2-E1** film (**Figure 2.35**) was similar to its powder and they seemed to show higher uniformity in particle dispersion in comparison to the UiO-66 films.

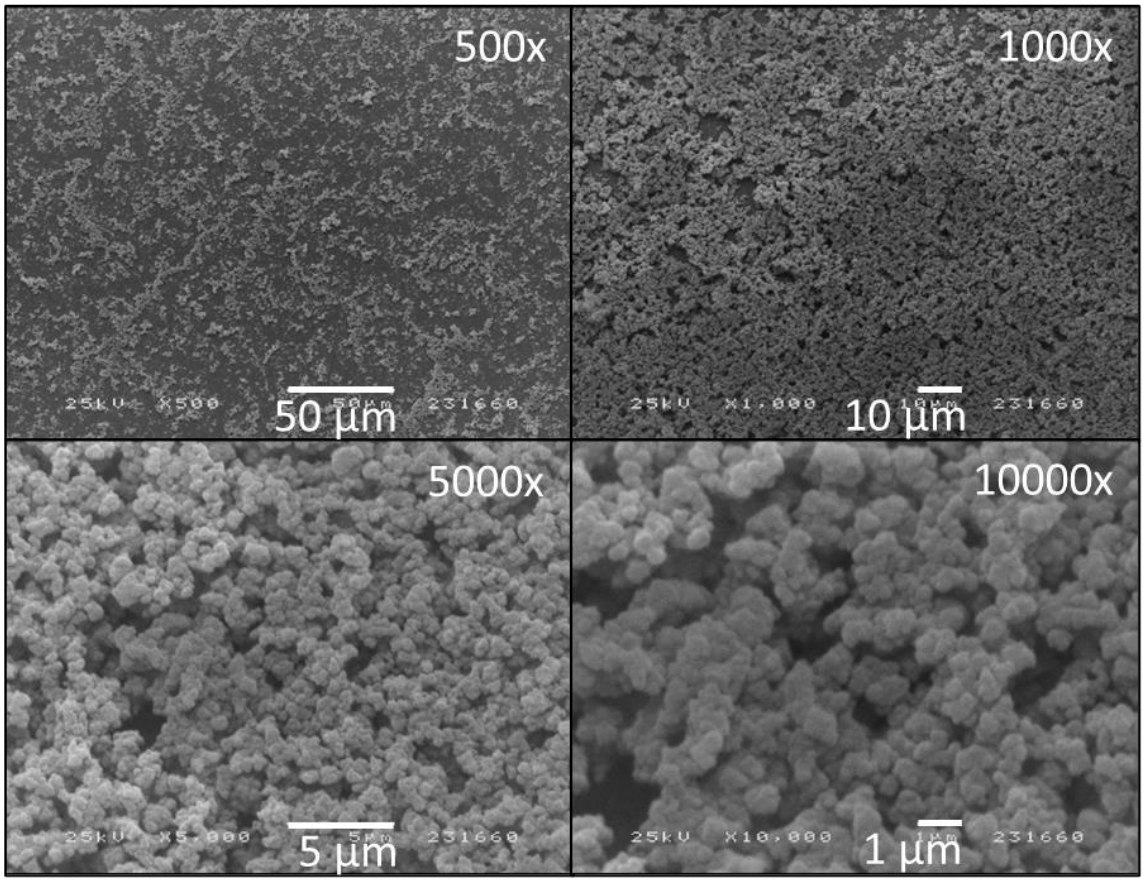

Figure 2.35 - SEM images of **UiO-66-NH_2-E1**. Magnified at 500x, 1000x, 5000x and 10000x.

2.2.3 Conclusions

No MOF films were obtained using cathodic deposition, however, using electrophoretic deposition three of the six different MOFs were able to be deposited: Ni-MOF-74, UiO-66 and UiO-66-NH_2 as can be seen in **Figure 2.36**.

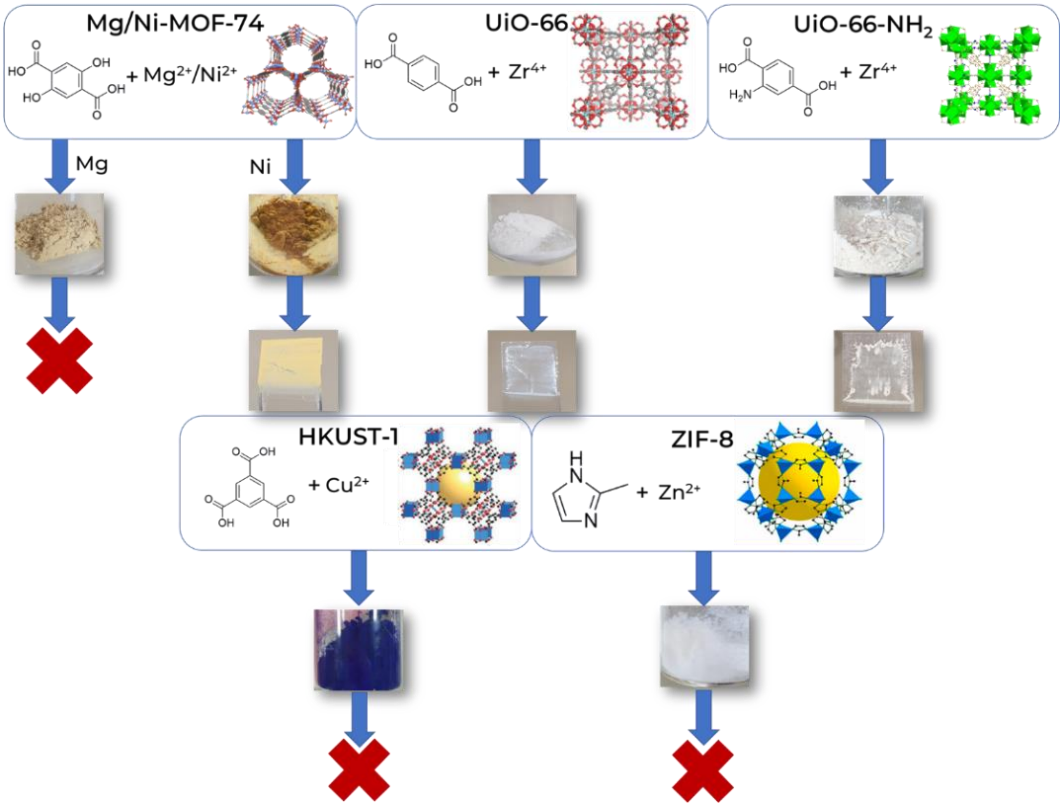

Figure 2.36 – Results of the six MOFs attempted to deposit using electrophoretic deposition.

However, further optimisations are still required both in the solvothermal synthesis and the suspension formation. In the solvothermal synthesis there still needs to be further experiments to create higher charged MOF powder particles, such as with the formation of defects in the MOF as well as post synthetic modification to incorporate alternative species in the skeleton of the structure. In the suspension solvent optimisations would need to be found, for example with ionic liquids. Using a sophisticated setup and experimenting with different electrodes would benefit the process as well.

2.3 Ammonia Conversion

2.3.1 Electrochemical Studies – Cyclic Voltammetry

After the successful immobilisation of the three MOF powders, Ni-MOF-74, UiO-66 and UiO-66-NH_2 via electrophoretic deposition the films were studied using cyclic voltammetry. The MOF films were used as the working electrode (WE), while the Pt wire and Ag/AgCl, 3M NaCl were used as the counter electrode (CE) and reference electrode (RE), respectively.

The behaviour of the films was studied in two different environments – one based on an ammonia electrolyte, and another based on a phosphate electrolyte. The reason for using these two different environments is because it was planned the CPE of ammonia in aqueous environment due to the operation conditions when compared with liquid ammonia. However, due to the similar mechanisms that were presented and discussed in **Chapter 1.4**, if the *E* used is higher than expected, there is the possibility of not only converting the ammonia into hydrogen via its oxidation but also via the water splitting process. Expecting this, the behaviour of the films was studied in the presence of ammonia (the

ammonium electrolyte NH_4Cl and aqueous ammonia NH_4OH added) and in the absence of ammonia (using a phosphate-buffered saline (PBS) buffer solution at the same pH of the ammonia-based electrolyte used). Therefore, it is possible to compare both systems to differentiate the electrocatalytic activity between both processes. Further details about the setup are available in **Chapter 3.4**.

2.3.1.1 Ni-MOF-74

Starting with the Ni-MOF-74 film at FTO (**Ni-MOF-74-E4**) in the ammonia electrolyte and varying concentrations of NH_4OH added to control the pH (**Figure 2.37**), an increase in anodic current with the increase in concentration of NH_4OH added is observed. This anodic current increase starts approximately at 0.7 V (E_{onset}). The anodic current achieves a maximum with a value of approximately 7.5 mA with the highest concentration of ammonia added (50 mM).

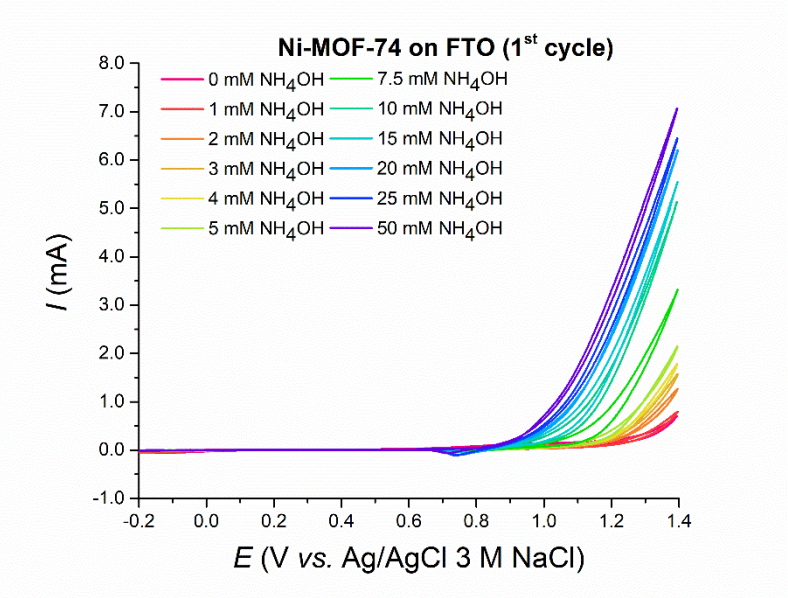

Figure 2.37 – CVs of **Ni-MOF-74-E4** at FTO (area of the electrode: 1 cm^2) in 0.5 M NH_4Cl in water with the addition of 0-50 mM NH_4OH. Pt wire and Ag/AgCl, 3M NaCl were used as CE and RE, respectively. Scan rate: 0.01 Vs^{-1}.

The oxidation process shows a decrease in anodic current with the increase in concentration until 5 mM of NH_4OH and at 7.5 mM, an increase in current is seen (**Figure 2.38 a)**). Additionally, visually the film started decomposing and dissolving in the solution with the increasing concentration of NH_4OH and repeated cycles. That degradation is accompanied with a reduction process which starts being noticeable in the concentrations of 7.5 mM of NH_4OH and hitting a current maximum at 25 mM between 0.6-0.9 V. The maximum for each concentration shifts to lower *E* (from 0.8 V in 7.5 mM to 0.7 V in 50 mM) with the increase in concentration (**Figure 2.38 b)**. A possible justification for this is the degradation of the MOF into a different active species in the surface of the film.

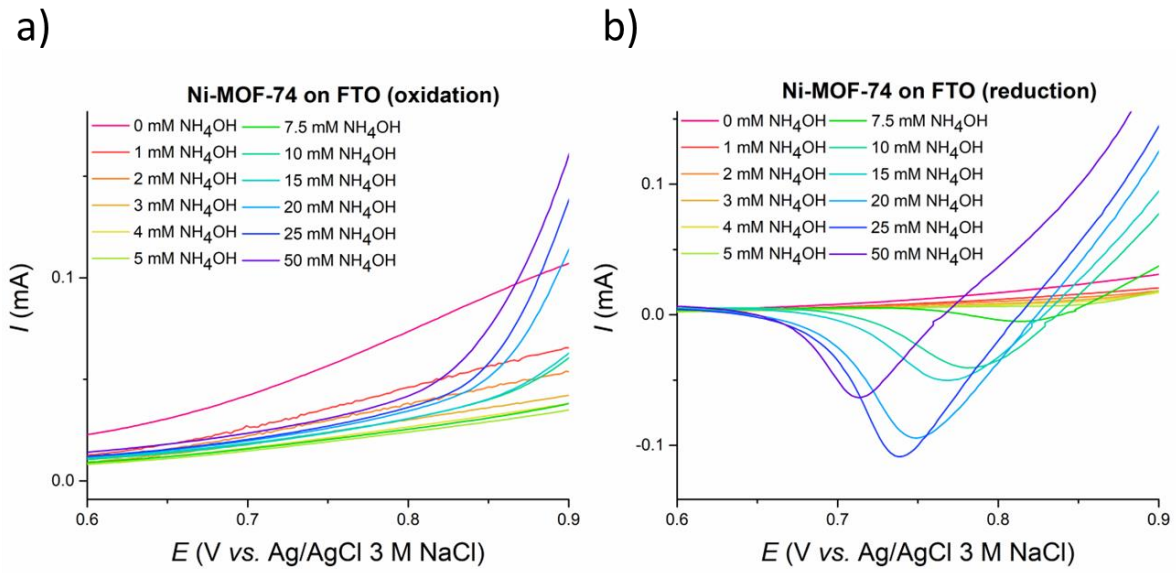

Figure 2.38 - CVs of the oxidation **a)** and reduction **b)** of **Ni-MOF-74-E4** at FTO (area of the electrode: 1 cm^2) in 0.5 M NH_4Cl in water with the addition of 0-50 mM NH_4OH with focus in the 0.6-0.9 V range. Pt wire and Ag/AgCl, 3M NaCl were used as CE and RE, respectively. Scan rate: 0.01 Vs^{-1}.

A concentration of NH_4OH (4 mM) was chosen based on the difference between the E_{onset} of the film and the bare FTO. The stability of the film was also studied at 4 mM using repeated cycles (**Figure 2.39**). An increase in anodic current is seen with each cycle, as well as the initial formation of the reduction peak mentioned above. However, visually the film was maintained.

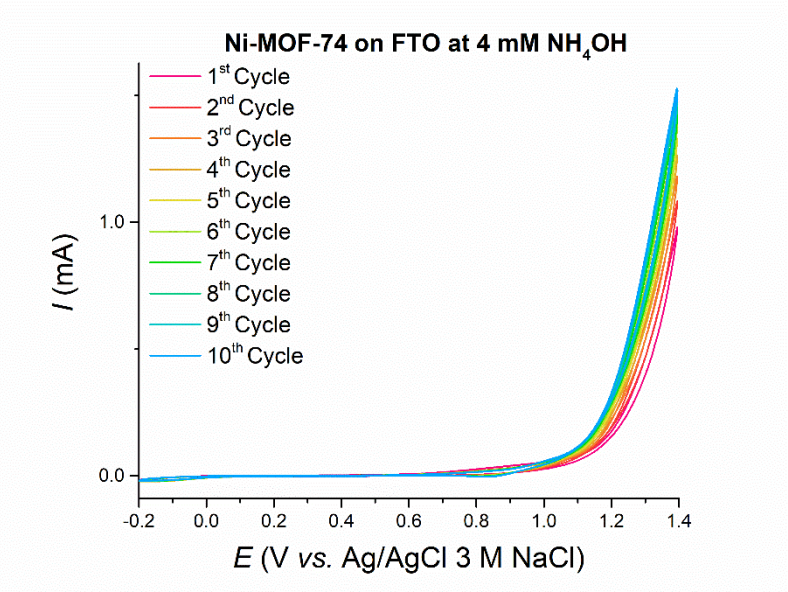

Figure 2.39 – CVs of **Ni-MOF-74-E4** at FTO (area of the electrode: 1 cm^2) in 0.5 M NH_4Cl in water with the addition of 4 mM NH_4OH (10 cycles). Pt wire and Ag/AgCl, 3M NaCl were used as CE and RE, respectively. Scan rate: 0.01 Vs^{-1}.

Additionally, the electrochemical behaviour of the film in the absence of ammonia but in the same pH using a PBS solution was also studied. These comparisons can be seen in **Figure 2.40**.

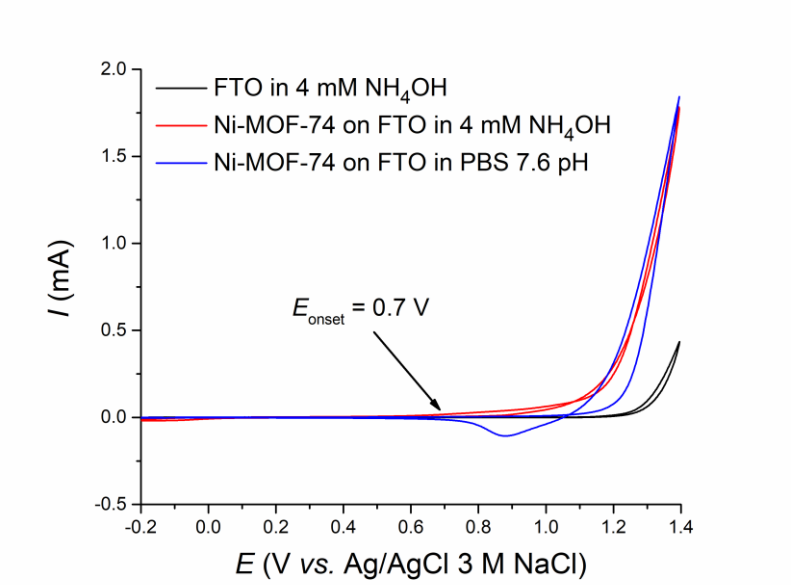

Figure 2.40 – CVs of **Ni-MOF-74-E4** at FTO (area of the electrode: 1 cm^2) and FTO in 0.5 M NH_4Cl in water with the addition of 4 mM NH_4OH and **Ni-MOF-74-E4** in PBS. Pt wire and Ag/AgCl, 3M NaCl were used as CE and RE, respectively. Scan rate: 0.01 Vs^{-1}.

At the chosen concentration (4 mM of NH_4OH) the **Ni-MOF-74-E4** film shows a higher current and an earlier E_{onset} (0.7 V) than the bare FTO. However, when the MOF film is compared in both electrolytes, the current maximum is identical (2 mA), although the E_{onset} in the ammonia-based electrolyte occurs at a lower E as expected. This indicates that the **Ni-MOF-74-E4** may be active for the oxidation of ammonia.

Additionally, the electrochemical behaviour of the **Ni-MOF-74-E5** (Ni-MOF-74 at graphite foil) was also studied as we can observe in **Figure 2.41**.

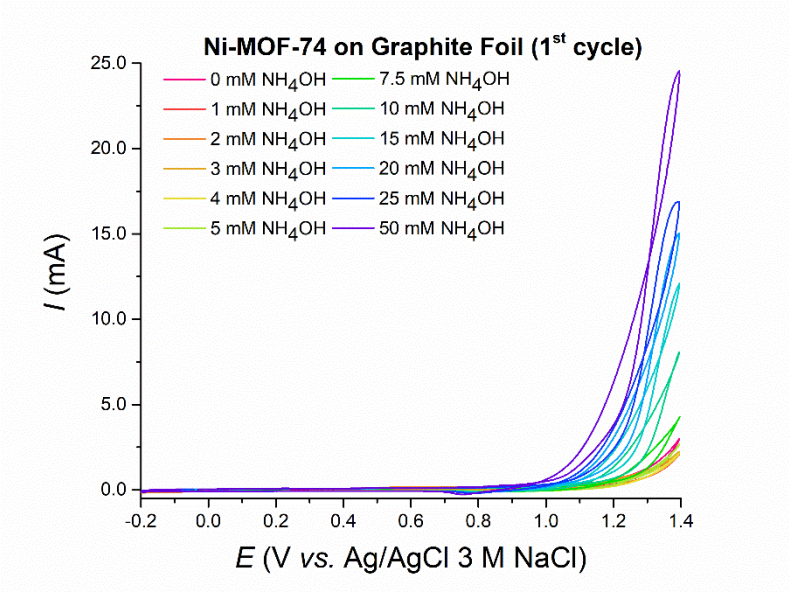

Figure 2.41 – CVs of **Ni-MOF-74-E5** at graphite foil (area of the electrode: 0.5 cm^2) in 0.5 M NH_4Cl in water with the addition of 0-50 mM NH_4OH. Pt wire and Ag/AgCl, 3M NaCl were used as CE and RE, respectively. Scan rate: 0.01 Vs^{-1}.

The maximum current is three times higher than the observed for **Ni-MOF-74-E4** due to differences in the porosity of the substrate when compared to FTO. The degradation of the MOF can be visually seen in the same concentration as the MOF degradation in the FTO (7.5 mM). The reduction peak between 0.6 V and 0.9 V is also observed when the concentration of NH_4OH rises.

The bare graphite foil was also studied in the same ammonia electrolyte. Comparison of both the **Ni-MOF-74-E5** film and the graphite foil in the previously chosen concentration of NH_4OH (4 mM) can be seen in **Figure 2.42**. The **Ni-MOF-74-E5** shows higher activity than the bare electrode. Unfortunately, the film in PBS solution was unable to be tested due to the lack of stock of graphite foil.

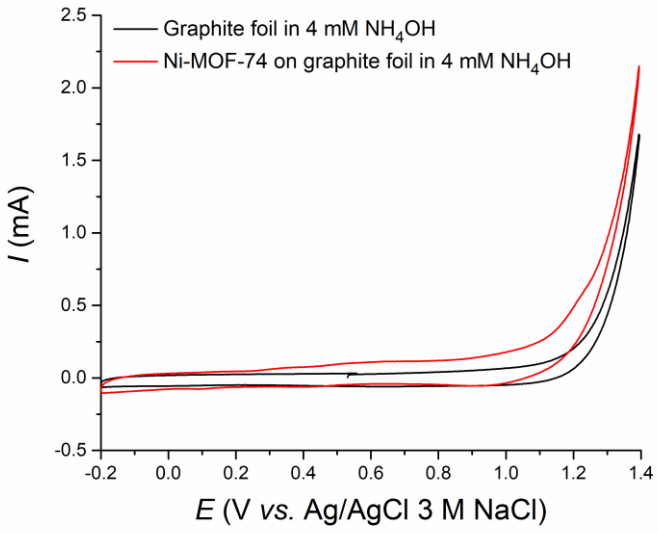

Figure 2.42 – CVs of **Ni-MOF-74-E5** at graphite foil (area of the electrode: 0.5 cm^2) and graphite foil in 0.5 M NH_4Cl in water with the addition of 4 mM NH_4OH. Pt wire and Ag/AgCl, 3M NaCl were used as CE and RE, respectively. Scan rate: 0.01 Vs^{-1}.

2.3.1.2 UiO-66

The UiO-66 film at FTO using electrophoretic deposition (**UiO-66-E1**) showed promising results. The anodic current increase with the concentration of NH_4OH is represented in **Figure 2.43 a)**. Anodic current saturation is reached approximately at 75 mM concentration of NH_4OH added with a value of 2.3 mA.

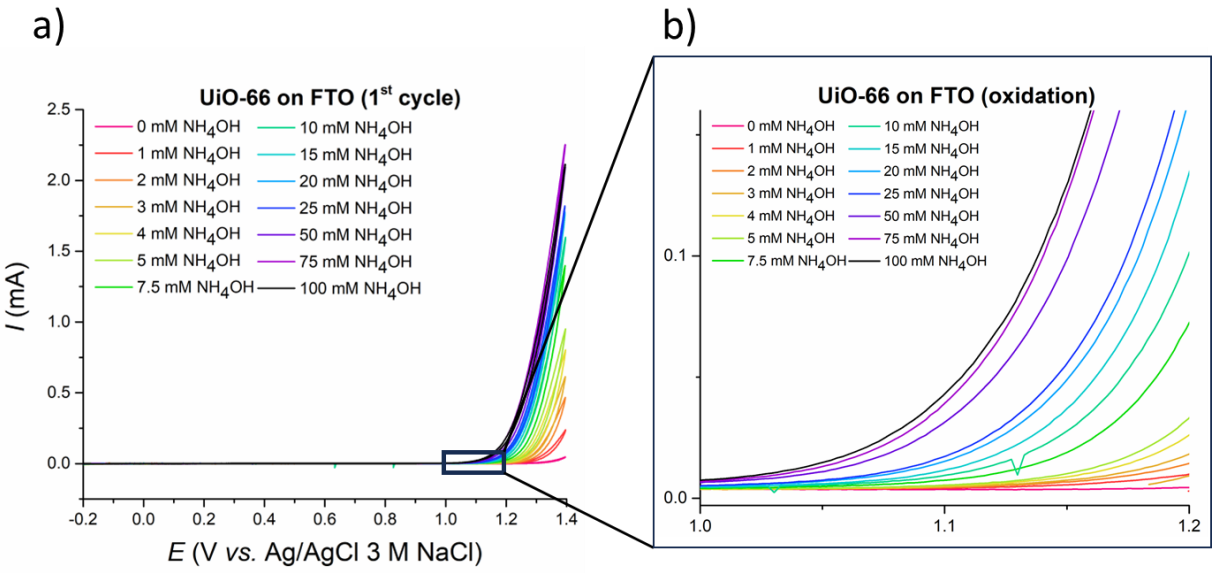

Figure 2.43 - CVs of **UiO-66-E1** at FTO (area of the electrode: 1 cm^2) in 0.5 M NH_4Cl in water with the addition of 0-100 mM NH_4OH **a)** full scale; **b)** focus in 1.1-1.2 V. Pt wire and Ag/AgCl, 3M NaCl were used as CE and RE, respectively. Scan rate: 0.01 Vs^{-1}.

No signs of possible film degradation were detected, both visually and in the CV results. The E_{onset} for the anodic current increase is approximately at 1.1 V and can potentially be assigned to the catalytic activity due to its consistent increase with the concentration of NH_4OH added (**Figure 2.43 b)**).

Similar for the Ni-MOF-74 film, a concentration of NH_4OH was chosen (4 mM) where the difference between the E_{onset} of the film is more noticeable when compared with the bare FTO. The film was also tested in the PBS electrolyte, where ammonia is not present. Comparing the three voltammograms, the E_{onset} is identical at approximately 1.1 V, as seen in **Figure 2.44.** However, the **UiO-66-E1** film shows as a higher maximum current in the presence of ammonia in comparison with both the bare FTO and the film in the absence of ammonia (PBS electrolyte).

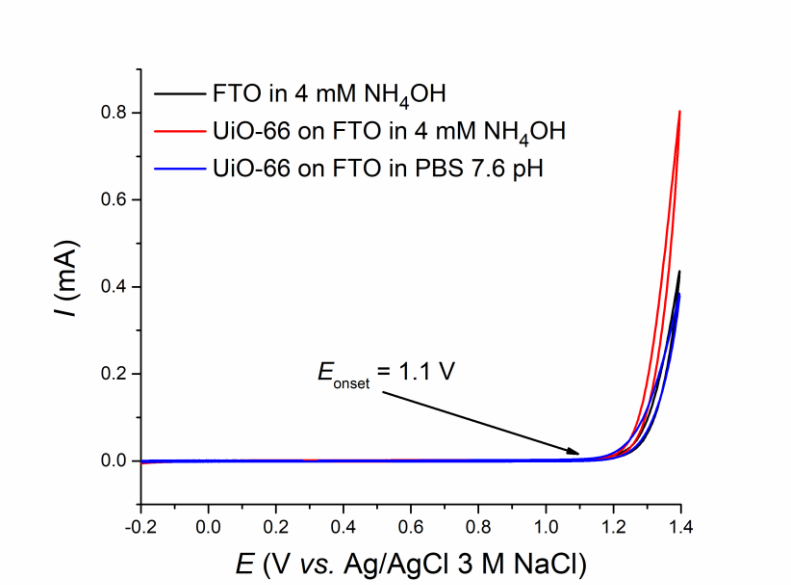

Figure 2.44 - CVs of **UiO-66-E1** at FTO (area of the electrode: 1 cm^2) and FTO in 0.5 M NH_4Cl in water with the addition of 4 mM NH_4OH and **UiO-66-E1** in PBS solution. Pt wire and Ag/AgCl, 3M NaCl were used as CE and RE, respectively. Scan rate: 0.01 Vs^{-1}.

The stability of the **UiO-66-E1** film was also tested using CV through repeated cycles (**Figure 2.45**). There is no notable loss in activity during the 10 cycles tested. There is, however, an increase in the maximum current with each cycle.

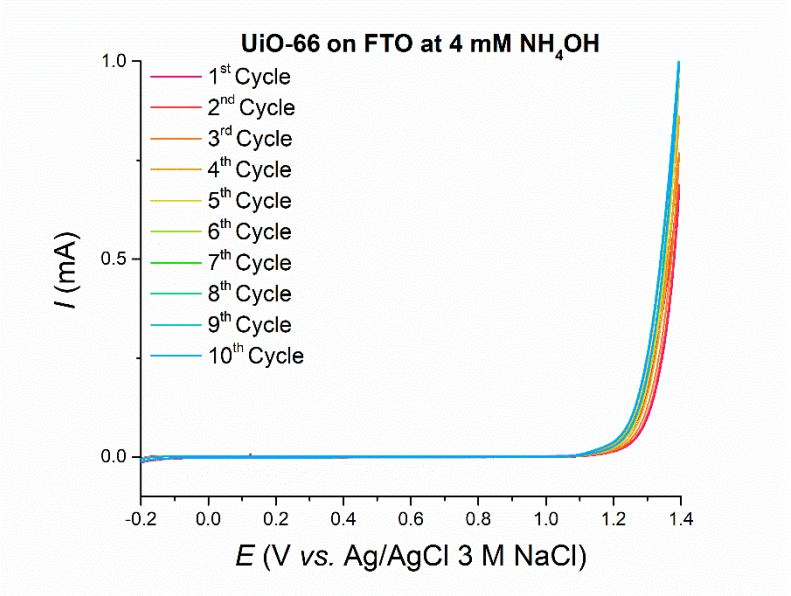

Figure 2.45 – CVs of **UiO-66-E1** at FTO (area of the electrode: 1 cm^2) in 0.5 M NH_4Cl in water with the addition of 4 mM NH_4OH (10 cycles). Pt wire and Ag/AgCl, 3M NaCl were used as CE and RE, respectively. Scan rate: 0.01 Vs^{-1}.

UiO-66-E2 (UiO-66 on graphite foil) was also electrochemically tested (**Figure 2.46**). However, the activity of the combined substrate with the MOF is highly irregular as the current is barely affected by

the difference in concentration of NH_4OH shifting without a pattern. This led to the conclusion that **UiO-66-E2** is not a suitable electrocatalyst for the conversion of ammonia.

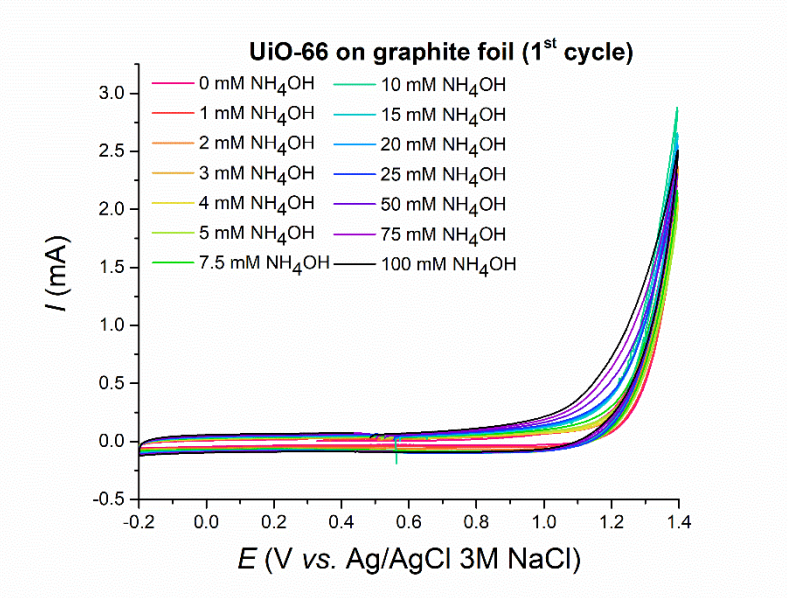

Figure 2.46 - CVs of **UiO-66-E2** at graphite foil (area of the electrode: 0.5 cm^2) in 0.5 M NH_4Cl in water with the addition of 0-100 mM NH_4OH. Pt wire and Ag/AgCl, 3M NaCl were used as CE and RE, respectively. Scan rate: 0.01 Vs^{-1}.

2.3.1.3 UiO-66-NH_2

The third and last film studied was the functionalised version of UiO-66, named **UiO-66-NH_2-E1**. As one can see in **Figure 2.47**, there is an increase of the maximum anodic current with the concentration of the NH_4OH added, which reaches saturation at 50 mM with an anodic current value of 2.15 mA.

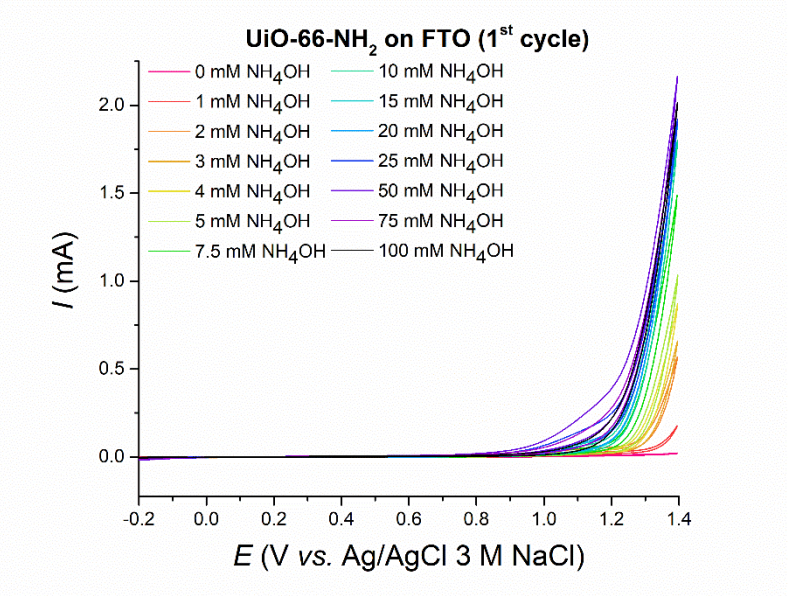

Figure 2.47 - CVs of **UiO-66-NH_2-E1** at FTO (area of the electrode: 1 cm^2) in 0.5 M NH_4Cl in water with the addition of 0-100 mM NH_4OH. Pt wire and Ag/AgCl, 3M NaCl were used as CE and RE, respectively. Scan rate: 0.01 Vs^{-1}.

Similar with the Ni-MOF-74 and UiO-66 films at FTO, the concentration of NH_4OH chosen was at 4 mM. As it is possible to see in **Figure 2.48**, the **UiO-66-NH_2-E1** offers higher maximum current in the presence of ammonia than in the absence of ammonia (PBS electrolyte), as well as for the FTO. The **UiO-66-NH_2-E1** shows less current in the absence of ammonia than the FTO in the presence of ammonia. This means that in the absence of ammonia the function amine present in the UiO-66-NH_2 seems to reduce the activity of the film since in comparison with the analogous without amine function, **UiO-66-E1** (**Figure 2.44**).

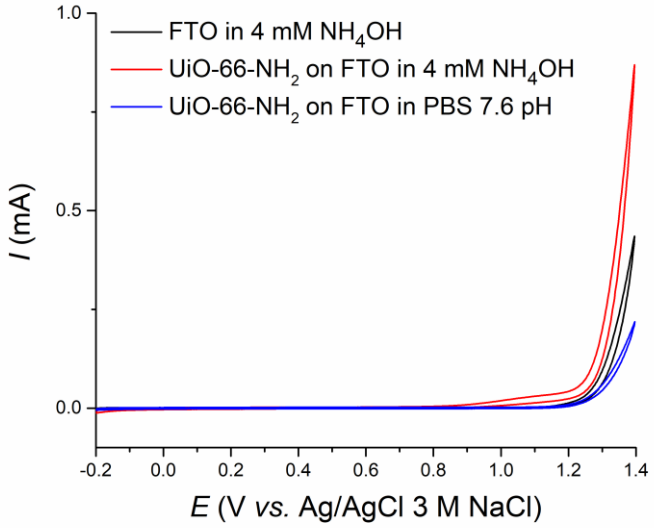

Figure 2.48 - CVs of **UiO-66-NH_2-E1** at FTO (area of the electrode: 1 cm^2) and FTO in 0.5 M NH_4Cl in water with the addition of 4 mM NH_4OH and **UiO-66-NH_2-E1** in PBS solution. Pt wire and Ag/AgCl, 3M NaCl were used as CE and RE, respectively. Scan rate: 0.01 Vs^{-1}.

For the stability studies, the same method was applied as the other films, using repeated cycles in the CV experiments. There is only a slight reduction in the current with each cycle, no major loss of activity as seen in **Figure 2.49**.

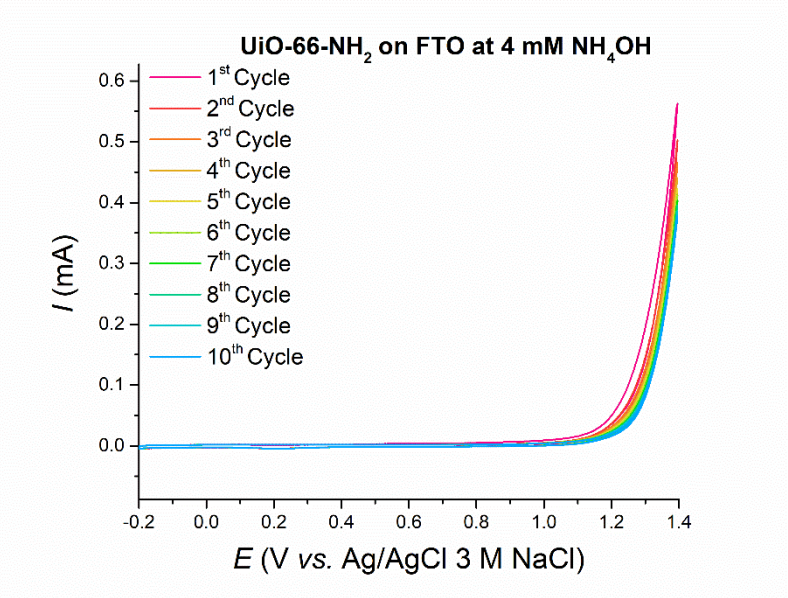

Figure 2.49 – CVs of **UiO-66-NH$_2$-E1** at FTO (area of the electrode: 1 cm^2) in 0.5 M NH_4Cl in water with the addition of 4 mM NH_4OH (10 cycles). Pt wire and Ag/AgCl, 3M NaCl were used as CE and RE, respectively. Scan rate: 0.01 Vs^{-1}.

2.3.2 Controlled Potential Electrolysis and Gases Quantification

After the electrochemical studies the controlled potential electrolyses (CPE) were performed for the proper detection and quantification of the hydrogen produced. Due to the lack of stock of graphite foil and the more irregular results obtained during the electrochemical studies, especially for UiO-66, the CPE were performed using as electrocatalysts the three MOF films deposited on FTO using electrophoretic deposition: **Ni-MOF-74-E4**, **UiO-66-E1** and **UiO-66-NH$_2$-E1**.

Multiple CPE (both repetitions or different conditions) were done for each MOF and the films after CPE were characterised by PXRD to study their integrity. The gases produced (H_2, O_2, N_2) were quantified by GC-TCD. For further details see experimental part.

2.3.2.1 Ni-MOF-74

The E_{onset} for the **Ni-MOF-74-E4** in the presence of ammonia was approximately 0.7 V, as mentioned in **Chapter 2.3.1.1**. With this in mind, CPEs at 0.9, 1.0, 1.1 and 1.3 V were used to determine the best E for H_2 production while minimising the film degradation. Multiple experiments were performed, and an example of the chromatograms obtained, and the gases detected and quantified are present in **Figure 2.50** and **Table 2.5**, respectively. The remaining chromatograms are present in **Figures A.55** to **A.60** in the Annexes.

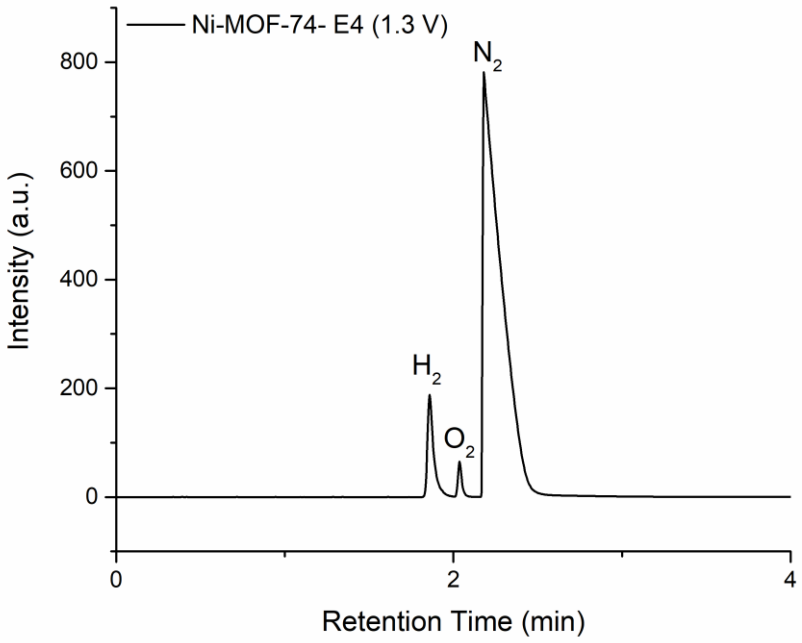

Figure 2.50 – Chromatogram obtained for the **Ni-MOF-74-E4** (**Entry 7**) using an applied *E* of 1.3 V.

Table 2.5 – Quantification of the obtained H_2, O_2 and N_2 after CPE using the **Ni-MOF-74-E4**. Values obtained via GC-TCD using the respective gases calibration curves. For the CPE experiments: Pt coil and Ag/AgCl, 3M NaCl were used as CE and RE in the CPE experiments. Area of the electrode: 1 cm^2

			Quantity (µmol)		
Solution Contents	E (V)	Entry	H_2	O_2	N_2
0.5 M NH_4Cl + 4 mM NH_4OH in 10 mL of water	0.9	**1**	**0.00**	34.33	1957.93
		2	**0.00**	46.95	2445.60
	1	**3**	**0.00**	65.14	1999.08
	1.1	**4**	**17.09**	107.36	2601.00
		5	**2.41**	229.89	1707.10
		6	**0.37**	84.43	2576.55
	1.3	**7**	**28.11**	184.54	2675.43

In the two attempts using 0.9 V (**Entries 1** and **2**), there was no production of H_2 and no visible film degradation. This means that neither the conversion of ammonia nor the water splitting occurred. When 1.0 V (**Entry 3**, **Table 2.5**) was used similar results were observed. When the *E* was increased to 1.1 V, 17.09 µmol of H_2 was produced (**Entry 4**). The amount of O_2 is higher than for the experiments at 0.9 V (**Entries 1** and **2**) which may be either due the manual injection in the GC-TCD, air entering in the cell during the CPE or due to the water splitting process. The film was completely decomposed after 45 min of CPE, visually observed in **Figure A.61** in the Annexes. Unfortunately, these results were unable to be replicated likely due to the decomposition of the MOF film. These two additional repetitions at 1.1 V yielded 2.41 µmol (**Entry 5**) and 0.37 µmol (**Entry 6**) of H_2 and although degradation was visually noticeable, part of the film remained, unlike the first attempt. Lastly, when the *E* was increased to 1.3

V, 28.11 µmol of H_2 were produced (**Entry 7**) and the film was completely decomposed as well in the first 45 min. The bare FTO in the presence of ammonia per comparison produced an average of 1.37 µmol (**Table A.7** in the Annexes), which is a clear indication of the activity of the MOF. A conclusion was reached that the lower the H_2, the lower the degradation detected. No further repetition attempts were performed nor the realisation of the CPE in the PBS electrolyte using the **Ni-MOF-E4** FTO film due to the decomposition of the film and the lack of time.

The three films used in the **Entries 4**, **5** and **6** at 1.1 V were characterised by PXRD after the CPE as seen in **Figure 2.51**.

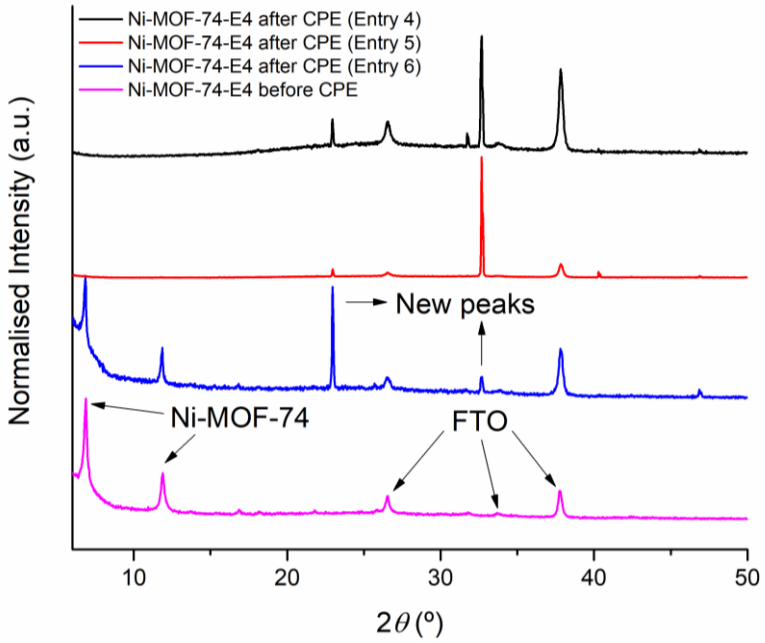

Figure 2.51 – PXRD of the used **Ni-MOF-74-E4** (**Entry 4**, **5** and **6**) in the presence of ammonia, both before and after.

The obtained PXRD are represented in descending order of film degradation. The appearance of two new diffraction patterns at the 2θ angles of 23º and 32.7º was observed. These two new peaks are from the recrystallisation of the NH_4Cl on the surface of the film.

As the results obtained were not promising there were no further CPE attempts in the absence of ammonia in the PBS electrolyte.

2.3.2.2 UiO-66

The E_{onset} for the **UiO-66-E1** in the presence of ammonia was approximately 1.1 V, as mentioned in **Chapter 2.3.1.2**. With this in mind, CPEs at 1.3 V were performed. Three repetitions under the same conditions for the film in the presence of ammonia were performed, and two repetitions in the PBS electrolyte. The obtained chromatograms are present in the **Figures A.62** to **A.66** in the Annexes and the results of the multiple attempts in both solutions in the **Table 2.6**.

Table 2.6 - Quantification of the obtained H_2, O_2 and N_2 after CPE using the **UiO-66-E1**. Values obtained via GC-TCD using the respective gases calibration curves. For the CPE experiments: Pt coil and Ag/AgCl, 3M NaCl were used as CE and RE in the CPE experiments. Area of the electrode: 1 cm^2

			Quantity (µmol)			
Solution Contents	E (V)	Entry	Average	H_2	O_2	N_2
0.5 M NH_4Cl + 4 mM NH_4OH in 10 mL of water	1.3	**1**	**7.37**	**8.63**	56.38	1994.76
		2		**9.27**	68.91	1965.25
		3		**4.21**	37.11	1877.40
10 mL of PBS solution		**4**	**0.49**	**0.33**	45.97	1763.35
		5		**0.64**	51.19	2603.52

In comparison with the **Ni-MOF-74-E4**, the results obtained for **UiO-66-E1** were more reproducible. In the presence of ammonia, the three repetitions yielded 8.63 µmol (**Entry 1**), 9.27 µmol (**Entry 2**) and 4.21 µmol (**Entry 3**) of H_2 with similar H_2:O_2 ratios. As seen in **Table A.7** in the Annexes, the production of the UiO-66 film in comparison with the bare FTO is about 7 times higher. Visually there seemed to be no film degradation, and the obtained PXRD in the presence of ammonia indicated no major reduction in the MOF crystallinity (**Figure 2.52**).

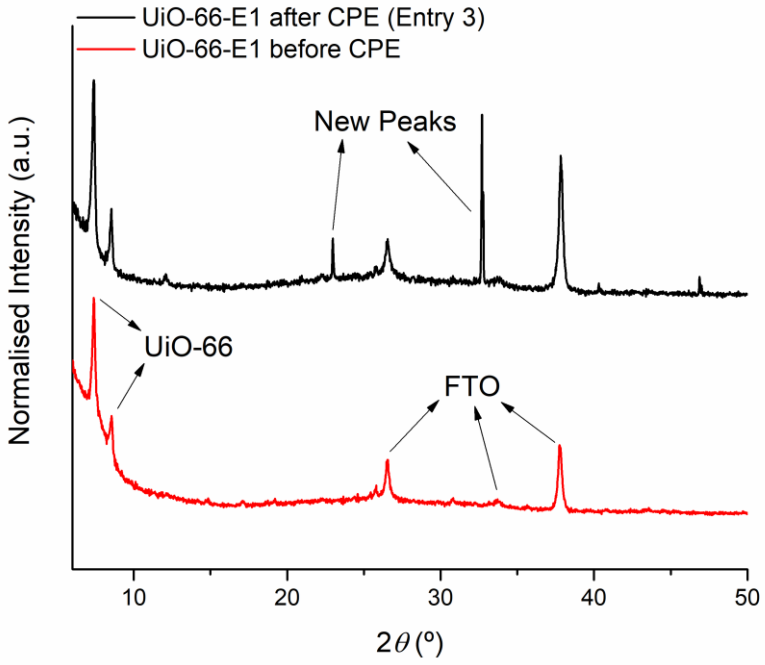

Figure 2.52 - PXRD of the used **UiO-66-E1** (**Entry 3**) in the presence of ammonia, both before and after.

Comparing the H_2 obtained in the presence of ammonia and in its absence, it is possible to observe a clear difference. The two attempts in the PBS electrolyte produced less H_2 when compared (0.33 µmol for **Entry 4** and 0.64 µmol for **Entry 5**). On average the **UiO-66-E1** films produce 15 times more H_2 in the presence of ammonia than in its absence.

2.3.2.3 UiO-66-NH_2

The last film tested was the **UiO-66-NH_2-E1** using the same *E* that was used for **UiO-66-E1** for comparison (1.3 V). The obtained chromatograms and quantification of the gases produced are present in the **Figures A.67** to **A.69** in the Annexes and **Table 2.7**, respectively.

Table 2.7 - Quantification of the obtained H_2, O_2 and N_2 after CPE using the **UiO-66-NH_2-E1**. Values obtained via GC-TCD using the respective gases calibration curves. For the CPE experiments: Pt coil and Ag/AgCl, 3M NaCl were used as CE and RE in the CPE experiments. Area of the electrode: 1 cm^2

			Quantity (µmol)			
Solution Contents	E(V)	Entry	Average	H_2	O_2	N_2
0.5 M NH_4Cl + 4 mM NH_4OH in 10 mL of water	1.3	**1**	**1.03**	**1.59**	44.32	2531.11
		2		**1.01**	57.44	2663.81
		3		**0.50**	89.71	2723.03

The results obtained were reproducible, although there was lower H_2 production in comparison to what was seen for **UiO-66-E1**. On average 1.03 µmol of H_2 were produced, which is similar to what is obtained for the bare FTO (**Table A.7** in the Annexes). Unfortunately, no further tests were performed to confirm these results due to the lack of time.

The **UiO-66-NH_2-E1** film used for the CPE was characterised by PXRD (**Figure 2.53**). The obtained PXRD in comparison with the film before the CPE, indicated no loss in crystallinity, similar to what was visible for the **UiO-66-E1** film. This further confirms that something is different when compared to the previous results obtained for the other MOF films.

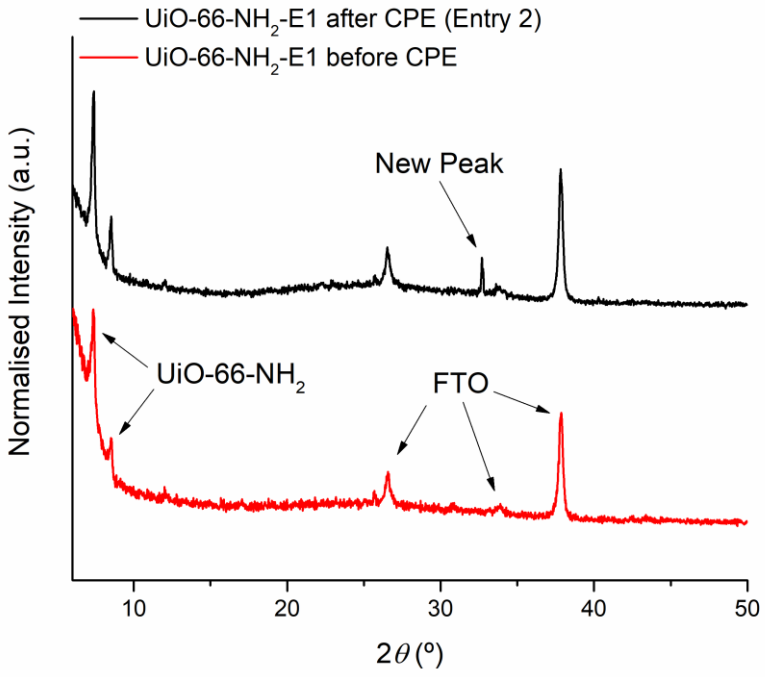

Figure 2.53 - PXRD of the used **UiO-66-NH_2-E1** (**Entry 2**) in the presence of ammonia, both before and after.

No further tests or quantifications were performed for the UiO-66-NH_2 films due time constraints.

2.3.3 Conclusions

In this chapter, the electrochemical behaviour of five different films (**Ni-MOF-74-E4**, **UiO-66-E1**, **UiO-66-NH_2** films at FTO electrode and **Ni-MOF-74-E5**, **UiO-66-E2** films at graphite foil electrode) was studied. The **Ni-MOF-74-E4**, **UiO-66-E1** and the **UiO-66-NH_2-E1** films showed promising results indicated by the higher activity in the presence of ammonia in comparison with both the bare electrode and the film in the absence of ammonia (PBS electrolyte). However, films at the graphite foil electrode, **Ni-MOF-74-E5** and **UiO-66-E2**, were less promising, especially the **UiO-66-E2** film were there was no noticeable difference in the activity with different concentrations of NH_4OH.

The CPEs were performed using the three FTO films - **Ni-MOF-74-E4**, **UiO-66-E1** and **UiO-66-NH_2**. The **Ni-MOF-74-E4** showed the highest H_2 production and the highest film degradation. The **UiO-66-E1** showed the most promising results having obtained a higher production of H_2 than the film in the absence of ammonia and the bare electrode, with minimal film degradation. The **UiO-66-NH_2** however, produced the lowest H_2 and needs further testing to confirm the results. These results highlight the catalytic activity of the Ni-MOF-74 and UiO-66 on the surface of the FTO in the presence of ammonia. A common factor witnessed was the appearance of two new diffraction pattern in the 2θ values of 23.7º and 32º, which is from the recrystallisation of the NH_4Cl electrolyte. The current during the CPE could not be measured due to the low voltage compliance of the main potentiostat, leading to the use of an analogic potentiostat where an analog-to-digital converter was only later built with the help of Dr. José Augusto from the FCUL department of physics. Further experiments with this setup will be performed to be able to ultimately calculate the faradaic efficiency of the process.

2.4 Conclusions and Future Work

During this thesis, MOF films were obtained to study their applicability in the electrolytic conversion of ammonia into H_2 as a carbon-free fuel.

9 different reported MOFs were attempted to synthesise using solvothermal methods (MOF-5, IMORF-3, ZIF-8, ZnMn-ZIF-8, Mg-MOF-74, Ni-MOF-74, HKUST-1, UiO-66 and UiO-66-NH_2). Of those MOFs only 6 were successfully synthesised (ZIF-8, Mg-MOF-74, Ni-MOF-74, HKUST-1, UiO-66 and UiO-66-NH_2). All the powders obtained were characterised by PXRD and FTIR, additionally the successful ones were as well characterised by SEM and stability tests were performed in aqueous medium. Only HKUST-1 indicated low stability in the presence of water originating a new species confirmed by PXRD characterisation. MOF-5 and IRMOF-3 proved unsuccessful probably due to the conditions used during the self-assembly step, while in the case of the ZnMn-ZIF-8 there was no metal-exchange between the added Mn and the Zn in the structure.

Afterwards, using the cathodic deposition method the unsuccessful MOFs and the ones that proved stable in aqueous medium were attempted to directly be formed at the surface of the electrode, aside from ZIF-8 due to the precursors reacting very fast at ambient conditions. Unfortunately, all the attempts using this direct method failed as the only results obtained were amorphous films, crystalline films that did not correspond to the MOF structure or nothing formed. Additionally, using the electrophoretic deposition as the indirect method, the 6 MOFs successfully synthesised were attempted to be deposit at

electrodes. Only three MOFs were able to be deposited, one that showed a uniform film (Ni-MOF-74) and two with low uniformity (UiO-66 and UiO-66-NH_2). The optimal conditions used for the Ni-MOF-74 deposition are: 60 V cm^{-1}, in 20 mL ethanol and 10 µL acetic acid for 2 h 30 min. For the UiO-66 and UiO-66-NH_2 films the optimal conditions are: 90 V cm^{-1}, in 20 mL ethanol and 10 µL acetic acid for 5 min. The Ni-MOF-74 and UiO-66 were also deposited on graphite foil electrodes aside from the FTO electrodes. Unfortunately, the remaining three MOFs were unsuccessful. The ZIF-8 and Mg-MOF-74 formed suspensions with low stability and the HKUST-1 was decomposed due to the presence of water.

The obtained films were electrochemically studied in the presence of ammonia using an ammonia-based electrolyte (NH_4Cl) with varying concentrations of NH_4OH and absence of ammonia using a phosphate-based electrolyte (PBS). The FTO films for the three MOFs showed promising results indicated by the higher current in the presence of ammonia in relation with the films in the absence of ammonia and the bare FTO. However, the films at the graphite foil electrodes were less promising due to the irregular variation in the current with different concentrations of NH_4OH. Finally, the FTO films were applied in CPE experiments for the conversion of ammonia. The UiO-66 films at FTO showed the most promising results, with replicability, producing higher amounts of H_2 in comparison with the film in the absence of ammonia and the bare FTO, with minimal degradation. Although, there was more production of H_2 using the Ni-MOF-74 films, these films had extremely low stability during long periods of time under an applied *E*, having completely decomposed in merely 45 min of the CPE process. Due to time constraints the UiO-66-NH_2 were not thoroughly explored.

There is untapped potential in the research of MOF films for the conversion of ammonia. Of course, the results obtained are not final, as there is a lot of further optimisations that can be made. Starting at the beginning, optimisations in the solvothermal syntheses can be made, for example, using modulators to control the particle growth or post-synthetic modification which modifies the structure to either create defects on the structure of the MOF or incorporate alternative species which will increase the reactivity and conductivity of the MOF. Next, optimisations in the electrophoretic deposition should also be done. Some examples are finding a more suitable substrate, addition of alternate species to try and obtain a more uniform suspension with improved properties, such as an accessible conductivity and zeta potential using, for example, acids or maybe, ionic liquids. The setup used is also not sophisticated, which means there is also room for improvement in this area. In the electrochemical part, improvements can also be made in the solution containing ammonia, for example, performing studies in organic medium or even using liquid ammonia. Finding an appropriate substrate is also important in the CPEs as it increases the film stability and reactivity under applied *E* and high pH conditions for long periods of time.

3 Experimental Part

3.1 Reagents and Solvents

All the chemicals used were purchased from TCl, Fluorochem, Sigma-Aldrich, Honeywell and Acros Organic without further modification unless stated otherwise.

3.2 Characterisation Techniques

Powder X-Ray Diffraction (PXRD) – Powder X-ray diffractograms were obtained using Philips Analytical PW 3050/60 X'Pert PRO automatic diffractometer, equipped with an X'Celerator detector. Data was acquired using X'Pert Data Collector version 2.0b software. CuKα was used as the radiation source, operating with a current of 30 mA and a voltage of 40 kV. The PXRD were acquired by Prof. Dr. Maria E. Melo Jorge using a continuous scan of the Bragg angles (2θ) between 5º and 50º, with a step of 0.017 and an acquisition time of 200 s per step.

Diffuse Reflectance Infrared Fourier Transform Spectroscopy (DRIFT) – DRIFT spectra were obtained using a Nicolet Nexus 6700 FTIR spectrophotometer in the range of 4000-650 cm^{-1}, a resolution of 4 cm^{-1} and 256 scans. The powders were prepared by grinding the powder with KBr. The films were added on the spectrophotometer directly in the same configurations.

Attenuated Total Reflectance (ATR) – ATR spectra were obtained using a Shimadzu IRSpirit QATR-S spectrophotometer in the range of 4000-500 cm^{-1}, a resolution of 4 cm^{-1} and 32 scans. Both the powders and the films were applied directly on the surface of the diamond crystal using both the same configurations.

Scanning Electron Microscopy (SEM) – SEM analysis was performed by Dr. Telmo Nunes from the FCUL Microscopy Facility and Dr. Isabel Nogueira from the IST Electron Microscopy Laboratory. In FCUL the samples were prepared by coating the surface of both the films and powders with gold. The samples were added to a JEOL JFC-1200 chamber and analysed using a JEOL JSM-5200LV scanning electron microscope. In IST a ThermoScientific, Phenom ProX G6 with a CsB6 filament and an EDS detector scanning electron microscope was used.

3.3 MOFs Solvothermal Synthesis and Characterisation

All MOFs were synthesised via solvothermal synthesis using already reported methods. In some cases, minor modifications to the procedures were performed.

ZIF-8 - $Zn(Hmim)_2$

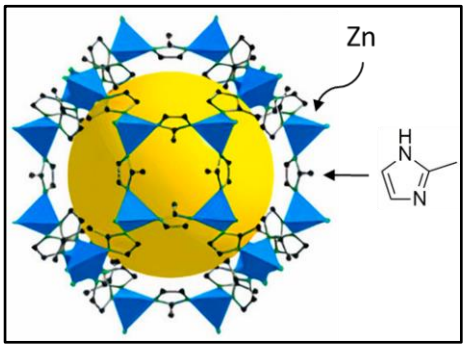

Figure 3.1 – ZIF-8 3D structure using Zn^{2+} as the metal centre and Hmim as the organic ligand. Adapted from[155].

Following a reported procedure from Pan *et. al.*[95] with few modifications, ZIF-8 was synthesised yielding a white powder (**369 mg**). Those modifications were: washing only using methanol and the activation was done at 50 °C under vacuum. **FTIR** (cm^{-1}): 3500-3200 (w/br, νO-H), 3133 (m, νC-$H_{(aliphatic)}$), 2929 (m, νC-$H_{(aromatic)}$), 1670 (m, δN-H), 1636 (w, νC=C), 1584 (m, νC=N), 1460-1305 (s, νC-C), 1146 (s, νC-N), 995,760 (m, δC-N), 694 (s, δC=C). **PXRD** (º): 7.3 (110), 10.4 (200), 12.7 (211).

Mg-MOF-74 - $Mg_2(DHTA)$

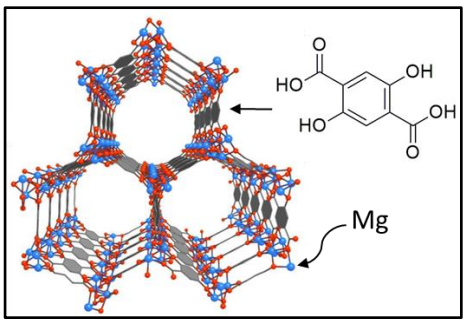

Figure 3.2 – Mg-MOF-74 3D structure using Mg^{2+} as the metal centre and DHTA as the organic ligand. Adapted from[162].

Following the published procedure from Grant *et. al.*[161] with few modifications, Mg-MOF-74 was synthesised yielding a light brown powder (**162 mg**). Those modifications were: the activation was done at 120 °C and the powders were not separated into different vials. **FTIR** (cm^{-1}): 3500-3200 (w/br, νO-H), 2930, 2858 (w, νC-H), 1581 (s, ν_sO-C-O), 1420 (s, ν_aO-C-O), 1457-1369 (s, νC-C), 1208 (s, νC-O), 889, 821 (m, δC-H). **PXRD** (º): 6.8 (110), 11.8 (300).

Ni-MOF-74 - $Ni_2(DHTA)$

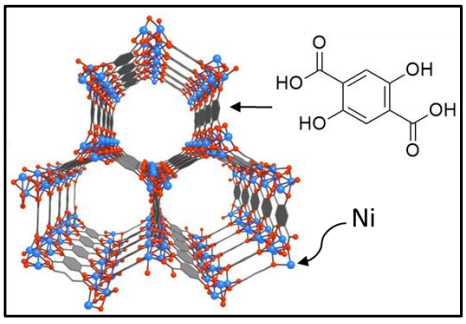

Figure 3.3 – Ni-MOF-74 3D structure using Ni^{2+} as the metal centre and DHTA as the organic ligand. Adapted from[162].

Following the published procedure from Xie *et. al.*[165] with few modifications, Ni-MOF-74 was synthesised yielding a light brown powder (**351 mg**). Those modifications were: the proportion was reduced to a third and the activation was done at 120 °C. **FTIR** (cm^{-1}): 3500-3200 (w/br, νO-H), 2956, 2840 (w, νC-H), 1563 (s, ν_sO-C-O), 1414 (s, ν_aO-C-O), 1445-1361 (s, νC-C), 1198 (s, νC-O), 893, 823 (m, δC-H). **PXRD** (º): 6.8 (110), 11.8 (300).

HKUST-1 – $Cu_3(BTC)_2$

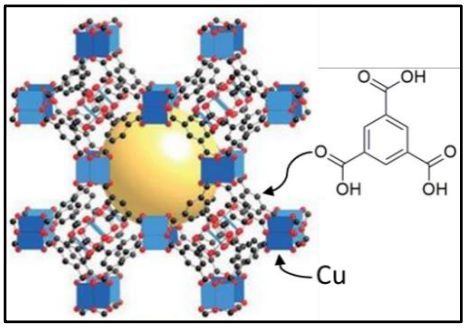

Figure 3.4 – HKUST-1 3D structure using Cu^{2+} as the metal centre and H_3BTC as the organic ligand. Adapted from[168].

Following the published procedure from Peng *et. al.*[77], with the proportion reduced by half, HKUST-1 was synthesised yielding a Persian blue powder (**582 mg**). **FTIR** (cm^{-1}): 3500-3200 (w/br, νO-H), 2924 (w, νC-H), 1648, 1585 (s, ν_sO-C-O), 1613-1553 (s, νC-C), 1449, 1369 (s, ν_aO-C-O), 1108 (m, νC-O), 765, 728 (s, δC-H). **PXRD** (º): 6.7 (200), 9.5 (220), 11.6 (222), 13.4 (400).

UiO-66 – $Zr_6O_4(OH)_4(BDC)_6$

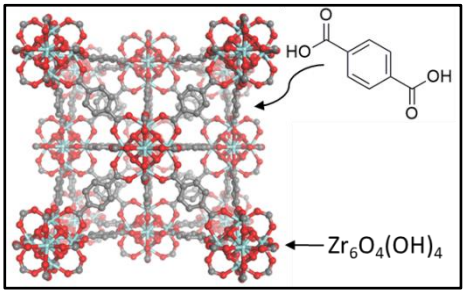

Figure 3.5 – UiO-66 3D structure using Zr^{4+} as the metal centre and H_2BDC as the organic ligand. Adapted from[174].

Following the procedure from Katz *et. al.*[176], doubling the proportion, UiO-66 was synthesised yielding a white powder (**289 mg**). **FTIR** (cm^{-1}): 3500-3200 (w/br, νO-H), 2928, 2861 (w, νC-H), 1584 (s, ν_sO-C-O), 1505 (s, νC=C), 1435-1319 (s, νC-C), 1390 (s, ν_aO-C-O), 887, 814 (s, δC-H). **PXRD** (º): 7.4 (111), 8.5 (002).

UiO-66-NH_2 - $Zr_6O_4(OH)_4(NH_2BDC)_6$

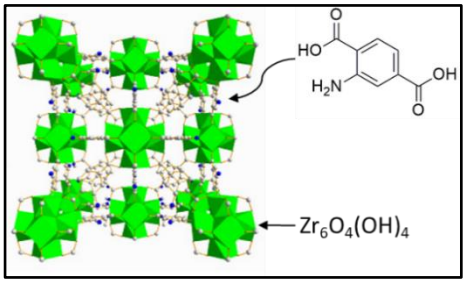

Figure 3.6 – UiO-66-NH_2 3D structure using Zr^{4+} as the metal centre and NH_2-H_2BDC as the organic ligand. Adapted from[177].

Following the procedure from Katz *et. al.*[176], doubling the proportion, UiO-66-NH_2 was synthesised yielding a light-yellow powder (**297 mg**). **FTIR** (cm^{-1}): 3500-3200 (w/br, νO-H), 2978, 2872 (w, νC-H), 1578 (s, ν_sO-C-O), 1379 (s, ν_aO-C-O), 1427-1332 (s, νC-C), 1254 (s, νC-N) 893, 829 (s, δC-H). **PXRD** (º): 7.4 (111), 8.5 (002).

3.4 Electrochemical Measurements and Depositions

3.4.1 General Conditions

A PGSTAT 12 AUT71019 potentiostat managed by NOVA 2.0 software and a heart-shaped electrochemical cell with a three-electrode system was used for the cathodic depositions and the cyclic voltammetry studies, as well as for some controlled potential electrolysis. FTO and graphite foil were used as the WE, Pt wire as the CE and a Ag/AgCl, 3 M NaCl (0.278 V *vs*. NHE) as the RE. The surface area of the FTO was maintained at 0.8-1 cm^2 and the area of the graphite foil was maintained at 0.5 cm^2. The FTO was previously washed under sonication with water and soap for 15 minutes, then methanol, and finally acetone. The graphite foil was previously washed under sonication with acetone for 15 min, isopropanol and Milli-Q water and afterwards the electrodes were dried in the oven at 110 ºC for 1 h. Before each experiment, the electrolyte was purged with N_2 bubbling for at least 15 min. An experiment containing just the solvent and the supporting electrolyte was always performed before adding the respective compounds in study.

3.4.2 Direct Method – Cathodic Deposition

The direct method used was the cathodic deposition method. Using the three-electrode system and the heart-shaped cell (**Figure 3.7**), direct film formations were performed by dissolving the MOF precursors in 10 mL DMF. Non-dried or dry DMF was used, and the latter was obtained by drying DMF from the bottle using activated 4Å molecular sieves for several days before. Additionally, the electrolyte solution contained 0.1 M $TBAPF_6$ as the supporting electrolyte and Et_3NHCl or H_2O_2 as the probases. Afterwards, a reductive *E* between -1.5 and -0.5 V *vs.* Ag/AgCl, 3 M NaCl (depending on the probase) was applied to the working electrode for 15-30 min and in some cases up to 2 h. Different metal:ligand:probase proportions and concentrations were tested. The films obtained were also characterised using PXRD and FTIR.

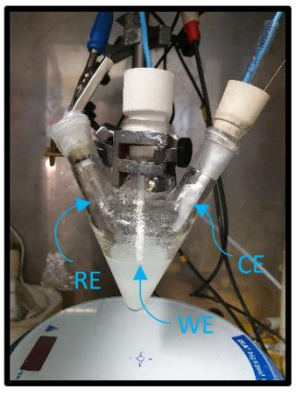

Figure 3.7 – Three-electrode system used in the cyclic voltammetry studies and cathodic deposition using FTO and graphite foil as the WE, Pt wire as the CE and a Ag/AgCl, 3 M NaCl (0.278 V vs. NHE) as the RE.

3.4.3 Indirect Method – Electrophoretic Deposition

The indirect method used was the electrophoretic deposition method. Under sonication (15 min) a uniform suspension is formed containing 10 mg of the synthesised MOF particles, 20 mL of solvent (toluene, ethanol, or acetone) and 10-100 µL of acetic acid to change the pH between 3-4. Using a power supply (Leybold – 3000 V max. lent to us by the department of physics from FCUL), the films were obtained by immersing two parallel FTO or graphite foil electrodes in the suspension under a fixed area (1 cm^2) and distance (1.1 cm) and applying a *E* to form an electric field (30-90 V cm^{-1}). Deposition times also differed from 5 min to 2 h 30 min. The setup used is represented in **Figure 3.8** and the conditions and MOFs we successfully attempted to immobilise using electrophoretic deposition is represented in **Table 3.1**. The films obtained were also characterised using PXRD and FTIR.

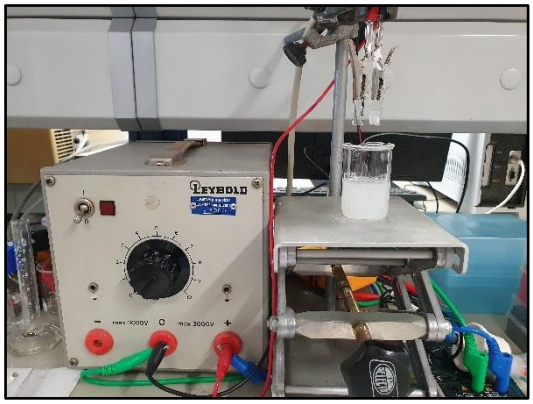

Figure 3.8 – Setup used in the electrophoretic deposition.

Table 3.1 – Conditions and components used in the sucessful electrophoretic deposition of the MOFs: Ni-MOF-74, UiO-66 and UiO-66-NH_2.

MOF Particles	Films Name	Solvent	Time	Electric Field (V cm^{-1})
Ni-MOF-74 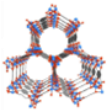	FTO: **Ni-MOF-74-E4** Graphite foil: **Ni-MOF-74-E5**	EtOH + 10 µL Acetic Acid	2 h 30 min	60
UiO-66 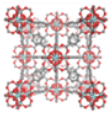	FTO: **UiO-66-E1** Graphite foil: **UiO-66-E2**		5 min	90
UiO-66-NH_2 	FTO: **UiO-66-NH_2-E1**			90

3.4.4 Cyclic Voltammetry Studies

CVs were performed in the same setup as the one used for the cathodic deposition. The CV experiments were done previously to each deposition, both supporting electrolyte (0.1 M $TBAPF_6$) and after adding the MOF components. A scan rate of 0.01 V s^{-1} and an applied *E* varying from -1.5 V to 1.5 V *vs.* Ag/AgCl, 3 M NaCl, during 3 cycles and starting from the open circuit potential (OCP).

For the electrocatalytic testing two different aqueous electrolytes were used, an ammonia and a phosphate-based electrolyte. For the ammonia-based electrolyte its contents were 0.5 M NH_4Cl in 10 mL of Milli-Q water and a varying concentration of 0-100 mM of NH_4OH, while for the phosphate-based electrolyte 10 mL of a PBS solution with the pH of 7.6.

The **Ni-MOF-74-E4/5**, **UiO-66-E1/2** and **UiO-66-NH_2-E1** films, as well as both bare electrodes (FTO and graphite foil) were investigated using CV in both electrolytes. The same measurement conditions were applied aside from the *E*, which varied from -0.2 V to 1.4 V. In the ammonia-based electrolyte, the CVs were obtained at additive concentrations of NH_4OH (total concentration from 0 to 100 mM). Afterwards, in the phosphate-based electrolyte the studies were conducted using the same measurement conditions. The last studies examined the stability of the MOF films in the ammonia-based electrolyte at 4-10 mM total concentration of NH_4OH for 10 cycles (scan rate of 0.01 Vs^{-1}).

3.5 Controlled Potential Electrolysis

Most of the CPEs were performed using a small potentiostat (Potentiostat MP81 from Bank Elektronik) with a custom setup (with the help of Dr. José Augusto from the physics department from FCUL) using a lab-made analog-to-digital converter with an Arduino system (**Figure 3.9**). Some CPE were also performed using the AutoLab potentiostat depending on the availability of the devices. The films were used as the working electrode, a Pt coil as the counter electrode and a Ag/AgCl, 3 M NaCl (0.278 V *vs.* NHE) as the reference electrode. The electrolysis setup is represented in **Figure 3.10**.

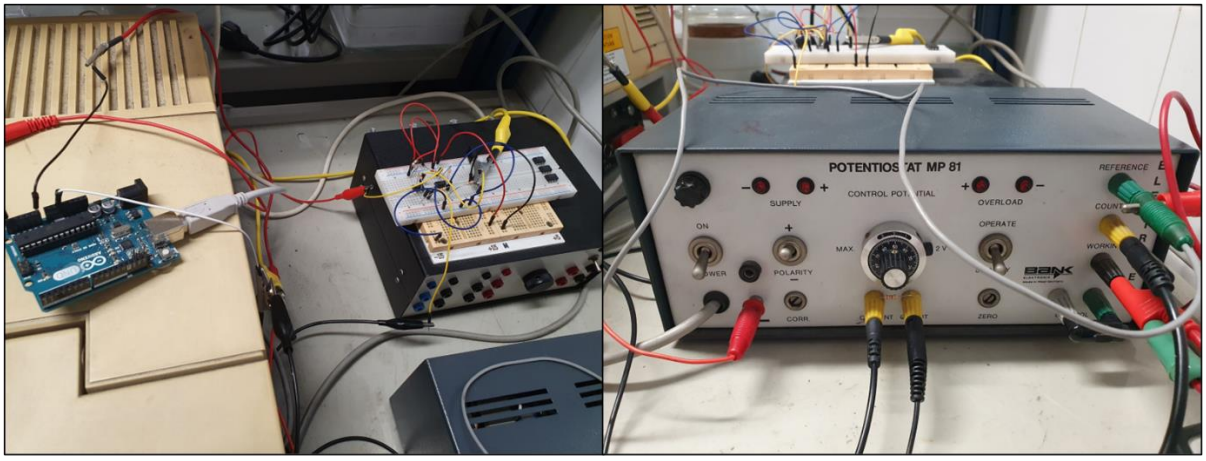

Figure 3.9 – Custom setup using an Arduino system used for most of the CPE.

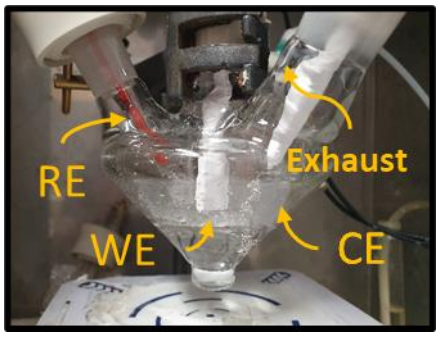

Figure 3.10 – CPE cell setup using the films as the WE, a Pt coil as the CE and a Ag/AgCl, 3 M NaCl (0.278 V vs. NHE) as the RE.

The CPE conditions were, for the ammonia-based electrolyte the 10 mL of pure water using 0.5 M NH_4Cl as the electrolyte and adding 4 mM of NH_4OH. For the water system 10 mL of the PBS solution at 7.6 pH. After adding the contents to the cell and the electrodes, the cell is sealed (with an exhaust) and bubbled with N_2 for 25-30 min. After bubbling, the needle hole in the suba-seal is sealed using silicone. The CPEs were maintained for 3 h under stirring using 700 RPM. The films **Ni-MOF-74-E4**, **UiO-66-E1** and **UiO-66-NH_2-E1** and the bare electrode were tested for the CPE using both electrolytes.

3.6 Quantification of the H_2 Produced Using GC-TCD

Chromatograms were obtained using a gas chromatography equipment fitted with a thermal conductivity detector from Agilent Technology (GC-TCD 7820A) controlled by OpenLAB ChemStation edition software. A HP-MOLESIEVE capillary GC column (L x I.D. 30 m x 0.32 mm, average thickness 12 µm) was used for H_2, O_2 and N_2 detection. Temperature was held at 200 ℃ for the injector and 220 ℃ for the detector. Ar was used as carrier gas flowing at 1.7 mL min^{-1} and injections were done using 500 µL gas tight syringes previously purged with N_2. The method used was: (I) keep at 40 ℃ for 7 min; (II) gradually increase until 200 ℃ for 5 min; keep it at 200 ℃ for 3 min. The retention times for each gas (min) were: H_2 1.91, O_2 2.14 and N_2 2.64. Air was first injected before removing a sample from the cell headspace. The calibration curves used for the quantification of H_2, O_2 and N_2 are represented in **Equations 3.1**, **3.2** and **3.3**, respectively, where *y* is the area of the peak obtained and *x* the volume of that species in the syringe.

$$Y = 104.54x \quad \textbf{(Equation 3.1)}$$

$$Y = 3.49x \quad \textbf{(Equation 3.2)}$$

$$Y = 13.39x \quad \textbf{(Equation 3.3)}$$

4 References

(1) Panwar, N. L.; Kaushik, S. C.; Kothari, S. Role of Renewable Energy Sources in Environmental Protection: A Review. *Renewable and Sustainable Energy Reviews* **2011**, *15* (3), 1513–1524. https://doi.org/10.1016/j.rser.2010.11.037.

(2) *What Is Climate Change? | United Nations*. https://www.un.org/en/climatechange/what-is-climate-change (accessed 2023-03-25).

(3) *AR6 Synthesis Report: Climate Change 2023*. https://www.ipcc.ch/report/ar6/syr/ (accessed 2023-03-30).

(4) *Air pollution*. https://www.who.int/data/gho/data/themes/air-pollution (accessed 2023-03-28).

(5) *Climate Change 101 - Township of Langley*. https://www.tol.ca/en/services/climate-change-101.aspx (accessed 2023-09-27).

(6) *World Energy Outlook 2022 – Analysis - IEA*. https://www.iea.org/reports/world-energy-outlook-2022 (accessed 2023-03-25).

(7) Chu, S.; Cui, Y.; Liu, N. The Path towards Sustainable Energy. *Nature Materials* **2017**, *16*, 16–22. https://doi.org/10.1038/nmat4834.

(8) *Renewable energy – powering a safer future | United Nations*. https://www.un.org/en/climatechange/raising-ambition/renewable-energy (accessed 2023-03-28).

(9) Gebremariam, S. K.; Dumée, L. F.; Llewellyn, P. L.; AlWahedi, Y. F.; Karanikolos, G. N. Metal-Organic Framework Hybrid Adsorbents for Carbon Capture – A Review. *Journal of Environmental Chemical Engineering* **2023**, *11* (2), 109291. https://doi.org/10.1016/j.jece.2023.109291.

(10) Ding, M.; Flaig, R. W.; Jiang, H.-L.; Yaghi, O. M. Carbon Capture and Conversion Using Metal–Organic Frameworks and MOF-Based Materials. *Chemical Society Reviews* **2019**, *48*, 2783–2828. https://doi.org/10.1039/C8CS00829A.

(11) Zaker, A.; ben Hammouda, S.; Sun, J.; Wang, X.; Li, X.; Chen, Z. Carbon-Based Materials for CO2 Capture: Their Production, Modification and Performance. *Journal of Environmental Chemical Engineering* **2023**, *11* (3), 109741. https://doi.org/10.1016/j.jece.2023.109741.

(12) D'Alessandro, D. M.; Smit, B.; Long, J. R. Carbon Dioxide Capture: Prospects for New Materials. *Angewandte Chemie International Edition* **2010**, *49* (35), 6058–6082. https://doi.org/10.1002/anie.201000431.

(13) Juangsa, F. B.; Prananto, L. A.; Mufrodi, Z.; Budiman, A.; Oda, T.; Aziz, M. Highly Energy-Efficient Combination of Dehydrogenation of Methylcyclohexane and Hydrogen-Based Power Generation. *Applied Energy* **2018**, *226*, 31–38. https://doi.org/10.1016/j.apenergy.2018.05.110.

(14) Aziz, M.; Wijayanta, A. T.; Nandiyanto, A. B. D. Ammonia as Effective Hydrogen Storage: A Review on Production, Storage and Utilization. *Energies* **2020**, *13* (12), 3062. https://doi.org/10.3390/en13123062.

(15) Schlapbach, L.; Züttel, A. Hydrogen-Storage Materials for Mobile Applications. *Nature* **2001**, *414*, 353–358. https://doi.org/10.1038/35104634.

(16) Murakami, Y. Hydrogen Embrittlement. In *Metal Fatigue*; Academic Press; 2nd ed., 2019; pp 567–607. https://doi.org/10.1016/B978-0-12-813876-2.00021-2.

(17) Yue, M.; Lambert, H.; Pahon, E.; Roche, R.; Jemei, S.; Hissel, D. Hydrogen Energy Systems: A Critical Review of Technologies, Applications, Trends and Challenges. *Renewable and Sustainable Energy Reviews* **2021**, *146*, 111180. https://doi.org/10.1016/j.rser.2021.111180.

(18) *Hydrogen Storage | Department of Energy*. https://www.energy.gov/eere/fuelcells/hydrogen-storage (accessed 2023-08-12).

(19) *Green, Blue and Grey Hydrogen: the main differences*. https://www.hellonext.world/green-blue-and-grey-hydrogen-the-main-differences/ (accessed 2023-08-12).

(20) Amin, M.; Butt, A. S.; Ahmad, J.; Lee, C.; Azam, S. U.; Mannan, H. A.; Naveed, A. B.; Farooqi, Z. U. R.; Chung, E.; Iqbal, A. Issues and Challenges in Hydrogen Separation Technologies. *Energy Reports* **2023**, *9*, 894–911. https://doi.org/10.1016/j.egyr.2022.12.014.

(21) Amin, M.; Shah, H. H.; Fareed, A. G.; Khan, W. U.; Chung, E.; Zia, A.; Rahman Farooqi, Z. U.; Lee, C. Hydrogen Production through Renewable and Non-Renewable Energy Processes and Their Impact on Climate Change. *International Journal of Hydrogen Energy* **2022**, *47* (77), 33112–33134. https://doi.org/10.1016/j.ijhydene.2022.07.172.

(22) *Hydrogen | Herbert Smith Freehills | Global law firm*. https://www.herbertsmithfreehills.com/latest-thinking/hydrogen (accessed 2023-07-15).

(23) Ibrahim, A. A. Hydrogen Production from Light Hydrocarbons. In *Advances In Hydrogen Generation Technologies*; InTech, Edited by Murat Eyvaz, **2018**. https://doi.org/10.5772/intechopen.76813.

(24) Li, J.; Cheng, W. Comparative Life Cycle Energy Consumption, Carbon Emissions and Economic Costs of Hydrogen Production from Coke Oven Gas and Coal Gasification. *International Journal of Hydrogen Energy* **2020**, *45* (51), 27979–27993. https://doi.org/10.1016/j.ijhydene.2020.07.079.

(25) Xiao, N.; Li, S.; Li, X.; Ge, L.; Gao, Y.; Li, N. The Roles and Mechanism of Cocatalysts in Photocatalytic Water Splitting to Produce Hydrogen. *Chinese Journal of Catalysis* **2020**, *41* (4), 642–671. https://doi.org/10.1016/S1872-2067(19)63469-8.

(26) Gupta, A.; Likozar, B.; Jana, R.; Chanu, W. C.; Singh, M. K. A Review of Hydrogen Production Processes by Photocatalytic Water Splitting – From Atomistic Catalysis Design to Optimal Reactor Engineering. *International Journal of Hydrogen Energy* **2022**, *47* (78), 33282–33307. https://doi.org/10.1016/j.ijhydene.2022.07.210.

(27) Sharma, V. Metal-Organic Frameworks Driven Electrocatalytic and Photocatalytic Hydrogen Production: A Mini-Review. *Biointerface Research in Applied Chemistry* **2022**, *13* (3), 220. https://doi.org/10.33263/BRIAC133.220.

(28) Chatenet, M.; Pollet, B. G.; Dekel, D. R.; Dionigi, F.; Deseure, J.; Millet, P.; Braatz, R. D.; Bazant, M. Z.; Eikerling, M.; Staffell, I.; Balcombe, P.; Shao-Horn, Y.; Schäfer, H. Water Electrolysis: From Textbook Knowledge to the Latest Scientific Strategies and Industrial

Developments. *Chemical Society Reviews* **2022**, *51* (11), 4583–4762. https://doi.org/10.1039/D0CS01079K.

(29) Safari, F.; Dincer, I. A Review and Comparative Evaluation of Thermochemical Water Splitting Cycles for Hydrogen Production. *Energy Conversion Management* **2020**, *205*, 112182. https://doi.org/10.1016/j.enconman.2019.112182.

(30) Holladay, J. D.; Hu, J.; King, D. L.; Wang, Y. An Overview of Hydrogen Production Technologies. *Catalysis Today* **2009**, *139* (4), 244–260. https://doi.org/10.1016/j.cattod.2008.08.039.

(31) Ajanovic, A.; Haas, R. Prospects and Impediments for Hydrogen and Fuel Cell Vehicles in the Transport Sector. *International Journal of Hydrogen Energy* **2021**, *46* (16), 10049–10058. https://doi.org/10.1016/j.ijhydene.2020.03.122.

(32) Wang, C.; Liao, M.; Liang, B.; Jiang, Z.; Zhong, W.; Chen, Y.; Luo, X.; Shu, R.; Tian, Z.; Lei, L. Enhancement Effect of Catalyst Support on Indirect Hydrogen Production from Propane Partial Oxidation towards Commercial Solid Oxide Fuel Cell (SOFC) Applications. *Applied Energy* **2021**, *288*, 116362. https://doi.org/10.1016/j.apenergy.2020.116362.

(33) Tang, D.; Tan, G.-L.; Li, G.-W.; Liang, J.-G.; Ahmad, S. M.; Bahadur, A.; Humayun, M.; Ullah, H.; Khan, A.; Bououdina, M. State-of-the-Art Hydrogen Generation Techniques and Storage Methods: A Critical Review. *Journal of Energy Storage* **2023**, *64*, 107196. https://doi.org/10.1016/j.est.2023.107196.

(34) Kothari, R.; Buddhi, D.; Sawhney, R. L. Comparison of Environmental and Economic Aspects of Various Hydrogen Production Methods. *Renewable and Sustainable Energy Reviews* **2008**, *12* (2), 553–563. https://doi.org/10.1016/j.rser.2006.07.012.

(35) Dalebrook, A. F.; Gan, W.; Grasemann, M.; Moret, S.; Laurenczy, G. Hydrogen Storage: Beyond Conventional Methods. *Chemical Communications* **2013**, *49* (78), 8735. https://doi.org/10.1039/c3cc43836h.

(36) Chen, P.; Zhu, M. Recent Progress in Hydrogen Storage. *Materials Today* **2008**, *11* (12), 36–43. https://doi.org/10.1016/S1369-7021(08)70251-7.

(37) Jeerh, G.; Zhang, M.; Tao, S. Recent Progress in Ammonia Fuel Cells and Their Potential Applications. *Journal of Materials Chemistry A* **2021**, *9* (2), 727–752. https://doi.org/10.1039/D0TA08810B.

(38) Klerke, A.; Christensen, C. H.; Nørskov, J. K.; Vegge, T. Ammonia for Hydrogen Storage: Challenges and Opportunities. *Journal of Materials Chemistry* **2008**, *18* (20), 2304. https://doi.org/10.1039/b720020j.

(39) Guo, X.; Du, H.; Qu, F.; Li, J. Recent Progress in Electrocatalytic Nitrogen Reduction. *Journal of Materials Chemistry A* **2019**, *7* (8), 3531–3543. https://doi.org/10.1039/C8TA11201K.

(40) Juangsa, F. B.; Irhamna, A. R.; Aziz, M. Production of Ammonia as Potential Hydrogen Carrier: Review on Thermochemical and Electrochemical Processes. *International Journal of Hydrogen Energy* **2021**, *46* (27), 14455–14477. https://doi.org/10.1016/j.ijhydene.2021.01.214.

(41) Zheng, W.; Zhu, L.; Yan, Z.; Lin, Z.; Lei, Z.; Zhang, Y.; Xu, H.; Dang, Z.; Wei, C.; Feng, C. Self-Activated Ni Cathode for Electrocatalytic Nitrate Reduction to Ammonia: From

Fundamentals to Scale-Up for Treatment of Industrial Wastewater. *Environmental Science and Technology* **2021**, *55* (19), 13231–13243. https://doi.org/10.1021/acs.est.1c02278.

(42) Liu, H.-Y.; Lant, H. M. C.; Cody, C. C.; Jelušić, J.; Crabtree, R. H.; Brudvig, G. W. Electrochemical Ammonia Oxidation with Molecular Catalysts. *ACS Catalysis* **2023**, *13* (7), 4675–4682. https://doi.org/10.1021/acscatal.3c00032.

(43) Wu, Z.; Ambrožová, N.; Eftekhari, E.; Aravindakshan, N.; Wang, W.; Wang, Q.; Zhang, S.; Kočí, K.; Li, Q. Photocatalytic H2 Generation from Aqueous Ammonia Solution Using TiO2 Nanowires-Intercalated Reduced Graphene Oxide Composite Membrane under Low Power UV Light. *Emergent Materials* **2019**, *2* (3), 303–311. https://doi.org/10.1007/s42247-019-00029-5.

(44) Mukherjee, S.; Devaguptapu, S. V.; Sviripa, A.; Lund, C. R. F.; Wu, G. Low-Temperature Ammonia Decomposition Catalysts for Hydrogen Generation. *Applied Catalysis B: Environmental* **2018**, *226*, 162–181. https://doi.org/10.1016/j.apcatb.2017.12.039.

(45) Banoth, P.; Kandula, C.; Kollu, P. Introduction to Electrocatalysts. In *Noble Metal-Free Electrocatalysts: New Trends in Electrocatalysts for Energy Applications*; UTC, 2022; Vol. 2, pp 1–37. https://doi.org/10.1021/bk-2022-1432.ch001.

(46) Sugiura, K.; Yamamoto, Y.; Tsumura, M. Optimization of Hydrogen Production by Ammonia Electrolysis. *ECS Transactions* **2010**, *26* (1), 485–491. https://doi.org/10.1149/1.3429021.

(47) Little, D. J.; Smith, III, M. R.; Hamann, T. W. Electrolysis of Liquid Ammonia for Hydrogen Generation. *Energy & Environmental Science* **2015**, *8* (9), 2775–2781. https://doi.org/10.1039/C5EE01840D.

(48) Cheddie, D. Ammonia as a Hydrogen Source for Fuel Cells: A Review. In *Hydrogen Energy - Challenges and Perspectives*; InTech, Edited by Dragica Minic, **2012**. https://doi.org/10.5772/47759.

(49) Vitse, F.; Cooper, M.; Botte, G. G. On the Use of Ammonia Electrolysis for Hydrogen Production. *Journal of Power Sources* **2005**, *142* (1–2), 18–26. https://doi.org/10.1016/j.jpowsour.2004.09.043.

(50) Liu, H.-Y.; Lant, H. M. C.; Troiano, J. L.; Hu, G.; Mercado, B. Q.; Crabtree, R. H.; Brudvig, G. W. Electrocatalytic, Homogeneous Ammonia Oxidation in Water to Nitrate and Nitrite with a Copper Complex. *Journal of the American Chemical Society* **2022**, *144* (19), 8449–8453. https://doi.org/10.1021/jacs.2c01788.

(51) Bard, A. J.; Parsons, R.; Jordan, J. *Standard Potentials in Aqueous Solution, 1st Edition*; Routledge, **2017**. https://doi.org/10.1201/9780203738764.

(52) de Vooys, A. C. A.; Koper, M. T. M.; van Santen, R. A.; van Veen, J. A. R. The Role of Adsorbates in the Electrochemical Oxidation of Ammonia on Noble and Transition Metal Electrodes. *Journal of Electroanalytical Chemistry* **2001**, *506* (2), 127–137. https://doi.org/10.1016/S0022-0728(01)00491-0.

(53) Oswin, H. G.; Salomon, M. The Anodic Oxidation of Ammonia at Platinum Black Electrodes in Aqueous KOH Electrolyte. *Canadian Journal of Chemistry* **1963**, *41* (7), 1686–1694. https://doi.org/10.1139/v63-243.

(54) Bunce, N. J.; Bejan, D. Mechanism of Electrochemical Oxidation of Ammonia. *Electrochimica Acta* **2011**, *56* (24), 8085–8093. https://doi.org/10.1016/j.electacta.2011.07.078.

(55) Endo, K.; Katayama, Y.; Miura, T. A Rotating Disk Electrode Study on the Ammonia Oxidation. *Electrochimica Acta* **2005**, *50* (11), 2181–2185. https://doi.org/10.1016/j.electacta.2004.09.024.

(56) Zhou, H.-C. "Joe"; Kitagawa, S. Metal–Organic Frameworks (MOFs). *Chemical Society Reviews* **2014**, *43* (16), 5415–5418. https://doi.org/10.1039/C4CS90059F.

(57) Kitagawa, S.; Kitaura, R.; Noro, S. Functional Porous Coordination Polymers. *Angewandte Chemie International Edition* **2004**, *43* (18), 2334–2375. https://doi.org/10.1002/anie.200300610.

(58) Furukawa, H.; Cordova, K. E.; O'Keeffe, M.; Yaghi, O. M. The Chemistry and Applications of Metal-Organic Frameworks. *Science* **2013**, *341* (6149). https://doi.org/10.1126/science.1230444.

(59) Kalmutzki, M. J.; Hanikel, N.; Yaghi, O. M. Secondary Building Units as the Turning Point in the Development of the Reticular Chemistry of MOFs. *Science Advances* **2018**, *4* (10). https://doi.org/10.1126/sciadv.aat9180.

(60) Ha, J.; Lee, J. H.; Moon, H. R. Alterations to Secondary Building Units of Metal–Organic Frameworks for the Development of New Functions. *Inorganic Chemistry Frontiers* **2020**, *7* (1), 12–27. https://doi.org/10.1039/C9QI01119F.

(61) Tranchemontagne, D. J.; Mendoza-Cortés, J. L.; O'Keeffe, M.; Yaghi, O. M. Secondary Building Units, Nets and Bonding in the Chemistry of Metal–Organic Frameworks. *Chemical Society Reviews* **2009**, *38* (5), 1257. https://doi.org/10.1039/b817735j.

(62) Moumen, E.; Assen, A. H.; Adil, K.; Belmabkhout, Y. Versatility vs Stability. Are the Assets of Metal–Organic Frameworks Deployable in Aqueous Acidic and Basic Media? *Coordination Chemistry Reviews* **2021**, *443*, 214020. https://doi.org/10.1016/j.ccr.2021.214020.

(63) Zhou, H.-C.; Long, J. R.; Yaghi, O. M. Introduction to Metal–Organic Frameworks. *Chemical Reviews* **2012**, *112* (2), 673–674. https://doi.org/10.1021/cr300014x.

(64) Howarth, A. J.; Liu, Y.; Li, P.; Li, Z.; Wang, T. C.; Hupp, J. T.; Farha, O. K. Chemical, Thermal and Mechanical Stabilities of Metal–Organic Frameworks. *Nature Reviews Materials* **2016**, *1*, 15018. https://doi.org/10.1038/natrevmats.2015.18.

(65) O'Keeffe, M.; Yaghi, O. M. Deconstructing the Crystal Structures of Metal–Organic Frameworks and Related Materials into Their Underlying Nets. *Chemical Reviews* **2012**, *112* (2), 675–702. https://doi.org/10.1021/cr200205j.

(66) Kim, D.; Liu, X.; Lah, M. S. Topology Analysis of Metal–Organic Frameworks Based on Metal–Organic Polyhedra as Secondary or Tertiary Building Units. *Inorganic Chemistry Frontiers* **2015**, *2* (4), 336–360. https://doi.org/10.1039/C4QI00236A.

(67) Eddaoudi, M.; Kim, J.; Rosi, N.; Vodak, D.; Wachter, J.; O'Keeffe, M.; Yaghi, O. M. Systematic Design of Pore Size and Functionality in Isoreticular MOFs and Their Application in Methane Storage. *Science* **2002**, *295* (5554), 469–472. https://doi.org/10.1126/science.1067208.

(68) Wang, Z.; Cohen, S. M. Postsynthetic Covalent Modification of a Neutral Metal−Organic Framework. *Journal of the American Chemical Society* **2007**, *129* (41), 12368–12369. https://doi.org/10.1021/ja074366o.

(69) Khalil, I. E.; Xue, C.; Liu, W.; Li, X.; Shen, Y.; Li, S.; Zhang, W.; Huo, F. The Role of Defects in Metal–Organic Frameworks for Nitrogen Reduction Reaction: When Defects Switch to Features. *Advanced Functional Materials* **2021**, *31* (17), 2010052. https://doi.org/10.1002/adfm.202010052.

(70) Li, D.; Zhang, P.; Ge, S.; Sun, G.; He, Q.; Fa, W.; Li, Y.; Ma, J. A Green Route to Prepare Metal-Free Phthalocyanine Crystals with Controllable Structures by a Simple Solvothermal Method. *RSC Adv* **2021**, *11* (50), 31226–31234. https://doi.org/10.1039/D1RA04064B.

(71) Yaghi, O. M.; O'Keeffe, M.; Kanatzidis, M. Design of Solids from Molecular Building Blocks: Golden Opportunities for Solid State Chemistry. *Journal of Solid State Chemistry* **2000**, *152* (1), 1–2. https://doi.org/10.1006/jssc.2000.8733.

(72) Han, Y.; Yang, H.; Guo, X. Synthesis Methods and Crystallization of MOFs. In *Synthesis Methods and Crystallization*; InTech, Edited by Riadh Marzouki, **2020**. https://doi.org/10.5772/intechopen.90435.

(73) Kalmutzki, M. J.; Hanikel, N.; Yaghi, O. M. Secondary Building Units as the Turning Point in the Development of the Reticular Chemistry of MOFs. *Science Advances* **2018**, *4* (10). https://doi.org/10.1126/sciadv.aat9180.

(74) Rocío-Bautista, P.; Taima-Mancera, I.; Pasán, J.; Pino, V. Metal-Organic Frameworks in Green Analytical Chemistry. *Separations* **2019**, *6* (3), 33. https://doi.org/10.3390/separations6030033.

(75) Mason, J. A.; Veenstra, M.; Long, J. R. Evaluating Metal–Organic Frameworks for Natural Gas Storage. *Chemical Science* **2014**, *5* (1), 32–51. https://doi.org/10.1039/C3SC52633J.

(76) Hirscher, M.; Panella, B. Hydrogen Storage in Metal–Organic Frameworks. *Scripta Materialia* **2007**, *56* (10), 809–812. https://doi.org/10.1016/j.scriptamat.2007.01.005.

(77) Peng, Y.; Krungleviciute, V.; Eryazici, I.; Hupp, J. T.; Farha, O. K.; Yildirim, T. Methane Storage in Metal–Organic Frameworks: Current Records, Surprise Findings, and Challenges. *Journal of the American Chemical Society* **2013**, *135* (32), 11887–11894. https://doi.org/10.1021/ja4045289.

(78) Baumann, A. E.; Burns, D. A.; Liu, B.; Thoi, V. S. Metal-Organic Framework Functionalization and Design Strategies for Advanced Electrochemical Energy Storage Devices. *Communications Chemistry* **2019**, *2* (1), 86. https://doi.org/10.1038/s42004-019-0184-6.

(79) DeSantis, D.; Mason, J. A.; James, B. D.; Houchins, C.; Long, J. R.; Veenstra, M. Techno-Economic Analysis of Metal–Organic Frameworks for Hydrogen and Natural Gas Storage. *Energy & Fuels* **2017**, *31* (2), 2024–2032. https://doi.org/10.1021/acs.energyfuels.6b02510.

(80) Millward, A. R.; Yaghi, O. M. Metal−Organic Frameworks with Exceptionally High Capacity for Storage of Carbon Dioxide at Room Temperature. *Journal of the American Chemical Society* **2005**, *127* (51), 17998–17999. https://doi.org/10.1021/ja0570032.

(81) Lee, J.; Farha, O. K.; Roberts, J.; Scheidt, K. A.; Nguyen, S. T.; Hupp, J. T. Metal–Organic Framework Materials as Catalysts. *Chemical Society Reviews* **2009**, *38* (5), 1450. https://doi.org/10.1039/b807080f.

(82) Corma, A.; García, H.; Llabrés i Xamena, F. X. Engineering Metal Organic Frameworks for Heterogeneous Catalysis. *Chemical Reviews* **2010**, *110* (8), 4606–4655. https://doi.org/10.1021/cr9003924.

(83) Huang, C.-W.; Nguyen, V.-H.; Zhou, S.-R.; Hsu, S.-Y.; Tan, J.-X.; Wu, K. C.-W. Metal–Organic Frameworks: Preparation and Applications in Highly Efficient Heterogeneous Photocatalysis. *Sustain Energy Fuels* **2020**, *4* (2), 504–521. https://doi.org/10.1039/C9SE00972H.

(84) Gomes Silva, C.; Luz, I.; Llabrés i Xamena, F. X.; Corma, A.; García, H. Water Stable Zr-Benzenedicarboxylate Metal-Organic Frameworks as Photocatalysts for Hydrogen Generation. *Chemistry - A European Journal* **2010**, *16* (36), 11133–11138. https://doi.org/10.1002/chem.200903526.

(85) Nath, A.; Asha, K. S.; Mandal, S. Conductive Metal-Organic Frameworks: Electronic Structure and Electrochemical Applications. *Chemistry – A European Journal* **2021**, *27* (45), 11482–11538. https://doi.org/10.1002/chem.202100610.

(86) Halls, J. E.; Jiang, D.; Burrows, A. D.; Kulandainathan, M. A.; Marken, F. Chapter 6. Electrochemistry within Metal-Organic Frameworks. In *SPR Electrochemistry*; Royal Society of Chemistry, **2014**; Vol. 12, pp 187–210. https://doi.org/10.1039/9781849737333-00187.

(87) Samadi-Maybodi, A.; Ghasemi, S.; Ghaffari-Rad, H. Application of Nano-Sized Nanoporous Zinc 2-Methylimidazole Metal-Organic Framework for Electrocatalytic Oxidation of Methanol in Alkaline Solution. *Journal of Power Sources* **2016**, *303*, 379–387. https://doi.org/10.1016/j.jpowsour.2015.10.060.

(88) Wang, Y.; Hou, P.; Wang, Z.; Kang, P. Zinc Imidazolate Metal–Organic Frameworks (ZIF-8) for Electrochemical Reduction of CO_2 to CO. *ChemPhysChem* **2017**, *18* (22), 3142–3147. https://doi.org/10.1002/cphc.201700716.

(89) Zhang, S.; Li, M.; Li, J.; Song, Q.; Liu, X. High-Ammonia Selective Metal–Organic Framework–Derived Co-Doped Fe/Fe_2O_3 Catalysts for Electrochemical Nitrate Reduction. *Proceedings of the National Academy of Sciences* **2022**, *119* (6). https://doi.org/10.1073/pnas.2115504119.

(90) Hu, Y.; Verdegaal, W. M.; Yu, S.-H.; Jiang, H.-L. Alkylamine-Tethered Stable Metal-Organic Framework for CO_2 Capture from Flue Gas. *ChemSusChem* **2014**, *7* (3), 734–737. https://doi.org/10.1002/cssc.201301163.

(91) Zhou, S.; Wei, Y.; Li, L.; Duan, Y.; Hou, Q.; Zhang, L.; Ding, L.-X.; Xue, J.; Wang, H.; Caro, J. Paralyzed Membrane: Current-Driven Synthesis of a Metal-Organic Framework with Sharpened Propene/Propane Separation. *Science Advances* **2018**, *4* (10). https://doi.org/10.1126/sciadv.aau1393.

(92) Zhan, W.; Kuang, Q.; Zhou, J.; Kong, X.; Xie, Z.; Zheng, L. Semiconductor@Metal–Organic Framework Core–Shell Heterostructures: A Case of ZnO@ZIF-8 Nanorods with Selective Photoelectrochemical Response. *Journal of the American Chemical Society* **2013**, *135* (5), 1926–1933. https://doi.org/10.1021/ja311085e.

(93) Ji, L.; Hao, J.; Wu, K.; Yang, N. Potential-Tunable Metal–Organic Frameworks: Electrosynthesis, Properties, and Applications for Sensing of Organic Molecules. *The Journal of Physical Chemistry C* **2019**, *123* (4), 2248–2255. https://doi.org/10.1021/acs.jpcc.8b10448.

(94) Horcajada, P.; Gref, R.; Baati, T.; Allan, P. K.; Maurin, G.; Couvreur, P.; Férey, G.; Morris, R. E.; Serre, C. Metal–Organic Frameworks in Biomedicine. *Chemical Reviews* **2012**, *112* (2), 1232–1268. https://doi.org/10.1021/cr200256v.

(95) Pan, Y.-B.; Wang, S.; He, X.; Tang, W.; Wang, J.; Shao, A.; Zhang, J. A Combination of Glioma *in Vivo* Imaging and *in Vivo* Drug Delivery by Metal–Organic Framework Based Composite Nanoparticles. *Journal of Materials Chemistry B* **2019**, *7* (48), 7683–7689. https://doi.org/10.1039/C9TB01651A.

(96) Li, Y.; Chen, C.; Sun, X.; Dou, J.; Wei, M. Metal-Organic Frameworks at Interfaces in Dye-Sensitized Solar Cells. *ChemSusChem* **2014**, *7* (9), 2469–2472. https://doi.org/10.1002/cssc.201402143.

(97) Stavila, V.; Talin, A. A.; Allendorf, M. D. MOF-Based Electronic and Opto-Electronic Devices. *Chemical Society Reviews* **2014**, *43* (16), 5994–6010. https://doi.org/10.1039/C4CS00096J.

(98) Zhao, Y.; Song, Z.; Li, X.; Sun, Q.; Cheng, N.; Lawes, S.; Sun, X. Metal Organic Frameworks for Energy Storage and Conversion. *Energy Storage Mater* **2016**, *2*, 35–62. https://doi.org/10.1016/j.ensm.2015.11.005.

(99) Wang, H.; Zhu, Q.-L.; Zou, R.; Xu, Q. Metal-Organic Frameworks for Energy Applications. *Chem* **2017**, *2* (1), 52–80. https://doi.org/10.1016/j.chempr.2016.12.002.

(100) Cao, Z.; Momen, R.; Tao, S.; Xiong, D.; Song, Z.; Xiao, X.; Deng, W.; Hou, H.; Yasar, S.; Altin, S.; Bulut, F.; Zou, G.; Ji, X. Metal–Organic Framework Materials for Electrochemical Supercapacitors. *Nano-Micro Letters* **2022**, *14* (1), 181. https://doi.org/10.1007/s40820-022-00910-9.

(101) Li, S.-L.; Xu, Q. Metal–Organic Frameworks as Platforms for Clean Energy. *Energy & Environmental Science* **2013**, *6* (6), 1656. https://doi.org/10.1039/c3ee40507a.

(102) Britt, D.; Tranchemontagne, D.; Yaghi, O. M. Metal-Organic Frameworks with High Capacity and Selectivity for Harmful Gases. *Proceedings of the National Academy of Sciences* **2008**, *105* (33), 11623–11627. https://doi.org/10.1073/pnas.0804900105.

(103) Li, C.; Shen, J.; Wu, K.; Yang, N. Metal Centers and Organic Ligands Determine Electrochemistry of Metal–Organic Frameworks. *Small* **2022**, *18* (11), 2106607. https://doi.org/10.1002/smll.202106607.

(104) Britt, D.; Furukawa, H.; Wang, B.; Glover, T. G.; Yaghi, O. M. Highly Efficient Separation of Carbon Dioxide by a Metal-Organic Framework Replete with Open Metal Sites. *Proceedings of the National Academy of Sciences* **2009**, *106* (49), 20637–20640. https://doi.org/10.1073/pnas.0909718106.

(105) Daglar, H.; Altintas, C.; Erucar, I.; Heidari, G.; Zare, E. N.; Moradi, O.; Srivastava, V.; Iftekhar, S.; Keskin, S.; Sillanpää, M. Metal-Organic Framework-Based Materials for the Abatement of Air Pollution and Decontamination of Wastewater. *Chemosphere* **2022**, *303*, 135082. https://doi.org/10.1016/j.chemosphere.2022.135082.

(106) Cavka, J. H.; Jakobsen, S.; Olsbye, U.; Guillou, N.; Lamberti, C.; Bordiga, S.; Lillerud, K. P. A New Zirconium Inorganic Building Brick Forming Metal Organic Frameworks with Exceptional Stability. *Journal of the American Chemical Society* **2008**, *130* (42), 13850–13851. https://doi.org/10.1021/ja8057953.

(107) Lee, J.; Farha, O. K.; Roberts, J.; Scheidt, K. A.; Nguyen, S. T.; Hupp, J. T. Metal–Organic Framework Materials as Catalysts. *Chemical Society Reviews* **2009**, *38* (5), 1450. https://doi.org/10.1039/b807080f.

(108) Ravon, U.; Domine, M. E.; Gaudillère, C.; Desmartin-Chomel, A.; Farrusseng, D. MOFs as Acid Catalysts with Shape Selectivity Properties. *New Journal of Chemistry* **2008**, *32* (6), 937. https://doi.org/10.1039/b803953b.

(109) Alaerts, L.; Séguin, E.; Poelman, H.; Thibault-Starzyk, F.; Jacobs, P. A.; De Vos, D. E. Probing the Lewis Acidity and Catalytic Activity of the Metal–Organic Framework [Cu3(Btc)2] (BTC=Benzene-1,3,5-Tricarboxylate). *Chemistry - A European Journal* **2006**, *12* (28), 7353–7363. https://doi.org/10.1002/chem.200600220.

(110) Jiao, L.; Wang, Y.; Jiang, H.; Xu, Q. Metal–Organic Frameworks as Platforms for Catalytic Applications. *Advanced Materials* **2018**, *30* (37), 1703663. https://doi.org/10.1002/adma.201703663.

(111) Zhang, Y.; Chang, C.-H. Metal–Organic Framework Thin Films: Fabrication, Modification, and Patterning. *Processes* **2020**, *8* (3), 377. https://doi.org/10.3390/pr8030377.

(112) Zacher, D.; Shekhah, O.; Wöll, C.; Fischer, R. A. Thin Films of Metal–Organic Frameworks. *Chemical Society Reviews* **2009**, *38* (5), 1418. https://doi.org/10.1039/b805038b.

(113) Guo, W.; Monnens, W.; Zhang, W.; Xie, S.; Han, N.; Zhou, Z.; Chanut, N.; Vanstreels, K.; Ameloot, R.; Zhang, X.; Fransaer, J. Anodic Electrodeposition of Continuous Metal-Organic Framework Films with Robust Adhesion by Pre-Anchored Strategy. *Microporous and Mesoporous Materials* **2023**, *350*, 112443. https://doi.org/10.1016/j.micromeso.2023.112443.

(114) Xie, S.; Monnens, W.; Wan, K.; Zhang, W.; Guo, W.; Xu, M.; Vankelecom, I. F. J.; Zhang, X.; Fransaer, J. Cathodic Electrodeposition of MOF Films Using Hydrogen Peroxide. *Angewandte Chemie International Edition* **2021**, *60* (47), 24950–24957. https://doi.org/10.1002/anie.202108485.

(115) Xie, S.; Zhang, X.; Tan, X.; Zhang, W.; Guo, W.; Han, N.; Zhou, Z.; Jiang, Y.; Vankelecom, I. F. J.; Fransaer, J. One-Step Reductive Electrodeposition of MOF Film on Polymer Membrane. *ACS Materials Letters* **2022**, *4* (9), 1721–1725. https://doi.org/10.1021/acsmaterialslett.2c00294.

(116) Lan, H.; Pan, D.; Sun, Y.; Guo, Y.; Wu, Z. Thin Metal Organic Frameworks Coatings by Cathodic Electrodeposition for Solid-Phase Microextraction and Analysis of Trace Exogenous Estrogens in Milk. *Analytica Chimica Acta* **2016**, *937*, 53–60. https://doi.org/10.1016/j.aca.2016.07.041.

(117) Zhu, H.; Liu, H.; Zhitomirsky, I.; Zhu, S. Preparation of Metal–Organic Framework Films by Electrophoretic Deposition Method. *Materials Letters* **2015**, *142*, 19–22. https://doi.org/10.1016/j.matlet.2014.11.113.

(118) He, G.; Babu, D. J.; Agrawal, K. V. Electrophoretic Crystallization of Ultrathin High-Performance Metal-Organic Framework Membranes. *Journal of Visualized Experiments* **2018**, *2018* (138). https://doi.org/10.3791/58301.

(119) Hod, I.; Bury, W.; Karlin, D. M.; Deria, P.; Kung, C.-W.; Katz, M. J.; So, M.; Klahr, B.; Jin, D.; Chung, Y.-W.; Odom, T. W.; Farha, O. K.; Hupp, J. T. Directed Growth of Electroactive Metal-Organic Framework Thin Films Using Electrophoretic Deposition. *Advanced Materials* **2014**, *26* (36), 6295–6300. https://doi.org/10.1002/adma.201401940.

(120) Jia, Z.; Hao, S.; Wen, J.; Li, S.; Peng, W.; Huang, R.; Xu, X. Electrochemical Fabrication of Metal–Organic Frameworks Membranes and Films: A Review. *Microporous and Mesoporous Materials* **2020**, *305*, 110322. https://doi.org/10.1016/j.micromeso.2020.110322.

(121) Campagnol, N.; Van Assche, T. R. C.; Li, M.; Stappers, L.; Dincă, M.; Denayer, J. F. M.; Binnemans, K.; De Vos, D. E.; Fransaer, J. On the Electrochemical Deposition of Metal–Organic Frameworks. *Journal of Materials Chemistry A* **2016**, *4* (10), 3914–3925. https://doi.org/10.1039/C5TA10782B.

(122) Ghoorchian, A.; Afkhami, A.; Madrakian, T.; Ahmadi, M. Electrochemical Synthesis of MOFs. *Metal-Organic Frameworks for Biomedical Applications*; Woodhead Publishing, 2020; pp 177–195. https://doi.org/10.1016/B978-0-12-816984-1.00011-1.

(123) Linnemann, J.; Taudien, L.; Klose, M.; Giebeler, L. Electrodeposited Films to MOF-Derived Electrochemical Energy Storage Electrodes: A Concept of Simplified Additive-Free Electrode Processing for Self-Standing, Ready-to-Use Materials. *Journal of Materials Chemistry A* **2017**, *5* (35), 18420–18428. https://doi.org/10.1039/C7TA01874F.

(124) Zhang, X.; Luo, J.; Tang, P.; Ye, X.; Peng, X.; Tang, H.; Sun, S.-G.; Fransaer, J. A Universal Strategy for Metal Oxide Anchored and Binder-Free Carbon Matrix Electrode: A Supercapacitor Case with Superior Rate Performance and High Mass Loading. *Nano Energy* **2017**, *31*, 311–321. https://doi.org/10.1016/j.nanoen.2016.11.024.

(125) Zhao, G.; Sun, X.; Zhang, L.; Chen, X.; Mao, Y.; Sun, K. A Self-Supported Metal-Organic Framework Derived Co3O4 Film Prepared by an in-Situ Electrochemically Assistant Process as Li Ion Battery Anodes. *Journal of Power Sources* **2018**, *389*, 8–12. https://doi.org/10.1016/j.jpowsour.2018.04.001.

(126) Li, W.-J.; Lü, J.; Gao, S.-Y.; Li, Q.-H.; Cao, R. Electrochemical Preparation of Metal–Organic Framework Films for Fast Detection of Nitro Explosives. *Journal of Materials Chemistry A* **2014**, *2* (45), 19473–19478. https://doi.org/10.1039/C4TA04203D.

(127) Campagnol, N.; Van Assche, T.; Boudewijns, T.; Denayer, J.; Binnemans, K.; De Vos, D.; Fransaer, J. High Pressure, High Temperature Electrochemical Synthesis of Metal–Organic Frameworks: Films of MIL-100 (Fe) and HKUST-1 in Different Morphologies. *Journal of Materials Chemistry A* **2013**, *1* (19), 5827. https://doi.org/10.1039/c3ta10419b.

(128) Stassen, I.; Styles, M.; Van Assche, T.; Campagnol, N.; Fransaer, J.; Denayer, J.; Tan, J.-C.; Falcaro, P.; De Vos, D.; Ameloot, R. Electrochemical Film Deposition of the Zirconium Metal–Organic Framework UiO-66 and Application in a Miniaturized Sorbent Trap. *Chemistry of Materials* **2015**, *27* (5), 1801–1807. https://doi.org/10.1021/cm504806p.

(129) Cheng, K.-Y.; Wang, J.-C.; Lin, C.-Y.; Lin, W.-R.; Chen, Y.-A.; Tsai, F.-J.; Chuang, Y.-C.; Lin, G.-Y.; Ni, C.-W.; Zeng, Y.-T.; Ho, M.-L. Electrochemical Synthesis, Characterization of Ir–Zn Containing Coordination Polymer, and Application in Oxygen and Glucose Sensing. *Dalton Transactions* **2014**, *43* (17), 6536. https://doi.org/10.1039/c3dt53504e.

(130) Van de Voorde, B.; Ameloot, R.; Stassen, I.; Everaert, M.; De Vos, D.; Tan, J.-C. Mechanical Properties of Electrochemically Synthesised Metal–Organic Framework Thin Films. *Journal of Materials Chemistry C* **2013**, *1* (46), 7716. https://doi.org/10.1039/c3tc31039f.

(131) Ameloot, R.; Stappers, L.; Fransaer, J.; Alaerts, L.; Sels, B. F.; De Vos, D. E. Patterned Growth of Metal-Organic Framework Coatings by Electrochemical Synthesis. *Chemistry of Materials* **2009**, *21* (13), 2580–2582. https://doi.org/10.1021/cm900069f.

(132) Zhang, L.; Zhou, Y.; Han, S. The Role of Metal–Organic Frameworks in Electronic Sensors. *Angewandte Chemie* **2021**, *133* (28), 15320–15340. https://doi.org/10.1002/ange.202006402.

(133) Ji, L.; Wang, J.; Wu, K.; Yang, N. Tunable Electrochemistry of Electrosynthesized Copper Metal–Organic Frameworks. *Advanced Functional Materials* **2018**, *28* (13), 1706961. https://doi.org/10.1002/adfm.201706961.

(134) Xiao, Y.; Wu, Z.; Zhang, Q.; Li, P.; Yu, H.; Lu, G. Oxygen-Assisted Cathodic Deposition of Copper-Carboxylate Metal–Organic Framework Films. *Crystal Growth & Design* **2020**, *20* (6), 3997–4004. https://doi.org/10.1021/acs.cgd.0c00297.

(135) Hu, P.; Zhu, X.; Luo, X.; Hu, X.; Ji, L. Cathodic Electrodeposited Cu-BTC MOFs Assembled from Cu(II) and Trimesic Acid for Electrochemical Determination of Bisphenol A. *Microchimica Acta* **2020**, *187* (2), 145. https://doi.org/10.1007/s00604-020-4124-z.

(136) Li, M.; Dincă, M. Selective Formation of Biphasic Thin Films of Metal–Organic Frameworks by Potential-Controlled Cathodic Electrodeposition. *Chemical Science* **2014**, *5* (1), 107–111. https://doi.org/10.1039/C3SC51815A.

(137) Besra, L.; Liu, M. A Review on Fundamentals and Applications of Electrophoretic Deposition (EPD). *Progress in Materials Science* **2007**, *52* (1), 1–61. https://doi.org/10.1016/j.pmatsci.2006.07.001.

(138) Stappers, L.; Zhang, L.; Van der Biest, O.; Fransaer, J. The Effect of Electrolyte Conductivity on Electrophoretic Deposition. *Journal of Colloid and Interface Science* **2008**, *328* (2), 436–446. https://doi.org/10.1016/j.jcis.2008.09.022.

(139) Elimelech, M.; O'Melia, C. R. Effect of Electrolyte Type on the Electrophoretic Mobility of Polystyrene Latex Colloids. *Colloids and Surfaces* **1990**, *44* (C), 165–178. https://doi.org/10.1016/0166-6622(90)80194-9.

(140) Feng, J.; Gao, S.; Liu, T.; Shi, J.; Cao, R. Preparation of Dual-Emitting Ln@UiO-66-Hybrid Films via Electrophoretic Deposition for Ratiometric Temperature Sensing. *ACS Applied Materials & Interfaces* **2018**, *10* (6), 6014–6023. https://doi.org/10.1021/acsami.7b17947.

(141) Mahfoudh, M.; Khenoussi, N.; Haj Said, A. Submicron Particles of Metal–Organic Framework HKUST-1 with Negative Surface Charge and Their Electrophoretic Deposition on ITO. *Theoretical and Experimental Chemistry* **2018**, *54* (3), 206–209. https://doi.org/10.1007/s11237-018-9563-9.

(142) Farrokhi-Rad, M.; Fateh, A.; Shahrabi, T. Effect of PH on the Electrophoretic Deposition of Chitosan in Different Alcoholic Solutions. *Surfaces and Interfaces* **2018**, *12*, 145–150. https://doi.org/10.1016/j.surfin.2018.05.010.

(143) Han, H.; Yuan, X.; Zhang, Z.; Zhang, J. Preparation of a ZIF-67 Derived Thin Film Electrode via Electrophoretic Deposition for Efficient Electrocatalytic Oxidation of Vanillin. *Inorganic Chemistry* **2019**, *58* (5), 3196–3202. https://doi.org/10.1021/acs.inorgchem.8b03281.

(144) Ji, Y.; Song, Y.; Huang, Y.; Zhu, H.; Yue, C.; Liu, F.; Zhao, J. One-Step Synthesis of Ultrathin Zeolitic Imidazole Framework-8 (ZIF-8) Membrane on Unmodified Porous Support via Electrophoretic Deposition. *Membranes* **2022**, *12* (11), 1062. https://doi.org/10.3390/membranes12111062.

(145) He, G.; Dakhchoune, M.; Zhao, J.; Huang, S.; Agrawal, K. V. Electrophoretic Nuclei Assembly for Crystallization of High-Performance Membranes on Unmodified Supports. *Advanced Functional Materials* **2018**, *28* (20), 1707427. https://doi.org/10.1002/adfm.201707427.

(146) Li, H.; Eddaoudi, M.; O'Keeffe, M.; Yaghi, O. M. Design and Synthesis of an Exceptionally Stable and Highly Porous Metal-Organic Framework. *Nature* **1999**, *402* (6759), 276–279. https://doi.org/10.1038/46248.

(147) Sun, Y.; Zhou, H.-C. Recent Progress in the Synthesis of Metal–Organic Frameworks. *Science and Technology of Advanced Materials* **2015**, *16* (5), 054202. https://doi.org/10.1088/1468-6996/16/5/054202.

(148) Zhao, Z.; Li, Z.; Lin, Y. S. Adsorption and Diffusion of Carbon Dioxide on Metal−Organic Framework (MOF-5). *Industrial & Engineering Chemistry Research* **2009**, *48* (22), 10015–10020. https://doi.org/10.1021/ie900665f.

(149) Tranchemontagne, D. J.; Hunt, J. R.; Yaghi, O. M. Room Temperature Synthesis of Metal-Organic Frameworks: MOF-5, MOF-74, MOF-177, MOF-199, and IRMOF-0. *Tetrahedron* **2008**, *64* (36), 8553–8557. https://doi.org/10.1016/j.tet.2008.06.036.

(150) Eddaoudi, M.; Kim, J.; Rosi, N.; Vodak, D.; Wachter, J.; O'Keeffe, M.; Yaghi, O. M. Systematic Design of Pore Size and Functionality in Isoreticular MOFs and Their Application in Methane Storage. *Science* **2002**, *295* (5554), 469–472. https://doi.org/10.1126/science.1067208.

(151) Morris, W.; Taylor, R. E.; Dybowski, C.; Yaghi, O. M.; Garcia-Garibay, M. A. Framework Mobility in the Metal–Organic Framework Crystal IRMOF-3: Evidence for Aromatic Ring and Amine Rotation. *Journal of Molecular Structure* **2011**, *1004* (1–3), 94–101. https://doi.org/10.1016/j.molstruc.2011.07.037.

(152) Zhang, T.; Han, X.; Liu, H.; Biset-Peiró, M.; Li, J.; Zhang, X.; Tang, P.; Yang, B.; Zheng, L.; Morante, J. R.; Arbiol, J. Site-Specific Axial Oxygen Coordinated FeN_4 Active Sites for Highly Selective Electroreduction of Carbon Dioxide. *Advanced Functional Materials* **2022**, *32* (18), 2111446. https://doi.org/10.1002/adfm.202111446.

(153) Zhou, X.; Zhang, Y.; Yang, X.; Zhao, L.; Wang, G. Functionalized IRMOF-3 as Efficient Heterogeneous Catalyst for the Synthesis of Cyclic Carbonates. *Journal of Molecular Catalysis A: Chemical* **2012**, *361–362*, 12–16. https://doi.org/10.1016/j.molcata.2012.04.008.

(154) Park, K. S.; Ni, Z.; Côté, A. P.; Choi, J. Y.; Huang, R.; Uribe-Romo, F. J.; Chae, H. K.; O'Keeffe, M.; Yaghi, O. M. Exceptional Chemical and Thermal Stability of Zeolitic Imidazolate

Frameworks. *Proceedings of the National Academy of Sciences* **2006**, *103* (27), 10186–10191. https://doi.org/10.1073/pnas.0602439103.

(155) Liu, Y.; Cheng, H.; Cheng, M.; Liu, Z.; Huang, D.; Zhang, G.; Shao, B.; Liang, Q.; Luo, S.; Wu, T.; Xiao, S. The Application of Zeolitic Imidazolate Frameworks (ZIFs) and Their Derivatives Based Materials for Photocatalytic Hydrogen Evolution and Pollutants Treatment. *Chemical Engineering Journal* **2021**, *417*, 127914. https://doi.org/10.1016/j.cej.2020.127914.

(156) Cravillon, J.; Nayuk, R.; Springer, S.; Feldhoff, A.; Huber, K.; Wiebcke, M. Controlling Zeolitic Imidazolate Framework Nano- and Microcrystal Formation: Insight into Crystal Growth by Time-Resolved In Situ Static Light Scattering. *Chemistry of Materials* **2011**, *23* (8), 2130–2141. https://doi.org/10.1021/cm103571y.

(157) Tang, Y.; Dubbeldam, D.; Guo, X.; Rothenberg, G.; Tanase, S. Efficient Separation of Ethanol–Methanol and Ethanol–Water Mixtures Using ZIF-8 Supported on a Hierarchical Porous Mixed-Oxide Substrate. *ACS Applied Materials & Interfaces* **2019**, *11* (23), 21126–21136. https://doi.org/10.1021/acsami.9b02325.

(158) Kadota, K.; Sivaniah, E.; Bureekaew, S.; Kitagawa, S.; Horike, S. Synthesis of Manganese ZIF-8 from $[Mn(BH_4)_2 \cdot 3THF] \cdot NaBH_4$. *Inorganic Chemistry* **2017**, *56* (15), 8744–8747. https://doi.org/10.1021/acs.inorgchem.7b01322.

(159) Dietzel, P. D. C.; Blom, R.; Fjellvåg, H. Base-Induced Formation of Two Magnesium Metal-Organic Framework Compounds with a Bifunctional Tetratopic Ligand. *European Journal of Inorganic Chemistry* **2008**, *2008* (23), 3624–3632. https://doi.org/10.1002/ejic.200701284.

(160) Zuluaga, S.; Fuentes-Fernandez, E. M. A.; Tan, K.; Xu, F.; Li, J.; Chabal, Y. J.; Thonhauser, T. Understanding and Controlling Water Stability of MOF-74. *Journal of Materials Chemistry A* **2016**, *4* (14), 5176–5183. https://doi.org/10.1039/C5TA10416E.

(161) Grant Glover, T.; Peterson, G. W.; Schindler, B. J.; Britt, D.; Yaghi, O. MOF-74 Building Unit Has a Direct Impact on Toxic Gas Adsorption. *Chemical Engineering Science* **2011**, *66* (2), 163–170. https://doi.org/10.1016/j.ces.2010.10.002.

(162) Britt, D.; Furukawa, H.; Wang, B.; Glover, T. G.; Yaghi, O. M. Highly Efficient Separation of Carbon Dioxide by a Metal-Organic Framework Replete with Open Metal Sites. *Proceedings of the National Academy of Sciences* **2009**, *106* (49), 20637–20640. https://doi.org/10.1073/pnas.0909718106.

(163) Voskanyan, A. A.; Goncharov, V. G.; Novendra, N.; Guo, X.; Navrotsky, A. Thermodynamics Drives the Stability of the MOF-74 Family in Water. *ACS Omega* **2020**, *5* (22), 13158–13163. https://doi.org/10.1021/acsomega.0c01189.

(164) Dietzel, P. D. C.; Panella, B.; Hirscher, M.; Blom, R.; Fjellvåg, H. Hydrogen Adsorption in a Nickel Based Coordination Polymer with Open Metal Sites in the Cylindrical Cavities of the Desolvated Framework. *Chemical Communications* **2006**, No. 9, 959. https://doi.org/10.1039/b515434k.

(165) Xie, S.; Qin, Q.; Liu, H.; Jin, L.; Wei, X.; Liu, J.; Liu, X.; Yao, Y.; Dong, L.; Li, B. MOF-74-M (M = Mn, Co, Ni, Zn, MnCo, MnNi, and MnZn) for Low-Temperature NH_3-SCR and In Situ DRIFTS Study Reaction Mechanism. *ACS Applied Materials & Interfaces* **2020**, *12* (43), 48476–48485. https://doi.org/10.1021/acsami.0c11035.

(166) Chui, S. S.-Y.; Lo, S. M.-F.; Charmant, J. P. H.; Orpen, A. G.; Williams, I. D. A Chemically Functionalizable Nanoporous Material $[Cu_3(TMA)_2(H_2O)_3]_n$. *Science* **1999**, *283* (5405), 1148–1150. https://doi.org/10.1126/science.283.5405.1148.

(167) Chong, K. C.; Lai, S. O.; Mah, S. K.; Thiam, H. S.; Chong, W. C.; Shuit, S. H.; Lee, S. S.; Chong, W. E. A Review of HKUST-1 Metal-Organic Frameworks in Gas Adsorption. *IOP Conference Series: Earth Environmental Science* **2023**, *1135* (1), 012030. https://doi.org/10.1088/1755-1315/1135/1/012030.

(168) Alshammari, A.; Jiang, Z.; Cordova, K. E. Metal Organic Frameworks as Emerging Photocatalysts. In *Semiconductor Photocatalysis - Materials, Mechanisms and Applications*; InTech, Edited by Wenbin Cao, 2016. https://doi.org/10.5772/63489.

(169) Qi, Y.; Lin, S.; Chen, C.; Liu, Y.; Qiao, Z.; Kuang, X.; Su, Q.; Chao, H.-Y. Increased Proton Conductivity of Metal–Organic Framework Micro-Film Prepared by a Facile Salt-Free Approach. *Journal of Materials Chemistry A* **2014**, *2* (23), 8849. https://doi.org/10.1039/c4ta00336e.

(170) Yang, A.; Li, P.; Zhong, J. Facile Preparation of Low-Cost HKUST-1 with Lattice Vacancies and High-Efficiency Adsorption for Uranium. *RSC Advances* **2019**, *9* (18), 10320–10325. https://doi.org/10.1039/C9RA01427F.

(171) Álvarez, J. R.; Sánchez-González, E.; Pérez, E.; Schneider-Revueltas, E.; Martínez, A.; Tejeda-Cruz, A.; Islas-Jácome, A.; González-Zamora, E.; Ibarra, I. A. Structure Stability of HKUST-1 towards Water and Ethanol and Their Effect on Its CO_2 Capture Properties. *Dalton Transactions* **2017**, *46* (28), 9192–9200. https://doi.org/10.1039/C7DT01845B.

(172) Cavka, J. H.; Jakobsen, S.; Olsbye, U.; Guillou, N.; Lamberti, C.; Bordiga, S.; Lillerud, K. P. A New Zirconium Inorganic Building Brick Forming Metal Organic Frameworks with Exceptional Stability. *Journal of the American Chemical Society* **2008**, *130* (42), 13850–13851. https://doi.org/10.1021/ja8057953.

(173) Gomes Silva, C.; Luz, I.; Llabrés i Xamena, F. X.; Corma, A.; García, H. Water Stable Zr-Benzenedicarboxylate Metal-Organic Frameworks as Photocatalysts for Hydrogen Generation. *Chemistry - A European Journal* **2010**, *16* (36), 11133–11138. https://doi.org/10.1002/chem.200903526.

(174) Liu, L.; Chen, Z.; Wang, J.; Zhang, D.; Zhu, Y.; Ling, S.; Huang, K.-W.; Belmabkhout, Y.; Adil, K.; Zhang, Y.; Slater, B.; Eddaoudi, M.; Han, Y. Imaging Defects and Their Evolution in a Metal–Organic Framework at Sub-Unit-Cell Resolution. *Nature Chemistry* **2019**, *11* (7), 622–628. https://doi.org/10.1038/s41557-019-0263-4.

(175) Huang, Y.; Jiao, Y.; Chen, T.; Gong, Y.; Wang, S.; Liu, Y.; Sholl, D. S.; Walton, K. S. Tuning the Wettability of Metal–Organic Frameworks via Defect Engineering for Efficient Oil/Water Separation. *ACS Applied Materials & Interfaces* **2020**, *12* (30), 34413–34422. https://doi.org/10.1021/acsami.0c08803.

(176) Katz, M. J.; Brown, Z. J.; Colón, Y. J.; Siu, P. W.; Scheidt, K. A.; Snurr, R. Q.; Hupp, J. T.; Farha, O. K. A Facile Synthesis of UiO-66, UiO-67 and Their Derivatives. *Chemical Communications* **2013**, *49* (82), 9449. https://doi.org/10.1039/c3cc46105j.

(177) Zhang, Z.; Tao, C.-A.; Zhao, J.; Wang, F.; Huang, J.; Wang, J. Microwave-Assisted Solvothermal Synthesis of UiO-66-NH2 and Its Catalytic Performance toward the Hydrolysis of a Nerve Agent Simulant. *Catalysts* **2020**, *10* (9), 1086. https://doi.org/10.3390/catal10091086.

(178) Trickett, C. A.; Gagnon, K. J.; Lee, S.; Gándara, F.; Bürgi, H.-B.; Yaghi, O. M. Definitive Molecular Level Characterization of Defects in UiO-66 Crystals. *Angewandte Chemie International Edition* **2015**, *54* (38), 11162–11167. https://doi.org/10.1002/anie.201505461.

(179) Li, M.; Dincă, M. On the Mechanism of MOF-5 Formation under Cathodic Bias. *Chemistry of Materials* **2015**, *27* (9), 3203–3206. https://doi.org/10.1021/acs.chemmater.5b00899.

(180) Li, M.; Dincă, M. Reductive Electrosynthesis of Crystalline Metal–Organic Frameworks. *Journal of the American Chemical Society* **2011**, *133* (33), 12926–12929. https://doi.org/10.1021/ja2041546.

(181) Reis, A. R. Sensing of Biorelevant Molecules With Metal-Organic Framework Films, Master's Thesis, NOVA University, Lisbon, 2022.

(182) Zhang, H.; Zhao, M.; Lin, Y. S. Stability of ZIF-8 in Water under Ambient Conditions. *Microporous and Mesoporous Materials* **2019**, *279*, 201–210. https://doi.org/10.1016/j.micromeso.2018.12.035.

Annexes

Figure A.1 – a) MOF-5-S1 and b) MOF-5-S2 obtained powders via solvothermal synthesis.

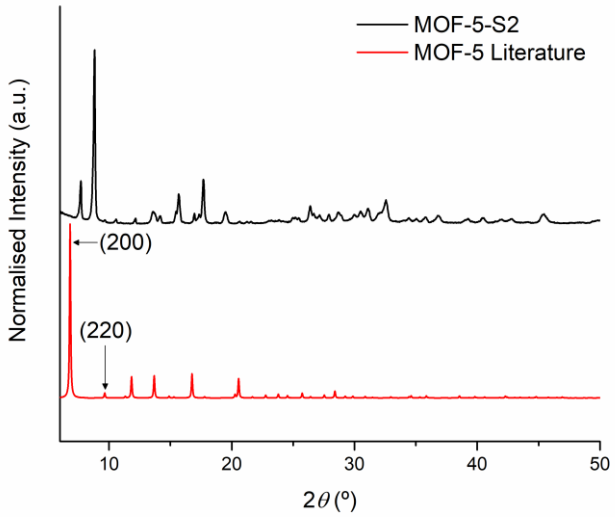

Figure A.2 - PXRD of MOF-5-S2 and comparison with MOF-5 diffraction pattern from the literature.[146]

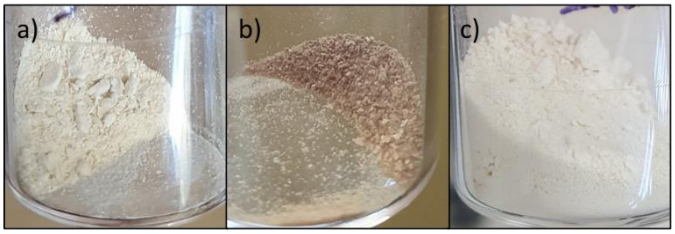

Figure A.3 – a) IRMOF-3-S1, b) IRMOF-3-S2 and c) IRMOF-3-S3 obtained powders via solvothermal synthesis.

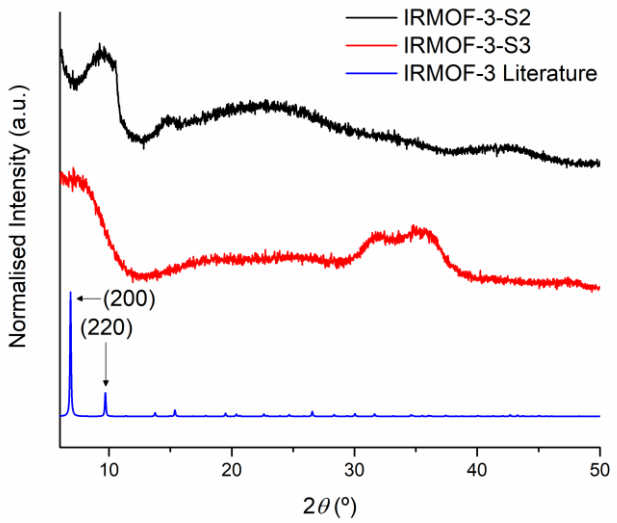

Figure A.4 - PXRD of **IRMOF-3-S2**, **IRMOF-3-S3** and comparison with IRMOF-3 diffraction pattern from the literature.[150]

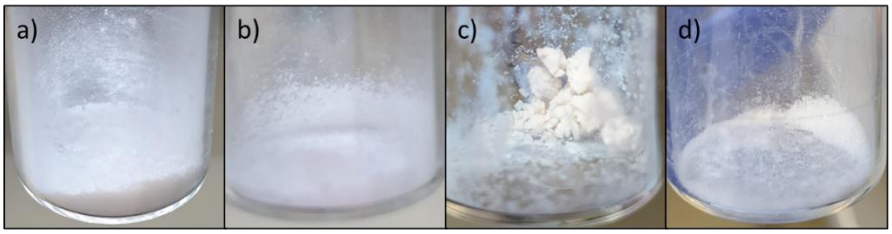

Figure A.5 – a) **ZIF-8-S1**, b) **ZIF-8-S2**, c) **ZIF-8-S3** and d) **ZIF-8-S4** obtained powders via solvothermal synthesis.

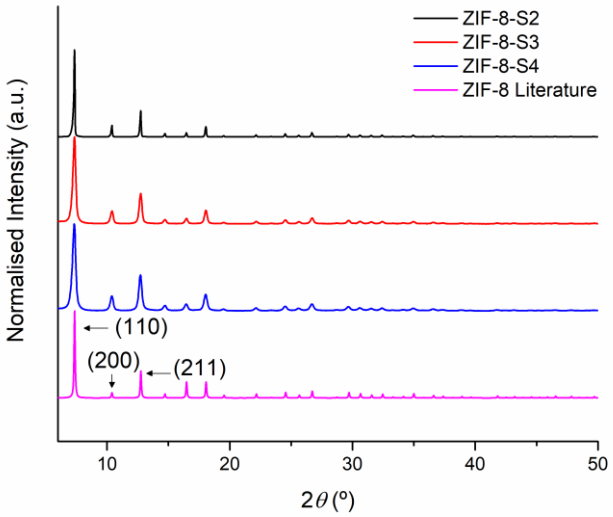

Figure A.6 - PXRD of **ZIF-8-S2**, **ZIF-8-S3**, **ZIF-8-S4** and comparison with the ZIF-8 diffraction pattern from the literature.[154]

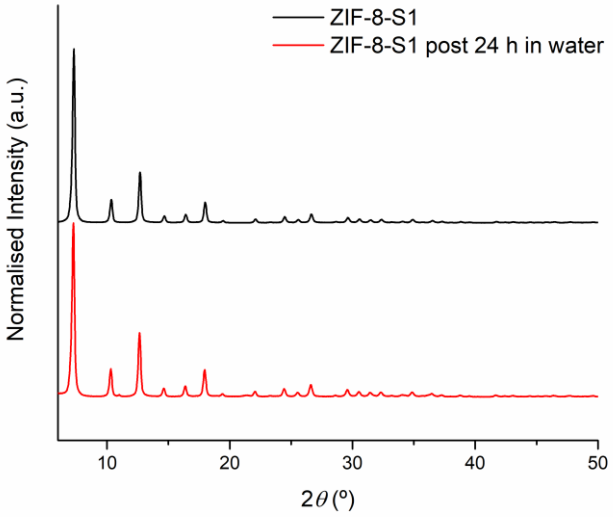

Figure A.7 – PXRD of the stability test of **ZIF-8-S1** after 24 h in water.

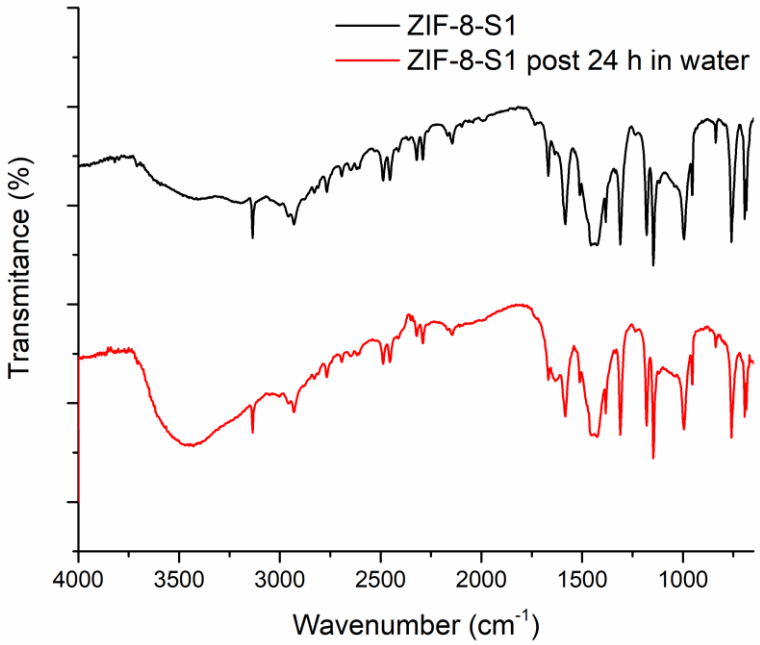

Figure A.8 - FTIR spectra (DRIFT) of **ZIF-8-S1** post 24 h in water.

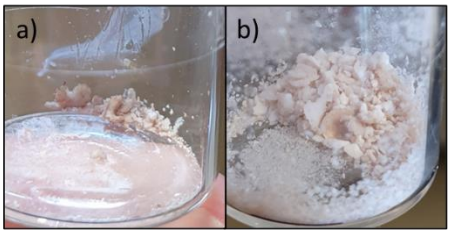

Figure A.9 - a) **ZnMn-ZIF-8-S1** and b) **ZnMn-ZIF-8-S2** obtained powders via solvothermal synthesis.

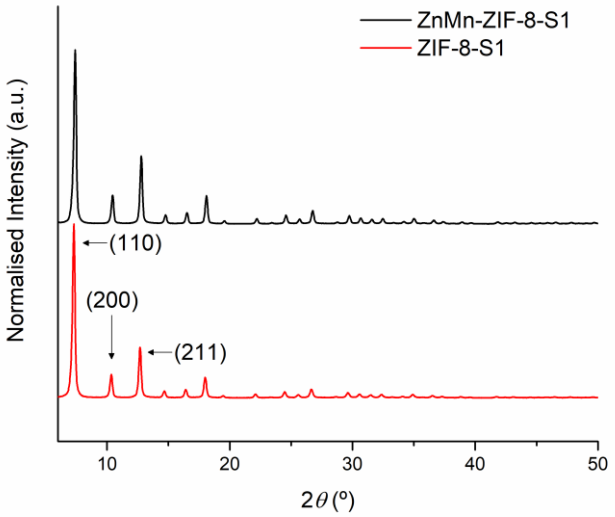

Figure A.10 – PXRD of **ZnMn-ZIF-8-S1** in comparison with the precursor **ZIF-8-S1**.

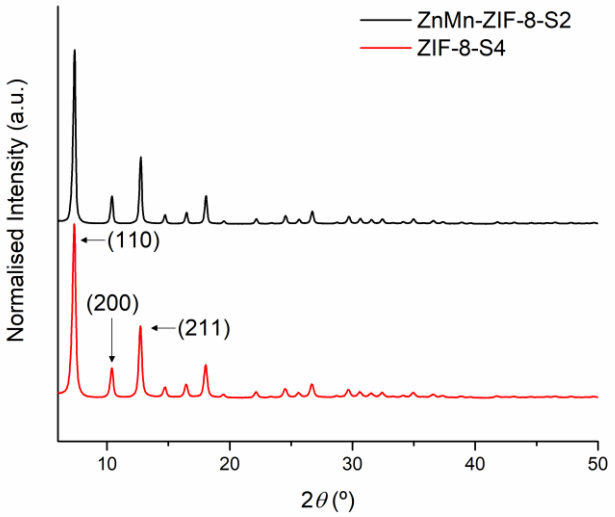

Figure A.11 – PXRD of **ZnMn-ZIF-8-S2** in comparison with the precursor **ZIF-8-S4**.

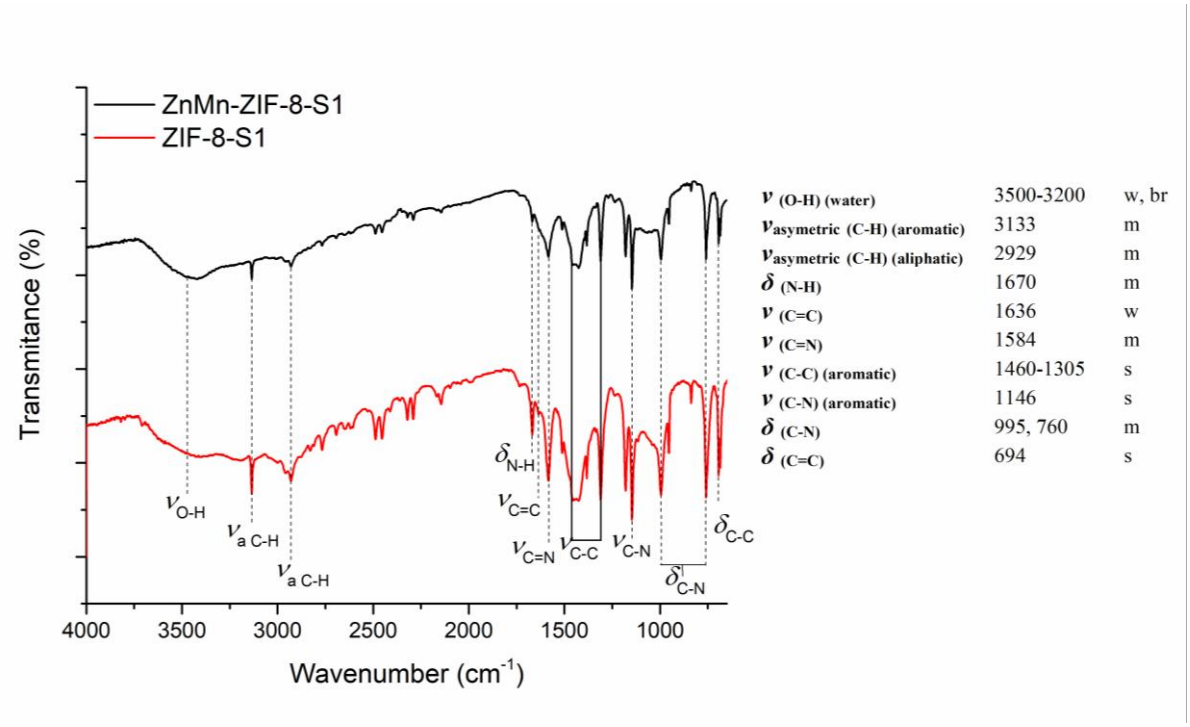

Figure A.12 – FTIR spectra (DRIFT) of **ZnMn-ZIF-8-S1**, used **ZIF-8-S1** and main wavenumber values for the corresponding vibrational modes.

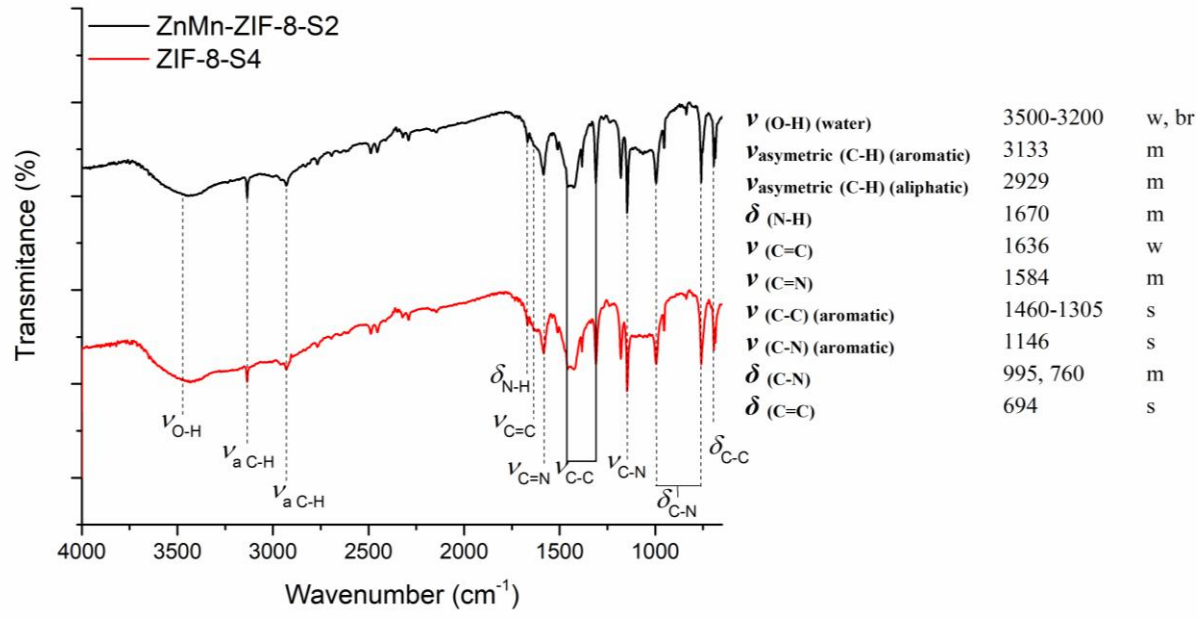

Figure A.13 – FTIR spectra (DRIFT) of **ZnMn-ZIF-8-S2**, used **ZIF-8-S4** and main wavenumber values for the corresponding vibrational modes.

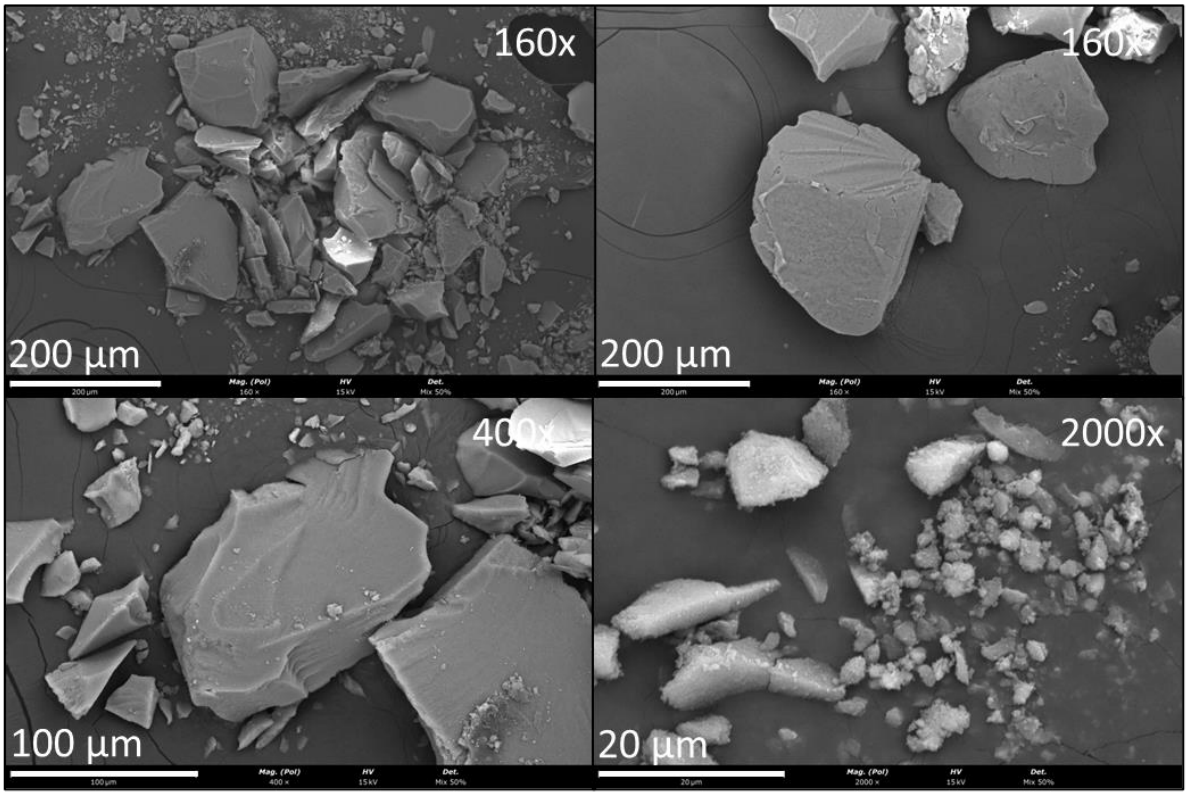

Figure A.14 - SEM images of **ZnMn-ZIF-8-S2**. Magnified at 160x, 400x and 2000x.

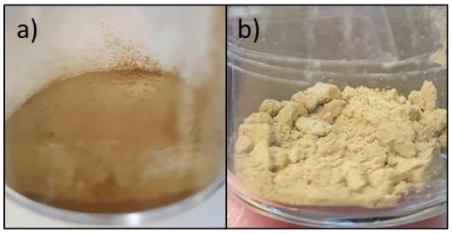

Figure A.15 - a) **Mg-MOF-74-S1** and b) **Mg-MOF-74-S2** obtained powders via solvothermal synthesis.

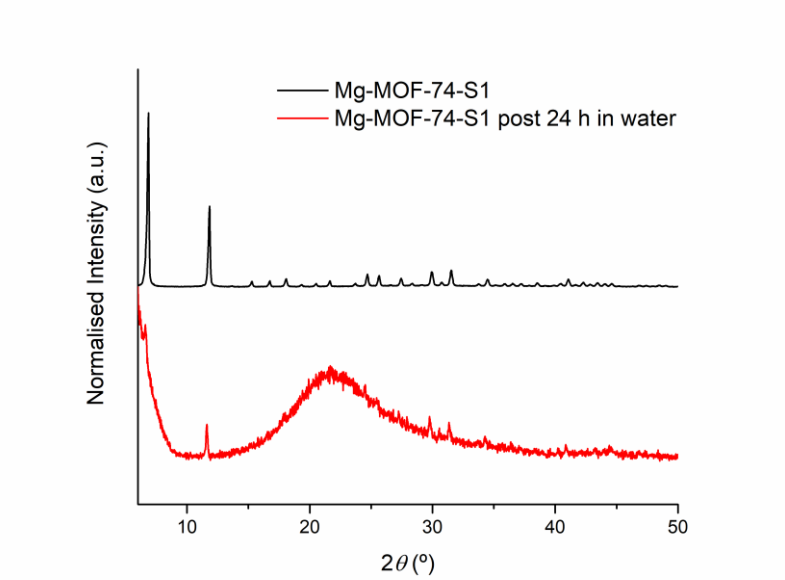

Figure A.16 - PXRD of the stability test of **Mg-MOF-74-S1** after 24 h in water.

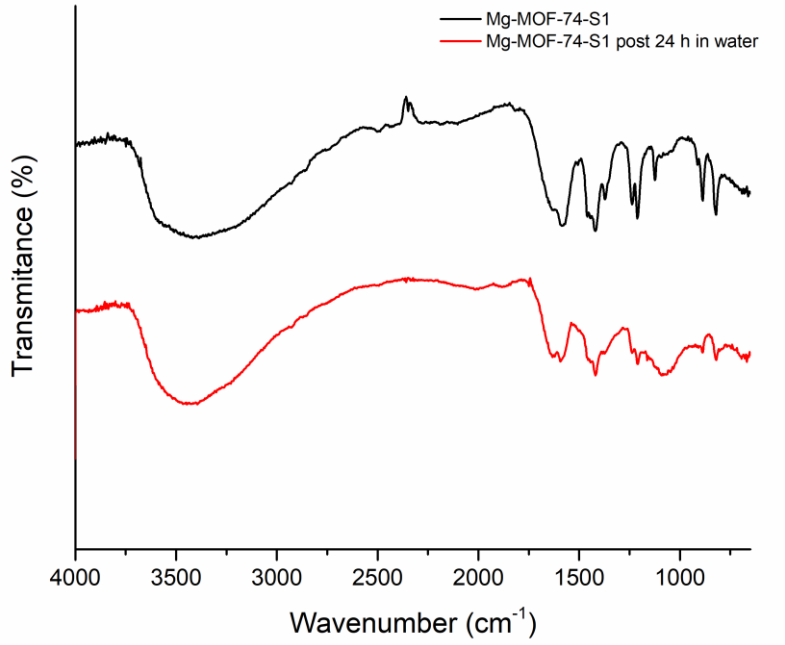

Figure A.17 - FTIR spectra (DRIFT) of **Mg-MOF-74-S1** post 24 h in water.

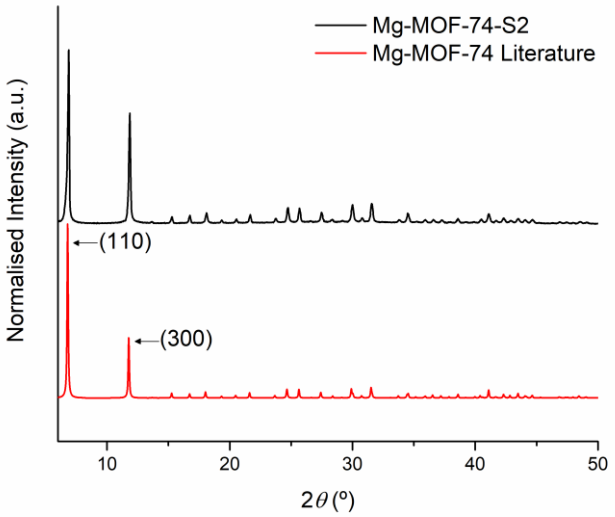

Figure A.18 - PXRD of **Mg-MOF-74-S2** and comparison with the Mg-MOF-74 diffraction pattern from the literature.[159]

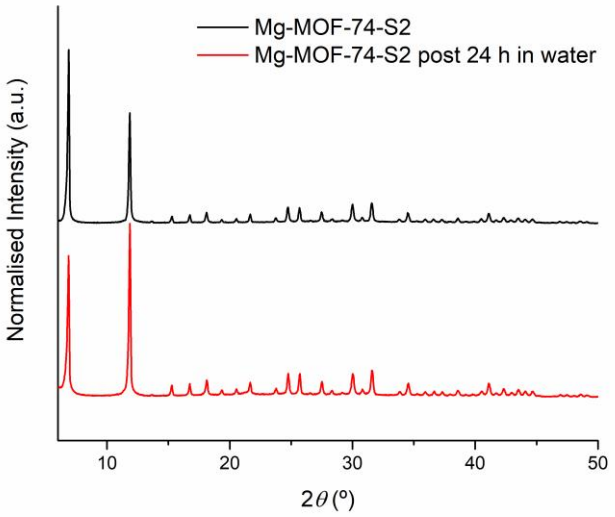

Figure A.19 - PXRD of the stability test of **Mg-MOF-74-S2** after 24 h in water.

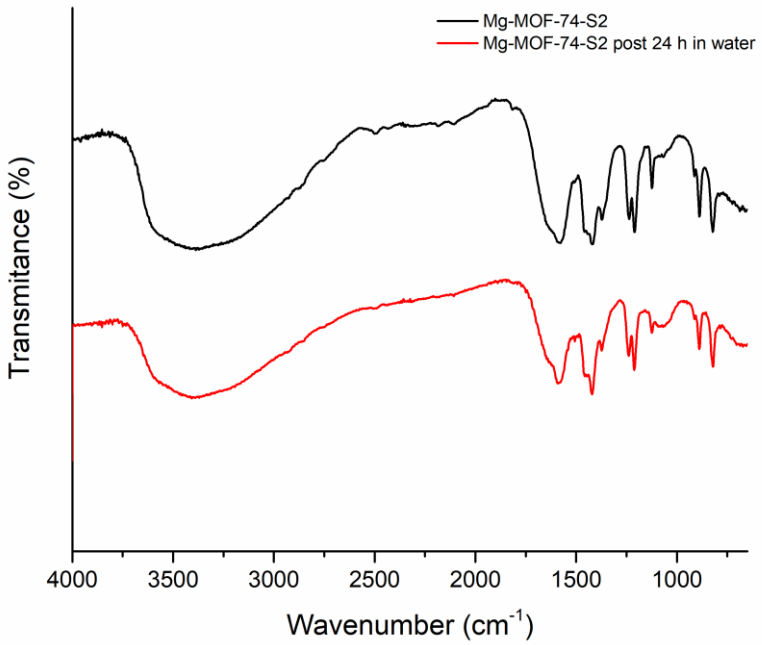

Figure A.20 - FTIR spectra (DRIFT) of **Mg-MOF-74-S2** post 24 h in water.

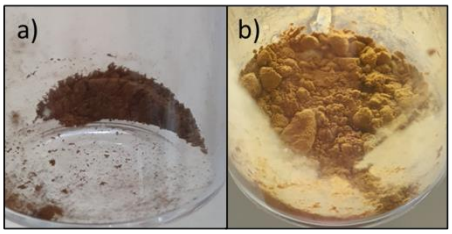

Figure A.21 - a) **Ni-MOF-74-S1** and b) **Ni-MOF-74-S2** obtained powders via solvothermal synthesis.

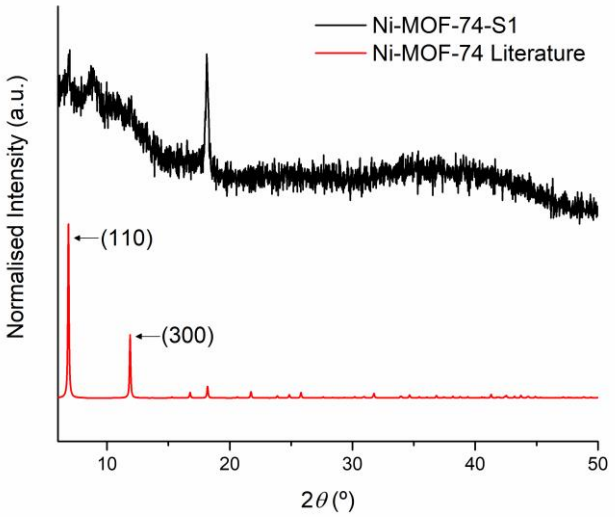

Figure A.22 - PXRD of **Ni-MOF-74-S1** and comparison with the Ni-MOF-74 diffraction pattern from the literature.[164]

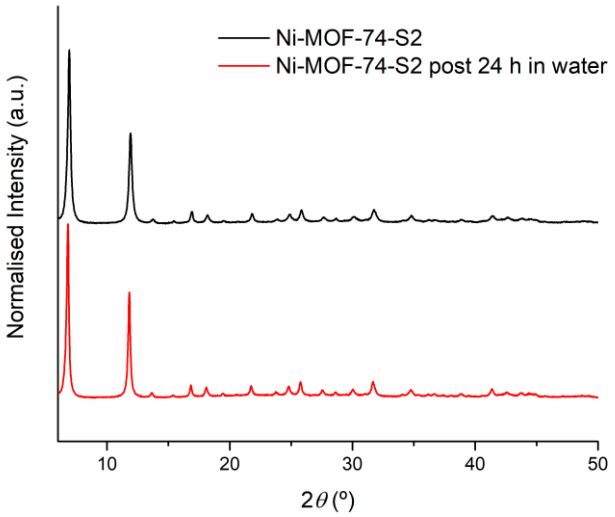

Figure A.23 - PXRD of the stability test of **Ni-MOF-74-S2** after 24 h in water.

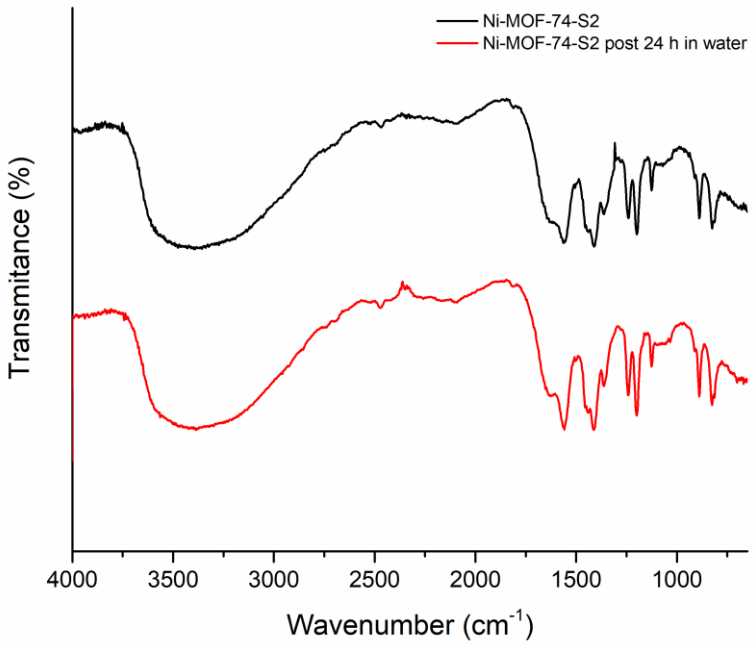

Figure A.24 - FTIR spectra (DRIFT) of **Ni-MOF-74-S2** post 24 h in water.

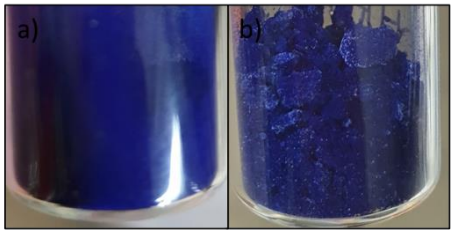

Figure A.25 - a) **HKUST-1-S1** and b) **HKUST-1-S2** obtained powders via solvothermal synthesis.

Figure A.26 - **HKUST-1-S1** after immersion in water for 24 h.

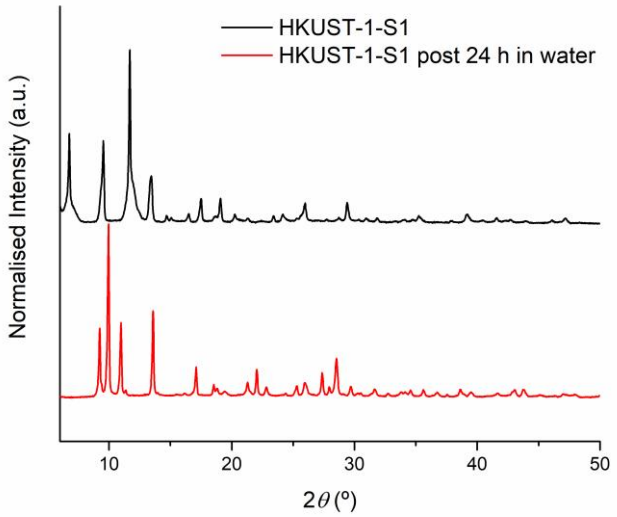

Figure A.27 - PXRD of the stability test of **HKUST-1-S1** after 24 h in water.

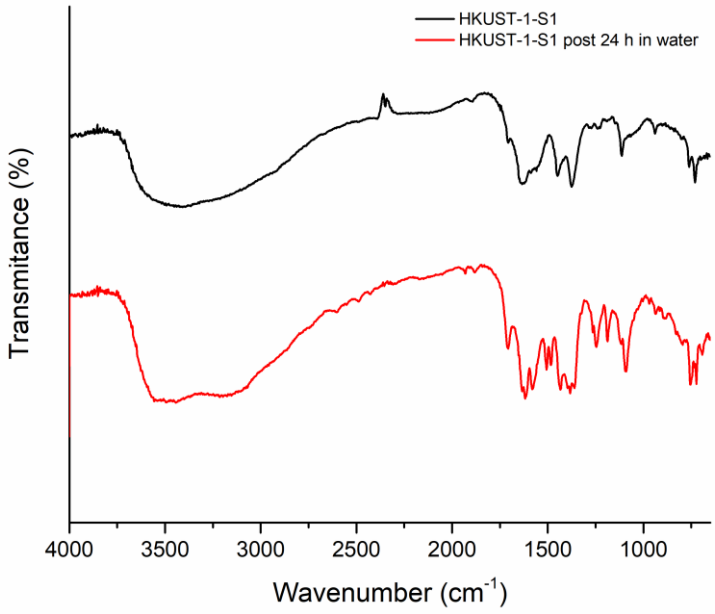

Figure A.28 – FTIR spectra (DRIFT) of **HKUST-1-S1** post 24 h in water.

M

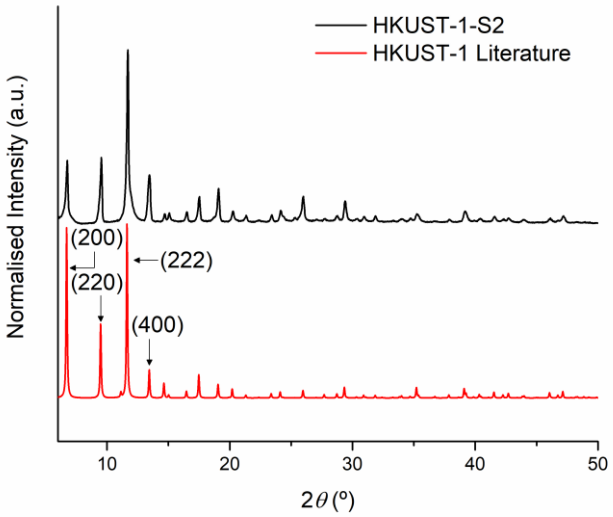

Figure A.29 – PXRD of **HKUST-1-S2** and comparison with the HKUST-1 diffraction pattern from the literature.[166]

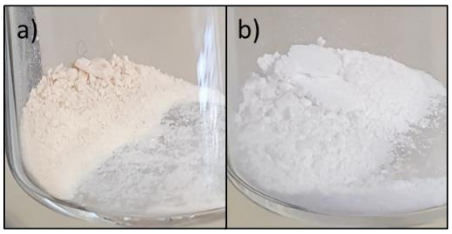

Figure A.30 - a) **UiO-66-S1** and b) **UiO-66-S2** obtained powders via solvothermal synthesis.

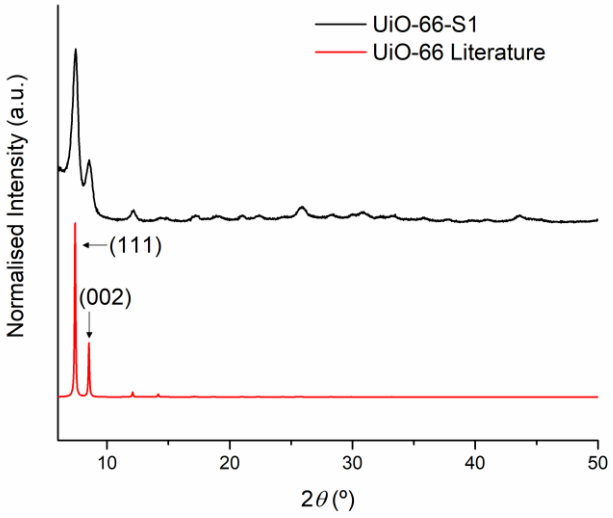

Figure A.31 – PXRD of **UiO-66-S1** and comparison with the UiO-66 diffraction pattern from the literature.[172]

N

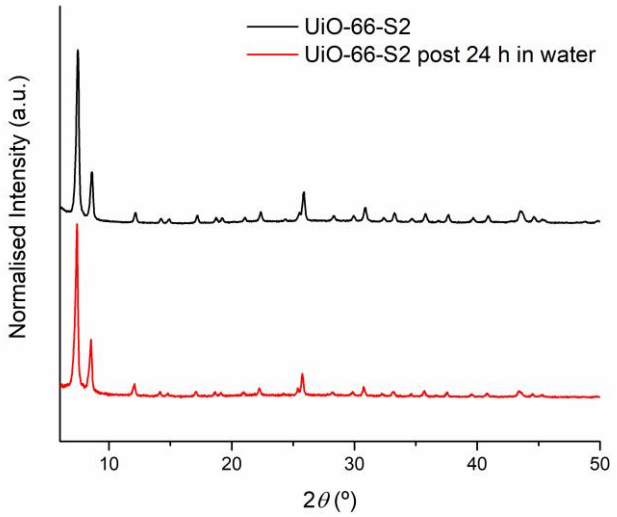

Figure A.32 - PXRD of the stability test of **UiO-66-S2** after 24 h in water.

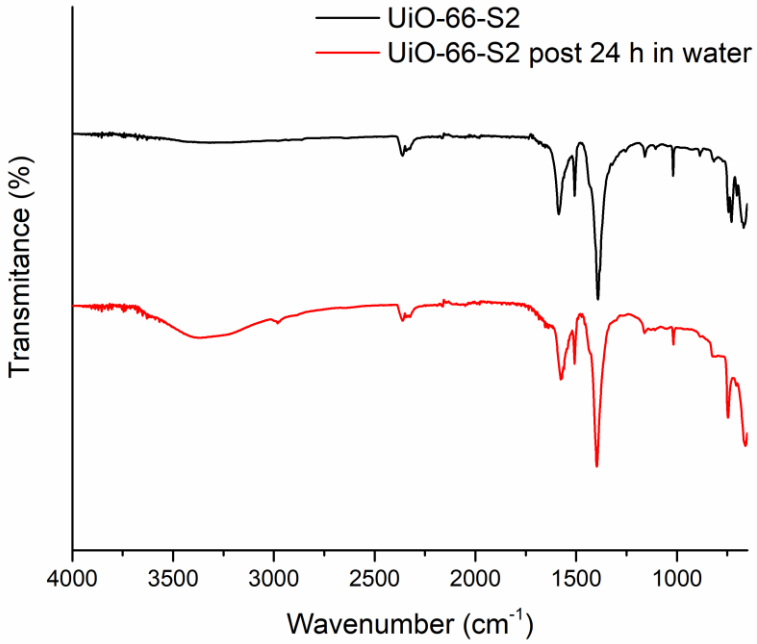

Figure A.33 – FTIR spectra (ATR) of **UiO-66-S2** post 24 h in water.

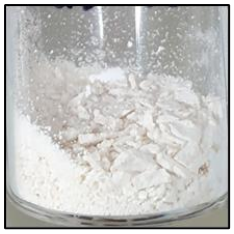

Figure A.34 - UiO-66-NH_2-S1 obtained powder via solvothermal synthesis.

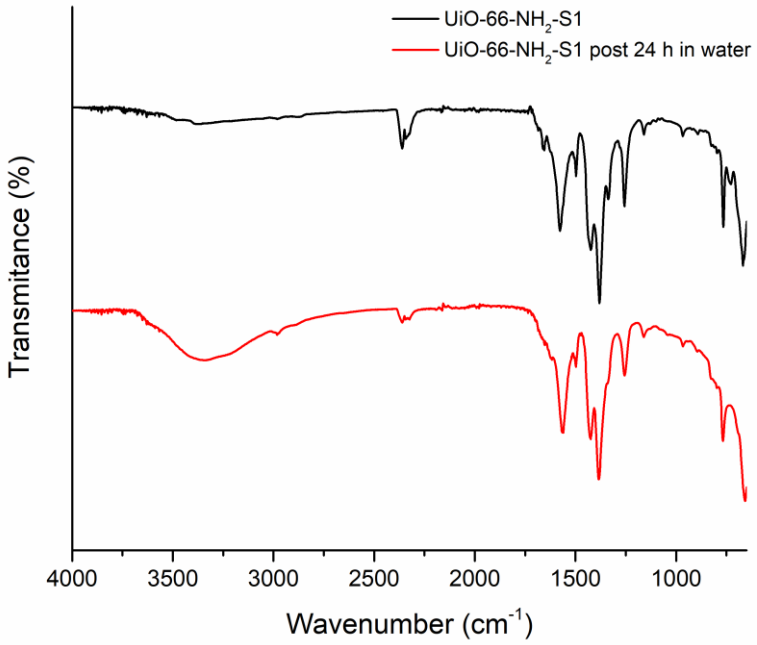

Figure A.35 – FTIR spectra (ATR) of UiO-66-NH_2-S1 post 24 h in water.

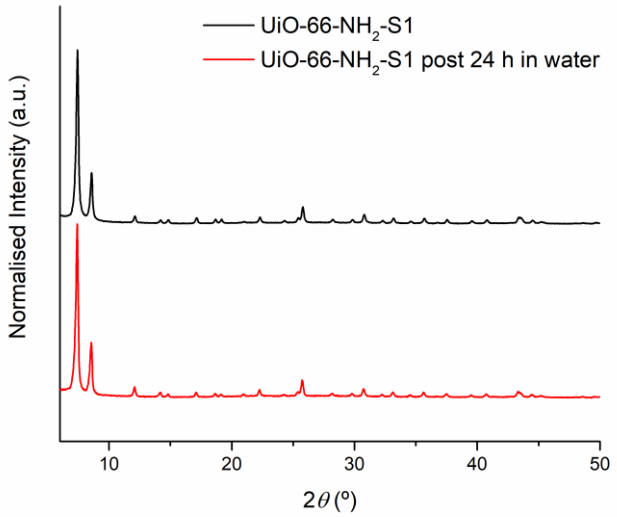

Figure A.36 - PXRD of the stability test of **UiO-66-NH_2-S1** after 24 h in water.

Table A.1 – MOF-5 conditions used in the cathodic deposition.

Metal Ion/Cluster	Organic Ligand	Probase	Solvent	Time	E (V)
100 mM $Zn(NO_3)_2 \cdot 6H_2O$	50 mM H_2BDC	100 mM Et_3NHCl	10 mL DMF	30 min	-1.4
10 mM $Zn(NO_3)_2 \cdot 6H_2O$	5 mM H_2BDC	10 mM Et_3NHCl	10 mL Dry DMF	30 min	-1.4
10 mM $Zn(NO_3)_2 \cdot 6H_2O$	5 mM H_2BDC	10 mM Et_3NHCl	10 mL Dry DMF	1 h 30 min	-1.4
10 mM $Zn(NO_3)_2 \cdot 6H_2O$	5 mM H_2BDC	20 mM H_2O_2	10 mL Dry DMF	30 min	-1.4
150 mM $Zn(NO_3)_2 \cdot 6H_2O$	50 mM H_2BDC	300 mM Et_3NHCl	10 mL Dry DMF	15 min	-1.5
100 mM $Zn(NO_3)_2 \cdot 6H_2O$	100 mM H_2BDC	200 mM H_2O_2	10 mL DMF	10 min	-1.5
100 mM $Zn(NO_3)_2 \cdot 6H_2O$	100 mM H_2BDC	200 mM H_2O_2	10 mL DMF	15 min	-0.5

Q

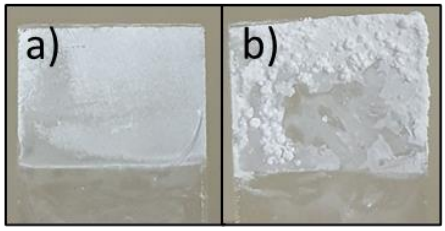

Figure A.37 – a) **MOF-5-C1** and b) **MOF-5-C2** obtained using cathodic deposition.

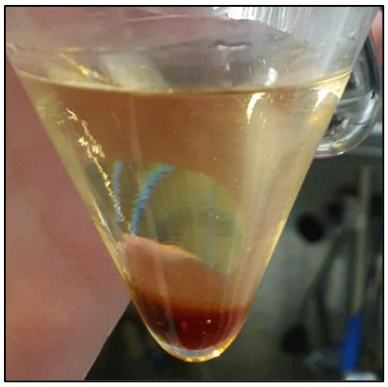

Figure A.38 – Detected precipitation during IRMOF-3 cathodic deposition.

Table A.2 – Mg-MOF-74 (yellow) and Ni-MOF-74 (green) conditions used in the cathodic deposition.

Metal Ion/Cluster	Organic Ligand	Probase	Solvent	Time	E (V)
4 mM $MgCl_2 \cdot 6H_2O$	2 mM DHTA	2 mM Et_3NHCl	10 mL DMF	1 h	-1.3
4 mM $MgCl_2 \cdot 6H_2O$	2 mM DHTA	8 mM H_2O_2	10 mL DMF	1 h	-1.3
100 mM $Ni(NO_3)_2 \cdot 6H_2O$	50 mM DHTA	100 mM Et_3NHCl	10 mL Dry DMF	30 min	-1.3
4 mM $NiCl_2 \cdot 6H_2O$	2 mM DHTA	2 mM Et_3NHCl	10 mL DMF	30 min	-1.3
4 mM $NiCl_2 \cdot 6H_2O$	2 mM DHTA	2 mM H_2O_2	10 mL DMF	30 min	-1.3
4 mM $NiCl_2 \cdot 6H_2O$	2 mM DHTA	2 mM Et_3NHCl	10 mL DMF	1 h	-1.3

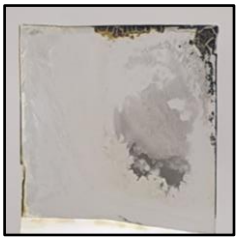

Figure A.39 – **Mg-MOF-74-C1** obtained using cathodic deposition.

Table A.3 – UiO-66 conditions used in the cathodic deposition.

Metal Ion/Cluster	Organic Ligand	Probase	Solvent	Time	E (V)
100 mM $ZrCl_4$	100 mM H_2BDC	200 mM H_2O_2	10 mL DMF	30 min	-0.5
4 mM $ZrCl_4$	4 mM H_2BDC	8 mM H_2O_2	10 mL DMF	30 min	-0.5
4 mM $ZrCl_4$	4 mM H_2BDC	2 mM Et_3NHCl	10 mL DMF	30 min	-1.4
4 mM $ZrCl_4$	4 mM H_2BDC	8 mM H_2O_2	10 mL DMF	2 h	-0.5

Table A.4 – ZIF-8 conditions used in the electrophoretic deposition.

Precursor	Solvent	Time	Electric Field ($V\ cm^{-1}$)
10 mg ZIF-8	20 mL Isopropanol	30 min	20
9.26 mM $Zn(NO_3)_2 \cdot 6H_2O$ + 691mM Hmim	20 mL H_2O	4 min	1
10 mg ZIF-8	20 mL Toluene	2 h 30 min	90
10 mg ZIF-8	20 mL EtOH	2 h 30 min	90

Table A.5 - Mg-MOF-74 (yellow) and Ni-MOF-74 (green) conditions used in the electrophoretic deposition.

Precursor	Solvent	Time	Electric Field ($V\ cm^{-1}$)
10 mg Mg-MOF-74	20 mL EtOH + 100 µl Acetic Acid	2 h 30 min	60
10 mg Mg-MOF-74	20 mL EtOH + 10 µl Acetic Acid	2 h 30 min	60
10 mg Mg-MOF-74	20 mL Toluene	2 h 30 min	60
10 mg Ni-MOF-74	20 mL Toluene	6 h	25
10 mg Ni-MOF-74	20 mL Toluene	2 h 30 min	60
10 mg Ni-MOF-74	20 mL Toluene	2 h 30 min	90
10 mg Ni-MOF-74	20 mL Toluene	2 h 30 min	30
10 mg Ni-MOF-74	20 mL Acetone	2 h 30 min	90
10 mg Ni-MOF-74	20 mL Toluene	6 h	90
10 mg Ni-MOF-74	20 mL EtOH	2 h 30 min	60
10 mg Ni-MOF-74	20 mL EtOH + Acetic Acid	2 h 30 min	60

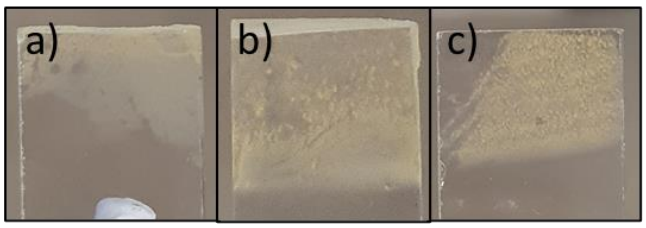

Figure A.40 – a) **Ni-MOF-74-E1**, b) **Ni-MOF-74-E2** and c) **Ni-MOF-74-E3** obtained using electrophoretic deposition.

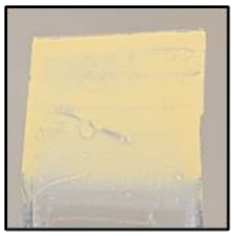

Figure A.41 – Ni-MOF-74-E4 obtained using electrophoretic deposition.

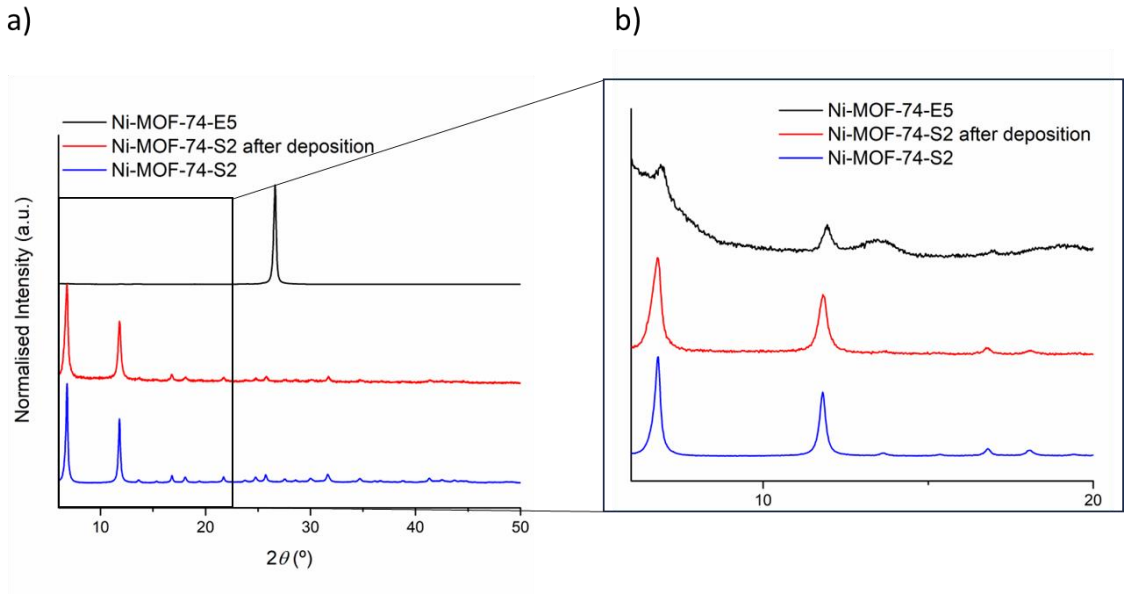

Figure A.42 – PXRD of Ni-MOF-74-S5, used powder Ni-MOF-74-S2 both before and after deposition normalised using a) full range and b) 5-20º.

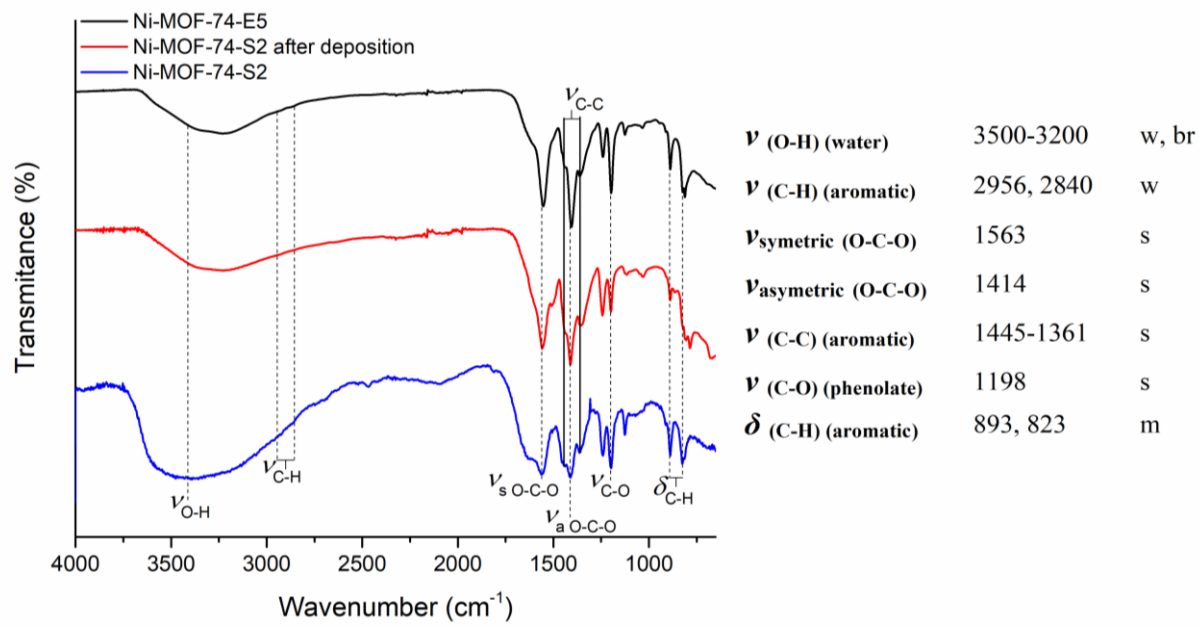

Figure A.43 – FTIR spectra (DRIFT/ATR) of Ni-MOF-74-E5, used powder Ni-MOF-74-S2 both before and after deposition and wavenumber values of the corresponding main vibrational modes.

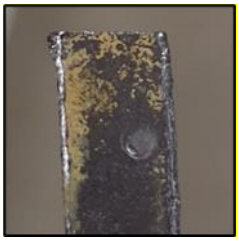

Figure A.44 – Ni-MOF-74-E5 obtained using electrophoretic deposition.

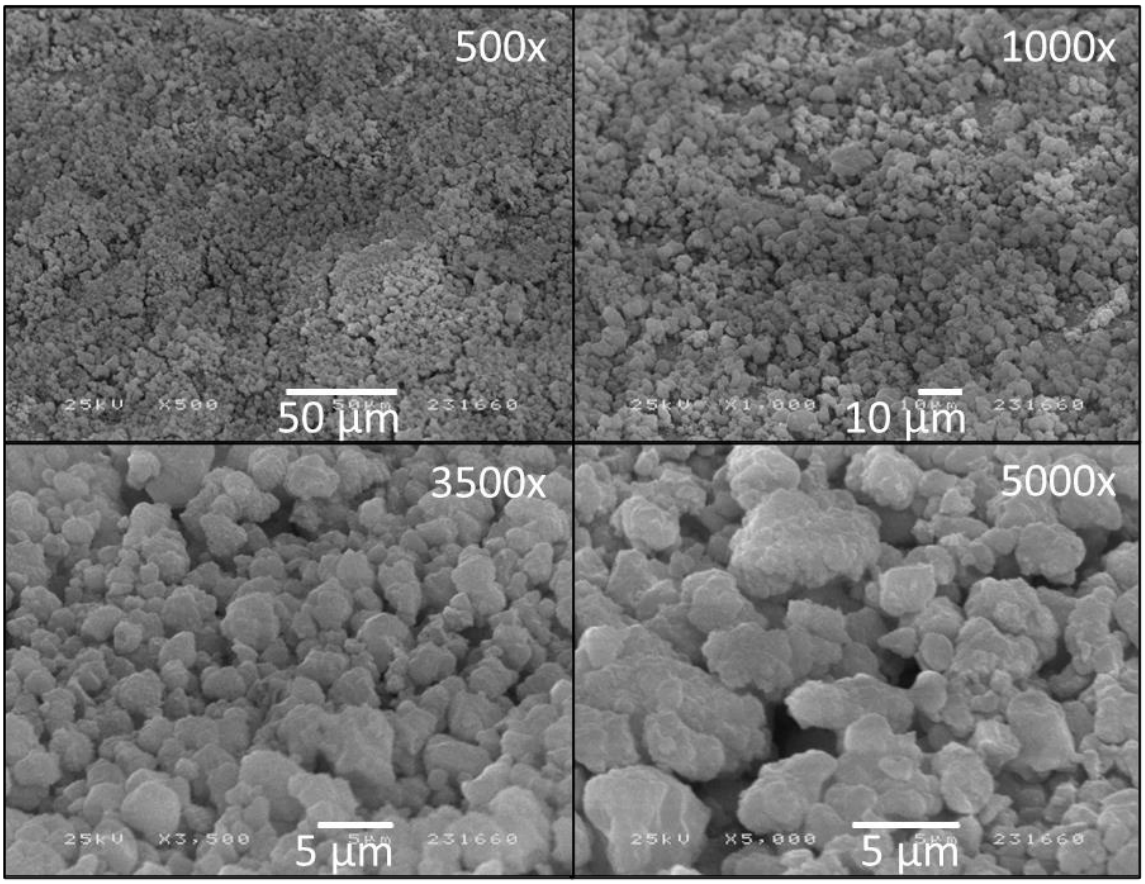

Figure A.45 – SEM images of Ni-MOF-74-E5. Magnified at 500x, 1000x, 3500x and 5000x.

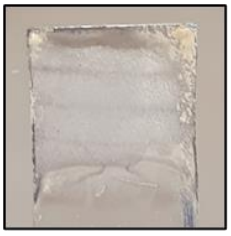

Figure A.46 – Mg-MOF-74-E1 obtained using electrophoretic deposition.

Table A.6 – UiO-66 (blue) and UiO-66-NH_2 (orange) conditions used in the electrophoretic deposition.

Precursor	Solvent	Time	Electric Field (Vcm^{-1})
10 mg UiO-66	20 mL Toluene	2 h 30 min	60
10 mg UiO-66	20 mL EtOH + 10 µl Acetic Acid	2 h 30 min	60
10 mg UiO-66	20 mL Toluene	2 h 30 min	90
10 mg UiO-66	20 mL Toluene + 10 µl Acetic Acid	2 h 30 min	60
10 mg UiO-66	20 mL EtOH	2 h 30 min	60
10 mg UiO-66	20 mL EtOH + 10 µl Acetic Acid	1 h	60
10 mg UiO-66	20 mL EtOH + 10 µl Acetic Acid	15 min	90
10 mg UiO-66	20 mL EtOH + 10 µl Acetic Acid	5 min	90
10 mg UiO-66-NH_2	20 mL EtOH + 10 µl Acetic Acid	5 min	90

Figure A.47 – **UiO-66-E1** obtained using electrophoretic deposition.

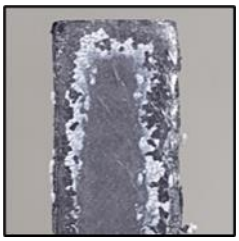

Figure A.48 – **UiO-66-E2** obtained using electrophoretic deposition.

Figure A.49 – **UiO-66-NH$_2$-E1** obtained using electrophoretic deposition.

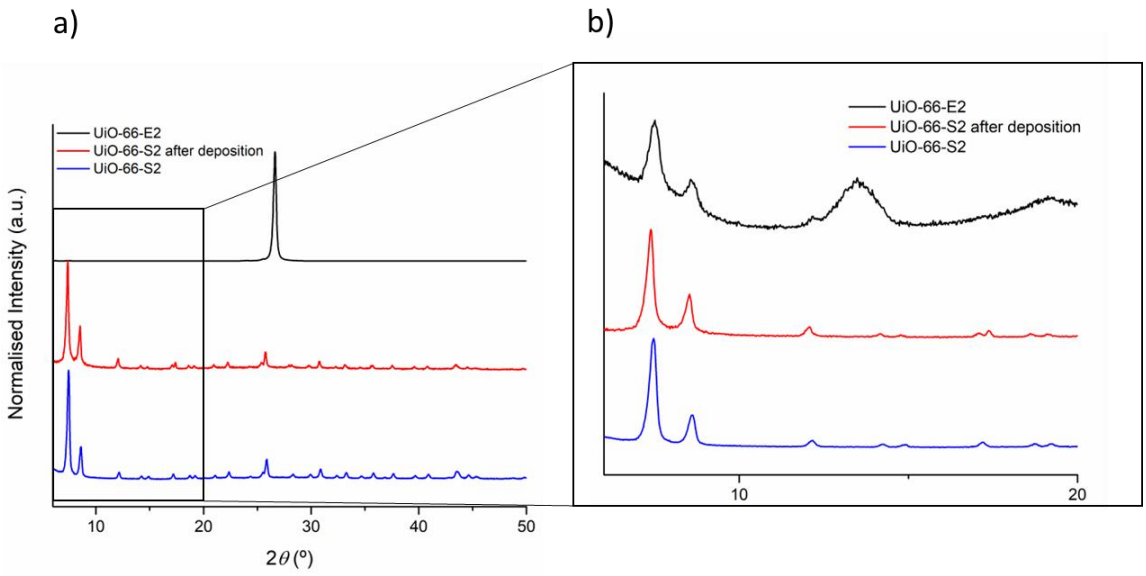

Figure A.50 - PXRD of **UiO-66-E2**, used powder **UiO-66-S2** both before and after deposition normalised using a) full range and b) 5-20º.

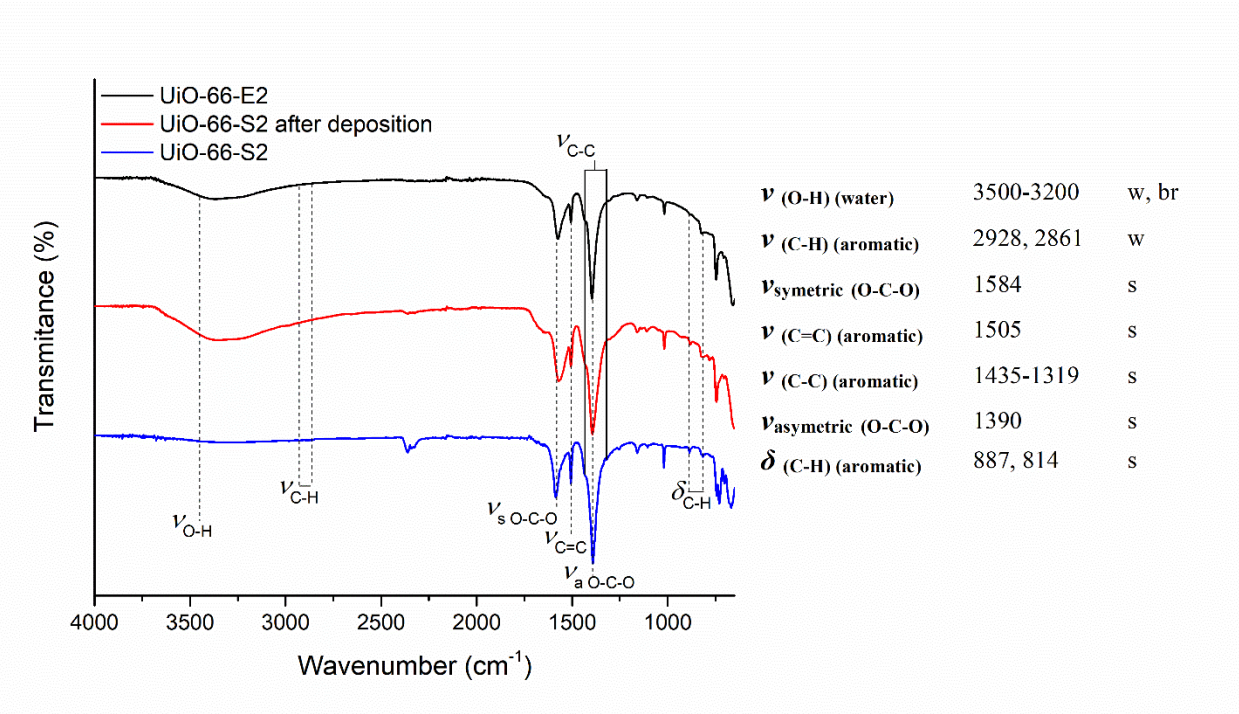

Figure A.51 – FTIR spectra (ATR) of **UiO-66-E2**, used powder **UiO-66-S2** both before and after deposition and wavenumber values of the corresponding main vibrational modes.

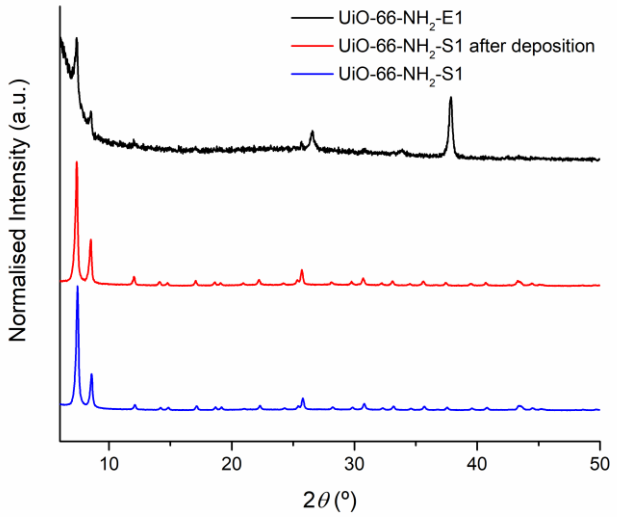

Figure A.52 - PXRD of **UiO-66-NH$_2$-E1**, used powder **UiO-66-NH$_2$-S1** both before and after deposition.

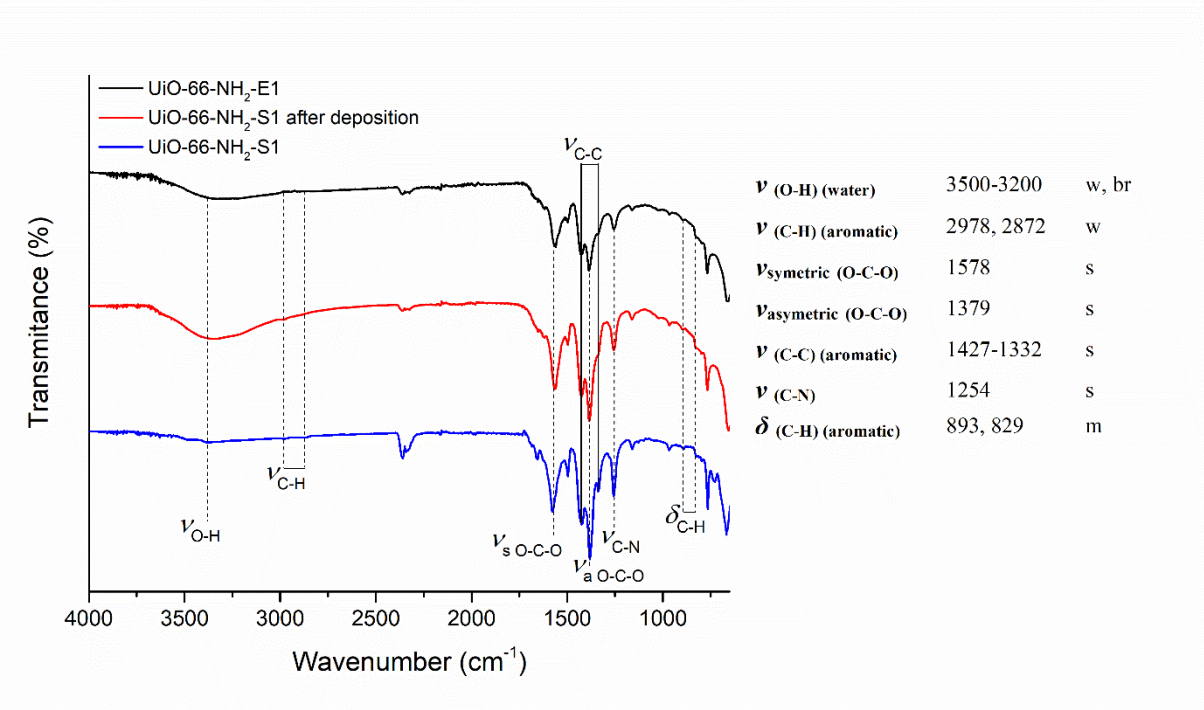

Figure A.53 - FTIR spectra (ATR) of **UiO-66-NH2-E1**, used powder **UiO-66-NH2-S1** both before and after deposition and wavenumber values of the corresponding main vibrational modes.

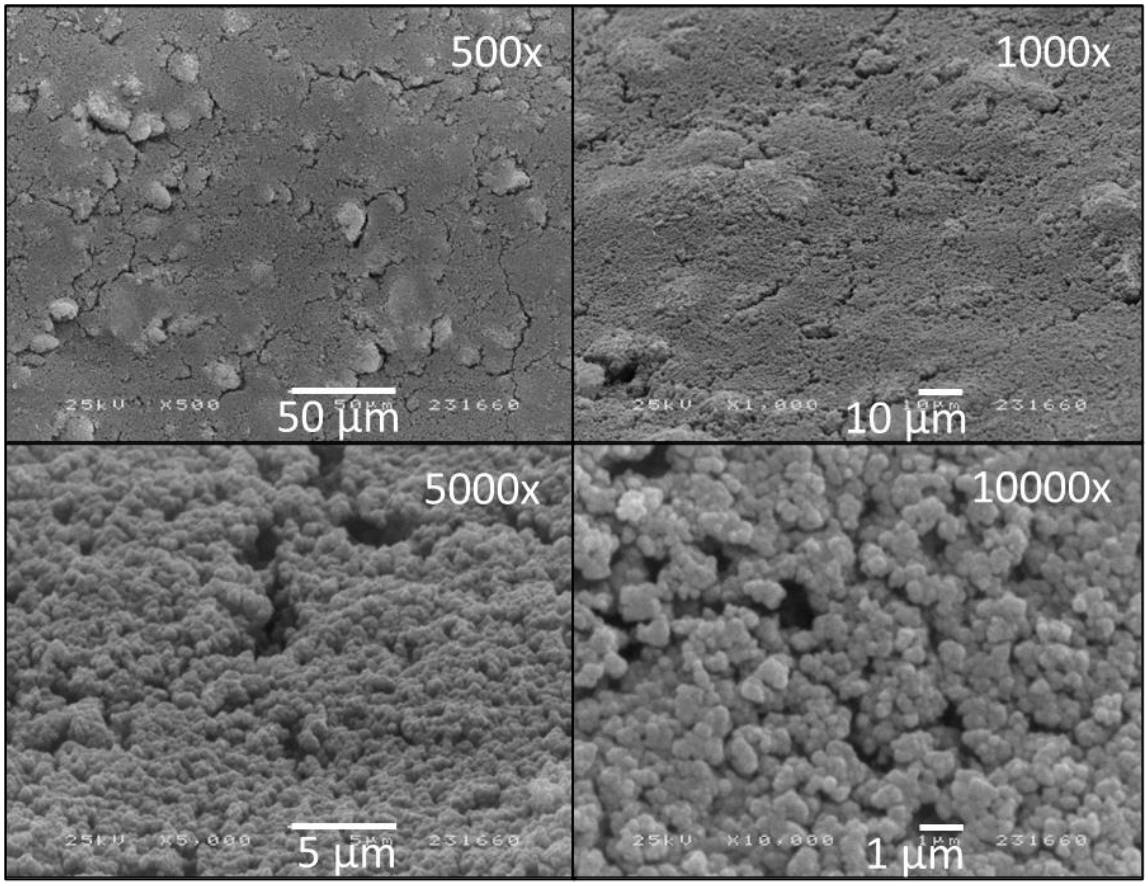

Figure A.54 - SEM images of **UiO-66-E2**. Magnified at 500x, 1000x, 5000x and 10000x.

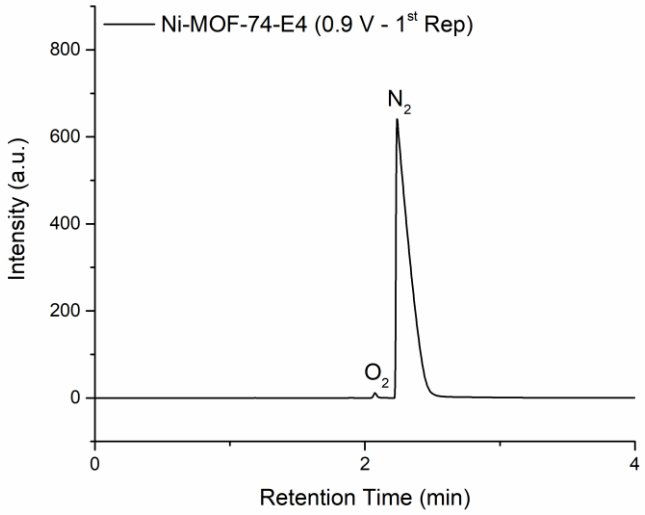

Figure A.55 - GC-TCD chromatogram obtained for **Entry 1** (**Table 2.5**) of the **Ni-MOF-74-E4** using an applied *E* of 0.9 V.

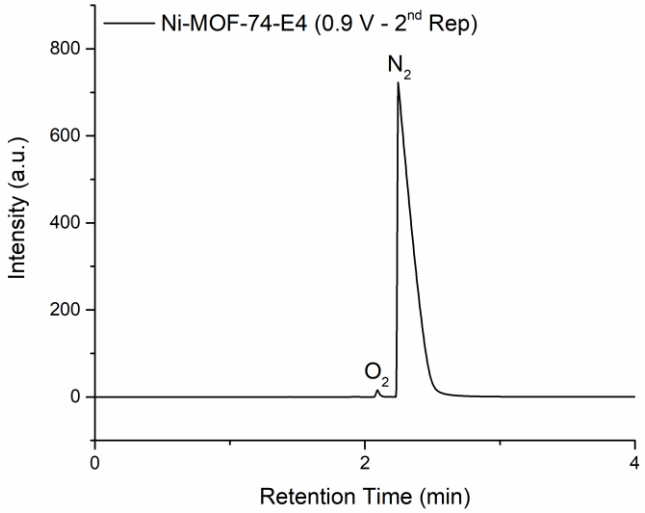

Figure A.56 - GC-TCD chromatogram obtained for **Entry 2** (**Table 2.5**) of the **Ni-MOF-74-E4** using an applied *E* of 0.9 V.

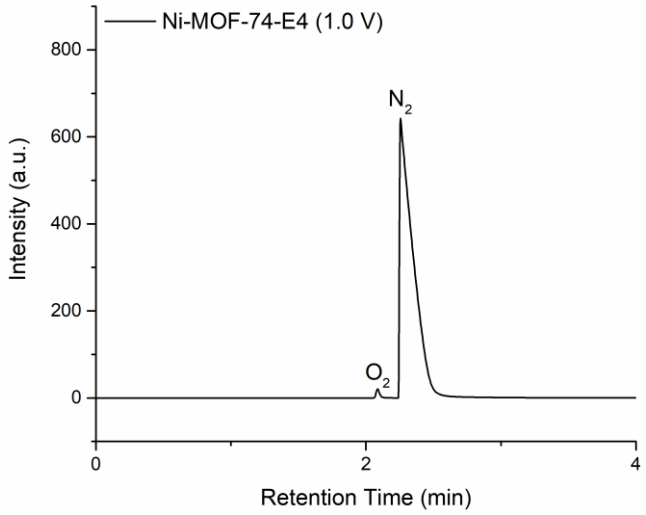

Figure A.57 - GC-TCD chromatogram obtained for **Entry 3** (**Table 2.5**) of the **Ni-MOF-74-E4** using an applied *E* of 1.0 V.

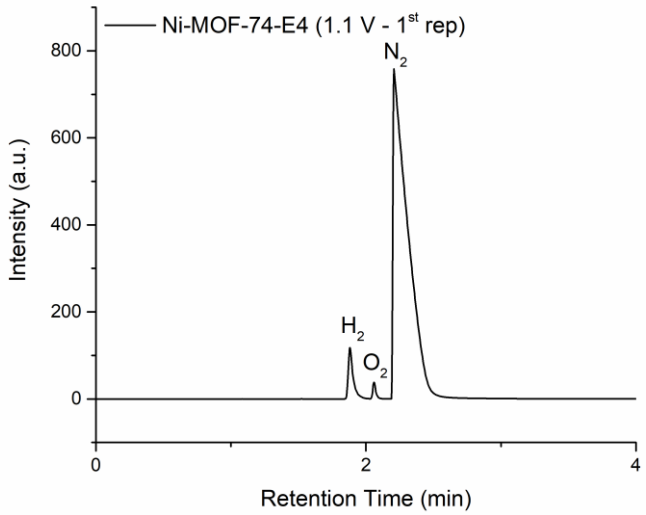

Figure A.58 - GC-TCD chromatogram obtained for the **Entry 4** (**Table 2.5**) of the **Ni-MOF-74-E4** using an applied *E* of 1.1 V.

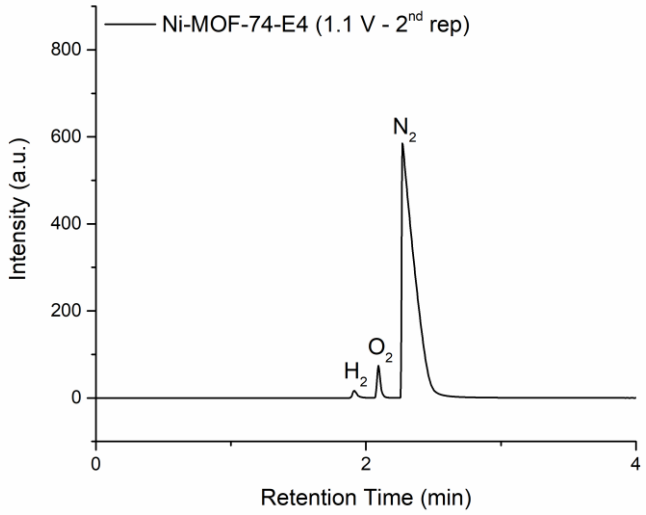

Figure A.59 - GC-TCD chromatogram obtained for **Entry 5** (**Table 2.5**) of the **Ni-MOF-74-E4** using an applied *E* of 1.1 V.

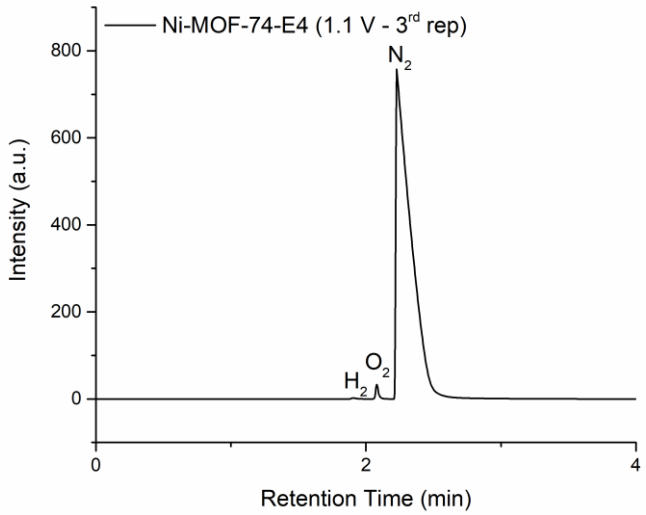

Figure A.60 - GC-TCD chromatogram obtained for **Entry 6** (**Table 2.5**) of the **Ni-MOF-74-E4** using an applied *E* of 1.1 V.

Figure A.61 – **Ni-MOF-74-E4** after CPE at 1.1 V (**Entry 4**).

Table A.7 - Quantification of the obtained H_2, O_2 and N_2 after CPE using the bare FTO. Values obtained via GC-TCD using the respective gases calibration curves. For the CPE experiments: Pt coil and Ag/AgCl, 3M NaCl were used as CE and RE in the CPE experiments. Area of the electrode: 1 cm^2

			Quantity (µmol)			
Solution Contents	E(V)	Entry	Average	H_2	O_2	N_2
0.5 M NH_4Cl + 4 mM NH_4OH in 10 mL of water	1.3	1	1.37	**1.78**	50.27	2088.91
		2		**0.55**	51.12	2151.70
		3		**1.78**	104.45	2546.65

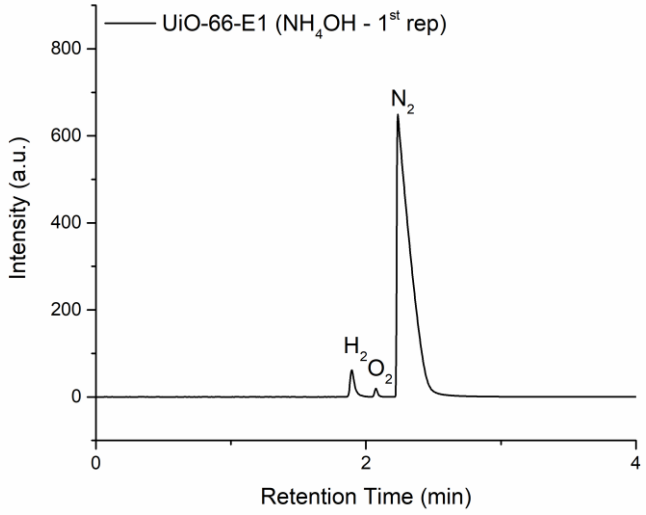

Figure A.62 - GC-TCD chromatogram obtained for **Entry 1** (**Table 2.6**) of the **UiO-66-E1** in the presence of ammonia using an applied *E* of 1.3 V.

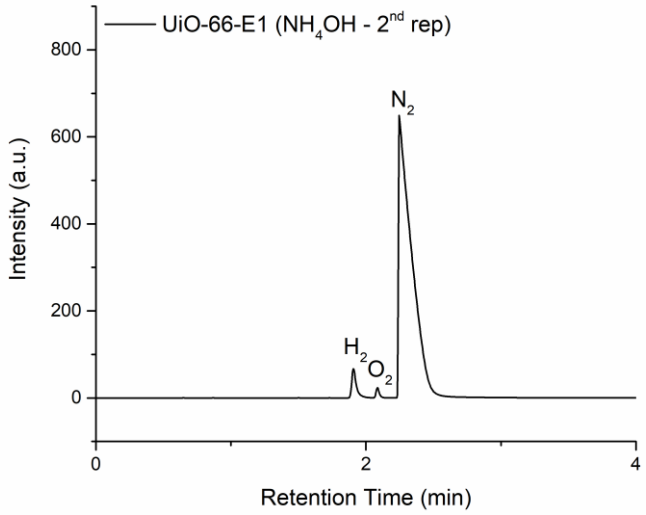

Figure A.63 - GC-TCD chromatogram obtained for **Entry 2** (**Table 2.6**) of the **UiO-66-E1** in the presence of ammonia using an applied *E* of 1.3 V.

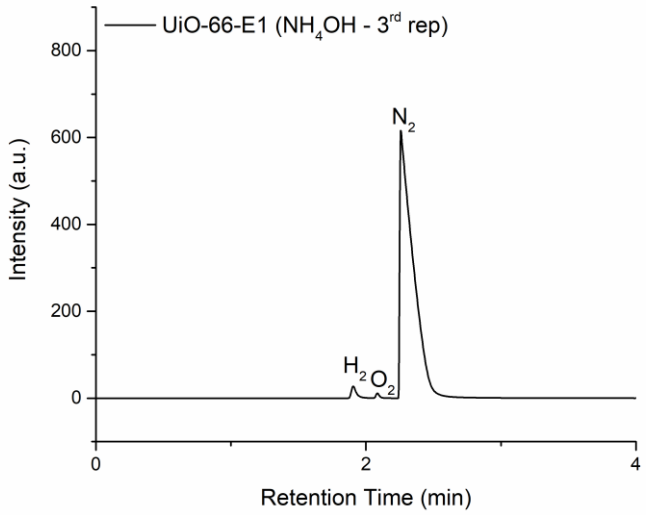

Figure A.64 - GC-TCD chromatogram obtained for **Entry 3** (**Table 2.6**) of the **UiO-66-E1** in the presence of ammonia using an applied *E* of 1.3 V.

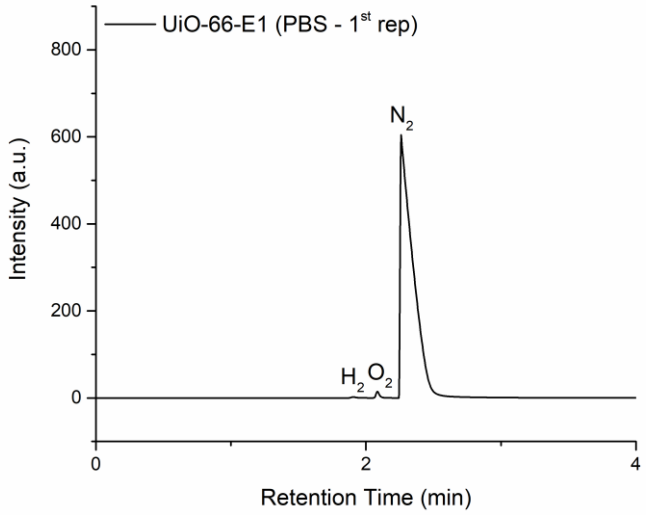

Figure A.65 - GC-TCD chromatogram obtained for **Entry 4** (**Table 2.6**) of the **UiO-66-E1** in the PBS solution using an applied *E* of 1.3 V.

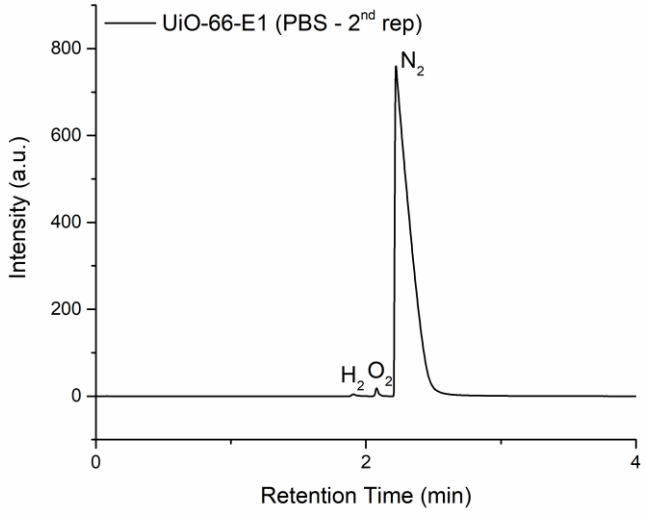

Figure A.66 - GC-TCD chromatogram obtained for **Entry 5** (**Table 2.6**) of the **UiO-66-E1** in the PBS solution using an applied *E* of 1.3 V.

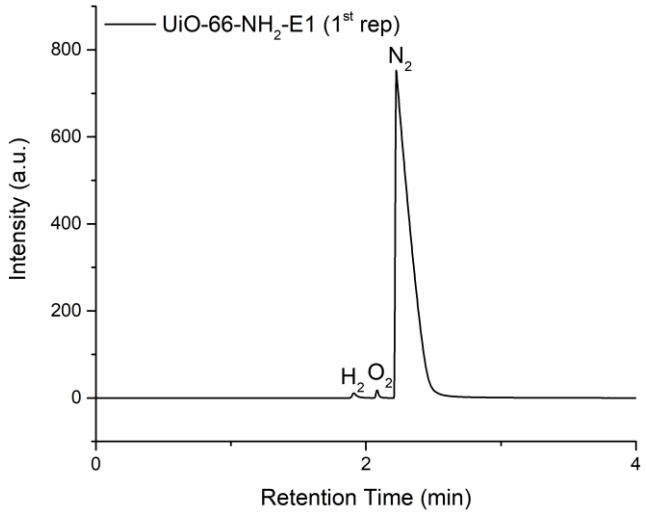

Figure A.67 - GC-TCD chromatogram obtained for **Entry 1** (**Table 2.7**) of the **UiO-66-NH$_2$-E1** in the presence of ammonia using an applied *E* of 1.3 V.

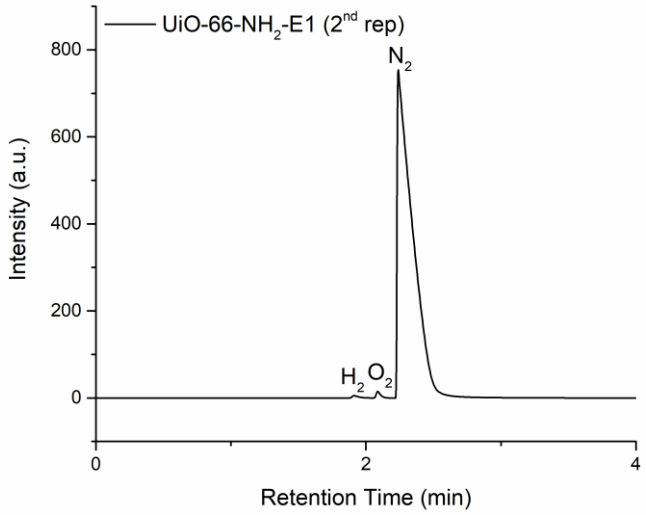

Figure A.68 - GC-TCD chromatogram obtained for **Entry 2** (**Table 2.7**) of **UiO-66-NH$_2$-E1** in the presence of ammonia using an applied *E* of 1.3 V.

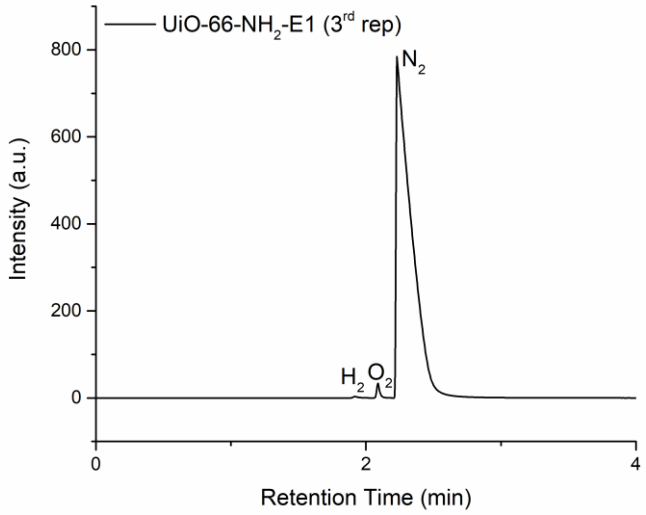

Figure A.69 - GC-TCD chromatogram obtained for **Entry 3** (**Table 2.7**) of **UiO-66-NH$_2$-E1** in the presence of ammonia using an applied *E* of 1.3 V.

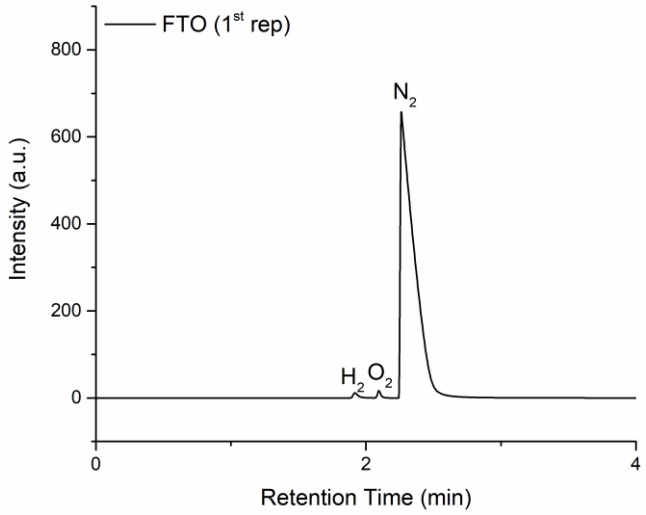

Figure A.70 - GC-TCD chromatogram obtained for **Entry 1** (**Table A.7**) of the bare FTO in the presence of ammonia using an applied *E* of 1.3 V.

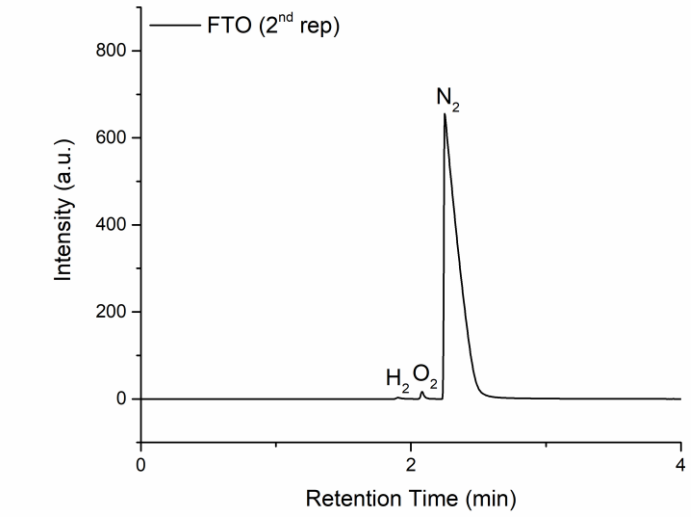

Figure A.71 - GC-TCD chromatogram obtained for **Entry 2** (**Table A.7**) of the bare FTO in the presence of ammonia using an applied *E* of 1.3 V.

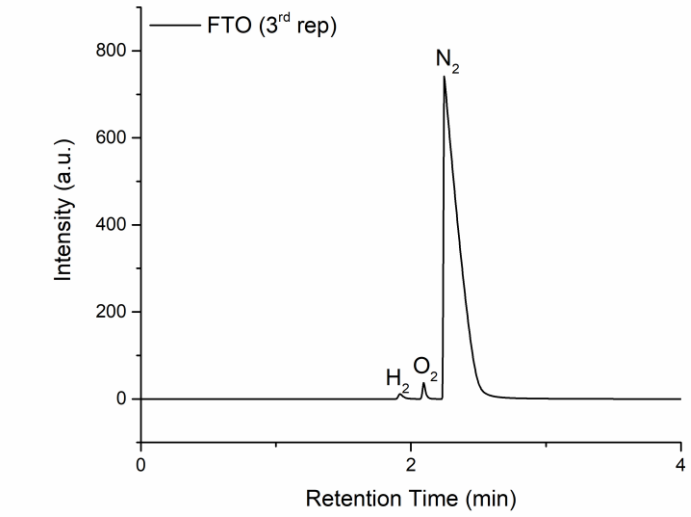

Figure A.72 - GC-TCD chromatogram obtained for **Entry 3** (**Table A.7**) of the bare FTO in the presence of ammonia using an applied *E* of 1.3 V.